Cell Press Selections

Reprint supplement

Stem Cells in Translation

Preclinical Work Moving Stem Cell Research towards the Clinic

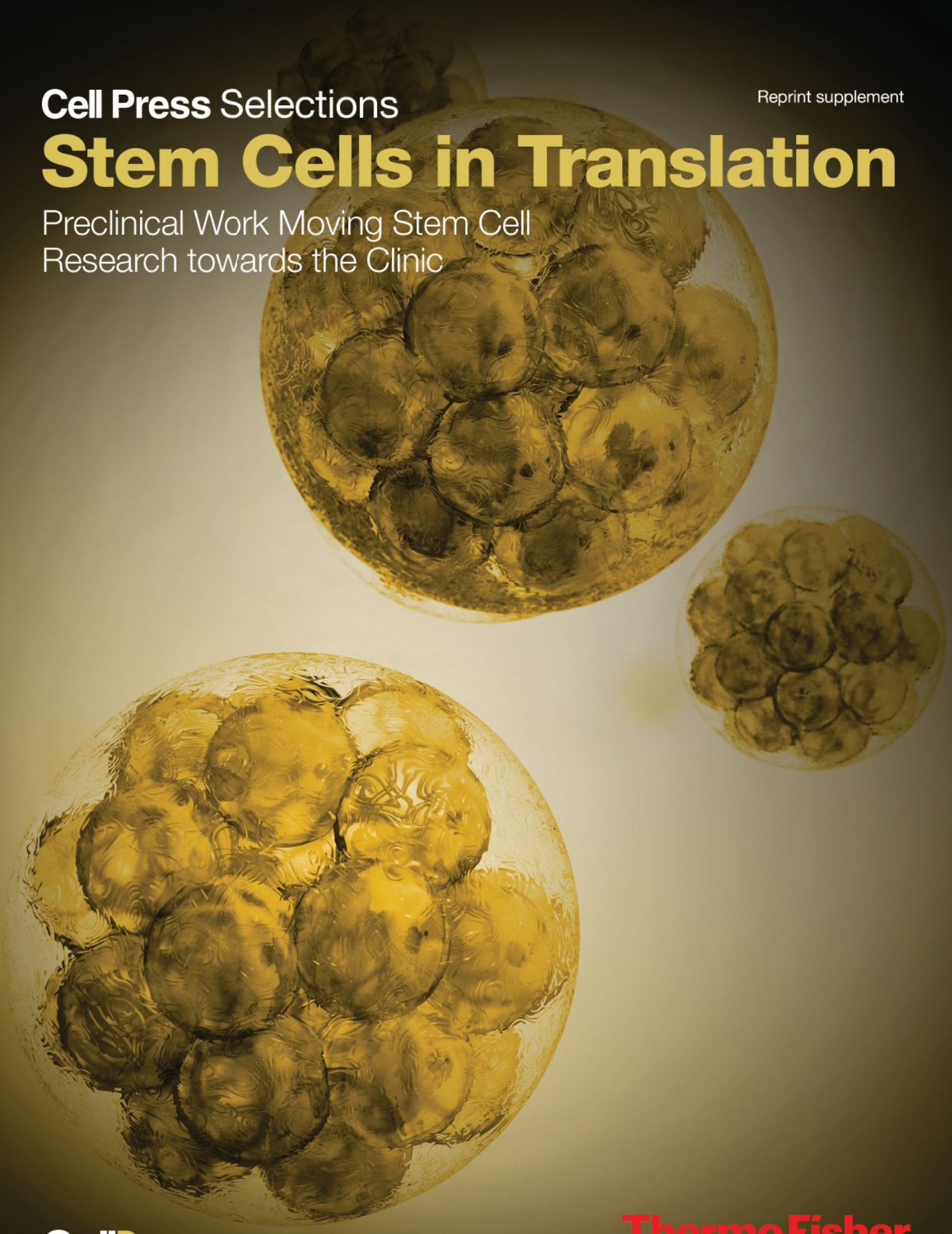

CellPress
www.cell.com

ThermoFisher SCIENTIFIC

gibco

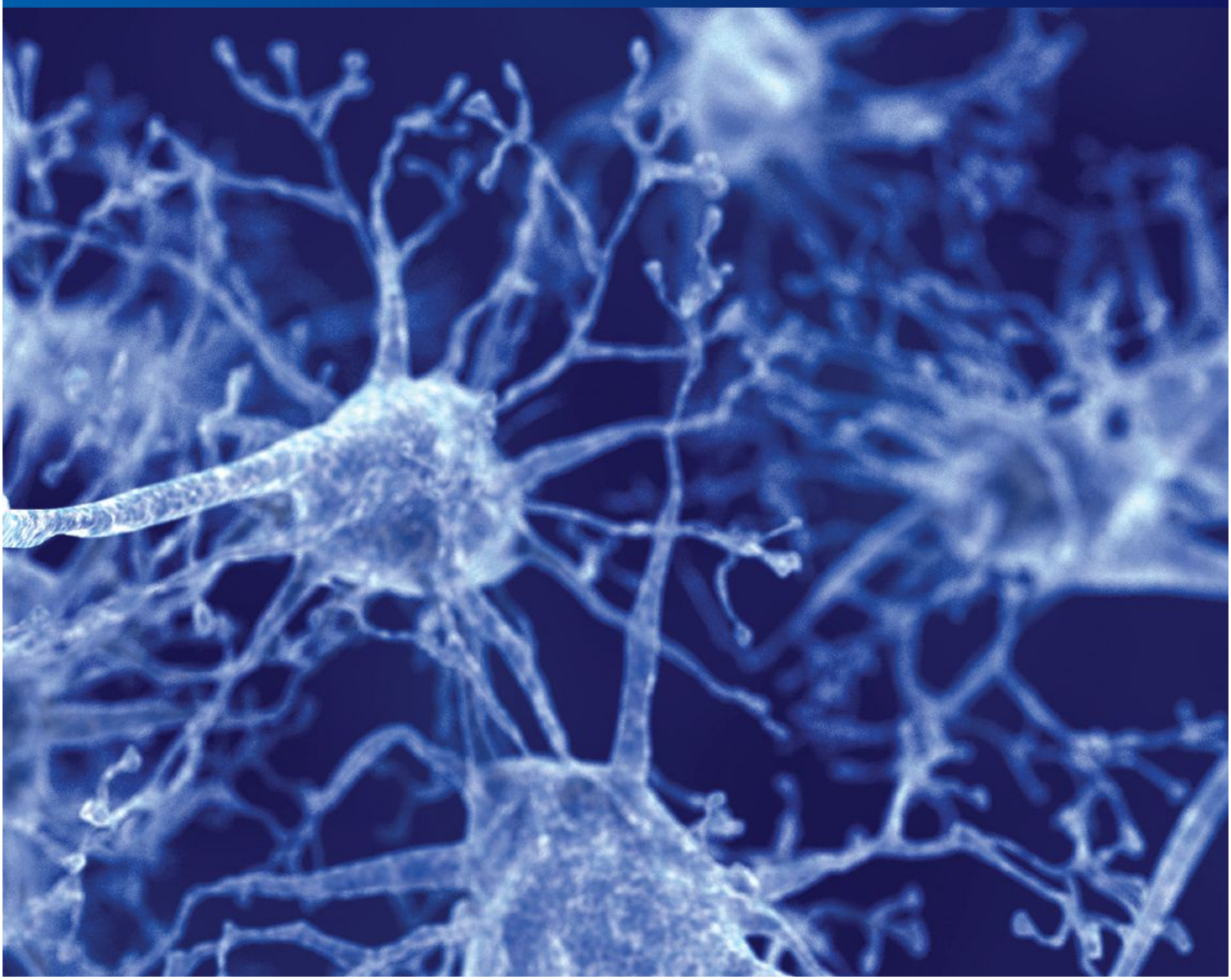

Modeling neurodegenerative disease

Stem cells help develop cellular models for understanding Parkinson's disease

From modeling diseases to discovering therapies, stem cells have the potential to change the way we think about medicine. Our researchers have partnered with The Parkinson's Institute to build a path to more physiologically relevant cellular models for Parkinson's disease using donor cells to generate induced pluripotent stem cells.

Read about the journey the researchers have started, the novel tools they have utilized, and the models they are producing to help advance Parkinson's disease research.

Access the free white papers at **lifetechnologies.com/pdmodels**

ThermoFisher SCIENTIFIC

Foreword

We are pleased to introduce the latest edition of *Cell Press Selections*. These editorially curated reprint collections highlight a particular area of life science by bringing together articles from the Cell Press journal portfolio. In this selection, we present *Cell Stem Cell* articles that focus on clinical translation of stem cell research. The majority of these articles are from the Clinical Progress section of the journal, which is devoted to research studies with an overall goal of moving basic research towards clinical application. The criteria for publication in this section are somewhat different from those of standard research articles and focus more on translational value. To complement these articles, we have also included a Perspective on stem cell therapeutics and a Brief Report describing a preclinical study on Parkinson's disease.

Much of the excitement that surrounds stem cell research, particularly among the general public, stems from the potential for clinical benefit. At *Cell Stem Cell*, we very much support that goal and look forward to moving with the field as clinical translation takes shape. We do believe, however, that all such progress needs to take place against a backdrop of rigorous basic research and careful preclinical analysis to provide clear evidence of both safety and efficacy of proposed therapies before they are tested in patients. The articles in this selection discuss the relevant issues and illustrate the type of preclinical and translational work that needs to take place to pave the way for future clinical application.

We hope you will enjoy reading this collection of articles and will visit www.cell.com to find other high-quality research and review articles across the entire spectrum of the stem cell field.

Finally, we are grateful for the generosity of ThermoFisher Scientific, who helped to make this reprint collection possible.

For more information about Cell Press Selections:
Gordon Sheffield
Program Director, Cell Press Selections
g.sheffield@cell.com
617-386-2189

Invitrogen™

LIPOFECTAMINE®
MessengerMAX™ is your ticket in

Introducing the mRNA transfection reagent with up to 5X the efficiency of DNA reagents in neurons and primary cells

To learn more visit
lifetechnologies.com/messengermax

ThermoFisher SCIENTIFIC

Stem Cells in Translation

(continued)

Introducing the China Gateway

The home for Chinese scientists

The new Cell Press China Gateway is the ultimate destination for Chinese scientists. Now highlights of the latest research, regional events, and featured content from Cell Press are accessible online, on a single webpage.

The Cell Press China Gateway was designed with you in mind. We hope you'll make yourself at home.

Visit us at **www.cell.com/china**

CellPress

Cell Stem Cell
Perspective

The Promise and Perils of Stem Cell Therapeutics

George Q. Daley[1,2,3,*]
[1]Stem Cell Transplantation Program, Division of Pediatric Hematology/Oncology, Manton Center for Orphan Disease Research, Howard Hughes Medical Institute, Children's Hospital Boston and Dana Farber Cancer Institute; Division of Hematology, Brigham and Women's Hospital; and Department of Biological Chemistry and Molecular Pharmacology, Harvard Medical School, Boston, MA 02115, USA
[2]Broad Institute, Cambridge, MA 02142, USA
[3]Harvard Stem Cell Institute; Boston, MA 02138, USA
*Correspondence: george.daley@childrens.harvard.edu
DOI 10.1016/j.stem.2012.05.010

Stem cells are the seeds of tissue repair and regeneration and a promising source for novel therapies. However, apart from hematopoietic stem cell (HSC) transplantation, essentially all other stem cell treatments remain experimental. High hopes have inspired numerous clinical trials, but it has been difficult to obtain unequivocal evidence for robust clinical benefit. In recent years, unproven therapies have been widely practiced outside the standard clinical trial network, threatening the cause of legitimate clinical investigation. Numerous challenges and technical barriers must be overcome before novel stem cell therapies can achieve meaningful clinical impact.

Cell Therapeutics: The Current Standard of Care

In the twentieth century small molecule and protein drugs proved remarkably successful in restoring health and extending life span, but in the twenty-first century our aging population will face an increasing burden of organ failure and neurodegenerative disease. Such conditions are unlikely to be cured by drugs alone and instead call for restoration of tissue function through novel therapeutic approaches. Transplantation of whole organs—heart, lung, liver, kidney, small bowel, and pancreas—has become routine in modern medicine and has saved countless lives, while grafts of the skin and cornea for burns or ocular injury and transfusions of red blood cells and platelets for disease-related or chemotherapy-induced cytopenias are likewise widely employed tissue and cell therapies. However, current therapeutic strategies either are limited by donor availability and immunologic barriers or pertain to only a minor range of conditions. For the many diseases and disorders of aging for which there is no cure, innovative applications of tissue engineering and novel cell therapies derived from pluripotent and tissue-restricted stem cells represent major frontiers for the future.

Hematopoietic stem cells (HSCs), the therapeutic constituents of whole bone marrow and umbilical cord blood, have been the most widely employed stem cell therapy. When successful, HSC transplantation can be curative for scores of genetic blood disorders like thalassemia and immune deficiency and for malignancies like leukemia and lymphoma. HSC transplantation is undoubtedly the most successful application of stem cells in medicine, yet for many conditions success rates remain frustratingly low and morbidity and mortality unacceptably high. The need for precise molecular matching of donor and recipient means that many patients lack a suitable donor, either within their own family or in the public at large, even when databases list many millions of potential unrelated donors. When a match can be found, minor mismatches between donor and recipient frequently incite graft versus host disease (GVHD), an attack of the donor immune effector T cells against host tissues that results in skin rash, mucositis, diarrhea, and liver and lung destruction. GVHD is a major cause of treatment associated morbidity and mortality. Finally, grafts can fail, and disease can relapse. Although it is difficult to give a precise figure for the overall success rate for HSC transplantation, even an optimist would acknowledge that some 50% of patients are left without a cure or with a permanent disability. Thus, even our most successful form of stem cell therapy remains a heroic effort, reserved only for the sickest patients who have no better alternative.

Lessons from the Historical Development of HSC Transplantation

The evolution of HSC transplantation from its experimental origins to its acceptance as a standard of care in medicine is a tale that is both inspiring and cautionary. E. Donnall Thomas and colleagues were the first to perform marrow transplantation for otherwise fatal leukemia in the 1950s (Thomas et al., 1957). The rationale was predicated upon the known capacity for radiation to suppress leukemic hematopoiesis and studies demonstrating that injections of marrow rescued mice from otherwise lethal radiation exposure (Jacobson et al., 1951; Lorenz et al., 1951). Thomas wrote in a memoir in 2005, "These patients inspired us to speculate that it might be possible to destroy leukemic cells and normal marrow by lethal whole body irradiation, with reconstitution of marrow by marrow transplantation." Arguably, the first studies in humans were founded upon rather minimal evidence of efficacy in rodent models, and Thomas further noted, "We recognized that it would be important to do similar studies in an animal model … [and] decided to move forward with studies of man and dog at the same time" (Thomas, 2005). Indeed, Thomas and colleagues suffered considerable failure in preclinical canine models and witnessed the deaths of many scores of patients, which prompted great skepticism about whether the human experiments should continue. Nevertheless, Thomas and his intrepid team of investigators forged ahead. It took almost two decades before advances in research on tissue matching to define compatible donor-recipient pairs, and improved treatment of graft versus host disease and the infectious complications of marrow transplant allowed marrow transplantation to achieve consistent success in the late 1970s.

Some important principles emerge from this lesson in the history of HSC transplantation. First, the risk of the intervention should be commensurate with the severity of the underlying condition to be treated. The aggressively malignant nature of the conditions being treated—fatal leukemia and marrow aplasia—meant that the first practitioners of marrow transplantation were justified and even compelled to attempt heroic and potentially highly toxic interventions for invariably fatal diseases. Second, although human biology is only partially predictable from animal models, preclinical animal models remain a key element in the scientific development of novel therapies. At the beginning of human marrow transplantation, it was understood that identical twins accepted skin and solid organ grafts, but only a minority of the time did siblings. Experiments in the murine and canine marrow transplantation models reflected similar transplantation barriers. Notwithstanding these sobering limitations, the early practice of marrow transplant in patients proceeded despite a lack of robust evidence in animal models for graft acceptance between unrelated individuals. Only later were methods for lymphocyte matching developed (the antecedent to HLA typing), which was the key development in advancing the success of marrow transplantation. Finally, important and fundamental insights into therapeutic mechanisms were required before the eventual success of clinical translation of HSC transplantation therapies.

With the benefit of hindsight, one could argue that the earliest human transplants were premature and doomed to fail. One might question whether a therapy as toxic as marrow transplant, with so little evidence for success in animal models prior to testing in humans, could emerge in the current era. Under today's more rigorous regulatory climate, institutional review boards weigh risks and potential benefit on behalf of patients, insist on an impartial process of informed consent to minimize misconceptions about therapeutic potential, and monitor adverse events in the course of clinical trials. Indeed, one might reasonably conclude that today's IRBs might not have approved the early studies of Thomas and colleagues, but if they had, would have interceded to stop the experiments when the high incidence of treatment-related mortality became apparent.

The conjecture that modern-day IRBs might not approve the early experiments in HSC transplant does not imply that HSC transplant would not emerge under the current regulatory climate. On the contrary, I believe that bone marrow transplant could be developed within today's environment of strict clinical research regulation, although by a more conservative path that would spare considerable patient morbidity and mortality. As we learned from premature attempts at gene therapy in the early 1990s, new therapeutic technologies require considerable understanding of fundamental mechanisms before they can be delivered with confidence. Indeed, roughly 70% of early phase clinical trials of pharmaceuticals fail and over 50% at phase III (Ledford, 2011), and thus it stands to reason that significant resources are squandered because of the imprecision of early stage clinical research. Yet, especially with novel technologies, clinical experimentation proceeds energetically, because hope triumphs over experience. From this author's perspective, a conservative approach to clinical translation of stem cell therapies is warranted at this time, not because stem cell treatments are excessively risky (though some may yet prove to be), but rather because our understanding of the mechanisms by which stem cells might prove useful, and in which diseases, remains primitive. In a climate where government and philanthropic funds for fundamental research are increasingly scarce, and investment capital from the private sector for biotechnology has dried up, purely empirical attempts at stem cell therapy are difficult to justify, given the high probability of failure. In a 1995 report assessing the investment in gene therapy by the U.S. National Institutes of Health, a panel chaired by Stuart Orkin and Arno Motulsky recommended "increased emphasis on research dealing with the mechanisms of disease pathogenesis, further development of animal models of disease, enhanced use of preclinical gene therapy approaches in these models, and greater study of stem cell biology in diverse organ systems" (http://oba.od.nih.gov/oba/rac/panelrep.pdf). Similar recommendations regarding the need for proper investments in fundamental aspects of stem cell therapeutics seems warranted and prudent at this time.

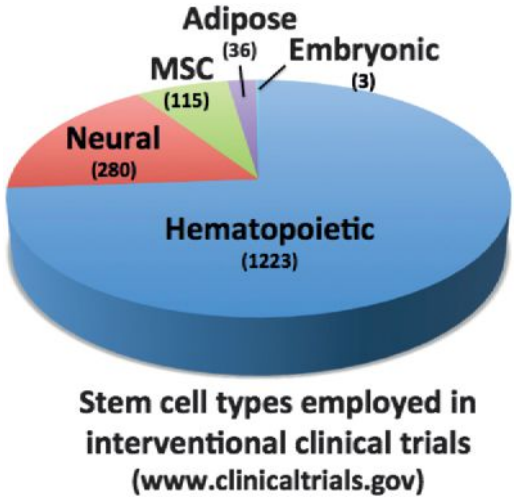

Figure 1. Clinical Trials of Major Stem Cell Types
Pie chart indicating the relative numbers of open trials testing clinical interventions for hematopoietic, neural, mesenchymal, adipose, and embryonic stem cells, as listed on the U.S. NIH website clinicaltrials.gov.

Stem Cell Therapeutics: Frontline Clinical Trials and Medical Innovations

A search of the Unites States government-sponsored website www.clinicaltrials.gov with the term "stem cells" lists over 4,000 past, current, and anticipated trials, with over 1,750 now open (Figure 1). The vast majority of open trials aim to build upon decades of research and clinical experience in hematopoietic transplantation (>1,200), and include strategies to expand the suboptimal dose of HSCs within umbilical cord blood, to complement gene defects in HSCs through viral transgene delivery ("gene therapy"), and to engineer T cells to attack malignancy via adoptive immunotherapy. Despite the relatively primitive understanding of therapeutic mechanisms for other stem cells, hundreds more trials are testing mesenchymal (115), adipose-derived (36), and neural stem cells (280), sometimes in quite bold and unconventional ways that bear little resemblance to the known differentiation potential or modes of tissue

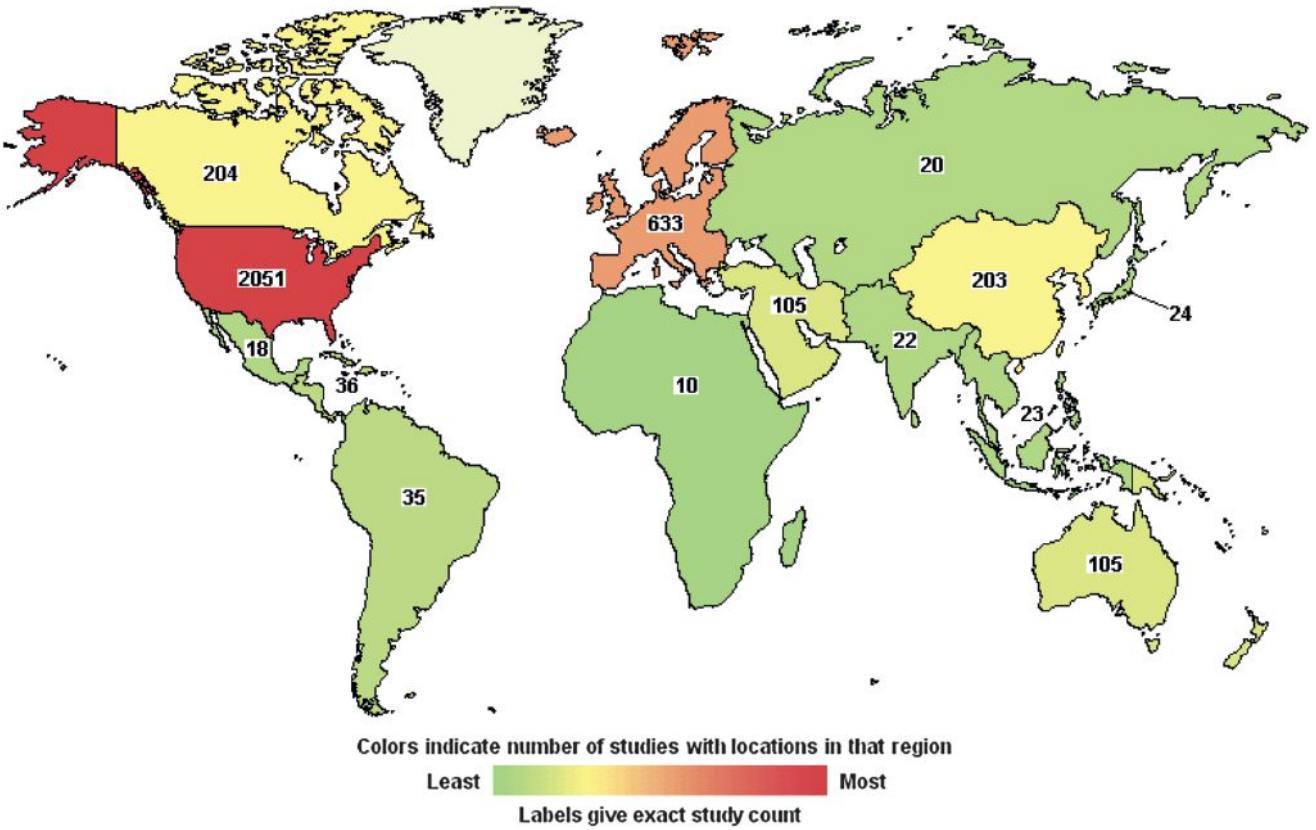

Figure 2. Worldwide Experimental Trials of Stem Cell-Based Therapies
World map showing locations of open, closed, and pending clinical trials of stem cell-based interventions as listed on clinicaltrials.gov. The relative numbers of trials performed outside of the U.S. may indeed be markedly understated because of reporting bias at the U.S. government clinical trials website.

regeneration or repair associated with these classes of stem cells. As of this writing, three trials pertain to products derived from ESCs. A wide array of stem cell studies are being carried out on a global basis on all continents, suggesting widespread clinical interest (Figure 2).

Mesenchymal stem cells (MSCs) are defined by their fibroblast-like morphology, adherence to plastic, expression of a specific set of surface antigens (CD105+, CD90+, CD73+), and capacity for osteogenic, chondrogenic, and adipogenic fates in vitro. MSCs are most often derived from bone marrow but can also be isolated from adipose tissue; adipose-derived stem cells may also consist of pericytes or endothelial progenitors that may differ somewhat in their properties from MSCs. Easy access to large quantities is an advantage for adipose-derived stem cells, which are being tested for soft-tissue repair and regeneration (Tobita et al., 2011). Both autologous (self) and allogeneic (foreign) MSCs are being tested in vivo to enhance healing that reflects their in vitro potential to form bone or cartilage, as in bone fracture and joint cartilage repair (Griffin et al., 2011). Although such studies are founded on strong preclinical evidence and sound scientific and clinical hypotheses, evidence for robust clinical efficacy of MSCs for orthopedic indications has been challenging to confirm, and to date no therapy based on MSCs has yet won approval by the U.S. Food and Drug Administration (FDA). The difficulty in proving the efficacy of regenerative treatments based on the well-characterized cellular potentials of MSCs suggests that our understanding of how even familiar stem cells can be exploited therapeutically in vivo remains primitive.

MSCs are being tested in a wide range of clinical indications where the clinical hypotheses are more speculative, the therapeutic mechanisms are incompletely defined, and in some instances the preclinical evidence is highly contentious. For example, from a scientific foundation that can be traced to a highly controversial report that whole bone marrow would regenerate cardiac muscle following transplantation into injured hearts (Orlic et al., 2001), an observation later disproven (Balsam et al., 2004), thousands of patients have been treated in trials worldwide with various cell preparations of bone marrow or MSCs, with the scientific community debating the significance of the results (Choi et al., 2011). Subsequent studies have invoked a variety of contingent mechanisms including salutary paracrine effects on resident cardiomyocytes and putative cardiac stem cells, neoangiogenesis, and biomechanical alterations due to scarring (Gnecchi et al., 2008; Menasche, 2011; Williams et al., 2011). The questions about underlying mechanism notwithstanding, combined meta-analyses of numerous trials has argued for measureable yet quite modest therapeutic effects, which has left practitioners unsure of the significance and robustness of these therapeutic approaches (Tongers et al., 2011).

MSCs have also been widely tested for their capacity to mitigate autoimmunity, following somewhat serendipitous

observations that MSCs can interfere with in vitro immunological assays such as mixed lymphocyte reactions and modulate production and function of the major classes of immune cells (Kode et al., 2009; Shi et al., 2011). Although it is unclear whether immune antagonism reflects any native function of MSCs in vivo, ex vivo expanded preparations have been infused in patients in hopes of mitigating transplant-related graft versus host disease and autoimmune conditions like Crohn's disease, multiple sclerosis, and systemic lupus (Kebriaei and Robinson, 2011; Shi et al., 2011). One can find numerous reports of efficacy in the literature, but these are mixed with negative data (Kebriaei and Robinson, 2011). The precise role of MSCs as agents for immune modulation remains to be proven.

When clinical indications stray yet further from the presumptive core functions of MSCs, and therapeutic mechanisms become increasingly speculative, clinical translation is a largely empirical rather than a rational effort. Likewise, while umbilical cord blood (UCB) has emerged as a viable alternative to other sources of HSCs (e.g., mobilized peripheral blood or bone marrow) for the treatment of leukemia and nonmalignant hematologic conditions (Rocha et al., 2004), it has also become a common source for experimental interventions in a wide variety of nonhematologic indications as disparate as myocardial infarction, multiple sclerosis, amyotrophic lateral sclerosis, cerebral palsy, traumatic brain injury, stroke, and inherited metabolic disorders (Copeland et al., 2009; Harris, 2009; McKenna and Sheth, 2011; Prasad and Kurtzberg, 2009). Evidence exists that a number of distinct cell types can be cultured from UCB, including multipotential stem cells (Kögler et al., 2004; Pelosi et al., 2012), but it is unclear whether such expandable cell populations exist at appreciable levels in unmanipulated samples. While in theory such cells could mediate therapeutic effects, nonhematologic indications for UCB transplantation have not been widely accepted into standard practice. When clinical investigation proceeds largely empirically, and without a deeper understanding of the basic therapeutic mechanisms, it is difficult to reformulate therapeutic strategies after clinical failures.

Neural stem cells (NSC) can be cultured from fetal and adult brain and demonstrated to differentiate into neurons, oligodendrocytes, and astrocytes in vitro. Given the wide array of neurologic conditions that have devastating clinical consequences, there is considerable interest in the therapeutic potential of neural regeneration therapies. However, neurodegenerative diseases, catastrophic stroke, traumatic brain injury, and spinal paralysis are among the most daunting challenges for regenerative medicine. The development of the brain and peripheral nerves and their interconnectedness with tissues throughout the body requires a remarkably complex choreography during fetal development. The proper milieu for directing the formation of highly specified neuronal subtypes and guiding their projection to and interconnectedness with critical targets is highly unlikely to exist in the adult body. But faced with compelling unmet medical need and desperation on the part of patients, there are hundreds of investigator-initiated clinical trials occurring in academic settings (Figure 1), and several companies have forged efforts to develop novel therapies through intracerebral or spinal transplantation of neural stem cells (Trounson et al., 2011). StemCells Inc (California, USA) has tested NSCs in Batten's disease (neuronal ceroid lipofuscinosis) and was able to document safe delivery but discontinued the trial because of the inability to accrue an adequate number of patients. Their current focus is Pelizaeus-Merzbacher disease, a myelin disorder, and chronic spinal cord injury. Other companies are testing NSC transplant for stroke (ReNeuron, United Kingdom), amyotropic lateral sclerosis (Neuralstem, Inc, Maryland, USA), and Parkinson's disease (NeuroGeneration, California, USA). In most of these cases, the clinical hypotheses being tested do not depend upon the generation of neurons de novo, but instead on complementation of enzyme deficiencies, remyelination, or modulation of endogenous repair through neoangiogenesis or neuroprotection.

Although widely publicized, there are comparatively few clinical trials of products derived from human embryonic stem cells (hESCs). The first trial conducted in humans delivered oligodendrocyte progenitors for the remyelination of spinal cord axons damaged through crush injury. These studies were based on extensive preclinical experience with the derivation and characterization of oligodendrocytes and their delivery in animal models that showed remyelination and restoration of motor function (Keirstead et al., 2005; Liu et al., 2000; McDonald and Belegu, 2006; McDonald and Howard, 2002; McDonald et al., 1999; Nistor et al., 2005). Moreover, this first trial required a herculean effort to satisfy FDA regulatory oversight, by report entailing the submission of over 20,000 pages of data and documentation. The trial, sponsored by the Geron Corporation (California, USA), enrolled and treated its first four patients before being discontinued due to a decision by company management to focus on alternative corporate priorities (Baker, 2011). No formal results have yet been released regarding the phase 1 clinical trial in this first small cohort of patients, but the primary endpoints were safety of the cells, and at the very least one hopes that some evidence will be gleaned that products of ESCs can be delivered without risk of teratoma, although long-term follow-up of all treated patients will be necessary.

The only other current clinical trials involve transplantation of hESC-derived cells to treat retinal blindness. This condition takes many forms, both genetic and age-related, and as a group of disorders has many appealing features for stem cell-based interventions. The retina is accessible for local delivery of cells, which can then be monitored via direct visualization. The retina may also provide some degree of immune privilege. Very preliminary results of a trial involving the subretinal injection of hESC-derived retinal pigment epithelial cells for Stargardt's macular degeneration and another for age-related macular degeneration sponsored by the company Advanced Cell Technologies (ACT) were recently reported, despite experience on only one patient in each trail (Schwartz et al., 2012). Only one of the two patients showed evidence of persistent cells but both were reported to show some restoration of visual perception. While it is difficult to draw conclusions from these early trials due to the limited numbers of patients involved and the very brief 4 month period of follow-up, the trials represent milestones in that the investigators succeeded in clearing considerable regulatory hurdles and met very high standards of preclinical cell characterization and quality control prior to exposing patients to the risk of ESC-based products. The experience alone, for both investigators and regulators, is an essential albeit small step forward in the long path to establishing ESC-based therapeutics.

While MSCs, NSCs, and products from ESCs are being tested in the context of numerous clinical trials, yet another arm of regenerative medicine—tissue engineering—is comingling MSCs or a variety of other cultured cell types with biocompatible materials to solve surgical challenges. Reconstruction of bladders (Aboushwareb and Atala, 2008; Atala, 2011; Tian et al., 2010), tendons (Sun et al., 2011), and complex structures like the trachea (Macchiarini et al., 2008) represent solutions to highly personal needs of specific patients and are acceptably performed as highly innovative and individualized surgical therapies, part of the long tradition of surgical innovation. The mechanisms for developing such novel interventions and gaining acceptance by the surgical and biomedical communities involve the same core principles required for medical interventions—sound scientific rationale and methods, institutional and practitioner accountability, thorough and rigorous informed consent, patient follow-up, timely reporting of adverse events, peer review of therapeutic claims, and publication in the medical literature. The potential for therapeutic innovation at the interface of stem cell biology and tissue engineering is particularly appealing but beyond the scope of this review. I refer the reader instead to excellent recent reviews (Griffin et al., 2011; Peck et al., 2012; Sun et al., 2011).

Anticipated Future Interventions and Opportunities

Among the many disparate conditions, disorders, and diseases for which stem cells have offered promise, a few stand out as particularly compelling. In general, they are conditions where defects are largely cell autonomous and entail the loss or dysfunction of a single class of cells or a monocellular component of a complex tissue, such that restoration of function through cell replacement would be curative or significantly ameliorate symptoms. Those conditions most amenable to treatment present the least anatomic complexity and affect tissues that do not typically regenerate spontaneously because they lack endogenous pools of tissue stem cells. We can predict ultimate success with most confidence if some clinical evidence already exists that cell replacement might indeed be therapeutic, for instance through prior assessments of cadaveric or fetal tissue transplantation. For conditions previously treated with cadaveric or fetal material, efficacy may be limited by the inadequate supply or quality of the cells, making pluripotent or reprogrammed cell sources advantageous.

Parkinson's Disease. Although neurologists recognize that Parkinson's disease (PD) has systemic features, the chief deficit remains the loss of a specific subtype of midbrain dopaminergic neurons located in a deep brain structure, the substantia nigra, whose many connections to the striatum are responsible for regulating movements, such that PD patients suffer from immobility, rigidity, and tremor. Drug replacement with precursors of dopamine (DA), dopamine agonists, or antagonists of dopamine metabolism serves to ameliorate symptoms but cannot stem the inexorable decline in most patients. Based on decades of experience from several groups with transplantation of fetal tissue sources of DA neurons, deep brain transplantation can indeed restore local DA production and ameliorate symptoms, with some patients showing durable improvement and graft integrity after two decades (Freed et al., 1992; Lindvall et al., 1990; Lindvall et al., 1994; Piccini et al., 1999, 2005). Functional imaging and postmortem analysis support the stable integration and persistence of grafts in some patients, prompting continued enthusiasm for this approach among some practitioners, provided that a suitable source of DA neurons can be defined (Freed et al., 1992; Lindvall et al., 1990, 1994; Ma et al., 2010; Nakamura et al., 2001; Piccini et al., 1999, 2000). Others, however, remain skeptical, in part because a trial of fetal grafts randomized against sham surgery was inconclusive, with some patients sustaining functional decline postsurgery due to dyskinesias as a result of excessive graft function (Freed et al., 2001). Supporters of cell therapy for PD point out that a more reliable, consistent, and defined source of DA neurons would justify further testing of transplantation strategies.

Many groups have differentiated DA neurons from both neural stem cell and pluripotent stem cell sources and proven functional in rodent models (Hargus et al., 2010; Sanchez-Pernaute et al., 2008; Tabar et al., 2008; Wernig et al., 2008). Analysis of this DA neuron production has not always distinguished among the many different classes of neurons that produce DA throughout the neuraxis, but recent advances have made possible the differentiation from pluripotent cell sources of regionally specific midbrain DA neuronal subtypes whose deficiency is most affected in PD is possible, and such cells have been documented to function in rodent and primate models (Chambers et al., 2009; Fasano et al., 2010; Kriks et al., 2011). Moreover, techniques for producing personalized autologous stem cells via somatic cell reprogramming now exist, and it has been shown that autologous cells function better than cells derived from unrelated donors in rodent models of PD transplant (Tabar et al., 2008). The availability of highly specified, defined, autologous DA neuron preparations creates legitimate opportunities for testing in PD patients, including the testing of specific doses to establish a dose-response curve. Nevertheless, even optimistic accounts identify the significant hurdles that remain (Lindvall and Kokaia, 2010). Notably, any cell therapy must ultimately be superior in safety and efficacy to any drug therapy, and establishing such utility will require large-scale and painstaking prospective trials to be conducted over many years. Thus, despite promise, cell therapy as the standard of care for PD is but a distant horizon.

Cell therapy for PD will need to be efficacious and safe to compete with the highly effective drug treatments that currently exist (Hjelmgren et al., 2006). In contrast, a condition like Huntington's disease, which has no viable drug therapy and is invariably fatal, is an appealing alternative therapeutic target for cell transplantation therapies derived from NSCs and ESCs. Intrastriatal transplantation of homotypic fetal tissues has shown graft durability and reports of amelioration of symptoms in HD patients (Gallina et al., 2010; Nicoleau et al., 2011). As for PD, an improved cell source would facilitate the necessary studies to optimize the dose and target region for cell transplantation. Techniques for directed differentiation of ESCs into relevant medium spiny neurons and amelioration of rodent models of HD have been reported and bode well for future translational clinical studies (Benraiss and Goldman, 2011).

Autoimmune Diabetes Mellitus. Type 1 diabetes (T1D; insulin-dependent, juvenile onset) is an autoimmune condition that involves active immune destruction of the beta cells of the islets of Langerhans of the pancreas, leaving the patient with inadequate supplies of insulin and susceptibility to hyperglycemic

crises characterized by life-threatening ketoacidosis. At diagnosis, patients harbor depleted pools of beta cells and are unable to mount a regenerative response to restore beta cell mass, even if their autoimmune response can be controlled. Whether beta cells regenerate after injury in the adult pancreas has been vigorously debated (Bonner-Weir and Weir, 2005; Dor et al., 2004; Dor and Melton, 2008), but endogenous regeneration under pathologic conditions is not robust, and alternative sources of beta cells would therefore be required. Deriving fully functional beta cells in vitro from pluripotent stem cells has proved challenging, but a group from the biotechnology company Novocell did report successful derivation of precursors in vitro that appear to fully differentiate and mature after transplantation in vivo (D'Amour et al., 2006; Kroon et al., 2008). In a more recent advance, Gadue and colleagues have derived a stably expandable endodermal progenitor that is more efficient at producing beta cells than if one proceeds directly from ESC (Cheng et al., 2012). If a reliable source of beta cells can be produced in vitro, a credible path toward clinical development could be envisioned. We know that transplantation of whole pancreas, or infusion of islet preparations from cadaveric sources in the context of a corticosteroid-sparing regimen of immune suppression (the "Edmondton Protocol"), can restore glycemic control for extended time periods (Shapiro et al., 2000, 2006). Although patients later relapse, the potential for repeated cell infusions would be greatly facilitated by a more abundant source of beta cells, and deriving purified beta cells from pluripotent stem cell sources thus remains a much sought after goal in stem cell biology. As T1D is an autoimmune disorder, it seems unlikely that autologous cells would be a preferable source of material to allogeneic cells, as immune suppression to protect the beta cells would still be required in either scenario. Attempts to convert exocrine pancreatic tissue into beta-like endocrine cells through ectopic expression of transcription factors, a type of direct reprogramming of cell fates in situ, is a new therapeutic concept with provocative appeal (Zhou et al., 2008).

Other Treatable Conditions on the Horizon. Corneal injury that leads to scarring and blindness has prompted efforts to culture and expand limbal stem cells into corneal patches in vitro, followed by corneal grafting. Recent reports confirm several independent studies that corneal grafting using alternative sources of epithelial cells can restore vision, and appears to be a promising novel stem cell-based treatment for a grave but rare human condition (Nishida et al., 2004; Rama et al., 2010; Tsai et al., 2000; Tsubota et al., 1999). Liver transplantation cannot meet the demands of patients suffering from liver failure around the globe, and production of hepatocyte-like cells from pluripotent stem cells sources has been reported by several groups. Despite considerable similarity to native hepatocytes, the in vitro derived cells have not yet been reported to be fully functional in animal models, and considerable challenges remain for achieving functional integration of in vitro derived hepatocytes, especially for conditions like cirrhosis that already entail markedly altered liver anatomy and compromised circulation. Similarly, production of cardiomyocytes appears to be robust in the petri dish, but achieving engraftment in the damaged heart of a clinically meaningful dose of cells, together with integration in a manner that restores pump function, remains a major challenge. In this case, clever engineering of biomaterials might enable the creation of contractile cardiac patches that could be sewn onto the heart. Finally, producing HSCs from personalized pluripotent stem cells, coupled to gene repair, is an appealing strategy for dozens of genetic disorders of the bone marrow including immune deficiency, hemoglobinopathy, and genetic marrow failure syndromes. Still other potential indications for tissue replacement therapies involve in vitro production of endothelial cells and potentially even human gametes, but none appear to have imminent clinical application. All cell replacement therapies face similar challenges of graft integration into the host environment, which entails trafficking, homing, and integration into native niches or microenvironments, connection to a host blood supply, immune compatibility, and graft durability. Solving such challenges will engage the research community for decades to come.

Who Will Translate Stem Cell Science into Regenerative Medicine?

Scientific advances in stem cell biology are being driven by the current intellectual ferment and excitement of the field, but when and how these advances will be translated into successful treatments remain fertile questions for debate. Will cell therapies remain a highly patient-focused endeavor performed solely in academic medical centers, akin to bone marrow or solid organ transplantation? Or will stem cells ever become commercial, pharmaceutical grade "off-the-shelf" products?

One might imagine a future in which medical centers offer highly customized, patient-focused approaches to stem cell treatments, perhaps utilizing the products of personalized induced pluripotent stem cells (see Yamanaka, 2012, this issue). IPS cells have enormous theoretical appeal as vehicles for combined gene repair and cell replacement therapy for genetic disease (Daley and Scadden, 2008). Newer forms of stem cell transplant could replicate the current status of bone marrow transplantation, which has developed into a remarkably complex infrastructure for capturing cellular and molecular information in international registries for literally millions of potential donors and entails lengthy, costly, and risky interventions in intensive clinical care settings. Given the imperative of treating patients in need, stem cell transplants for genetic and acquired diseases will emerge from academic centers because clinician investigators will develop them and patients will demand them. Like gene repair ("gene therapy"), cell replacement therapies will probably serve rare conditions first and pertain to small numbers of patients receiving highly individualized treatments, perhaps coupling gene repair with autologous cell replacement approaches, for example for blood diseases. Such small-scale applications will dominate until and unless generic interventions and off-the-shelf approaches prove feasible.

The prospects for more widespread stem cell-based treatments depends on either solving the immune rejection barrier, through advances in promoting immune tolerance to allogeneic tissues, or accepting the use of immune suppression—even lifelong—to facilitate allogeneic cell therapies. Immune suppression is already standard for organ transplantation, so we know that its use to facilitate life-sustaining cell therapy is feasible. Because cell manufacture is likely to be the most costly and time-consuming aspect limiting cell therapies, the prospects for realizing economies of scale would seem to call for the establishment of master cell banks that could be the source of cells

"off-the-shelf." The polymorphism of histocompatibility genes and the resulting variety of tissue types is far too great in human populations to expect banks to be able to supply perfect tissue matches for all potential patients. Instead, one might envision banks of cells derived from donors with highly common genotypes of the histocompatibility genes. This type of approach would be greatly facilitated by cell strains with homozygosity of histocompatibility loci. Past approximations of the number of cell lines that would be needed in such a repository or master cell bank, based on modeling data from pools of kidney transplant patients and recipients in the United Kingdom and Japan, have suggested that a bank comprised on the order of 10–50 cell lines might effectively provide a single HLA antigen match (deemed a minimal requirement for acceptable solid organ transplantation) for approximately 80% of the local population (Gourraud et al., 2012; Nakajima et al., 2007; Taylor et al., 2011, 2005). While encouraging, these numbers suggest that some kind of dual system might well be needed in which the vast majority of individuals can benefit from off-the-shelf therapies, but personalized autologous cells derived via reprogramming would be needed for those with difficult-to-match tissue types.

Alternatives to Cell Therapy

Because of the significant hurdles that remain in terms of cell manufacture, delivery, anatomical integration, and immune suppression for all but highly personalized therapies, it is entirely possible that more traditional modes of treatment will evolve from stem cell research and ultimately prove the most feasible. Indeed, the generation of patient-derived stem cells holds the most immediate promise for advancing traditional drug discovery paradigms (for a recent review, see Grskovic et al., 2011). Capturing diseases in a dish promises to enable cell-based phenotypic assays that could yield new drugs that repair cell and tissue defects, or perhaps act on endogenous pools of stem cells, stimulating repair and regeneration. For tissues that do not readily regenerate from endogenous pools of stem cells, such as the majority of the brain, the heart, and the kidney, another provocative possibility is the direct conversion of one cell or tissue identity to another that has been depleted by disease or injury. A host of such conversions have been realized in vitro, converting fibroblasts into cells that resemble and exhibit some functions like neurons, cardiomyocytes, and hepatocytes (Vierbuchen and Wernig, 2011). Cell conversion has considerable theoretical advantages, but whether this new cellular alchemy can be harnessed for therapeutic end remains almost science fiction at present, although it is clearly worthy of deeper exploration.

Threats to Clinical Translation and to the Integrity of Regenerative Medicine

Translating the basic discoveries of stem cell biology into robust, effective, and safe new modalities of care will mean solving new challenges; before success, regenerative medicine will suffer many setbacks. While translating too timidly might deprive needy patients of precious time and life quality, testing cells in patients before a deeper understanding of how stem cells work is risky, too. We need to be confident that we understand the full spectrum of safety concerns and can therefore avoid placing patients at undue risk. We also need to design rigorous, blinded, and when possible randomized trials where evidence for clinical efficacy can be defined precisely, rather than depend upon anecdote and clinical observation alone. Given that patients and practitioners may carry unrealistic expectations of clinical efficacy, there is a high likelihood for a robust placebo effect as well as interpretive bias in reporting of clinical results. We also need to be conscious of not exhausting resources that would be better spent on more practical health care needs. Premature application runs the risk of high-profile failure that would sully the credibility of this still-developing field.

With the goal of advancing clinical investigation while preserving rigor, promoting medical innovation while protecting patients, and ensuring integrity in regenerative medicine while respecting autonomy of individual practitioners and patients, the International Society for Stem Cell Research (ISSCR) assembled an international group of scientists, surgeons, gene therapists, bioethicists, patient advocates, and attorneys and composed "The ISSCR Guidelines for the Clinical Translation of Stem Cells" (Hyun et al., 2008). These guidelines articulated principles and standards as a roadmap for practitioners and regulatory bodies when considering if, when, and how to allow tests of experimental stem cell therapies in actual patients. The guidelines call for independent and rigorous analysis of the decision to test novel treatments in patients, by reviewers with relevant area-specific expertise, who are free of conflicts of interest that might lead to positive or negative bias. Expert judgment about the reliability and rigor of the preclinical evidence for efficacy and safety of cellular products is essential for weighing the potential risks against the potential benefits before launching a clinical trial.

Because no preclinical animal or cellular model is entirely predictive of outcomes in patients, a credible and rigorous process of informed consent is essential to protecting the autonomy of patients and their thoughtful engagement in the research process, where they consent to participate without heightened expectations or therapeutic misconception; such wishful thinking renders patients vulnerable to exploitation and contaminates interpretations of therapeutic efficacy.

Medical Innovations outside of Clinical Trials

Many in the medical field recognize the value of innovation outside the context of a clinical trial. However, especially if incorporating the use of highly manipulated cell preparations, such innovative attempts at therapy in the United States should fall under the jurisdiction of the Food and Drug Administration. To comply with accepted professional standards governing the practice of medicine, highly novel uses of any cellular product should not be performed on more than a small number of patients before such use is subject to independent review of the scientific rationale, informed consent, close patient follow-up, and reporting of adverse events. Any attempt to extend the innovative therapy to a larger group of patients should be preceded by a standard clinical trial. Although some may contend that requiring approval for the practice of novel clinical treatments from an independent body undermines the autonomy of practitioners to provide care to their patients, independent peer review ensures that the rationale for treatment is sound and represents a defensible community standard of medical practice.

Premature Clinical Translation

The traditional strategy for proving that a medical intervention works and is safe requires rigorous clinical trial design, can be

frustratingly slow and costly, and is generally best suited to highly organized medical settings. However, the history of even legitimate medical practice is rife with examples of instances whereby trust in medical intuition alone, or reliance on uncontrolled retrospective or purely observational studies, has led to mistaken presumptions about medical efficacy, only to be corrected when rigorous blinded, randomized trials proved our presumptions to be false (for example, high-dose chemotherapy and autologous marrow rescue for metastatic breast cancer, postmenopausal hormone replacement therapy and cardiovascular risk, to name just two).

The fledgling field of stem cells is already suffering from the taint of illegitimate clinical translation. A quick Google search for "stem cell treatments" returns a plethora of sponsored websites peddling cures for ailments as diverse as Alzheimer's disease and autism. As documented by Caulfield and colleagues, such websites systematically overpromise the potential efficacy of stem cells and trivialize the potential risks (Lau et al., 2008). Sadly, even sophisticated patients or their families can be misled by the veneer of scientific credibility on such websites.

As stated previously, apart from treatments using HSCs for blood diseases, and various dermal and corneal indications, essentially all other treatments based on stem cells must be considered experimental medical research and should be administered exclusively in organized clinical trials. Subjects in medical research are generally not required to pay for unproven interventions.

Administering interventions outside of controlled clinical trials threatens patients and jeopardizes the integrity of and public trust in medical research, compromising legitimate efforts to advance knowledge. Because of the particular vulnerabilities of patients, many governments have enacted laws to protect patients from exploitation and risk, but some practitioners see such regulation as burdensome and unwarranted restraints on their trade. The threat of litigation for medical malpractice serves as an additional constraint on unwarranted medical practice. Recently, the German government shut down the Xcell Clinic when a child died after receiving intracranial injections of cord blood in an unproven intervention. A recent report documented the development of glioneural masses in the brain and spinal cord of a child who was treated with intrathecal infusions of what were reportedly neural stem cells for ataxia telangectasia, a genetic movement disorder (Amariglio et al., 2009). While one hopes that most stem cell interventions are benign, the safety data are still rudimentary.

The history of "gene therapy" was shaped in a deleterious way by the untimely death of a young man, Jesse Gelsinger, in an FDA-approved clinical study. James Wilson, the physician responsible for the gene therapy clinical trial in question, has written a compelling admonition to practitioners of stem cell therapies, warning that much of the history that prompted premature clinical translation of gene therapy is being repeated by the practitioners of stem cell therapy (Wilson, 2009). He sees the same assumptions of a "simplistic, theoretical model indicating that the approach "ought to work"; "a large population of patients with disabling or lethal diseases … harboring fervent hopes"; and "unbridled enthusiasm of some scientists in the field, fueled by uncritical media coverage." He ends with, "I am concerned that expectations for the timeline and scope of clinical utility of hESCs have outpaced the field's actual state of development and threaten to undermine its success." The warning is just as appropriate for all kinds of stem cells—umbilical cord blood, neural stem cell, mesenchymal stem cells.

Conclusions

The maturation of new therapeutics takes decades. If one examines the history of any of the recent new thrusts in biomedicine—recombinant DNA, monoclonal antibodies, gene therapy, or RNAi—the vanguard treatments were introduced within a decade but 20 years passed before the full impact of the new form of medicine was felt widely in clinical medicine; for RNAi, we are still waiting for clinical success. Fifty years after the first attempts at HSC transplantation, and even with all the improved understanding we now have of both HSCs and immunological mismatch, our success rates are still woefully inadequate. Although the development of novel stem cell-based therapies will benefit greatly from the collective failures and acquired experience of marrow transplantation, our ignorance of the challenges of applying stem cells in distinct tissues with far greater anatomic complexity than the blood should give us pause as practitioners and inspire humility. Realistically, we should anticipate that new therapies based on stem cells for other tissues will likewise take decades to mature. In the short term, there will probably be more failures than successes, and one can only hope that the new field of regenerative medicine can learn the lessons of the past and proceed with prudence and caution.

ACKNOWLEDGMENTS

G.Q.D. is supported by grants from the NIH (R24DK092760, UO1-HL100001, RC4-DK090913, P50HG005550, and special funds from the ARRA stimulus package- RC2-HL102815), the Roche Foundation for Anemia Research, Alex's Lemonade Stand, Ellison Medical Foundation, Doris Duke Medical Foundation, and the Harvard Stem Cell Institute. G.Q.D. is an affiliate member of the Broad Institute and an investigator of the Howard Hughes Medical Institute and the Manton Center for Orphan Disease Research. Disclosure: GQD is a member of the scientific advisory board and receives consulting fees and holds equity in the following companies that work with stem cells: Johnson & Johnson, Verastem, iPierian, and MPM Capital.

REFERENCES

Aboushwareb, T., and Atala, A. (2008). Stem cells in urology. Nat. Clin. Pract. Urol. *5*, 621–631.

Amariglio, N., Hirshberg, A., Scheithauer, B.W., Cohen, Y., Loewenthal, R., Trakhtenbrot, L., Paz, N., Koren-Michowitz, M., Waldman, D., Leider-Trejo, L., et al. (2009). Donor-derived brain tumor following neural stem cell transplantation in an ataxia telangiectasia patient. PLoS Med. *6*, e1000029.

Atala, A. (2011). Tissue engineering of human bladder. Br. Med. Bull. *97*, 81–104.

Baker, M. (2011). Stem-cell pioneer bows out. Nature *479*, 459.

Balsam, L.B., Wagers, A.J., Christensen, J.L., Kofidis, T., Weissman, I.L., and Robbins, R.C. (2004). Haematopoietic stem cells adopt mature haematopoietic fates in ischaemic myocardium. Nature *428*, 668–673.

Benraiss, A., and Goldman, S.A. (2011). Cellular therapy and induced neuronal replacement for Huntington's disease. Neurotherapeutics *8*, 577–590.

Bonner-Weir, S., and Weir, G.C. (2005). New sources of pancreatic beta-cells. Nat. Biotechnol. *23*, 857–861.

Chambers, S.M., Fasano, C.A., Papapetrou, E.P., Tomishima, M., Sadelain, M., and Studer, L. (2009). Highly efficient neural conversion of human ES

and iPS cells by dual inhibition of SMAD signaling. Nat. Biotechnol. *27*, 275–280.

Cheng, X., Ying, L., Lu, L., Galvão, A.M., Mills, J.A., Lin, H.C., Kotton, D.N., Shen, S.S., Nostro, M.C., Choi, J.K., et al. (2012). Self-renewing endodermal progenitor lines generated from human pluripotent stem cells. Cell Stem Cell *10*, 371–384.

Choi, Y.H., Kurtz, A., and Stamm, C. (2011). Mesenchymal stem cells for cardiac cell therapy. Hum. Gene Ther. *22*, 3–17.

Copeland, N., Harris, D., and Gaballa, M.A. (2009). Human umbilical cord blood stem cells, myocardial infarction and stroke. Clin. Med. *9*, 342–345.

D'Amour, K.A., Bang, A.G., Eliazer, S., Kelly, O.G., Agulnick, A.D., Smart, N.G., Moorman, M.A., Kroon, E., Carpenter, M.K., and Baetge, E.E. (2006). Production of pancreatic hormone-expressing endocrine cells from human embryonic stem cells. Nat. Biotechnol. *24*, 1392–1401.

Daley, G.Q., and Scadden, D.T. (2008). Prospects for stem cell-based therapy. Cell *132*, 544–548.

Dor, Y., and Melton, D.A. (2008). Facultative endocrine progenitor cells in the adult pancreas. Cell *132*, 183–184.

Dor, Y., Brown, J., Martinez, O.I., and Melton, D.A. (2004). Adult pancreatic beta-cells are formed by self-duplication rather than stem-cell differentiation. Nature *429*, 41–46.

Fasano, C.A., Chambers, S.M., Lee, G., Tomishima, M.J., and Studer, L. (2010). Efficient derivation of functional floor plate tissue from human embryonic stem cells. Cell Stem Cell *6*, 336–347.

Freed, C.R., Breeze, R.E., Rosenberg, N.L., Schneck, S.A., Kriek, E., Qi, J.X., Lone, T., Zhang, Y.B., Snyder, J.A., Wells, T.H., et al. (1992). Survival of implanted fetal dopamine cells and neurologic improvement 12 to 46 months after transplantation for Parkinson's disease. N. Engl. J. Med. *327*, 1549–1555.

Freed, C.R., Greene, P.E., Breeze, R.E., Tsai, W.Y., DuMouchel, W., Kao, R., Dillon, S., Winfield, H., Culver, S., Trojanowski, J.Q., et al. (2001). Transplantation of embryonic dopamine neurons for severe Parkinson's disease. N. Engl. J. Med. *344*, 710–719.

Gallina, P., Paganini, M., Lombardini, L., Mascalchi, M., Porfirio, B., Gadda, D., Marini, M., Pinzani, P., Salvianti, F., Crescioli, C., et al. (2010). Human striatal neuroblasts develop and build a striatal-like structure into the brain of Huntington's disease patients after transplantation. Exp. Neurol. *222*, 30–41.

Gnecchi, M., Zhang, Z., Ni, A., and Dzau, V.J. (2008). Paracrine mechanisms in adult stem cell signaling and therapy. Circ. Res. *103*, 1204–1219.

Gourraud, P.A., Gilson, L., Girard, M., and Peschanski, M. (2012). The role of human leukocyte antigen matching in the development of multiethnic "haplobank" of induced pluripotent stem cell lines. Stem Cells *30*, 180–186.

Griffin, M., Iqbal, S.A., and Bayat, A. (2011). Exploring the application of mesenchymal stem cells in bone repair and regeneration. J. Bone Joint Surg. Br. *93*, 427–434.

Grskovic, M., Javaherian, A., Strulovici, B., and Daley, G.Q. (2011). Induced pluripotent stem cells—opportunities for disease modelling and drug discovery. Nat. Rev. Drug Discov. *10*, 915–929.

Hargus, G., Cooper, O., Deleidi, M., Levy, A., Lee, K., Marlow, E., Yow, A., Soldner, F., Hockemeyer, D., Hallett, P.J., et al. (2010). Differentiated Parkinson patient-derived induced pluripotent stem cells grow in the adult rodent brain and reduce motor asymmetry in Parkinsonian rats. Proc. Natl. Acad. Sci. USA *107*, 15921–15926.

Harris, D.T. (2009). Non-haematological uses of cord blood stem cells. Br. J. Haematol. *147*, 177–184.

Hjelmgren, J., Ghatnekar, O., Reimer, J., Grabowski, M., Lindvall, O., Persson, U., and Hagell, P. (2006). Estimating the value of novel interventions for Parkinson's disease: an early decision-making model with application to dopamine cell replacement. Parkinsonism Relat. Disord. *12*, 443–452.

Hyun, I., Lindvall, O., Ahrlund-Richter, L., Cattaneo, E., Cavazzana-Calvo, M., Cossu, G., De Luca, M., Fox, I.J., Gerstle, C., Goldstein, R.A., et al. (2008). New ISSCR guidelines underscore major principles for responsible translational stem cell research. Cell Stem Cell *3*, 607–609.

Jacobson, L.O., Simmons, E.L., Marks, E.K., and Eldredge, J.H. (1951). Recovery from radiation injury. Science *113*, 510–511.

Kebriaei, P., and Robinson, S. (2011). Treatment of graft-versus-host-disease with mesenchymal stromal cells. Cytotherapy *13*, 262–268.

Keirstead, H.S., Nistor, G., Bernal, G., Totoiu, M., Cloutier, F., Sharp, K., and Steward, O. (2005). Human embryonic stem cell-derived oligodendrocyte progenitor cell transplants remyelinate and restore locomotion after spinal cord injury. J. Neurosci. *25*, 4694–4705.

Kode, J.A., Mukherjee, S., Joglekar, M.V., and Hardikar, A.A. (2009). Mesenchymal stem cells: immunobiology and role in immunomodulation and tissue regeneration. Cytotherapy *11*, 377–391.

Kögler, G., Sensken, S., Airey, J.A., Trapp, T., Müschen, M., Feldhahn, N., Liedtke, S., Sorg, R.V., Fischer, J., Rosenbaum, C., et al. (2004). A new human somatic stem cell from placental cord blood with intrinsic pluripotent differentiation potential. J. Exp. Med. *200*, 123–135.

Kriks, S., Shim, J.W., Piao, J., Ganat, Y.M., Wakeman, D.R., Xie, Z., Carrillo-Reid, L., Auyeung, G., Antonacci, C., Buch, A., et al. (2011). Dopamine neurons derived from human ES cells efficiently engraft in animal models of Parkinson's disease. Nature *480*, 547–551.

Kroon, E., Martinson, L.A., Kadoya, K., Bang, A.G., Kelly, O.G., Eliazer, S., Young, H., Richardson, M., Smart, N.G., Cunningham, J., et al. (2008). Pancreatic endoderm derived from human embryonic stem cells generates glucose-responsive insulin-secreting cells in vivo. Nat. Biotechnol. *26*, 443–452.

Lau, D., Ogbogu, U., Taylor, B., Stafinski, T., Menon, D., and Caulfield, T. (2008). Stem cell clinics online: the direct-to-consumer portrayal of stem cell medicine. Cell Stem Cell *3*, 591–594.

Ledford, H. (2011). Translational research: 4 ways to fix the clinical trial. Nature *477*, 526–528.

Lindvall, O., and Kokaia, Z. (2010). Stem cells in human neurodegenerative disorders—time for clinical translation? J. Clin. Invest. *120*, 29–40.

Lindvall, O., Brundin, P., Widner, H., Rehncrona, S., Gustavii, B., Frackowiak, R., Leenders, K.L., Sawle, G., Rothwell, J.C., Marsden, C.D., et al. (1990). Grafts of fetal dopamine neurons survive and improve motor function in Parkinson's disease. Science *247*, 574–577.

Lindvall, O., Sawle, G., Widner, H., Rothwell, J.C., Björklund, A., Brooks, D., Brundin, P., Frackowiak, R., Marsden, C.D., Odin, P., et al. (1994). Evidence for long-term survival and function of dopaminergic grafts in progressive Parkinson's disease. Ann. Neurol. *35*, 172–180.

Liu, S., Qu, Y., Stewart, T.J., Howard, M.J., Chakrabortty, S., Holekamp, T.F., and McDonald, J.W. (2000). Embryonic stem cells differentiate into oligodendrocytes and myelinate in culture and after spinal cord transplantation. Proc. Natl. Acad. Sci. USA *97*, 6126–6131.

Lorenz, E., Uphoff, D., Reid, T.R., and Shelton, E. (1951). Modification of irradiation injury in mice and guinea pigs by bone marrow injections. J. Natl. Cancer Inst. *12*, 197–201.

Ma, Y., Tang, C., Chaly, T., Greene, P., Breeze, R., Fahn, S., Freed, C., Dhawan, V., and Eidelberg, D. (2010). Dopamine cell implantation in Parkinson's disease: long-term clinical and (18)F-FDOPA PET outcomes. J. Nucl. Med. *51*, 7–15.

Macchiarini, P., Jungebluth, P., Go, T., Asnaghi, M.A., Rees, L.E., Cogan, T.A., Dodson, A., Martorell, J., Bellini, S., Parnigotto, P.P., et al. (2008). Clinical transplantation of a tissue-engineered airway. Lancet *372*, 2023–2030.

McDonald, J.W., and Belegu, V. (2006). Demyelination and remyelination after spinal cord injury. J. Neurotrauma *23*, 345–359.

McDonald, J.W., and Howard, M.J. (2002). Repairing the damaged spinal cord: a summary of our early success with embryonic stem cell transplantation and remyelination. Prog. Brain Res. *137*, 299–309.

McDonald, J.W., Liu, X.Z., Qu, Y., Liu, S., Mickey, S.K., Turetsky, D., Gottlieb, D.I., and Choi, D.W. (1999). Transplanted embryonic stem cells survive, differentiate and promote recovery in injured rat spinal cord. Nat. Med. *5*, 1410–1412.

McKenna, D., and Sheth, J. (2011). Umbilical cord blood: current status & promise for the future. Indian J. Med. Res. *134*, 261–269.

Menasche, P. (2011). Cardiac cell therapy: lessons from clinical trials. J. Mol. Cell. Cardiol. *50*, 258–265.

Nakajima, F., Tokunaga, K., and Nakatsuji, N. (2007). Human leukocyte antigen matching estimations in a hypothetical bank of human embryonic stem cell lines in the Japanese population for use in cell transplantation therapy. Stem Cells *25*, 983–985.

Nakamura, T., Dhawan, V., Chaly, T., Fukuda, M., Ma, Y., Breeze, R., Greene, P., Fahn, S., Freed, C., and Eidelberg, D. (2001). Blinded positron emission tomography study of dopamine cell implantation for Parkinson's disease. Ann. Neurol. *50*, 181–187.

Nicoleau, C., Viegas, P., Peschanski, M., and Perrier, A.L. (2011). Human pluripotent stem cell therapy for Huntington's disease: technical, immunological, and safety challenges human pluripotent stem cell therapy for Huntington's disease: technical, immunological, and safety challenges. Neurotherapeutics *8*, 562–576.

Nishida, K., Yamato, M., Hayashida, Y., Watanabe, K., Yamamoto, K., Adachi, E., Nagai, S., Kikuchi, A., Maeda, N., Watanabe, H., et al. (2004). Corneal reconstruction with tissue-engineered cell sheets composed of autologous oral mucosal epithelium. N. Engl. J. Med. *351*, 1187–1196.

Nistor, G.I., Totoiu, M.O., Haque, N., Carpenter, M.K., and Keirstead, H.S. (2005). Human embryonic stem cells differentiate into oligodendrocytes in high purity and myelinate after spinal cord transplantation. Glia *49*, 385–396.

Orlic, D., Kajstura, J., Chimenti, S., Jakoniuk, I., Anderson, S.M., Li, B., Pickel, J., McKay, R., Nadal-Ginard, B., Bodine, D.M., et al. (2001). Bone marrow cells regenerate infarcted myocardium. Nature *410*, 701–705.

Peck, M., Gebhart, D., Dusserre, N., McAllister, T.N., and L'Heureux, N. (2012). The evolution of vascular tissue engineering and current state of the art. Cells Tissues Organs (Print) *195*, 144–158.

Pelosi, E., Castelli, G., and Testa, U. (2012). Human umbilical cord is a unique and safe source of various types of stem cells suitable for treatment of hematological diseases and for regenerative medicine. Blood Cells Mol. Dis., in press. Published online March 23, 2012. 10.1016/j.bcmd.2012.02.007.

Piccini, P., Brooks, D.J., Björklund, A., Gunn, R.N., Grasby, P.M., Rimoldi, O., Brundin, P., Hagell, P., Rehncrona, S., Widner, H., and Lindvall, O. (1999). Dopamine release from nigral transplants visualized in vivo in a Parkinson's patient. Nat. Neurosci. *2*, 1137–1140.

Piccini, P., Lindvall, O., Björklund, A., Brundin, P., Hagell, P., Ceravolo, R., Oertel, W., Quinn, N., Samuel, M., Rehncrona, S., et al. (2000). Delayed recovery of movement-related cortical function in Parkinson's disease after striatal dopaminergic grafts. Ann. Neurol. *48*, 689–695.

Piccini, P., Pavese, N., Hagell, P., Reimer, J., Björklund, A., Oertel, W.H., Quinn, N.P., Brooks, D.J., and Lindvall, O. (2005). Factors affecting the clinical outcome after neural transplantation in Parkinson's disease. Brain *128*, 2977–2986.

Prasad, V.K., and Kurtzberg, J. (2009). Umbilical cord blood transplantation for non-malignant diseases. Bone Marrow Transplant. *44*, 643–651.

Rama, P., Matuska, S., Paganoni, G., Spinelli, A., De Luca, M., and Pellegrini, G. (2010). Limbal stem-cell therapy and long-term corneal regeneration. N. Engl. J. Med. *363*, 147–155.

Rocha, V., Labopin, M., Sanz, G., Arcese, W., Schwerdtfeger, R., Bosi, A., Jacobsen, N., Ruutu, T., de Lima, M., Finke, J., et al; Acute Leukemia Working Party of European Blood and Marrow Transplant Group; Eurocord-Netcord Registry. (2004). Transplants of umbilical-cord blood or bone marrow from unrelated donors in adults with acute leukemia. N. Engl. J. Med. *351*, 2276–2285.

Sanchez-Pernaute, R., Lee, H., Patterson, M., Reske-Nielsen, C., Yoshizaki, T., Sonntag, K.C., Studer, L., and Isacson, O. (2008). Parthenogenetic dopamine neurons from primate embryonic stem cells restore function in experimental Parkinson's disease. Brain *131*, 2127–2139.

Schwartz, S.D., Hubschman, J.P., Heilwell, G., Franco-Cardenas, V., Pan, C.K., Ostrick, R.M., Mickunas, E., Gay, R., Klimanskaya, I., and Lanza, R. (2012). Embryonic stem cell trials for macular degeneration: a preliminary report. Lancet *379*, 713–720.

Shapiro, A.M., Lakey, J.R., Ryan, E.A., Korbutt, G.S., Toth, E., Warnock, G.L., Kneteman, N.M., and Rajotte, R.V. (2000). Islet transplantation in seven patients with type 1 diabetes mellitus using a glucocorticoid-free immunosuppressive regimen. N. Engl. J. Med. *343*, 230–238.

Shapiro, A.M., Ricordi, C., Hering, B.J., Auchincloss, H., Lindblad, R., Robertson, R.P., Secchi, A., Brendel, M.D., Berney, T., Brennan, D.C., et al. (2006). International trial of the Edmonton protocol for islet transplantation. N. Engl. J. Med. *355*, 1318–1330.

Shi, M., Liu, Z.W., and Wang, F.S. (2011). Immunomodulatory properties and therapeutic application of mesenchymal stem cells. Clin. Exp. Immunol. *164*, 1–8.

Sun, H., Liu, W., Zhou, G., Zhang, W., Cui, L., and Cao, Y. (2011). Tissue engineering of cartilage, tendon and bone. Front. Med. *5*, 61–69.

Tabar, V., Tomishima, M., Panagiotakos, G., Wakayama, S., Menon, J., Chan, B., Mizutani, E., Al-Shamy, G., Ohta, H., Wakayama, T., and Studer, L. (2008). Therapeutic cloning in individual parkinsonian mice. Nat. Med. *14*, 379–381.

Taylor, C.J., Bolton, E.M., Pocock, S., Sharples, L.D., Pedersen, R.A., and Bradley, J.A. (2005). Banking on human embryonic stem cells: estimating the number of donor cell lines needed for HLA matching. Lancet *366*, 2019–2025.

Taylor, C.J., Bolton, E.M., and Bradley, J.A. (2011). Immunological considerations for embryonic and induced pluripotent stem cell banking. Philos. Trans. R. Soc. Lond. B Biol. Sci. *366*, 2312–2322.

Thomas, E.D. (2005). Bone marrow transplantation from the personal viewpoint. Int. J. Hematol. *81*, 89–93.

Thomas, E.D., Lochte, H.L., Jr., Lu, W.C., and Ferrebee, J.W. (1957). Intravenous infusion of bone marrow in patients receiving radiation and chemotherapy. N. Engl. J. Med. *257*, 491–496.

Tian, H., Bharadwaj, S., Liu, Y., Ma, P.X., Atala, A., and Zhang, Y. (2010). Differentiation of human bone marrow mesenchymal stem cells into bladder cells: potential for urological tissue engineering. Tissue Eng. Part A *16*, 1769–1779.

Tobita, M., Orbay, H., and Mizuno, H. (2011). Adipose-derived stem cells: current findings and future perspectives. Discov. Med. *11*, 160–170.

Tongers, J., Losordo, D.W., and Landmesser, U. (2011). Stem and progenitor cell-based therapy in ischaemic heart disease: promise, uncertainties, and challenges. Eur. Heart J. *32*, 1197–1206.

Trounson, A., Thakar, R.G., Lomax, G., and Gibbons, D. (2011). Clinical trials for stem cell therapies. BMC Med. *9*, 52.

Tsai, R.J., Li, L.M., and Chen, J.K. (2000). Reconstruction of damaged corneas by transplantation of autologous limbal epithelial cells. N. Engl. J. Med. *343*, 86–93.

Tsubota, K., Satake, Y., Kaido, M., Shinozaki, N., Shimmura, S., Bissen-Miyajima, H., and Shimazaki, J. (1999). Treatment of severe ocular-surface disorders with corneal epithelial stem-cell transplantation. N. Engl. J. Med. *340*, 1697–1703.

Vierbuchen, T., and Wernig, M. (2011). Direct lineage conversions: unnatural but useful? Nat. Biotechnol. *29*, 892–907.

Wernig, M., Zhao, J.P., Pruszak, J., Hedlund, E., Fu, D., Soldner, F., Broccoli, V., Constantine-Paton, M., Isacson, O., and Jaenisch, R. (2008). Neurons derived from reprogrammed fibroblasts functionally integrate into the fetal brain and improve symptoms of rats with Parkinson's disease. Proc. Natl. Acad. Sci. USA *105*, 5856–5861.

Williams, A.R., Trachtenberg, B., Velazquez, D.L., McNiece, I., Altman, P., Rouy, D., Mendizabal, A.M., Pattany, P.M., Lopera, G.A., Fishman, J., et al. (2011). Intramyocardial stem cell injection in patients with ischemic cardiomyopathy: functional recovery and reverse remodeling. Circ. Res. *108*, 792–796.

Wilson, J.M. (2009). Medicine. A history lesson for stem cells. Science *324*, 727–728.

Yamanaka, S. (2012). Induced pluripotent stem cells: past, present, and future. Cell Stem Cell *10*, this issue, 675–681.

Zhou, Q., Brown, J., Kanarek, A., Rajagopal, J., and Melton, D.A. (2008). In vivo reprogramming of adult pancreatic exocrine cells to beta-cells. Nature *455*, 627–632.

With Cell Press Reviews

Looking for authoritative reviews on the forefront of science? Turn to Cell Press. Our editors stay abreast of the latest developments so they can commission expert, cutting-edge reviews.

To propel your research forward, faster, turn to Cell Press Reviews. Our insightful, authoritative reviews—published across the life sciences in our primary research and *Trends* journals—go beyond synthesis and offer a point of view.

Find your way with Cell Press Reviews

www.cell.com/reviews

CellPress
Your work is our life

Cell Stem Cell
Brief Report

Successful Function of Autologous iPSC-Derived Dopamine Neurons following Transplantation in a Non-Human Primate Model of Parkinson's Disease

Penelope J. Hallett,[1] Michela Deleidi,[1] Arnar Astradsson,[1] Gaynor A. Smith,[1] Oliver Cooper,[1] Teresia M. Osborn,[1] Maria Sundberg,[1] Michele A. Moore,[1,2] Eduardo Perez-Torres,[1] Anna-Liisa Brownell,[1,3] James M. Schumacher,[1] Roger D. Spealman,[1,2] and Ole Isacson[1,4,*]
[1]Neuroregeneration Research Institute, McLean Hospital and Harvard Medical School, Belmont, MA 02478, USA
[2]New England Primate Research Center, Harvard Medical School, Southborough, MA 01772, USA
[3]MGH/HST Athinoula A. Martinos Center for Biomedical Imaging, Massachusetts General Hospital and Harvard Medical School, Charlestown, MA 02129, USA
[4]Harvard Stem Cell Institute, Cambridge, MA 02138, USA
*Correspondence: isacson@hms.harvard.edu
http://dx.doi.org/10.1016/j.stem.2015.01.018

SUMMARY

Autologous transplantation of patient-specific induced pluripotent stem cell (iPSC)-derived neurons is a potential clinical approach for treatment of neurological disease. Preclinical demonstration of long-term efficacy, feasibility, and safety of iPSC-derived dopamine neurons in non-human primate models will be an important step in clinical development of cell therapy. Here, we analyzed cynomolgus monkey (CM) iPSC-derived midbrain dopamine neurons for up to 2 years following autologous transplantation in a Parkinson's disease (PD) model. In one animal, with the most successful protocol, we found that unilateral engraftment of CM-iPSCs could provide a gradual onset of functional motor improvement contralateral to the side of dopamine neuron transplantation, and increased motor activity, without a need for immunosuppression. Postmortem analyses demonstrated robust survival of midbrain-like dopaminergic neurons and extensive outgrowth into the transplanted putamen. Our proof of concept findings support further development of autologous iPSC-derived cell transplantation for treatment of PD.

Cellular therapies offer an exciting opportunity to replace specific populations of cells in neurodegenerative diseases where symptoms are defined by the loss of a specific cell type, such as the degeneration of substantia nigra (SN) dopamine neurons in Parkinson's disease (PD). The use of induced pluripotent stem cell (iPSC)-derived neurons as an autologous cell source overcomes the current limitations posed by allogeneic donor cells in PD. Fetal ventral midbrain allografts can survive and function in the human PD brain for over 18 years (C.R. Freed et al., 2013, Soc. Neurosci., abstract; Hallett et al., 2014; Kefalopoulou et al., 2014; Mendez et al., 2005; Politis et al., 2010); however, such techniques will never become an easily accessible therapeutic option for patients due to the requirement of fetal donor tissue from elective abortions. Allografting in the brain also creates a greater immune reaction over time compared with isogeneic grafting (Duan et al., 1995; Morizane et al., 2013). The generation of midbrain-like dopamine neurons from patient-specific iPSCs and subsequent autologous transplantation is a rational long-term strategy for cell replacement in PD. Previous reports of autologous transplantation in a non-human primate PD model have demonstrated the advantage of autologous versus allogeneic grafts and shown dopamine neuron survival in the primate brain for up to 6 months to 1 year after transplantation (Emborg et al., 2013; Morizane et al., 2013; Sundberg et al., 2013). However, the long-term function, survival, and safety of iPSC-derived dopamine neurons following autologous transplantation in a non-human primate model of PD has not yet been established.

All studies were approved by the Harvard Medical School Institutional Animal Care and Use Committee (IACUC). To induce parkinsonism in cynomolgus monkeys (CMs), we administered systemic low-dose 1-methyl-4-phenyl-1,2,3,6-tetrahydropyridine (MPTP), which resulted in a progressive and persistent reduction in global motor activity and a stable bilateral parkinsonian syndrome, including tremor, rigidity, bradykinesia, hypokinesia, posture/balance disturbances, and impairment in both gross and fine motor skills (Table S1) (Brownell et al., 1998a; Hantraye et al., 1992; Wüllner et al., 1994). All animals displayed a significant loss of dopamine transporters (DATs) in the putamen as measured by 11C-(2β-carbomethoxy-3β-(4-fluorophenyl) tropane) (^{11}C-CFT) binding potential, as previously described (Brownell et al., 1998a). In a successive series of studies, three MPTP-lesioned CMs (MF25-04, MF66-02, and MF27-04) received autologous transplantation of CM-iPSC-derived neural cells into the putamen in order to assess the function and survival of engrafted autologous iPSC-derived dopamine neurons. CM-iPSCs from MF25-04 were differentiated using the protocol of Cooper et al. (2010), and CM-iPSCs from MF27-04 and MF66-02 were differentiated using the protocol of Sundberg et al. (2013). No animals in this study received any immunosuppression for the duration of the study.

We recorded global daytime motor activity of MPTP-lesioned CMs that had received autologous transplantation of iPSC-derived neural cells, using an automated activity monitor (Figure 1A). At 6 months after transplantation, daytime activity counts in animal MF25-04 (autologous iPSC transplant) were

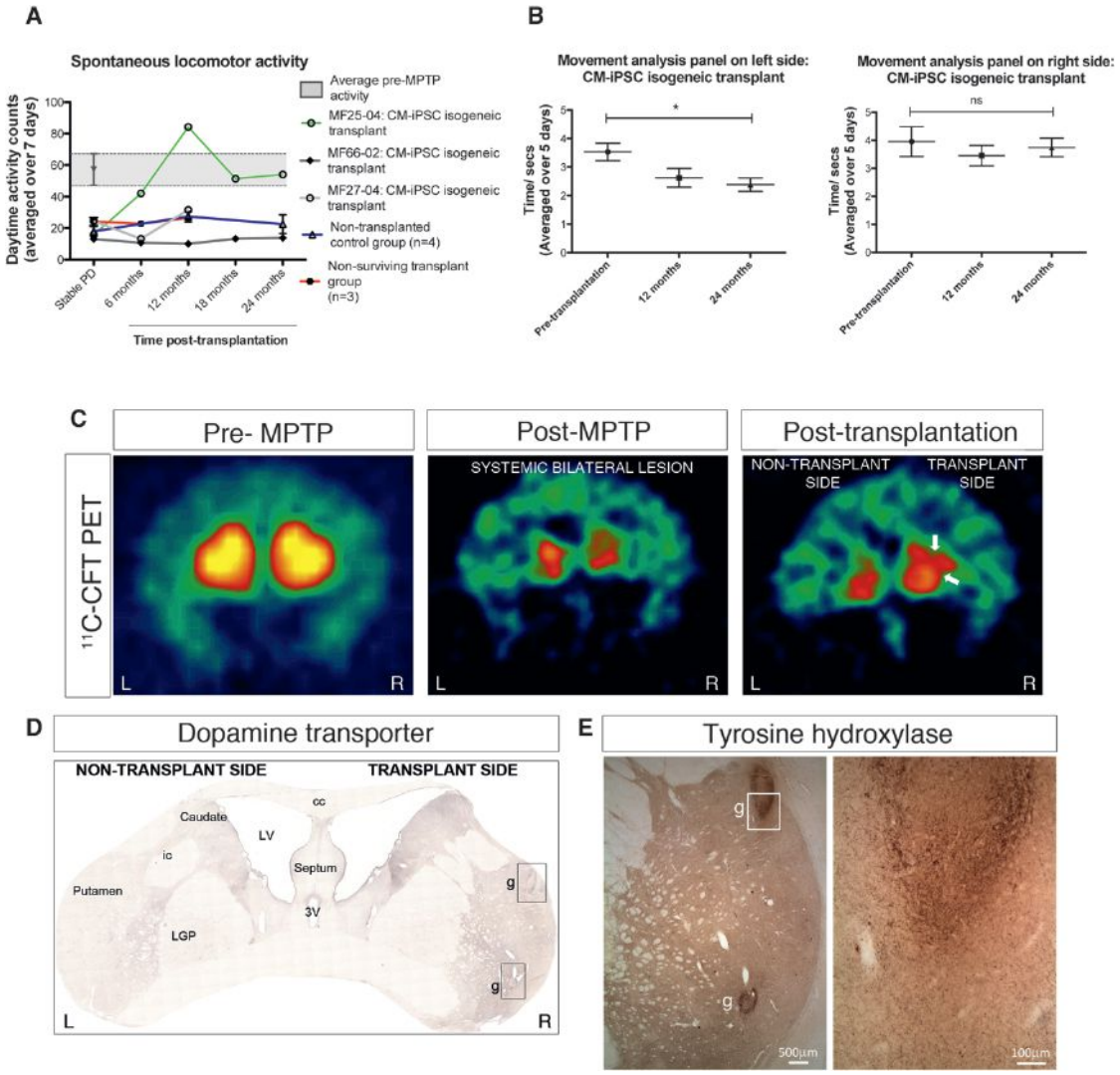

Figure 1. Functional Improvement of PD Motor Symptoms, Increased Dopamine Reuptake, and Reinnervation of the Transplanted Putamen after Autologous Transplantation of CM iPSC-Derived Dopamine Neurons

(A) Differentiated CM-iPSCs were transplanted unilaterally into the putamen of three CMs with stable, bilateral parkinsonism (MF25-04, MF66-02, MF27-04). The animals were followed for 1–2 years after transplantation. From 6 months after transplantation, functional improvement was observed in MF25-04, as determined by a sustained increase in global daytime (6 a.m. to 6 p.m.) activity. The non-transplanted control group and non-surviving transplant group represent the average data of n = 4 and n = 3 animals, respectively, and error bars show the SEM.

(B) Fine-motor skills in MF25-04 were assessed using a computerized reaching task MAP. At 2 years after transplantation, MAP performance in the left upper limb was significantly improved compared with pretransplantation values ($p < 0.05$, one-way ANOVA followed by Tukey's multiple comparison test). No change in performance was observed in the right upper limb. Data shown represent averages of five repeated tests (baseline), two repeated tests (1 year after transplantation), and three repeated tests (2 years after transplantation). Error bars represent the SEM.

(C) Functional analysis of dopamine reuptake in MF25-04 was measured by PET neuroimaging for ^{11}C-CFT, a marker of the DAT. Increased ^{11}C-CFT binding was observed in the transplanted putamen at 2 years after transplantation. White arrows indicate areas of hyperintense CFT PET signal.

(D) Low-power photomicrograph of DAT immunostaining in the transplanted (right, R) and non-transplanted (left, L) putamen in MF25-04 shows reinnervation of the transplanted side. Deposits of grafted dopamine neurons are indicated with boxes (g). IC, internal capsule; LGP, lateral globus pallidus; LV, lateral ventricle; 3V, third ventricle; cc, corpus callosum.

(E) Grafted dopamine neurons were also labeled using tyrosine hydroxylase (TH). The boxed area is shown at higher magnification in the right. Robust survival of dopamine neurons with outgrowth integration into the host putamen was observed.

increased by 146% compared with the stable parkinsonian pretransplantation activity in this animal. Over the subsequent 18 months of the study, motor activity in MF25-04 remained elevated and ranged from 178% to 292% above pretransplantation activity levels. At 2 years after transplantation, activity in this animal was 188% of stable MPTP baseline. The stable bilateral MPTP-lesion model used in this study provides an opportunity to assess asymmetry in movement functions following unilateral transplantation, using movement analysis panel (MAP) testing (Figure 1B). A progressive improvement in the use of left

(contralateral to the graft) upper limb motor function, compared with baseline values, was observed by 12 months after transplantation in MF25-04, and this reduction reached significance at 24 months after transplantation ($p < 0.05$, one-way ANOVA). Use of right upper limb motor function in MF25-04 was not significantly altered over the 24 months following the transplantation procedure. The severity of parkinsonian signs was also rated monthly using a parkinsonian rating scale (Table S1). We observed a reduction in the hypokinesia subsection of the parkinsonian rating scale in MF25-04, from a score of 2 prior to transplantation (maximum possible score is 3) to a score of 0 at 12 months after transplantation, and this remained stable at 0 until completion of the study (Table S1). Overall, the time course of functional recovery observed in MF25-04 was consistent with the developmental maturation, outgrowth, and connectivity of analogous fetal non-human primate dopamine neurons (Redmond et al., 2008; Tsui and Isacson, 2011). No marked changes in global motor activity, MAP test time, or hypokinesia were observed in animals MF27-04 and MF66-02 at 1–2 years after autologous transplantation of differentiated CM-iPSCs (Figure 1A; Table S1), suggestive of insufficient survival of engrafted CM-iPSC-derived midbrain dopamine neurons and reinnervation of the transplanted putamen (Grealish et al., 2010; Redmond et al., 2008). We also analyzed motor behavior in MPTP-lesioned CMs that received allogeneic transplantation with differentiated primate embryonic stem (ES) cells (Cyno-1) with no immunosuppression, as previously described (Sánchez-Pernaute et al., 2005), in which less than 50 surviving dopaminergic neurons were detected in the grafted putamen at postmortem (termed the ''non-surviving transplant'' group) ($n = 3$), and also in non-transplanted MPTP-lesioned CMs ($n = 4$) (Table S1). In the non-surviving transplant group, animals were followed for 12 months after the transplantation procedure before termination of the study; no significant changes in motor behavior were observed in these animals during this time (Figure 1A). Motor behavior was also not altered over a 2-year period in the non-transplant control group of parkinsonian animals (Figure 1A), consistent with the long-term functional stability of this bilateral MPTP non-human primate model (Brownell et al., 1998a; Hantraye et al., 1992; Wüllner et al., 1994).

Since functional improvement in parkinsonian motor symptoms was observed in the MF25-04 iPSC autologous transplant case, we performed ^{11}C-CFT-PET scanning to assess dopamine nerve terminals in the caudate and putamen at 2 years after transplantation of CM-iPSC-derived neural cells (Brownell et al., 1998a; Hantraye et al., 1992; Jenkins et al., 2004). At 2 years after transplantation, a marked increase in ^{11}C-CFT binding sites was observed in the right putamen compared with the non-transplanted left putamen, indicative of functional dopaminergic neurons on the transplanted side (Figure 1C).

Given the motor improvement and positive neuroimaging indicative of a functional graft in MF25-04, extensive postmortem examination of graft survival and morphology was performed at 2 years after transplantation. Macroscopic examination of the brain showed graft deposit sites within the putamen and normal striatal cytoarchitecture, with no displacement or compression of the host striatal parenchyma. Immunohistochemical labeling of DAT showed two distinct regions in the putamen containing clusters of DAT-immunoreactive (-ir) dopamine neurons (Figure 1D). Microscopic imaging of the entire transplanted and non-transplanted putamen showed markedly increased DAT labeling in the transplanted putamen compared with the non-transplant side, indicating robust reinnervation of the transplanted putamen from the engrafted CM-iPSC-derived dopaminergic neurons.

Stereological cell counts of TH-ir dopamine neurons showed the presence of 13,029 surviving transplanted dopaminergic neurons in the putamen. Engrafted TH-ir neurons (Figure 1E) were located predominantly around the periphery of the grafts and extended axons into the host putamen, similar to the pattern of A9-like dopamine neurons in rodent and human fetal VM transplant cases (Mendez et al., 2005; Vinuela et al., 2008). As a comparison, the number of surviving TH-ir dopamine neurons in the transplanted putamen of the CMs MF27-04 (Sundberg et al., 2013) and MF66-02 was also determined. These cases received autologous transplantation of iPSC-derived dopamine neurons, but in contrast to MF25-04, did not exhibit any functional improvement at 1–2 years after transplantation. A total of 8,551 and 7,938 TH-ir dopamine neurons was present in the transplanted putamen of MF27-04 and MF66-02, respectively. A comparison of outgrowth of TH-ir fibers into the putamen from the grafts of MF25-04, MF27-04, and MF66-02 showed far more extensive dopaminergic reinnervation in MF25-04 (Figures S2A–S2C), consistent with the functional recovery observed in this animal. These data indicate that improvement in motor function is achieved when an adequate number of transplanted midbrain dopamine neurons survive together with appropriate innervation of the transplanted putamen and that when there is not sufficient survival (less than 13,000 dopamine neurons) and poor dopamine axonal reinnervation of the putamen, CMs do not recover. Our data also show that in this series of iPSC transplantations, the Cooper et al. (2010) neuron differentiation protocol was the most successful. Dopamine neuron transplantation works at an adaptive level to provide a sufficient number of appropriate A9 dopaminergic neurons (and their synapses) in the striatum to initiate movement (function). In accord with this, we have also previously shown following fetal dopamine neuronal transplantation in a rat unilateral PD model (Brownell et al., 1998b) that behavioral recovery only occurs after a threshold of new striatal dopaminergic synapses is reached (75%–85% of the intact striatum). With the development of iPSC-derived midbrain-like dopamine neurons for clinical use in PD, it will be essential to take into consideration that survival of a minimal required dose of transplanted midbrain-like dopamine neurons (Grealish et al., 2014) and sufficient reinnervation of the denervated putamen is necessary for improvement of PD motor symptoms.

Colocalization of FOXA2/TH/βIII tubulin labeling confirmed the presence of midbrain-like dopamine neurons in the graft of MF25-04 (Figure 2A). A separate FOXA2/TH labeling was performed in parallel in each of the three CM-iPSC grafts (MF25-04, MF27-04, and MF66-02) and showed more frequent FOXA2/TH colabeled (midbrain-like) dopamine neurons in the graft of MF25-04 compared with the grafts in MF27-04 and MF66-02 (Figures S2D–S2F). A punctate expression of DAT along transplanted TH-ir cell bodies and processes confirmed the formation of mature synapses in MF25-04 (Figure 2B). For an additional measure of neuronal health, the localization of

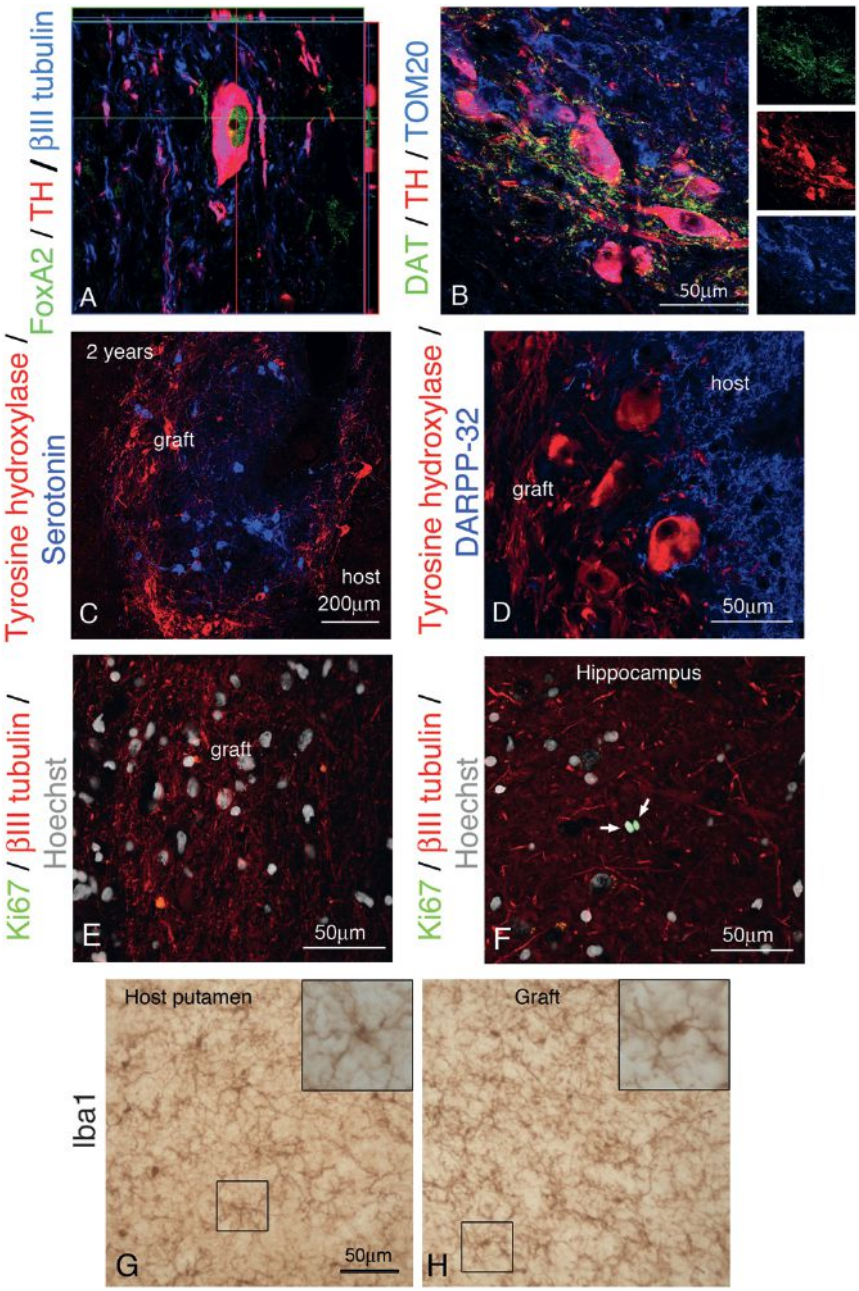

Figure 2. Phenotypes of Engrafted CM iPSC-Derived Neurons at 2 Years after Autologous Transplantation

Postmortem immunohistochemical analysis was used to further characterize the graft in MF25-04.

(A) Immunofluorescence staining confirmed that transplanted dopamine neurons were colabeled for FOXA2, TH, and βIII tubulin at 2 years after transplantation.

(B) Labeling for DAT, TH, and TOM20 (a mitochondrial outer membrane protein) showed a punctate expression of DAT along the fibers of transplanted dopamine neurons and a typical localization of mitochondria throughout the cell soma and neurites.

(C) Immunofluorescence staining for 5-HT demonstrated the presence and localization of serotonergic neurons within the graft.

(D) Labeling for DARPP-32, a marker of striatal GABAergic medium spiny neurons, shows robust labeling in the host putamen and occasional DARPP-32-ir fibers at the graft-host border.

(E and F) Ki-67 was used to determine whether proliferating cells were present in the CM-iPSC-derived neural cell graft from MF25-04. No Ki-67-immunoreactive cells were observed in the graft (E). As a positive control, several Ki-67-immunoreactive proliferating cells were observed in the hippocampus of the same animal (F) (identified with arrows).

(G and H) Histological analysis of microglia using Iba1 in the host putamen (G) and graft (H) shows typical resting microglia.

mitochondria within TH-ir neurons was assessed using the mitochondrial marker, translocase of outer mitochondrial membrane 20 (TOM20) (Hallett et al., 2014). A homogenous localization of TOM20-ir mitochondria throughout the cell soma and processes of transplanted neurons in MF25-04 was observed (Figure 2B), and there was no evidence of perinuclear accumulation or fragmentation of mitochondria, as has previously been reported during dopamine neuron stress or degeneration (Sterky et al., 2011).

Immunofluorescence labeling for 5HT (Figure 2C) was performed to examine serotonergic neurons contained in the CM-iPSC-derived transplant case, MF25-04. Serotonergic neurons were observed with a distribution and frequency similar to that previously reported for rodent and human fetal VM grafts (Mendez et al., 2008; Vinuela et al., 2008). Labeling for striatal medium spiny GABAergic neurons in the grafted putamen using DARPP-32 (Figure 2D) revealed robust DARPP-32 labeling in the host putamen perikarya and sparse DARPP-32-ir fibers at the graft-host border suggestive of some graft-host interaction as has been previously reported in fetal VM tissue (Doucet et al., 1989). Immunostaining with the proliferation marker, Ki-67, showed no positively labeled cells in the graft at 24 months after transplantation (Figures 2E and 2F). As a positive control, several Ki-67-labeled cells were observed in the dentate gyrus of the same animal (MF25-04). These data are in accord with our previous work using CM-iPSC-derived neural cell xenotransplantation in rats, where a low percentage of Ki-67-ir cells at 4 weeks after transplantation were observed, but no Ki-67-ir cells were found in mature grafts (16 weeks after transplantation) (Deleidi et al., 2011).

Histological analysis of microglial reactivity using immunohistochemistry for Iba1 revealed a local circumscribed increase in microglial cell density within the CM-iPSC-derived grafts (Figures 2G, 2H, S2H, and S2I). However, Iba1 labeling was not different to that observed in the needle tracts of the

"non-surviving" transplant group (Figure S2G), and there was no immune reaction in the host putamen surrounding the autologous iPSC grafts. A prior report indicates that compared with autologous transplantation, allogeneic iPSC-derived neural cells elicit greater microglial activation, as well as MHCII (class II major histocompatibility complex) microglial expression and infiltration of leukocytes at ~4 months after transplantation into the non-human primate brain (Morizane et al., 2013). The route of autologous transplantation, which requires no immunosuppression, may therefore be a more successful route for cell therapy than using cell sources that are not completely matched to the donor. Our work demonstrates in the successful case that dopamine synapse innervation is accompanied by the anticipated neurological improvement in parkinsonism. However, ~13,000 primate midbrain dopamine neurons were needed to reach the threshold of functional improvements. The next steps in this work require consistent protocols to provide equivalent or greater midbrain dopamine neuron survival, presumably by increasing the dose of midbrain dopamine neurons, and scale up toward potential future clinical trials.

The present findings provide the first proof of concept preclinical study to demonstrate that autologous iPSC-derived midbrain-like dopamine neurons can engraft and survive over an extended period of time (at least 2 years), and improve motor function, in a non-human primate model of PD. Such autologous iPSC-derived dopamine neurons can provide remarkable and complete reinnervation of the denervated putamen without any immunosuppression. We observed the most extensive dopaminergic axonal outgrowth reported in any study to date, including our own and others, after engraftment with iPSC-derived dopamine neurons in vivo (Emborg et al., 2013; Kikuchi et al., 2011; Sundberg et al., 2013). In addition, in the current study, we observed no graft overgrowth, tumor formation, or inflammatory reaction, which is consistent with our previous rodent studies using iPSC-derived neural cells (Hargus et al., 2010; Sundberg et al., 2013; Wernig et al., 2008).

A general concern about the use of autologous transplantation is whether underlying PD-associated genetic mutations present in transplanted neurons would increase the vulnerability of midbrain dopaminergic neurons to disease pathology. However, such vulnerabilities do not preclude cell function at a fairly optimal level for at least 50–60 years from birth in a typical patient with such genetic risk (which represents a minority of PD cases). In addition, given how transplanted fetal neurons remain healthy for many years in PD patients, despite ongoing disease processes in the host brain (Hallett et al., 2014), we would predict that even in cases with severe genetic risk, iPSC-derived neurons are a reasonable strategy.

In summary, our study clearly shows proof of concept for transplantation using iPSC-derived dopamine neurons in a preclinical context, and it is reasonable to infer that iPSC transplantation would provide clinical benefit and expected graft survival times similar to that observed with fetal transplantation (Barker et al., 2013; Hallett et al., 2014; Kefalopoulou et al., 2014). Our data showing neurologically relevant functional improvements with concomitant positive neuroimaging are essential for the continued development and clinical translation of cell therapy using iPSCs. Overall, there is a strong immunological, functional, and biological rationale for using midbrain dopamine neurons derived from iPSCs for cell replacement in PD in the future. Currently, it is essential to determine the optimal and safest dopamine neuron differentiation protocol to use, to evaluate the generation of different (non-neuronal) cell types, and to continue to refine the clinical protocols for generation of iPSC-derived midbrain dopamine neurons to be used for transplantation to PD patients.

SUPPLEMENTAL INFORMATION

Supplemental Information includes Supplemental Experimental Procedures, two figures, and one table and can be found with this article online at http://dx.doi.org/10.1016/j.stem.2015.01.018.

ACKNOWLEDGMENTS

We thank the veterinary and research staff, including Dr. Leah Makaron, Dr. Angela Carville, Dr. Andrew Miller, Matthew Beck, Jack McDowell, Melissa Hayes, Jonathan Beagan, Zachary Schneider-Lynch, Sayantan Deb, and Alex Casler, at the New England Primate Research Center and the Neuroregeneration Research Institute for excellent veterinary and technical assistance. This study was supported by the Harvard Stem Cell Institute Miller Consortium for the Development of Nervous System Therapies and the Udall Parkinson's Disease Center of Excellence grant P50 NS39793, Department of Defense WX81XWH-11-1-0069, Orchard Foundation, Poul Hansen Family, Consolidated Anti-Aging Foundation and Harold and Ronna Cooper Family (to O.I.), National Center for Research Resources RR00168, and the Office of Research Infrastructure Programs OD011103 (to R.D.S.).

Received: November 17, 2014
Revised: December 17, 2014
Accepted: January 30, 2015
Published: February 26, 2015

REFERENCES

Barker, R.A., Barrett, J., Mason, S.L., and Björklund, A. (2013). Fetal dopaminergic transplantation trials and the future of neural grafting in Parkinson's disease. Lancet Neurol. *12*, 84–91.

Brownell, A.-L., Jenkins, B.G., Elmaleh, D.R., Deacon, T.W., Spealman, R.D., and Isacson, O. (1998a). Combined PET/MRS brain studies show dynamic and long-term physiological changes in a primate model of Parkinson disease. Nat. Med. *4*, 1308–1312.

Brownell, A.L., Livni, E., Galpern, W., and Isacson, O. (1998b). In vivo PET imaging in rat of dopamine terminals reveals functional neural transplants. Ann. Neurol. *43*, 387–390.

Cooper, O., Hargus, G., Deleidi, M., Blak, A., Osborn, T., Marlow, E., Lee, K., Levy, A., Perez-Torres, E., Yow, A., and Isacson, O. (2010). Differentiation of human ES and Parkinson's disease iPS cells into ventral midbrain dopaminergic neurons requires a high activity form of SHH, FGF8a and specific regionalization by retinoic acid. Mol. Cell. Neurosci. *45*, 258–266.

Deleidi, M., Hargus, G., Hallett, P., Osborn, T., and Isacson, O. (2011). Development of histocompatible primate-induced pluripotent stem cells for neural transplantation. Stem Cells *29*, 1052–1063.

Doucet, G., Murata, Y., Brundin, P., Bosler, O., Mons, N., Geffard, M., Ouimet, C.C., and Björklund, A. (1989). Host afferents into intrastriatal transplants of fetal ventral mesencephalon. Exp. Neurol. *106*, 1–19.

Duan, W.M., Widner, H., and Brundin, P. (1995). Temporal pattern of host responses against intrastriatal grafts of syngeneic, allogeneic or xenogeneic embryonic neuronal tissue in rats. Exp. Brain Res. *104*, 227–242.

Emborg, M.E., Liu, Y., Xi, J., Zhang, X., Yin, Y., Lu, J., Joers, V., Swanson, C., Holden, J.E., and Zhang, S.C. (2013). Induced pluripotent stem cell-derived neural cells survive and mature in the nonhuman primate brain. Cell Rep. *3*, 646–650.

Grealish, S., Jönsson, M.E., Li, M., Kirik, D., Björklund, A., and Thompson, L.H. (2010). The A9 dopamine neuron component in grafts of ventral mesencephalon is an important determinant for recovery of motor function in a rat model of Parkinson's disease. Brain *133*, 482–495.

Grealish, S., Diguet, E., Kirkeby, A., Mattsson, B., Heuer, A., Bramoulle, Y., Van Camp, N., Perrier, A.L., Hantraye, P., Björklund, A., and Parmar, M. (2014). Human ESC-derived dopamine neurons show similar preclinical efficacy and potency to fetal neurons when grafted in a rat model of Parkinson's disease. Cell Stem Cell *15*, 653–665.

Hallett, P.J., Cooper, O., Sadi, D., Robertson, H., Mendez, I., and Isacson, O. (2014). Long-term health of dopaminergic neuron transplants in Parkinson's disease patients. Cell Rep. *7*, 1755–1761.

Hantraye, P., Brownell, A.L., Elmaleh, D., Spealman, R.D., Wüllner, U., Brownell, G.L., Madras, B.K., and Isacson, O. (1992). Dopamine fiber detection by [11C]-CFT and PET in a primate model of parkinsonism. Neuroreport *3*, 265–268.

Hargus, G., Cooper, O., Deleidi, M., Levy, A., Lee, K., Marlow, E., Yow, A., Soldner, F., Hockemeyer, D., Hallett, P.J., et al. (2010). Differentiated Parkinson patient-derived induced pluripotent stem cells grow in the adult rodent brain and reduce motor asymmetry in Parkinsonian rats. Proc. Natl. Acad. Sci. USA *107*, 15921–15926.

Jenkins, B.G., Sanchez-Pernaute, R., Brownell, A.L., Chen, Y.C., and Isacson, O. (2004). Mapping dopamine function in primates using pharmacologic magnetic resonance imaging. J. Neurosci. *24*, 9553–9560.

Kefalopoulou, Z., Politis, M., Piccini, P., Mencacci, N., Bhatia, K., Jahanshahi, M., Widner, H., Rehncrona, S., Brundin, P., Bjorklund, A., et al. (2014). Long-term clinical outcome of fetal cell transplantation for Parkinson disease: two case reports. JAMA Neurol. *71*, 83–87.

Kikuchi, T., Morizane, A., Doi, D., Onoe, H., Hayashi, T., Kawasaki, T., Saiki, H., Miyamoto, S., and Takahashi, J. (2011). Survival of human induced pluripotent stem cell-derived midbrain dopaminergic neurons in the brain of a primate model of Parkinson's disease. J. Parkinsons Dis. *1*, 395–412.

Mendez, I., Sanchez-Pernaute, R., Cooper, O., Viñuela, A., Ferrari, D., Björklund, L., Dagher, A., and Isacson, O. (2005). Cell type analysis of functional fetal dopamine cell suspension transplants in the striatum and substantia nigra of patients with Parkinson's disease. Brain *128*, 1498–1510.

Mendez, I., Viñuela, A., Astradsson, A., Mukhida, K., Hallett, P., Robertson, H., Tierney, T., Holness, R., Dagher, A., Trojanowski, J.Q., and Isacson, O. (2008). Dopamine neurons implanted into people with Parkinson's disease survive without pathology for 14 years. Nat. Med. *14*, 507–509.

Morizane, A., Doi, D., Kikuchi, T., Okita, K., Hotta, A., Kawasaki, T., Hayashi, T., Onoe, H., Shiina, T., Yamanaka, S., and Takahashi, J. (2013). Direct comparison of autologous and allogeneic transplantation of iPSC-derived neural cells in the brain of a non-human primate. Stem Cell Reports *1*, 283–292.

Politis, M., Wu, K., Loane, C., Quinn, N.P., Brooks, D.J., Rehncrona, S., Bjorklund, A., Lindvall, O., and Piccini, P. (2010). Serotonergic neurons mediate dyskinesia side effects in Parkinson's patients with neural transplants. Sci. Transl. Med. *2*, 38ra46.

Redmond, D.E., Jr., Vinuela, A., Kordower, J.H., and Isacson, O. (2008). Influence of cell preparation and target location on the behavioral recovery after striatal transplantation of fetal dopaminergic neurons in a primate model of Parkinson's disease. Neurobiol. Dis. *29*, 103–116.

Sánchez-Pernaute, R., Studer, L., Ferrari, D., Perrier, A., Lee, H., Viñuela, A., and Isacson, O. (2005). Long-term survival of dopamine neurons derived from parthenogenetic primate embryonic stem cells (cyno-1) after transplantation. Stem Cells *23*, 914–922.

Sterky, F.H., Lee, S., Wibom, R., Olson, L., and Larsson, N.G. (2011). Impaired mitochondrial transport and Parkin-independent degeneration of respiratory chain-deficient dopamine neurons in vivo. Proc. Natl. Acad. Sci. USA *108*, 12937–12942.

Sundberg, M., Bogetofte, H., Lawson, T., Jansson, J., Smith, G., Astradsson, A., Moore, M., Osborn, T., Cooper, O., Spealman, R., et al. (2013). Improved cell therapy protocols for Parkinson's disease based on differentiation efficiency and safety of hESC-, hiPSC-, and non-human primate iPSC-derived dopaminergic neurons. Stem Cells *31*, 1548–1562.

Tsui, A., and Isacson, O. (2011). Functions of the nigrostriatal dopaminergic synapse and the use of neurotransplantation in Parkinson's disease. J. Neurol. *258*, 1393–1405.

Vinuela, A., Hallett, P.J., Reske-Nielsen, C., Patterson, M., Sotnikova, T.D., Caron, M.G., Gainetdinov, R.R., and Isacson, O. (2008). Implanted reuptake-deficient or wild-type dopaminergic neurons improve ON L-dopa dyskinesias without OFF-dyskinesias in a rat model of Parkinson's disease. Brain *131*, 3361–3379.

Wernig, M., Zhao, J.P., Pruszak, J., Hedlund, E., Fu, D., Soldner, F., Broccoli, V., Constantine-Paton, M., Isacson, O., and Jaenisch, R. (2008). Neurons derived from reprogrammed fibroblasts functionally integrate into the fetal brain and improve symptoms of rats with Parkinson's disease. Proc. Natl. Acad. Sci. USA *105*, 5856–5861.

Wüllner, U., Pakzaban, P., Brownell, A.L., Hantraye, P., Burns, L., Shoup, T., Elmaleh, D., Petto, A.J., Spealman, R.D., Brownell, G.L., et al. (1994). Dopamine terminal loss and onset of motor symptoms in MPTP-treated monkeys: a positron emission tomography study with 11C-CFT. Exp. Neurol. *126*, 305–309.

Cell Stem Cell
Clinical Progress

Human ESC-Derived Dopamine Neurons Show Similar Preclinical Efficacy and Potency to Fetal Neurons when Grafted in a Rat Model of Parkinson's Disease

Shane Grealish,[1,2,*] Elsa Diguet,[3] Agnete Kirkeby,[1,2] Bengt Mattsson,[1] Andreas Heuer,[1,2] Yann Bramoulle,[3] Nadja Van Camp,[3] Anselme L. Perrier,[4,5] Philippe Hantraye,[3] Anders Björklund,[1] and Malin Parmar[1,2,*]
[1]Developmental and Regenerative Neurobiology, Department of Experimental Medical Science, Wallenberg Neuroscience Center, Lund University, 22184 Lund, Sweden
[2]Lund Stem Cell Center, Lund University, 22184 Lund, Sweden
[3]Molecular Imaging Research Centre (MIRCen), Commissariat à l'Energie Atomique (CEA), 92264 Fontenay-aux-Roses, France
[4]Inserm U861, I-Stem, AFM, 91030 Evry Cedex, France
[5]UEVE U861, I-Stem, AFM, 91030 Evry Cedex, France
*Correspondence: shane.grealish@med.lu.se (S.G.), malin.parmar@med.lu.se (M.P.)
http://dx.doi.org/10.1016/j.stem.2014.09.017

SUMMARY

Considerable progress has been made in generating fully functional and transplantable dopamine neurons from human embryonic stem cells (hESCs). Before these cells can be used for cell replacement therapy in Parkinson's disease (PD), it is important to verify their functional properties and efficacy in animal models. Here we provide a comprehensive preclinical assessment of hESC-derived midbrain dopamine neurons in a rat model of PD. We show long-term survival and functionality using clinically relevant MRI and PET imaging techniques and demonstrate efficacy in restoration of motor function with a potency comparable to that seen with human fetal dopamine neurons. Furthermore, we show that hESC-derived dopamine neurons can project sufficiently long distances for use in humans, fully regenerate midbrain-to-forebrain projections, and innervate correct target structures. This provides strong preclinical support for clinical translation of hESC-derived dopamine neurons using approaches similar to those established with fetal cells for the treatment of Parkinson's disease.

INTRODUCTION

Cell replacement therapy in Parkinson's disease (PD) is based on the premise that transplanted midbrain dopamine (DA) neurons can restore dopaminergic neurotransmission when transplanted to the DA-depleted striatum, providing a functionally efficient substitute for the neurons that are lost in the disease. Clinical trials using cells derived from human fetal ventral mesencephalon (VM) have shown that transplanted DA neurons can functionally reinnervate the denervated striatum, restore DA release, and at least in some PD patients, provide substantial long-term clinical improvement (Barker et al., 2013; Kefalopoulou et al., 2014). However, the use of tissue from aborted human embryos presents several ethical and logistical issues that hamper the effective translation of fetal tissue transplantation as a realistic therapeutic option.

In order to move to large-scale clinical applications, a readily available, renewable, and bankable source of cells with the potential to differentiate into fully functional DA neurons after transplantation is an absolute requirement. Among the different stem cell sources available, human pluripotent stem cells, in particular human embryonic stem cells (hESCs), have advanced the furthest (Lindvall and Kokaia, 2009; Barker, 2014). Using protocols entirely based on extrinsic patterning cues that mimic fetal midbrain development, it is now possible to generate DA neurons with an authentic midbrain phenotype from human pluripotent stem cells that survive transplantation and that can restore motor deficits in animal models of PD (Doi et al., 2014; Kirkeby et al., 2012a; Kriks et al., 2011).

However, a number of crucial issues need to be addressed in preclinical studies before these cells can be considered for clinical use: it is important to verify that their functional efficacy is robust, reproducible, and stable over significant time periods; that the transplanted cells have the capacity to grow axons and reinnervate the DA-denervated host striatum over distances that are relevant for the size of the human brain; and that they function with equal potency to human fetal VM DA neurons that have previously been used in clinical trials (Barker, 2014).

Here we have performed a rigorous preclinical assessment of long-term in vivo functionality and axonal outgrowth capacity of hESC-derived midbrain DA neurons, critical for their translation to the clinic. We show long-term survival and functionality using clinically relevant MRI and positron emission tomography (PET) imaging techniques and efficacy in restoration of motor function that is comparable to that seen with human fetal cells. Importantly, we provide a direct comparison of human DA neurons sourced from either hESCs or fetal VM and show that hESC-derived neurons, like their fetal counterparts, can project over long distances in the lesioned adult rodent brain and regenerate axonal projections with cell-type specific innervation of correct

target structures. These data represent an important milestone in the preclinical assessment of hESC-derived DA neurons and provide essential support for their usefulness in cell replacement therapy for PD.

RESULTS

Long-Term Survival and Restoration of Dopaminergic Neurotransmission by hESC-DA Neurons

First, we wanted to assess long-term survival and function of grafted cells using methodologies that are used in the clinic. We therefore transplanted hESC-derived DA (hESC-DA) neurons to the striatum of 6-hydroxydopamine (6-OHDA) lesioned athymic, adult rats, allowing for long-term graft survival in the absence of immunosuppressive treatment. The grafted animals were followed up to 6 months after transplantation, the point at which grafts of fetal VM in patients start to become functional (Piccini et al., 2000). T2-weighed MRI imaging showed surviving transplants that increased in volume from 1 to 5 months post-transplantation, indicating initial proliferation and subsequent maturation of the transplanted cells (Figure S1A available online), as previously described for transplants of proliferative midbrain progenitors (Kirkeby et al., 2012a). MR spectroscopy investigation 5 months postgrafting revealed a high *N*-acetylaspartic acid content within the transplanted area, indicative of a neuron-rich graft (Figures S1B and S1C). Pretransplantation, the rats were assessed for deficits in striatal dopaminergic neurotransmission by PET, using ^{18}F-fallypride as a measure of D_2/D_3-receptor occupancy (Moon et al., 2010) and ^{18}F-LBT999 as a tracer for the dopamine transporter (DAT) (Dollé et al., 2007) (Figure 1A). In the 6-OHDA-lesioned DA-denervated striatum ^{18}F-fallypride binding was significantly increased, as compared with the intact hemisphere, signifying a pronounced reduction in DA release. After grafting, ^{18}F-fallypride binding was normalized to intact levels as assessed 5 months posttransplantation, indicative of active DA release from the transplanted hESC-DA neurons (Figures 1A and 1B). Similarly, the near-complete loss of DAT binding, using ^{18}F-LBT999, seen after 6-OHDA lesion was reversed to around 50% of normal (Figures 1A and 1C). ^{18}F-DPA714 binding was used to measure microglial activation (Kuhnast et al., 2012), and no increase was observed at 5 months postgrafting, relative to the nontransplanted side (Figure 1A).

Histological Analysis and Innervation Capacity of hESC-DA Neurons after Intrastriatal Transplantation

Histological analysis confirmed the imaging data, showing neuron-rich transplants and revealing grafts rich in DA neurons, expressing both tyrosine hydroxylase (TH) and dopamine transporter (DAT), in the absence of a notable active microglial (Iba1$^+$) response, overgrowths, or necrotic areas (Figures S2A–S2C). To assess graft-derived axonal outgrowth we made use of an antibody specific for human neural cell adhesion molecule (hNCAM) (Figures 1D–1G), allowing selective and highly sensitive visualization of the grafted neurons and their projections. Dense hNCAM$^+$ innervation was observed throughout the caudate-putamen, including the dorsolateral striatum, which derives its innervation exclusively from the A9 neurons of the substantia nigra (SN) (Figure 1D). Similar innervation was also observed in other forebrain DA target areas outside the caudate-putamen, such as nucleus accumbens (NAc) (Figure 1E), olfactory tubercle (Figure 1D), and the perirhinal and prelimbic cortices (Figures 1F and 1G), which are essential targets for the A10 neuronal subtype, residing in the ventral tegmental area (VTA) (Figures S2D and S2E).

Taken together, these data prove the ability of hESC-DA neurons to provide extensive reinnervation of the host striatum and begin to restore DAergic neurotransmission 5 months posttransplantation, using clinically relevant methods to assess graft function, in the absence of significant adverse events. This is in line with previous clinical observations using human fetal VM grafted to patients, where progressive recovery of DA neurotransmission starts at 6 months, reflecting the gradual maturation of the transplanted cells (Piccini et al., 1999, 2000).

Functional Potency Assessment of hESC-DA Neurons Grafted to the Striatum

We and others have previously shown that hESC-DA neurons can release DA in vivo (Kirkeby et al., 2012a) and restore a number of motor deficits in 6-OHDA rodent models of PD when assessed 16–18 weeks after grafting (Kirkeby et al., 2012a; Kriks et al., 2011). However, these transplants contained 15,000–18,000 hESC-derived DA neurons, and the high cell number makes it difficult to estimate the efficacy of the cells (Barker, 2014). In previous preclinical and experimental studies using grafts of human fetal VM, it has been shown that normalization of amphetamine-induced rotation after intrastriatal transplantation can be achieved with an average number of 1,200 surviving TH$^+$ neurons (Brundin et al., 1986). On the basis of this information, we performed a potency experiment designed to determine the minimal number of hESC-DA neurons capable of inducing functional recovery in the amphetamine-induced rotation test. We transplanted 6-OHDA lesioned rats, aiming for at least a 10-fold lower number of hESC-DA than the grafts functionally assessed in earlier studies (Kirkeby et al., 2012a; Kriks et al., 2011). The rats were pretested to confirm the completeness of the lesion and immunosuppressed with daily injections of ciclosporin for 18 weeks. At this time point, the rats showed a significant recovery in amphetamine-induced rotation (Figure 2A: $t_4 = 6.76$, $p < 0.01$; $n = 5$), despite a much lower number of TH$^+$ neurons in the grafts (Figures 2B and 2C). Quantifications showed that the average number of surviving TH$^+$ neurons was 986 ± 333 per rat ($n = 5$). Two of the rats had less than 500 surviving hESC-DA neurons and yet showed a complete reduction in rotational bias (Figure 2B). Within TRANSERUO, a EU-funded research consortium formed to develop an efficacious and safe treatment methodology for PD using fetal cell based treatments (http://www.transeuro.org.uk), research groups including our own have optimized and standardized tissue preparation protocols across several centers throughout Europe. A recent report with cells prepared using this protocol show that a significant reduction in amphetamine-induced rotation could be achieved with transplants of human fetal VM with as few 657 ± 199 surviving TH$^+$ neurons (Rath et al., 2013). These results indicate that the functional potency of grafted hESC-DA neurons is on par with that of human DA neurons obtained from fetal VM (Brundin et al., 1986; Rath et al., 2013).

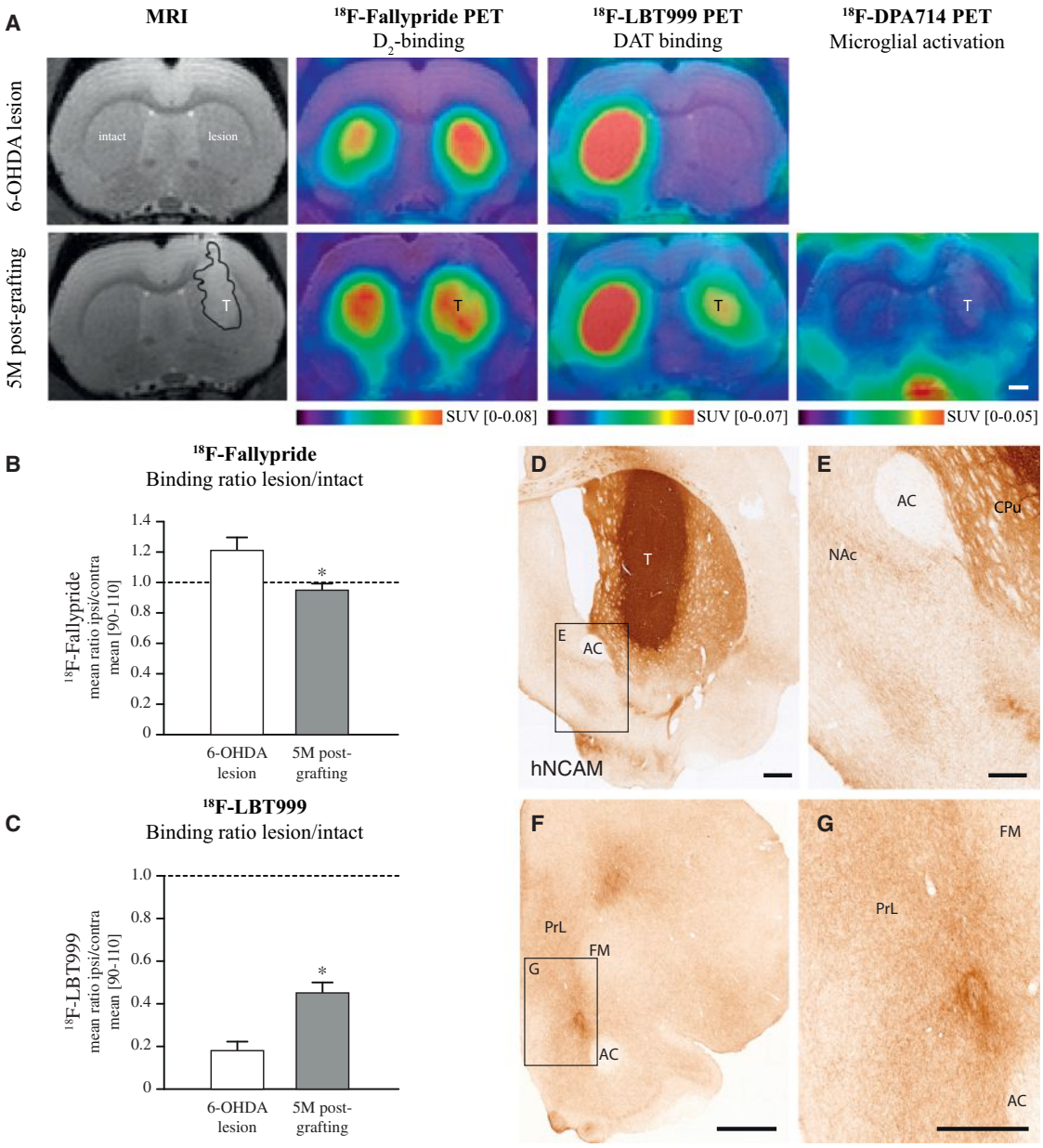

Figure 1. Functional Imaging of Long-Term Surviving Intrastriatal Transplants of hESC-DA Neurons

(A) MRI and PET scans for ^{18}F-fallypride, ^{18}F-LBT999 after 6-OHDA lesion, show an increase in binding of ^{18}F-fallypride (n = 6) on the side of lesion indicating an impaired DA release, confirmed by a loss of ^{18}F-LBT999 (n = 7) binding due to loss of DAT binding sites. At 5 months posttransplantation both ^{18}F-fallypride (n = 11) and ^{18}F-LBT999 (n = 14) binding are restored toward normal, indicative of a graft rich in functional DA neurons, in the absence of any detectable microglial response, as assessed with ^{18}F-DPA714 (n = 13).

(B) Quantitative measurements of binding ratios between intact and lesioned striatum revealed an increased binding potential of ^{18}F-fallypride in the 6-OHDA denervated striatum, which was normalized to intact levels 5 months posttransplantation of hESC-DA neurons.

(C) A 6-OHDA lesion resulted in a near complete loss of ^{18}F-LBT999 binding due to the loss of DAT-expressing dopaminergic terminals, which was restored toward normal posttransplantation.

(D and E) Immunohistochemistry of hNCAM revealed neuron-rich grafts of hESC-DA neurons 6 months posttransplantation, providing extensive innervation of the host CPu and surrounding extrastriatal dopaminergic targets, such as NAc.

(F and G) Away from the graft core, widespread innervation by human axons was found in known DA target structures within the prefrontal cortex.

See also Figure S1. AC, anterior commissure; CPu, caudate-putamen unit; FM, forceps minor; NAc, nucleus accumbens; PrL, prelimbic cortex; T, transplant. In (B) and (C), data are represented as mean ± SEM. *p < 0.01. In (A), (D), and (F), scale bars represent 1 mm. In (E) and (G), scale bars represent 0.5 mm.

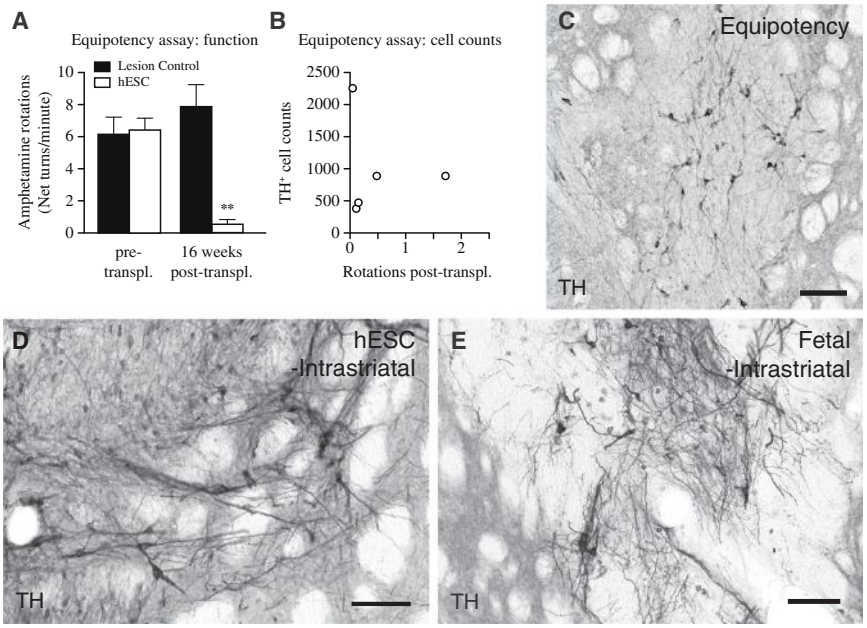

Figure 2. Functional Equipotency of Intrastriatal Transplanted hESC-DA Neurons and Comparable Morphology to Grafts of Fetal VM-Derived DA Neurons

(A) 6-hydroxydopamine lesioned rats displayed a strong unilateral rotational bias upon administration of amphetamine, which was significantly normalized 16 weeks after intrastriatal transplantation of hESC-DA neurons (white bars, n = 5), whereas lesion controls (black bars, n = 6), not receiving any transplant, showed no significant changes when monitored in parallel.

(B) Estimation of the number of surviving TH^+ neurons within the graft revealed a relatively low number that gave rise to graft-mediated functional recovery.

(C) Histological analysis revealed grafts with sparse numbers of TH^+ neurons dispersed throughout.

(D and E)When comparing transplants of hESC-derived (D) and fetal-derived (E) DA neurons 6 months posttransplantation, both groups revealed grafts rich in DA neurons that are indistinguishable on a gross morphological level.

See also Figure S2. TH, tyrosine hydroxylase. In (A), data are represented as mean ± SEM. $^{**}p < 0.01$. In (C)–(E), scale bars represent 100 μm.

Histological Comparison of DA Neurons Sourced from Human Fetal VM and hESCs after Intrastriatal Transplantation

We next performed a direct histological comparison between hESC-DA neurons and authentic human fetal DA neurons prepared according to Rath et al. (2013), grafted in parallel, in order to validate the morphology, maturation, and phenotypic properties of the transplanted DA neurons (Figures 2D and 2E). In this analysis, we observed the presence of TH^+ neurons with two distinct morphologies in the hESC-grafted animals (Mendez et al., 2005; Thompson et al., 2005): A9-like nigral neurons characterized by large angular somata and A10-like VTA neurons with small, round somata (Figure 3A). The morphology of the hESC-derived neurons was identical to that observed with intrastriatal transplants of fetal VM when analyzed at 6 months posttransplantation (Figure 3C) and consistent with graft appearance from previous postmortem reports from transplanted PD patients (Mendez et al., 2005). When staining the cells for markers commonly used to distinguish between SN (A9) and VTA (A10) neurons, TH^+ neurons expressing GIRK2 (A9), Calbindin (A10), or both markers were readily detected (Figures 3B and 3D). Quantifications showed that $TH^+/GIRK2^+$ neurons were the most abundant subtype in both hESC-derived and fetal grafts (Figure 3I) and that the proportion was similar in both hESC- and fetal-derived grafts (Figure 3J). Taken together, this analysis shows that hESC-DA neurons are indistinguishable from their fetal counterparts on the basis of graft appearance, morphology, and marker expression 6 months after grafting and that the hESC-derived grafts are rich in both A9-like and A10-like DA neurons.

Long-Distance Axonal Outgrowth of hESC-Derived Neurons after Transplantation into the Substantia Nigra

When assessing the cells for their suitability to be used in clinical trials, it is important to keep in mind that the human brain is a much larger structure than the rodent brain and that it is necessary for the transplanted cells to extend axons over long distances in order to sufficiently reinnervate the putamen in patients. We therefore sought to create an assay through which long-distance, target-specific outgrowth could be assessed in an adult rodent model of PD that would be predictive when translating to the larger human brain. Intrastriatal grafting, the standard used in preclinical and clinical studies, places the cells within their main target structure, thus making it difficult to assess the full innervation capacity of human cells when grafted to the rat brain. To investigate the ability of hESC-DA neurons to innervate specific structures across longer distances, we employed a homotopic grafting approach where we transplanted hESC-DA neurons into the lesioned SN, instead of the traditional ectopic placement in the striatum. Transplants of fetal VM served as an important reference to see if hESC-derived neurons could match their capacity for long-distance and target-specific innervation.

When grafted to the SN, both hESCs and fetal VM gave rise to grafts rich in TH^+ neurons expressing GIRK2 and Calbindin with morphologies indistinguishable from cells grafted to the striatum (compare Figures 3E–3H with Figures 3A–3D). In the majority of rats with fetal VM transplants (n = 7/8), we observed neuron-rich grafts, discretely placed within the host SN, extending large numbers of $hNCAM^+$ axons rostral along the medial forebrain bundle (MFB) and the adjacent nigrostriatal pathway, assembled in a well-defined and fasciculated tract (Figures 4A, 4G, 4I, S3A, and S3B). Rostral extending axonal bundles were seen to defasciculate and ramify within their terminal target fields, providing widespread innervation of specific host structures throughout the forebrain (Figure 4A), extending more than 10 mm from the graft core. $hNCAM^+$ terminal innervation was particularly dense in caudate-putamen (Figure 4C), NAc (Figure 4D), amygdala (Figure 4B), and perirhinal and anteromedial frontal cortices (Figures 4A and 4E).

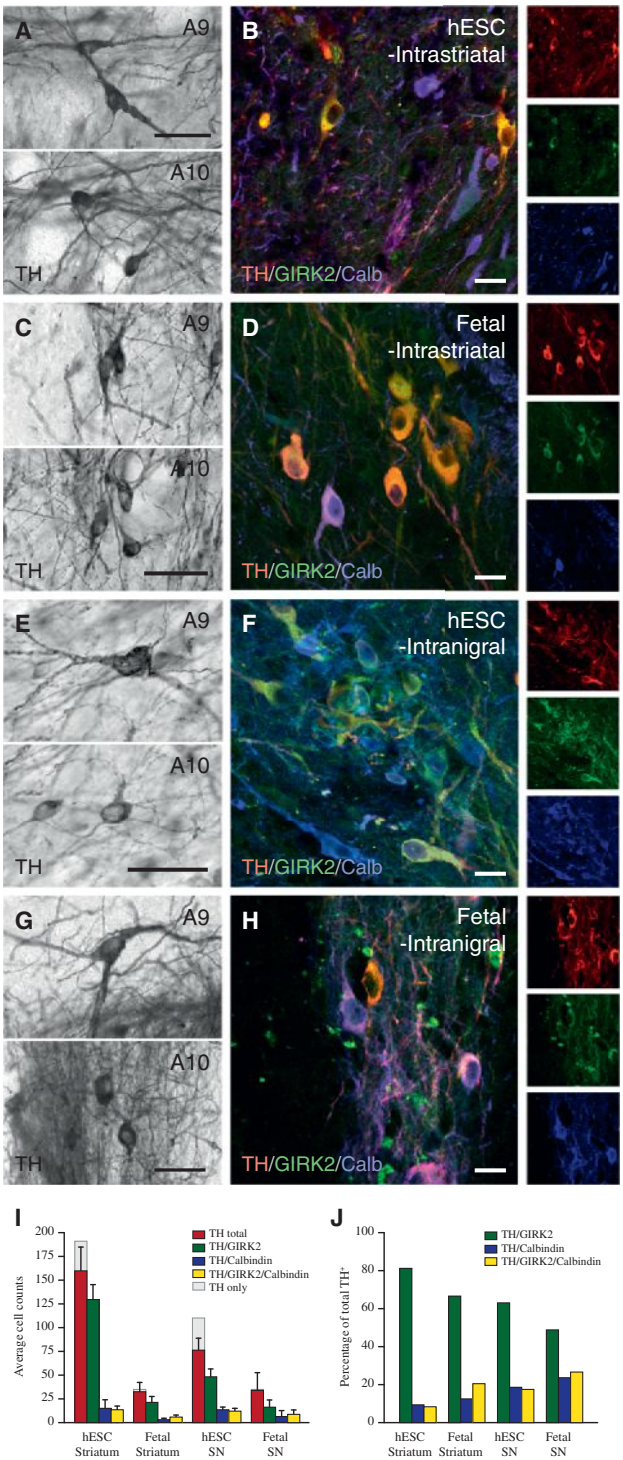

Figure 3. Comparison of A9 and A10 Midbrain DA Neuron Subtypes in Long-Term Grafts of hESC-DA Neurons and Human Fetal VM

(A) Upon close inspection, hESC-DA neurons gave rise to TH$^+$ dopaminergic neurons with an A9-like neuron morphology, characterized by large angular somas (upper panel), as well as A10-like neurons with small, round somas (lower panel).

(B) The presence of neurons coexpressing TH and GIRK2 (red and green) and TH and Calbindin (red and blue) indicates that both midbrain DA neuron subtypes, A9 and A10, were contained in grafts of hESC-derived neurons.

(C and D) Intrastriatal grafts of human fetal VM contained TH$^+$ dopaminergic neurons with A9 and A10 morphologies, coexpressing GIRK2 and/or Calbindin.

(E and F) Homotopic placement of hESC-DA neurons in SN resulted in large numbers of TH$^+$ dopaminergic neurons with mature A9 and A10 morphologies, confirmed by coexpression of TH with GIRK2 and Calbindin, respectively.

(G and H) Fetal VM tissue grafted to the SN displayed the same ability to generate transplants with dopaminergic neurons of A9 and A10 morphologies and protein expression (H).

(I and J) The number and proportion (J) of TH$^+$ neurons, coexpressing GIRK2, Calbindin, or both markers, was quantified in all groups (n = 3 per group).

Calb, Calbindin; GIRK2, G protein-regulated inward-rectifying potassium channel 2; TH, tyrosine hydroxylase. In (I) and (J), data are represented as mean ± SEM. In (A), (C), (E), and (G), scale bars represent 50 μm. In (B), (D), (F), and (H), scale bars represent 20 μm.

Notably, graft-derived hNCAM$^+$ glial cells were detected in the transplants derived from the 8-week-old fetus (Figures 4F and 4G), but not from the younger 5.5-week-old fetus (Figures 4H and 4I). In the grafts of 8-week fetal VM, the graft-derived glial cells could be traced along myelinated and nonmyelinated fiber tracts, accompanying the hNCAM$^+$ axons up to the level of the caudal caudate-putamen (Figure 4G), as described in previous xenografting studies (Gates et al., 1998; Isacson et al., 1995; Pundt et al., 1995). Despite the absence of graft-derived glia in the transplants of the younger embryo (Figure 4H), hNCAM$^+$ fiber outgrowth was comparable to grafts derived from older tissue (Figures S3B–S3G). This observation indicates that the extent and patterning of axonal outgrowth is largely independent of this glial population present within the transplant.

Six months posttransplantation we observed robust survival in all hESC grafted animals (n = 8/8), with no signs of overgrowth or necrosis, similar in morphology to the intrastriatal grafts of hESC-DA neurons described above (Figures 1, 2D, and S2A–S2C). As observed with intranigral transplants of fetal VM, large numbers of hNCAM$^+$ fibers projected rostral along the MFB and the adjacent nigrostriatal pathway (Figures 5A, 5F, S4A, and S4B). The axons extending along the MFB continued a distance more than 10 mm from the graft core and gave rise to dense terminal networks in amygdala (Figure 5B); dorsolateral striatum (Figure 5C) and piriform cortex; ventral striatum, including NAc (Figure 5D); olfactory tubercle; lateral septum; and large parts of the frontal lobe (Figures 5A, 5E, and 5G). hNCAM$^+$ cells with a glial morphology were not detected in any of the hESC-grafted rats, consistent with our hypothesis that they are not essential for extensive axonal outgrowth.

Subtype Identity and Target-Specific Innervation of hESC-DA Neurons after Transplantation into the Substantia Nigra

Although A9 and A10 midbrain DA neuron subtypes can be arbitrarily distinguished on the basis of morphology and GIRK2/Calbindin protein expression, true identification of the subtype is linked to the ability of the neurons to innervate their appropriate forebrain targets: the A9 preferentially innervating the caudate-putamen and A10 neurons innervating limbic and cortical areas, including ventral striatum and NAc. To determine the presence of authentic A9 or A10 subtypes in grafts of fetal VM and hESC-DA neurons, we performed quantitative fiber density measurements (Figures S5A and S5B) of human hNCAM$^+$ axons (Figure 6C) in

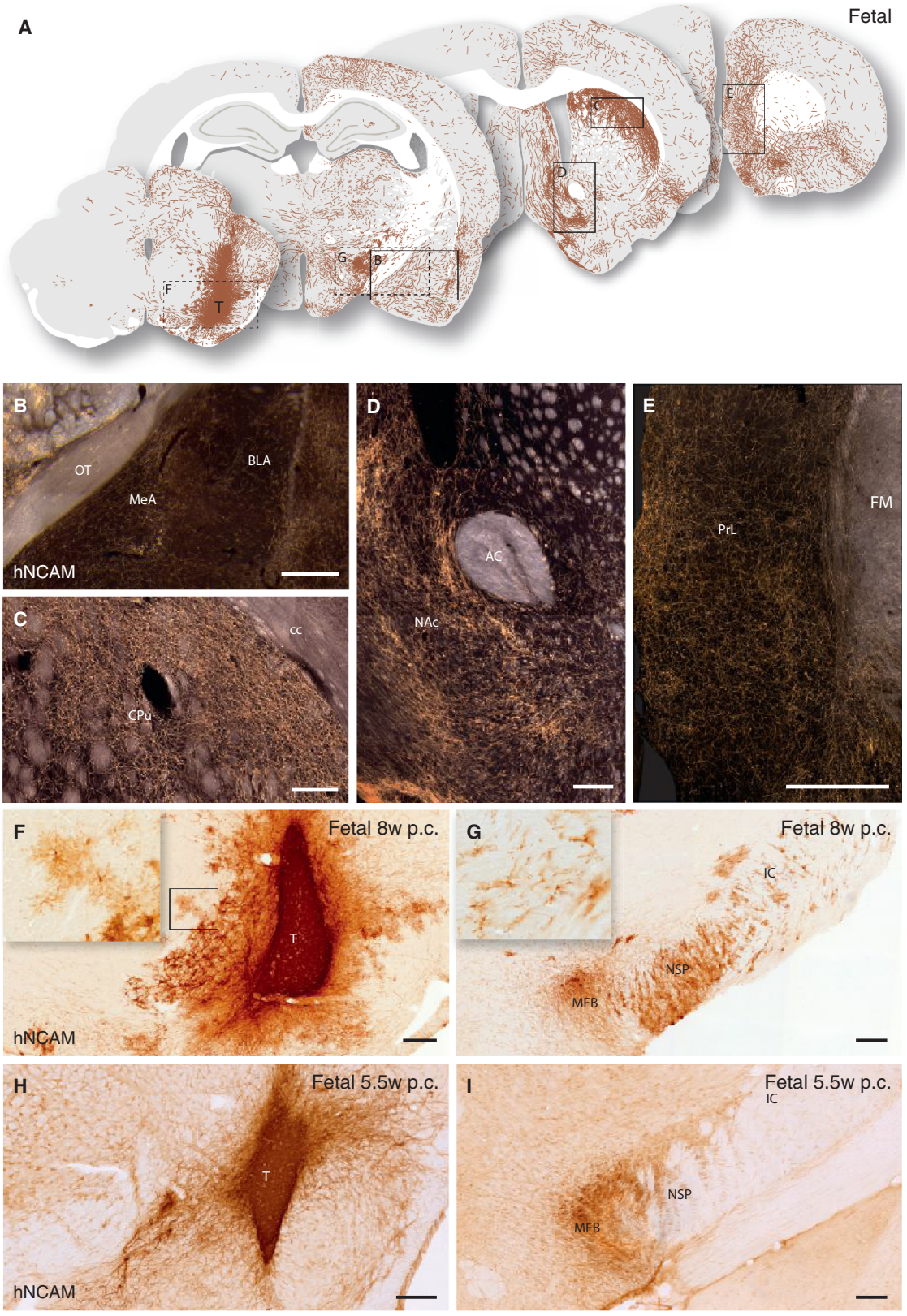

(legend on next page)

defined striatal areas (A9 targets), as well as limbic and cortical areas (A10 targets), as depicted in Figure S5C.We found that the number of axons projecting rostral was similar in the VM (2,169 ± 181; n = 3) and hESC (2,453 ± 774; n = 4) groups. Overall, the fiber density measurements showed that the midbrain-patterned hESCs exhibited the same A9/A10 target specificity and axonal outgrowth patterns as human fetal VM cells. Both fetal VM- and hESC-derived neurons innervated the caudate-putamen, which in the rat is targeted almost exclusively by A9 neurons, but that fetal VM tissue was more efficient at innervating the dorsolateral caudate-putamen (Figure 6A: dorsomedial, $t_{25} = 2.69$, $p < 0.01$; dorsolateral, $t_{25} = 4.38$, $p < 0.0001$; Medial, $t_{25} = 2.14$, $p < 0.05$). All A10-specific target structures were innervated at similar densities by fetal VM and hESCs, with the exception of the infralimbic cortex and septum, which received a more pronounced innervation from the hESC grafts (Figure 6B: ILC, $t_{25} = 5.99$, $p < 0.0001$; Sept, $t_{25} = 5.32$, $p < 0.0001$).

In order to identify the specific contribution from grafted DA neurons, we utilized immunofluorescence to detect human axons coexpressing TH and hNCAM (Figure 6F). Performing fiber density counts on double-positive fibers; we again found that fetal- and hESC-derived DA neurons demonstrated a similar propensity to innervate A9 and A10 specific striatal target structures (Figures 6D and 6E), although A9-specific innervation derived from fetal VM grafts was overall of higher density (Figure 6D: dorsomedial, $t_4 = 2.27$, $p < 0.05$; dorsolateral, $t_4 = 4.15$, $p < 0.01$).

In summary, midbrain-patterned hESCs exhibited the same remarkable ability as their fetal counterparts to extend axons over long distances and provide specific innervation of the relevant A9 and A10 host target structures. GIRK2 and Calbindin are commonly used as subtype markers for stem cell-derived DA neurons in vitro and after transplantation (Kirkeby et al., 2012a; Kriks et al., 2011; Ryan et al., 2013). However, we notice here that a high GIRK2$^+$ component (Figures 3I and 3J) does not directly translate to a strong innervation of the A9 target structures (Figures 6A and 6D). This observation is supported by the postmortem analysis of the adult human midbrain, which reveals that colocalization of TH and GIRK2 occurs in all DAergic neurons of the SN, but also in a substantial portion of DAergic neurons of the VTA (Reyes et al., 2012), thus calling for a more stringent analysis of A9 subtype of stem cell-derived DA neurons.

Expression of OTX2 Alters the Axonal Outgrowth Pattern of Transplants of hESC-Derived Neurons

Next, we sought to investigate if target-specific axonal outgrowth from hESC-DA neurons is a cell intrinsic property that can be regulated by transcriptional programming. Experiments in mice have established a major role for the transcription factor *Otx2* in the development of the midbrain DA progenitors. The expression of this transcription factor is maintained selectively in DA neurons with a mature A10 phenotype, where it acts to control the pattern of axonal outgrowth in forebrain structures (Chung et al., 2010, 2005; Di Salvio et al., 2010a, 2010b). We generated transgenic hESCs (*OTX2*-hESCs) using a lentiviral construct that expresses *OTX2* at physiologically relevant levels under the control of the PGK promoter and contains miRNA-292 target sequences to restrict expression to differentiated progeny (Sachdeva et al., 2010) (Figures S6A and S6B). We verified that the transgene did not disturb patterning toward a midbrain fate, as *OTX2*-hESCs gave rise to a similar number of LMX1A, FOXA2, and OTX2 expressing progenitors, as compared with wild-type (WT) hESCs (compare Figures S6D and S6E with Figures S4C and S4D). At a later time point in vitro, and consistent with the emergence of mature TH$^+$ neurons, OTX2 was downregulated in mature MAP2$^+$/TH$^+$ neurons from parental WT hESCs, but specifically maintained in differentiated *OTX2*-hESCs (Figures S6C and S6F). The *OTX2*-hESC-derived DA neuron progenitors were transplanted to the SN of 6-OHDA-lesioned athymic rats (n = 8). At 6 months, immunohistochemical analysis revealed a pronounced expression of OTX2 within the graft core at a level exceeding that observed in grafts of fetal VM and WT hESCs (Figures S6G–S6I). The *OTX2*-hESC grafts exhibited a similar axonal outgrowth pattern to the WT hESCs, with large numbers of hNCAM$^+$ axons extending rostral within the MFB (Figures 7A and 7B). However, the innervation derived from the *OTX2*-hESCs was restricted almost exclusively to A10 target structures, including NAc; ventral striatum; septum; amygdala; and antero-medial regions of the prefrontal cortex (Figures 7A–7E and S6K). Few, if any, hNCAM$^+$ fibers were observed in A9 target structures, such as dorsolateral caudate-putamen (Figures 7A and 7C). When quantifying the innervation of all measured A9 structures (dorsomedial, dorsolateral, medial, and central aspects of the caudate-putamen unit; Figure S5C), *OTX2*-hESCs displayed a reduced preference for innervating A9 target structures both when compared with grafts of the parental hESCs and with fetal-derived DA neurons (Figure 7H: $F_{(2,\ 105)} = 28.91$, $p < 0.0001$; difference confirmed using a Tukey's post hoc test, $p < 0.001$).

To exclude that this dramatic switch in target innervation was due to experimental variation or altered in vitro patterning, we replicated this experiment with a new cell differentiation and transplanted to immunocompetent rats under immunosuppression

Figure 4. Extent and Pattern of Axonal Outgrowth from Intranigral Transplants of Human Fetal VM 6 Months Posttransplantation

(A) Schematic overview of hNCAM$^+$ fibers from an intranigral transplant of fetal VM, innervating the host brain as visualized under dark-field illumination of DAB-developed sections (see Figure S3A).

(B–E) Transplants of fetal VM displayed a strong preference for innervating: amygdala (including MeA and BLA) (B); dorsolateral caudate-putamen (C); and nucleus accumbens, NAc (D). Graft-derived axons were found as far as 10 mm away from the graft core in areas of the prefrontal cortex (E).

(F–I) In bright-field illumination, the appearance of the 8-week (F) and 5.5-week (H) donor transplants and the associated outgrowth of hNCAM$^+$ axons in the MFB and the adjacent nigrostriatal pathway (G and I), including the presence of migrating hNCAM$^+$ graft-derived glial cells in the older donor transplants (Insets in F and G). See also Figure S3. AC, anterior commissure; BLA, basolateral amygdala; CPu, caudate-putamen; FM, forceps minor; IC, internal capsule; MeA, medial amygdaloid nucleus; MFB, medial forebrain bundle; NAc, nucleus accumbens; NSP, nigrostriatal pathway; p.c., postconception; PrL, prelimbic cortex; T, transplant. In (B), (D), (F), (G), (H), and (I), scale bars represent 0.2 mm. In (C) and (E), scale bars represent 0.5 mm.

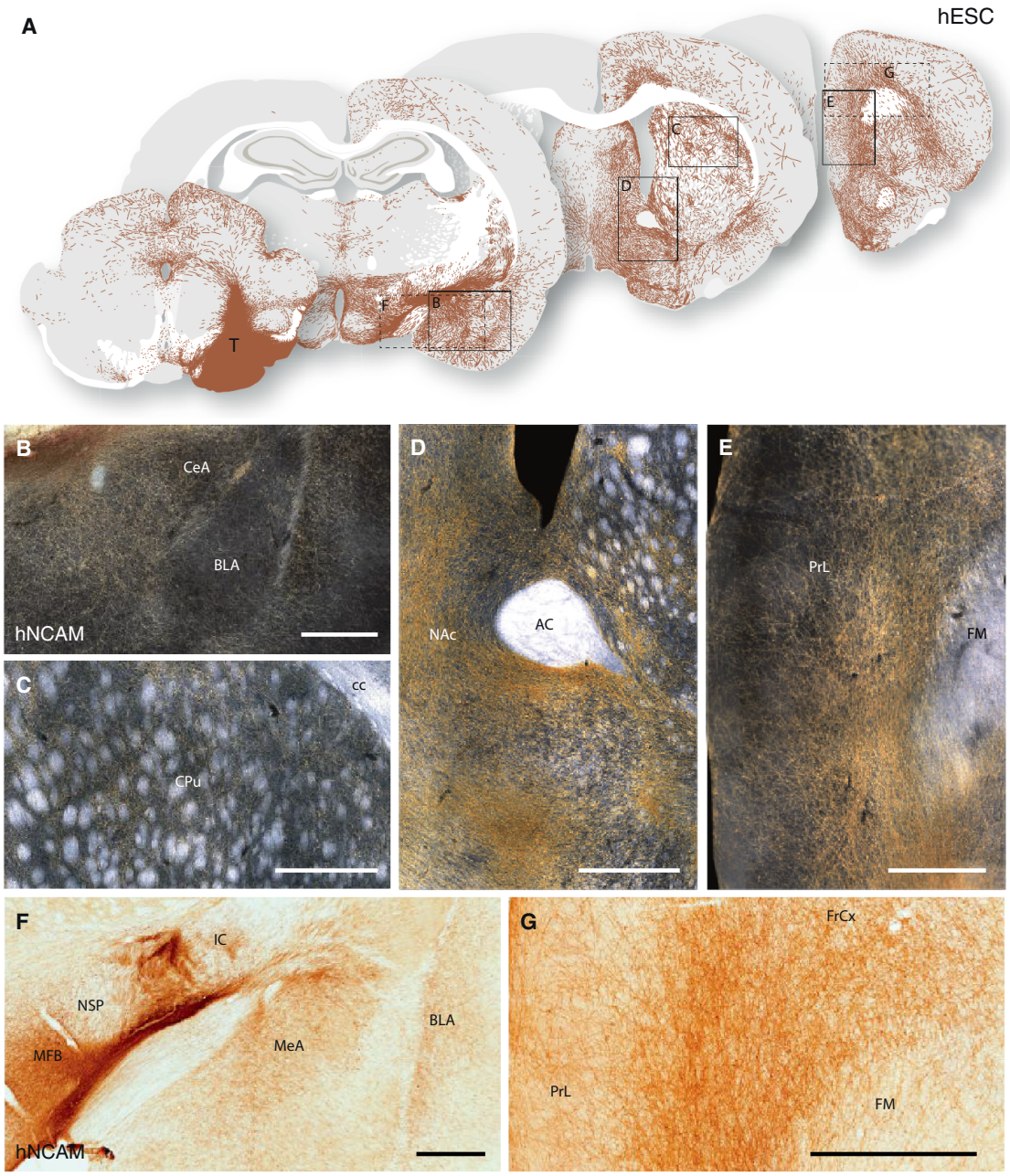

Figure 5. Overview of Neuronal Outgrowth of Intranigral Transplants of hESC-DA Neurons 6 Months after Transplantation

(A) Schematic overview of hNCAM$^+$ fiber outgrowth from an intranigral transplant of hESC-DA neurons, as visualized under dark-field illumination of DAB-developed sections (see Figure S4A).

(B–D) Higher magnification illustrates the hESC-derived innervation patterns of the amygdala (B), caudate-putamen (C), and NAc (D).

(E–G) hNCAM$^+$ fiber bundles were seen to extend rostral within the MFB and nigrostriatal pathway (E), and also within the myelinated white matter tracts of the internal capsule (F), over a distance of more than 10 mm from the graft core to innervate parts of the prefrontal cortex (E and G).

See also Figure S4. AC, anterior commissure; BLA, basolateral amygdala; CeA, Central Amygdaloid nucleus; CPu, caudate-putamen unit; FM, forceps minor; IC, internal capsule; MeA, medial amygdaloid nucleus; MFB, medial forebrain bundle; NAc, nucleus accumbens; NSP, nigrostriatal pathway; PrL, prelimbic cortex; T, transplant. In (B)–(G), scale bars represent 0.5 mm.

using daily injections of ciclosporin. In all animals (n = 7/7; 14-week survival), grafts of *OTX2*-hESCs were efficiently differentiated into mature TH$^+$ neurons (Figure S6J), and the identical pattern of A10-specific target innervation was observed (Figures 7F and 7G).

These findings provide evidence that target-specific outgrowth, attributed to a given midbrain DA neuron subtype, can be controlled and redirected in hESC-derived cell preparations, thus providing an opening for future efforts to enhance the fiber outgrowth to specific target nuclei.

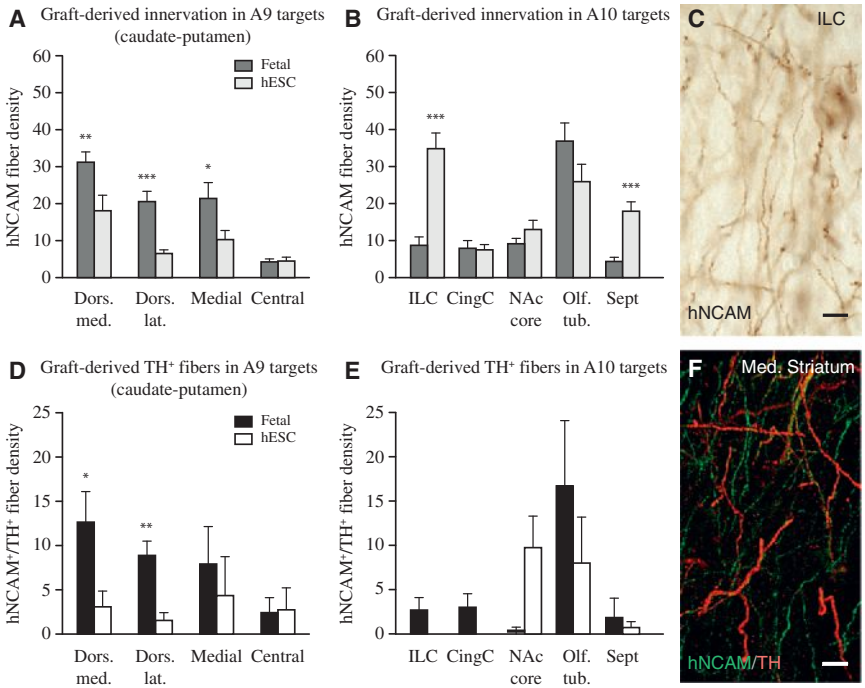

Figure 6. Quantitative Analysis of Neuronal Fiber Density in A9 and A10 Target Structures Derived from Intranigral Grafts

(A) Fetal VM grafts showed greater affinity to A9 targets in caudate-putamen (dark gray bars; n = 4) than to hESC-DA neurons (light gray bars; n = 4).

(B) Fetal VM and hESC-DA neurons were equally capable of innervating A10 targets, including NAc, olfactory tubercle, and cingulate cortex, while infralimbic cortex and septum received denser innervation from hESC-DA neurons.

(C) Example of a fiber density measurement performed on hNCAM immunostained sections.

(D) Colabeling with TH and hNCAM showed that both fetal VM and hESC-DA neurons were able to innervate the caudate-putamen, although DA neurons derived from fetal VM showed a stronger preference for the dorsal caudate-putamen than those derived from hESCs.

(E) $TH^+/hNCAM^+$ fibers were observed in all A10 targets innervated by fetal VM transplants (black bars; n = 3). hESC-derived $TH^+/hNCAM^+$ fibers were dense in NAc and olfactory bulb, but absent in cortical areas (white bars; n = 4).

(F) Confocal image of $TH^+/hNCAM^+$ section used for quantification.

See also Figure S5. CingC., cingulate cortex; Dors. lat., dorsolateral; Dors. med., dorsomedial; ILC, infralimbic cortex; MFB, medial forebrain bundle; NAc core, nucleus accumbens, core; Olf. tub., olfactory tubercle; Sept, septum. In (A), (B), (D), and (E), data are represented as mean ± SEM. *p < 0.05; **p < 0.01; ***p < 0.0001. In (C) and (F), scale bars represent 10 μm.

DISCUSSION

In this study, we have performed a comprehensive preclinical validation of hESC-derived DA neurons that fully supports their functional efficacy and capacity for long-distance, target-specific reinnervation, predictive of their therapeutic potential.

Using imaging techniques previously used to assess graft function in patients (Kefalopoulou et al., 2014; Piccini et al., 1999), we demonstrate that hESC-DA neurons survive, mature, and restore DA neurotransmission in the denervated striatum for up to 6 months postgrafting. When compared side-by-side with their fetal counterparts, the hESC-DA neurons appear identical in terms of morphology and marker expression, supporting their authenticity and stable phenotype. Importantly, we have also performed an equipotency assay, establishing that the hESC-DA neurons can completely reverse motor asymmetry in the drug-induced rotation test in numbers more than 10-fold lower than previously used (Kirkeby et al., 2012a; Kriks et al., 2011) and at a dose, i.e., a threshold number, of around 1,000 surviving DA neurons, similar to that seen with human fetal VM tissue (Brundin et al., 1986; Rath et al., 2013). Knowing that the number of surviving fetal DA neurons in a transplanted patient needs to be at least 100,000 in order to achieve a good clinical outcome (Hagell and Brundin, 2001), the equipotency data presented here will be important for guiding cell dosage when designing the first-in-man trial with hESCs.

We show that midbrain-patterned hESCs transplanted homotopically to the SN exhibit the same remarkable ability as their fetal counterparts to project axons over long distances in the adult brain, providing highly specific and appropriate innervation of midbrain DA target structures in the forebrain (Isacson et al., 1995; Wictorin et al., 1992). Intriguingly, and of clinical importance, this extensive axonal outgrowth occurs in the adult brain. While other reports have previously described long-distance outgrowth from transplants of hESC-derived neurons, these studies have been performed in neonatal rats and mice (Denham et al., 2012; Espuny-Camacho et al., 2013) and have not used hESCs patterned toward a specific dopaminergic fate. The capacity of the hESC-DA neurons to reinnervate previously denervated forebrain targets when transplanted to the SN is unparalleled and matched well the axonal outgrowth patterns obtained from grafts of authentic human fetal midbrain DA neurons.

Clinical studies show that grafts of fetal VM-derived DA neurons, transplanted to the DA-deficient putamen, can restore DA neurotransmission and provide functional benefits that are sustained over many years (Barker et al., 2013; Kefalopoulou et al., 2014). From preclinical studies we know that the efficacy of intrastriatal DA neuron grafts depends not only on the number of surviving DA neurons but also on their phenotype and their capacity to reinnervate a major part of the denervated target. We show here that the hESC-DA neurons generated by the current protocol are of the correct midbrain phenotype and contain the two major A9 and A10 DA neuron subtypes, similar to fetal VM grafts. This phenotype provides the grafts with the capacity to reinnervate both striatal and extrastriatal midbrain DAergic target structures. Importantly, we show that hESC-DA neurons are functionally equipotent to fetal VM neurons when grafted to the striatum and their axonal growth capacity matches that achieved by fetal VM neurons when grafted to the striatum and the SN. Data from transplantation studies in rodents and human autopsy cases indicate that DA neurons from human fetal VM have the capacity to extend axons for up to 5–7 mm in the

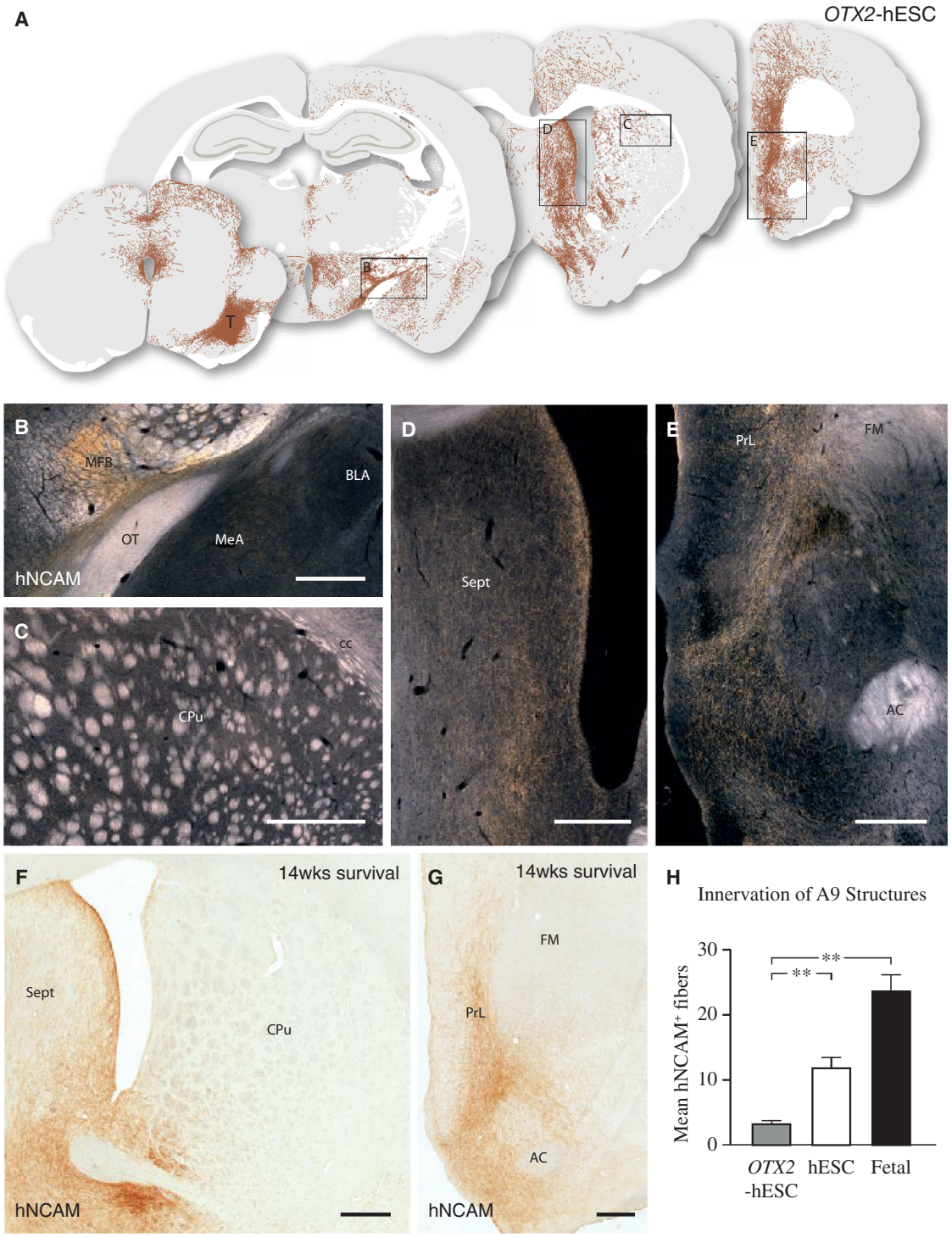

Figure 7. Maintained Expression of *OTX2* in hESC-Derived Neurons Results in an Altered Axonal Outgrowth Pattern

(A) Schematic overview of the pattern of hNCAM$^+$ axonal outgrowth derived from intranigral grafts of *OTX2*-hESCs 6 months posttransplantation, as visualized under dark-field illumination of DAB-developed sections (see Figure S6K). These cells displayed a strong preference for A10 target structures, such as septum, cingulate, prelimbic, and infralimbic cortices.

(B) The majority of axons extended rostral within the MFB, along both gray and white matter, with few axons innervating amygdala.

(C) Only rare hNCAM$^+$ axons were observed in caudate-putamen, the prime A9 target structure.

(D and E) Maintained expression of *OTX2* did not alter the long-distance growth capacity of the grafted neurons, as a dense fiber network was observed in both septum and NAc, as well as in prelimbic cortex.

(legend continued on next page)

striatum, which makes it possible to reinnervate a major part of the human putamen with a limited number of cell deposits (Freeman and Brundin, 2006; Kordower et al., 1995). The axonal outgrowth observed here, up to 10 mm from the graft deposit, indicates that the growth capacity of the hESC-derived DA neurons will be sufficient to provide efficient and widespread restoration of DA neurotransmission in the DA-denervated striatal targets in PD patients. The potency of the hESC-derived DA neurons, with respect to functional efficacy and long-distance targeted reinnervation, is on par with that of fetal VM cells, which provides important support for their therapeutic potential and use for cell replacement therapy in PD.

EXPERIMENTAL PROCEDURES

Research Animals

All procedures were conducted in accordance with the European Union Directive (2010/63/EU) and were approved by the ethical committee for the use of laboratory animals at Lund University and the Swedish Department of Agriculture (Jordbruksverket), as well as French legislation.

Athymic, nude rats were housed in individual ventilated cages, under a 12 hr light/dark cycle with ad libitum access to sterile food and water. Sprague-Dawley rats were kept in similar conditions as above, but in standard cages.

Experimental Design for Functional Imaging Experiment

Adult (<1 year) male, athymic, nude rats (Crl:NIH-*Foxn1*^{rnu}) were purchased from Charles River and used as graft recipients in all experiments and controls (n = 20). All rats received a 6-hydroxydopamine lesion of the medial forebrain bundle and 2 weeks later were assessed for lesion efficacy using amphetamine-induced rotations. All animals received longitudinal follow using MRI. The animals were stratified to the follow groups: baseline PET scanning, with subsequent follow-up scans at 5 to 6 months posttransplantation (n = 14), and MR spectroscopy of the grafts (n = 9).

Experimental Design for Circuit Reconstruction and Equipotency Experiments

Adult (<180 g) female, athymic, nude rats (Hsd:RH-*Foxn1*^{rnu}) were purchased from Harlan Laboratories and used as graft recipients and controls (n = 51). For repetition of the OTX2-overexpression and equipotency experiments, female Sprague-Dawley rats (225–250 g) were purchased from Charles River (n = 14 and n = 5, respectively). All surgical procedures, such as anesthetic doses, etc., were performed as described in detail (Grealish et al., 2010).

All rats received a 6-hydroxydopamine lesion of the medial forebrain bundle and 2 weeks later were assessed for lesion efficacy using amphetamine-induced rotations. The animals were stratified to the follow groups: intranigral grafting of fetal ventral mesencephalon (n = 8); intranigral grafting of hESC-derived DA neurons (n = 8); intranigral grafting of *OTX2*-hESCs, nude rats (n = 8), Sprague-Dawley rats (n = 14); equipotency intrastriatal grafting of hESC-derived DA neurons (n = 5); intrastriatal grafting of fetal tissue (n = 4); and lesion controls (n = 6).

Amphetamine-Induced Rotation

Rotational bias, after systemic amphetamine challenge (2.5 mg/kg, intraperitoneally; Apoteksbolaget), was recorded using an automated system (Omnitech Electronics). The animals were recorded for 90 min, and only full body turns were counted and then expressed as net turns per minute, with rotations toward the side of the lesion given a positive value. Only animals with more than 5 turns per minute were considered successfully lesioned.

Differentiation of hESCs

Human ESCs H9 (WA09, passages 31–45) were differentiated to a ventral midbrain fate, using the protocol as described in detail in Kirkeby et al. (2012b) and Supplemental Experimental Procedures.

Human Fetal Tissue

Human fetal tissue was obtained from legally terminated embryos with approval of the Swedish National Board of Health and Welfare in accordance with existing guidelines including informed consent from women seeking elective abortions. The gestational age of each embryo was determined by measuring the crown-to-rump length and/or estimated by ultrasound measurements. Embryos were then staged according to weeks postconception.

Transplantation Procedure

hESCs were prepared for transplantation as in Kirkeby et al. (2012a), while fetal tissue was prepared and transplanted as a semicrude suspension, as described in Rath et al. (2013).

Magnetic Resonance and PET Imaging

All specifications of these procedures are detailed in Supplemental Experimental Procedures.

Immunohistochemistry

All samples, cultured cells and brain tissue, were fixed in fresh 4% paraformaldehyde. A complete list of suppliers and concentrations of primary and secondary antibodies used is detailed in Supplemental Experimental Procedures.

Fiber Density Measurements

Quantitative analysis of the density of human fibers innervating specific areas was performed using a stereological method (Mouton et al., 2002). Details of sampling and acquisition are described in Supplemental Experimental Procedures.

Statistical Analysis

All data are presented as mean ± SEM.

Statistical tests and biological replicates are stated in results or in the figure legends. All statistical analyses were performed using GraphPad Prism v6.0 for Mac OS X. An alpha level of $p < 0.05$ was set as a threshold for significance.

In Figures 1B and 1C an unpaired t test was used to compare the baseline after 6-OHDA lesion and 5 months posttransplantation. In Figures 6A, 6B, and 6D, all fiber density was analyzed using a one-tailed unpaired t test. In Figure 7H the innervation of A9 structures in the *OTX2*-hESC group was compared with the hESCs and fetal VM grafted groups using a one-way ANOVA, with differences between groups confirmed using a Tukey's post hoc. The behavioral data in Figure 2A were analyzed with a two-tailed paired t test.

SUPPLEMENTAL INFORMATION

Supplemental information includes Supplemental Experimental Procedures and six figures and can be found with this article online at http://dx.doi.org/10.1016/j.stem.2014.09.017.

(F and G) In a repeat of this experiment in ciclosporin-treated rats, we confirmed that fiber outgrowth from *OTX2*-hESCs was confined almost exclusively to A10 target areas, such as NAc and septum (F) and prelimbic cortex (G). Notably, this outgrowth pattern was observed as early as 14 weeks after transplantation.
(H) *OTX2*-hESCs have a significantly impaired ability to extend hNCAM^{+} axons into A9 structures as compared with hESC and fetal grafts (all groups n = 3 animals with triplicate measures in four structures).
See also Figure S6. AC, anterior commissure; BLA, basolateral amygdala; CPu, caudate-putamen unit; FM, forceps minor; IC, internal capsule; MeA, medial amygdaloid nucleus; MFB, medial forebrain bundle; NAc, nucleus accumbens; OT, Olfactory Tract; PrL, prelimbic cortex; Sept, septum; T, transplant. In (H), data are represented as mean ± SEM. **p < 0.001
In (B)–(G), scale bars represent 0.5 mm.

ACKNOWLEDGMENTS

We would like to thank Jan Reimer, Olle Lindvall, and Jenny Nelander-Wahlestedt for acquisition and processing of human fetal material and Aurore Bugi for preparation and handling of hESC derivatives at I-Stem and Mircen. We would like to recognize the excellent technical assistance provided by Ulla Jarl, Michael Sparrenius, Anneli Josefsson, and Ingar Nilsson. The excellent technical support of Martine Guillermier in the PET imaging studies as well as the supply of PET radioligands by the radiochemistry unit of the Service Hospitalier Frédéric Joliot (directed by Frédéric Dollé) were very appreciated. This study was supported by grants from the European Community's 7th Framework Programme through NeuroStemcell (no. 222943), NeuroStemcellRepair (no. 602278), and TransEuro (HEALTH-F5-2010-242003); the strategic research area at Lund University Multipark (multidisciplinary research in Parkinson's disease); the Swedish Research Council (70862601/Bagadilico, K2012-99X-22324-01-5, and K2014-61X-20391-08-4); and the Swedish Parkinson Foundation (Parkinsonfonden). S.G. was supported by a postdoctoral stipend from the Swedish Brain Foundation (Hjärnfonden) and A.K. was supported via a grant from the Lundbeck foundation (R44-A3856). The research leading to these results has received funding from the European Research Council under the European Union's 7th Framework Programme (FP/2007-2013)/ERC Grant Agreement no. 309712.

Received: June 5, 2014
Revised: August 19, 2014
Accepted: September 24, 2014
Published: November 6, 2014

REFERENCES

Barker, R.A., Barrett, J., Mason, S.L., and Björklund, A. (2013). Fetal dopaminergic transplantation trials and the future of neural grafting in Parkinson's disease. Lancet Neurol. *12*, 84–91.

Barker, R.A. (2014). Developing Stem Cell Therapies for Parkinson's Disease: Waiting Until the Time is Right. Cell Stem Cell *15*, this issue, 539–542.

Brundin, P., Nilsson, O.G., Strecker, R.E., Lindvall, O., Astedt, B., and Björklund, A. (1986). Behavioural effects of human fetal dopamine neurons grafted in a rat model of Parkinson's disease. Exp. Brain Res. *65*, 235–240.

Chung, C.-Y., Seo, H., Sonntag, K.C., Brooks, A., Lin, L., and Isacson, O. (2005). Cell type-specific gene expression of midbrain dopaminergic neurons reveals molecules involved in their vulnerability and protection. Hum. Mol. Genet. *14*, 1709–1725.

Chung, C.-Y., Licznerski, P., Alavian, K.N., Simeone, A., Lin, Z., Martin, E., Vance, J., and Isacson, O. (2010). The transcription factor orthodenticle homeobox 2 influences axonal projections and vulnerability of midbrain dopaminergic neurons. Brain *133*, 2022–2031.

Denham, M., Parish, C.L., Leaw, B., Wright, J., Reid, C.A., Petrou, S., Dottori, M., and Thompson, L.H. (2012). Neurons derived from human embryonic stem cells extend long-distance axonal projections through growth along host white matter tracts after intra-cerebral transplantation. Front. Cell. Neurosci. *6*, 11.

Di Salvio, M., Di Giovannantonio, L.G., Acampora, D., Prosperi, R., Omodei, D., Prakash, N., Wurst, W., and Simeone, A. (2010a). Otx2 controls neuron subtype identity in ventral tegmental area and antagonizes vulnerability to MPTP. Nat. Neurosci. *13*, 1481–1488.

Di Salvio, M., Di Giovannantonio, L.G., Omodei, D., Acampora, D., and Simeone, A. (2010b). Otx2 expression is restricted to dopaminergic neurons of the ventral tegmental area in the adult brain. Int. J. Dev. Biol. *54*, 939–945.

Doi, D., Samata, B., Katsukawa, M., Kikuchi, T., Morizane, A., Ono, Y., Sekiguchi, K., Nakagawa, M., Parmar, M., and Takahashi, J. (2014). Isolation of human induced pluripotent stem cell-derived dopaminergic progenitors by cell sorting for successful transplantation. Stem Cell Rep. *2*, 337–350.

Dollé, F., Helfenbein, J., Hinnen, F., Mavel, S., Mincheva, Z., Saba, W., Schöllhorn Peyronneau, M.A., Valette, H., Garreau, L., Chalon, S., et al. (2007). One-step radiosynthesis of [18F]LBT-999: a selective radioligand for the visualization of the dopamine transporter with PET. J. Labelled Comp. Radiopharm. *50*, 716–723.

Espuny-Camacho, I., Michelsen, K.A., Gall, D., Linaro, D., Hasche, A., Bonnefont, J., Bali, C., Orduz, D., Bilheu, A., Herpoel, A., et al. (2013). Pyramidal neurons derived from human pluripotent stem cells integrate efficiently into mouse brain circuits in vivo. Neuron *77*, 440–456.

Freeman, T.B., and Brundin, P. (2006). Important aspects of surgical methodology for transplantation in Parkinson's disease. In Restorative Therapies in Parkinson's Disease, P. Brundin and C.W. Olanow, eds. (New York: Springer), pp. 131–165.

Gates, M.A., Olsson, M., Bjerregaard, K., and Björklund, A. (1998). Region-specific migration of embryonic glia grafted to the neonatal brain. Neuroscience *84*, 1013–1023.

Grealish, S., Jönsson, M.E., Li, M., Kirik, D., Björklund, A., and Thompson, L.H. (2010). The A9 dopamine neuron component in grafts of ventral mesencephalon is an important determinant for recovery of motor function in a rat model of Parkinson's disease. Brain *133*, 482–495.

Hagell, P., and Brundin, P. (2001). Cell survival and clinical outcome following intrastriatal transplantation in Parkinson disease. J. Neuropathol. Exp. Neurol. *60*, 741–752.

Isacson, O., Deacon, T.W., Pakzaban, P., Galpern, W.R., Dinsmore, J., and Burns, L.H. (1995). Transplanted xenogeneic neural cells in neurodegenerative disease models exhibit remarkable axonal target specificity and distinct growth patterns of glial and axonal fibres. Nat. Med. *1*, 1189–1194.

Kefalopoulou, Z., Politis, M., Piccini, P., Mencacci, N., Bhatia, K., Jahanshahi, M., Widner, H., Rehncrona, S., Brundin, P., Björklund, A., et al. (2014). Long-term clinical outcome of fetal cell transplantation for Parkinson disease: two case reports. JAMA Neurol. *71*, 83–87.

Kirkeby, A., Grealish, S., Wolf, D.A., Nelander, J., Wood, J., Lundblad, M., Lindvall, O., and Parmar, M. (2012a). Generation of regionally specified neural progenitors and functional neurons from human embryonic stem cells under defined conditions *1*, 703–714.

Kirkeby, A., Nelander, J., and Parmar, M. (2012b). Generating regionalized neuronal cells from pluripotency, a step-by-step protocol. Front. Cell. Neurosci. *6*, 64.

Kordower, J.H., Freeman, T.B., Snow, B.J., Vingerhoets, F.J., Mufson, E.J., Sanberg, P.R., Hauser, R.A., Smith, D.A., Nauert, G.M., Perl, D.P., et al. (1995). Neuropathological evidence of graft survival and striatal reinnervation after the transplantation of fetal mesencephalic tissue in a patient with Parkinson's disease. N. Engl. J. Med. *332*, 1118–1124.

Kriks, S., Shim, J.-W., Piao, J., Ganat, Y.M., Wakeman, D.R., Xie, Z., Carrillo-Reid, L., Auyeung, G., Antonacci, C., Buch, A., et al. (2011). Dopamine neurons derived from human ES cells efficiently engraft in animal models of Parkinson's disease. Nature *480*, 547–551.

Kuhnast, B., Damont, A., Hinnen, F., Catarina, T., Demphel, S., Le Helleix, S., Coulon, C., Goutal, S., Gervais, P., and Dollé, F. (2012). [18F]DPA-714, [18F]PBR111 and [18F]FEDAA1106-selective radioligands for imaging TSPO 18 kDa with PET: automated radiosynthesis on a TRACERLAb FX-FN synthesizer and quality controls. Appl. Radiat. Isot. *70*, 489–497.

Lindvall, O., and Kokaia, Z. (2009). Prospects of stem cell therapy for replacing dopamine neurons in Parkinson's disease. Trends Pharmacol. Sci. *30*, 260–267.

Mendez, I., Sanchez-Pernaute, R., Cooper, O., Viñuela, A., Ferrari, D., Björklund, L., Dagher, A., and Isacson, O. (2005). Cell type analysis of functional fetal dopamine cell suspension transplants in the striatum and substantia nigra of patients with Parkinson's disease. Brain *128*, 1498–1510.

Moon, B.S., Park, J.H., Lee, H.J., Kim, J.S., Kil, H.S., Lee, B.S., Chi, D.Y., Lee, B.C., Kim, Y.K., and Kim, S.E. (2010). Highly efficient production of [(18)F]fallypride using small amounts of base concentration. Appl. Radiat. Isot. *68*, 2279–2284.

Mouton, P.R., Gokhale, A.M., Ward, N.L., and West, M.J. (2002). Stereological length estimation using spherical probes. J. Microsc. *206*, 54–64.

Piccini, P., Brooks, D.J., Björklund, A., Gunn, R.N., Grasby, P.M., Rimoldi, O., Brundin, P., Hagell, P., Rehncrona, S., Widner, H., and Lindvall, O. (1999). Dopamine release from nigral transplants visualized in vivo in a Parkinson's patient. Nat. Neurosci. *2*, 1137–1140.

Piccini, P., Lindvall, O., Björklund, A., Brundin, P., Hagell, P., Ceravolo, R., Oertel, W., Quinn, N., Samuel, M., Rehncrona, S., et al. (2000). Delayed recovery of movement-related cortical function in Parkinson's disease after striatal dopaminergic grafts. Ann. Neurol. *48*, 689–695.

Pundt, L.L., Kondoh, T., and Low, W.C. (1995). The fate of human glial cells following transplantation in normal rodents and rodent models of neurodegenerative disease. Brain Res. *695*, 25–36.

Rath, A., Klein, A., Papazoglou, A., Pruszak, J., Garcia, J., Krause, M., Maciaczyk, J., Dunnett, S.B., and Nikkhah, G. (2013). Survival and functional restoration of human fetal ventral mesencephalon following transplantation in a rat model of Parkinson's disease. Cell Transplant. *22*, 1281–1293.

Reyes, S., Fu, Y., Double, K., Thompson, L., Kirik, D., Paxinos, G., and Halliday, G.M. (2012). GIRK2 expression in dopamine neurons of the substantia nigra and ventral tegmental area. J. Comp. Neurol. *520*, 2591–2607.

Ryan, S.D., Dolatabadi, N., Chan, S.F., Zhang, X., Akhtar, M.W., Parker, J., Soldner, F., Sunico, C.R., Nagar, S., Talantova, M., et al. (2013). Isogenic human iPSC Parkinson's model shows nitrosative stress-induced dysfunction in MEF2-PGC1α transcription. Cell *155*, 1351–1364.

Sachdeva, R., Jönsson, M.E., Nelander, J., Kirkeby, A., Guibentif, C., Gentner, B., Naldini, L., Björklund, A., Parmar, M., and Jakobsson, J. (2010). Tracking differentiating neural progenitors in pluripotent cultures using microRNA-regulated lentiviral vectors. Proc. Natl. Acad. Sci. USA *107*, 11602–11607.

Thompson, L., Barraud, P., Andersson, E., Kirik, D., and Björklund, A. (2005). Identification of dopaminergic neurons of nigral and ventral tegmental area subtypes in grafts of fetal ventral mesencephalon based on cell morphology, protein expression, and efferent projections. J. Neurosci. *25*, 6467–6477.

Wictorin, K., Brundin, P., Sauer, H., Lindvall, O., and Björklund, A. (1992). Long distance directed axonal growth from human dopaminergic mesencephalic neuroblasts implanted along the nigrostriatal pathway in 6-hydroxydopamine lesioned adult rats. J. Comp. Neurol. *323*, 475–494.

CellPress

Cell Stem Cell
Clinical Progress

Human Embryonic Stem Cell-Derived Oligodendrocyte Progenitors Remyelinate the Brain and Rescue Behavioral Deficits following Radiation

Jinghua Piao,[1,6] Tamara Major,[1,6] Gordon Auyeung,[1] Edelweiss Policarpio,[1] Jayanthi Menon,[1] Leif Droms,[1] Philip Gutin,[1] Kunihiro Uryu,[3] Jason Tchieu,[2] Denis Soulet,[4,5] and Viviane Tabar[1,*]

[1]Department of Neurosurgery and Center for Stem Cell Biology, Memorial Sloan Kettering Cancer Center, New York, NY, 10065, USA
[2]Developmental Biology Program, Sloan Kettering Institute, New York, NY 10065, USA
[3]Resource Center (EMRC), The Rockefeller University, New York, NY 10065, USA
[4]Department of Psychiatry and Neuroscience, Faculty of Medicine, Laval University, QC, Canada, G1V 0A6
[5]Axe Neuroscience, Centre de recherche du CHU de Québec, QC, Canada, G1V 0A6
[6]Co-first author
*Correspondence: tabarv@mskcc.org
http://dx.doi.org/10.1016/j.stem.2015.01.004

SUMMARY

Radiation therapy to the brain is a powerful tool in the management of many cancers, but it is associated with significant and irreversible long-term side effects, including cognitive decline and impairment of motor coordination. Depletion of oligodendrocyte progenitors and demyelination are major pathological features that are particularly pronounced in younger individuals and severely limit therapeutic options. Here we tested whether human ESC-derived oligodendrocytes can functionally remyelinate the irradiated brain using a rat model. We demonstrate the efficient derivation and prospective isolation of human oligodendrocyte progenitors, which, upon transplantation, migrate throughout the major white matter tracts resulting in both structural and functional repair. Behavioral testing showed complete recovery of cognitive function while additional recovery from motor deficits required concomitant transplantation into the cerebellum. The ability to repair radiation-induced damage to the brain could dramatically improve the outlook for cancer survivors and enable more effective use of radiation therapies, especially in children.

INTRODUCTION

The ability to direct pluripotent stem cells (hPSC) into specific fates has raised hopes of translating these efforts into effective therapies. There has been notable progress in the neural field, where several therapeutically relevant cell types have been derived using greatly improved and highly reproducible protocols (Tabar and Studer, 2014). The derivation of engraftable glia has also been reported and the most recent studies have convincingly demonstrated the ability of human pluripotent stem-cell-derived oligodendrocytes to achieve extensive myelination in vivo following transplantation into neonatal *Shiverer* mice (Hu et al., 2009, Wang et al., 2013; Douvaras et al. 2014). These are promising data, though oligodendrocyte differentiation protocols remain complex and protracted, and applications have not been tested much beyond this genetic neonatal model.

Here, we present a novel indication for human PSC-derived oligodendrocytes, namely the repair of diffuse demyelination occurring as a consequence of radiation injury to the brain, a clinically important but largely unmet need among cancer survivors. Radiation therapy to the brain is a commonly prescribed treatment for many cancers, including primary and metastatic brain tumors, as well as in prophylactic regimens in small cell cancers (Paumier et al., 2011) or leukemia (Gibbs et al., 2006). It is often associated with significant long-term cognitive symptoms, even at standard doses and using modern techniques (Greene-Schloesser et al., 2012). Progressive impairments in memory, attention, executive function, and motor coordination are described, as well as learning difficulties and a decrease in intelligence quotients (IQ) in children (Schatz et al., 2000). The clinical course is often progressive and irreversible, and there is no effective treatment for radiation-induced cognitive decline. Nevertheless, the use of high volume CNS radiation continues to be a therapeutic cornerstone in many cancers, for palliative or curative purposes (Ringborg et al., 2003). The pathogenesis of the late effects (months to years) of radiation is not completely understood, and studies in animals and humans support an important role for the depletion of the oligodendrocyte precursor pool and subsequent demyelination (Kurita et al., 2001; Oi et al., 1990; Panagiotakos et al., 2007). In addition to autopsy data, there is increasing evidence from recent diffusion tensor imaging studies that support the premise that radiation results in early and progressive damage to the white matter and that the latter's integrity correlates with intellectual outcome (Mabbott et al., 2006; Uh et al., 2013). Other areas of potential injury include the vascular compartment, whereby thrombosis and hyalinization can be seen subacutely, particularly following high doses of radiation (Duffner et al., 1985), as well as the subventricular zone (SVZ) and hippocampus where transit amplifying and/or neural stem cells reside (Monje et al., 2002, 2003). However, it is evident that the plethora of radiation-related symptoms cannot

be solely attributed to the disruption of neurogenesis in the hippocampus and the SVZ, especially in humans. Data from our lab and others demonstrate that radiation extensively targets the large pool of mitotically active oligodendrocyte progenitors. These cells are acutely reduced in number and eventually depleted, followed by progressive, often patchy, demyelination (Sano et al., 2000; Panagiotakos et al., 2007). Here, we model the effects of radiation in young rats, using a clinically relevant fractionated regimen of 50 Gy to the whole brain. Our data show depletion of the oligodendrocyte pool and a delayed onset of demyelination, as well as cognitive and motor deficits. Concomitantly, we optimize a protocol for the derivation and selective enrichment of late oligodendrocyte progenitors (O4-expressing) from human embryonic stem cells (ESCs) and demonstrate that these cells can remyelinate the brain and ameliorate behavioral deficits. The clinical impact of these studies can be substantial as the need to address quality of life in cancer survivors grows more pressing.

RESULTS

Impact of Radiation on the Young Rat Brain

We subjected 4-week-old Sprague-Dawley rats to a dose of 50 Gy of radiation, administered in 10 fractions to the whole brain. Analysis of the brains at 14 weeks demonstrated a significant decrease in the number of oligodendrocyte progenitors throughout the brain as determined by the number of oligodendrocyte transcription factor 2 (olig2)-expressing cells and the decrease in O4 expression (Figure 1A; Figure S1A). This was associated with a decrease in myelin basic protein (MBP) expression and in the volume of the corpus callosum by ~25%, as determined by stereological volume analysis. The loss of MBP encompassed all major white matter pathways including the corpus callosum, the hippocampal fimbria, the commissures, as well as the subcortical areas and the cerebellum (Figure 1B; Figure S1A). The irradiated brain showed mild evidence of an inflammatory response demonstrated by an increase in the number of activated microglial/macrophages (ED1/Iba-1), and no significant gliosis at 14 weeks after radiation (Figure S1B). Behavioral testing was conducted on the irradiated and the normal age-matched groups. It consisted of cognitive and memory tests, including novel object preference and object location tasks, as well as water maze and rotarod testing with acceleration conditions. The data showed a significant decline in performance on the novel object preference and object location tasks (Barker et al., 2007), as well as a decrease in the duration of time spent on the rotarod wheel (from 11.8 to 2.2 s) and a substantial decrease in the distance traversed during that test (from ~1 m to 0.18 m) (Figures 1C and 1D). The water maze task did not result in a statistically significant difference in either the time spent or distance traveled in the target quadrant in probe test, as previously reported (Saxe et al., 2006; Vorhees and Williams, 2006) (Figure S1C).

Derivation of Late Oligodendrocyte Progenitors from Human Embryonic Stem Cells

Recent advances in the field of human pluripotent stem cell biology have led to highly robust protocols for neural differentiation and specification into various neural and non-neural fates. However, the oligodendrocyte lineage has been a long-standing challenge in the field, due to the requirement for lengthy in vitro differentiation periods (Wang et al., 2013; Douvaras et al. 2014), perhaps compatible with the protracted developmental timeline followed in utero. We optimized a human pluripotent stem cell protocol that allows the derivation of well characterized oligodendrocyte progenitors by 70 days in vitro (DIV) through several stages, including neural induction, patterning of neural precursors, oligodendrocyte progenitor proliferation, and differentiation (Figure 1E). Undifferentiated hESCs were subjected to neural induction by dual SMAD and Wnt/β-catenin inhibition using LDN193189 (LDN), SB431542 (SB), and XAV939 (XAV) (Chambers et al., 2009), resulting in the emergence of ZO-1/LIN-28/Nestin-expressing CNS neural rosettes. Neural precursors emerging from rosettes express Pax6 and FOXG1, suggesting an anterior forebrain identity; they are replated in the presence of purmorphamine, a smoothened agonist that activates the hedgehog pathway. Cells are then passaged in the presence of FGF8, and on DIV 40, they are exposed to glial media containing PDGFRα, IGF-1, cAMP, and T3. Early oligodendrocyte progenitors are observed in the culture on day 45 and are characterized by NKx2.2/Olig2/PDGFRα expression (Figure 1F). PDGFRα$^+$ progenitors are highly proliferative (Ki-67 of 57%) and co-label for Sox10 (Figures S1D and S1E). Their proportion in the culture increases steadily from an average of 6% to 25% on DIV 100 (Figures S1F and S1G). Late oligodendrocyte progenitors (O4-expressing) emerge by DIV 50, increasing steadily to ~35% by DIV 100, while maintaining expression of Olig2, Nkx2.2, and Sox10 (Figure 1F; Figures S2A and S2B). These cells mature in overlapping waves, leading to the gradual appearance of oligodendrocytes that express O1 and MBP. Further in vitro maturation of the majority of the cells (>85%) is achieved by exposure to differentiation media (BDNF, AA, T3, and cAMP) for 2 weeks, leading to morphologically mature oligodendrocytes that express O1, myelin-associated glycoproteins such as MOG and MAG, and MBP (Figure 1G). FACS sorting for late oligodendrocyte progenitors (O4 expressing) (Figure S2C) leads to highly enriched cultures with >93% of cells expressing O4 (remaining cells are olig2$^+$, data not shown) and co-labeling for Olig2 and Nkx2.2; the majority of those cells are post-mitotic (Ki-67 of 3%) (Figure S2B). Efficient sorting can be performed on DIV 70 or later.

We further characterized the O4$^+$ sorted cells by global transcriptomal analysis (Figures S2D and S2E). Comparison of the expression profile of O4-enriched day 70 cells with that of undifferentiated H9 ESCs, showed the robust induction of transcription factors related to oligodendrocyte identity such as *OLIG1*, *OLIG2*, and *SOX10*, *Nkx2.2*, as well significant expression of myelin-related genes *MAG*, *OMG*, and *MBP*. A telencephalic identity was suggested by the upregulation of *FOXG1*, *OTX1*, *EMX2*, and *LHX2* forebrain markers and the absence of *Hox* genes (Figure 1H). RTqPCR (Figure 1I) further validated >10^4-fold change in transcription factors that are master regulators of the oligodendrocyte fate. Functional annotation of enriched gene sets was also compatible with glial and oligodendroglial development (Figure S2F).

To verify the reproducibility of the protocol for oligodendrocyte differentiation, we tested an additional hES line, WA-07 and two iPSC lines, J1 and J2. The iPSC lines were derived from

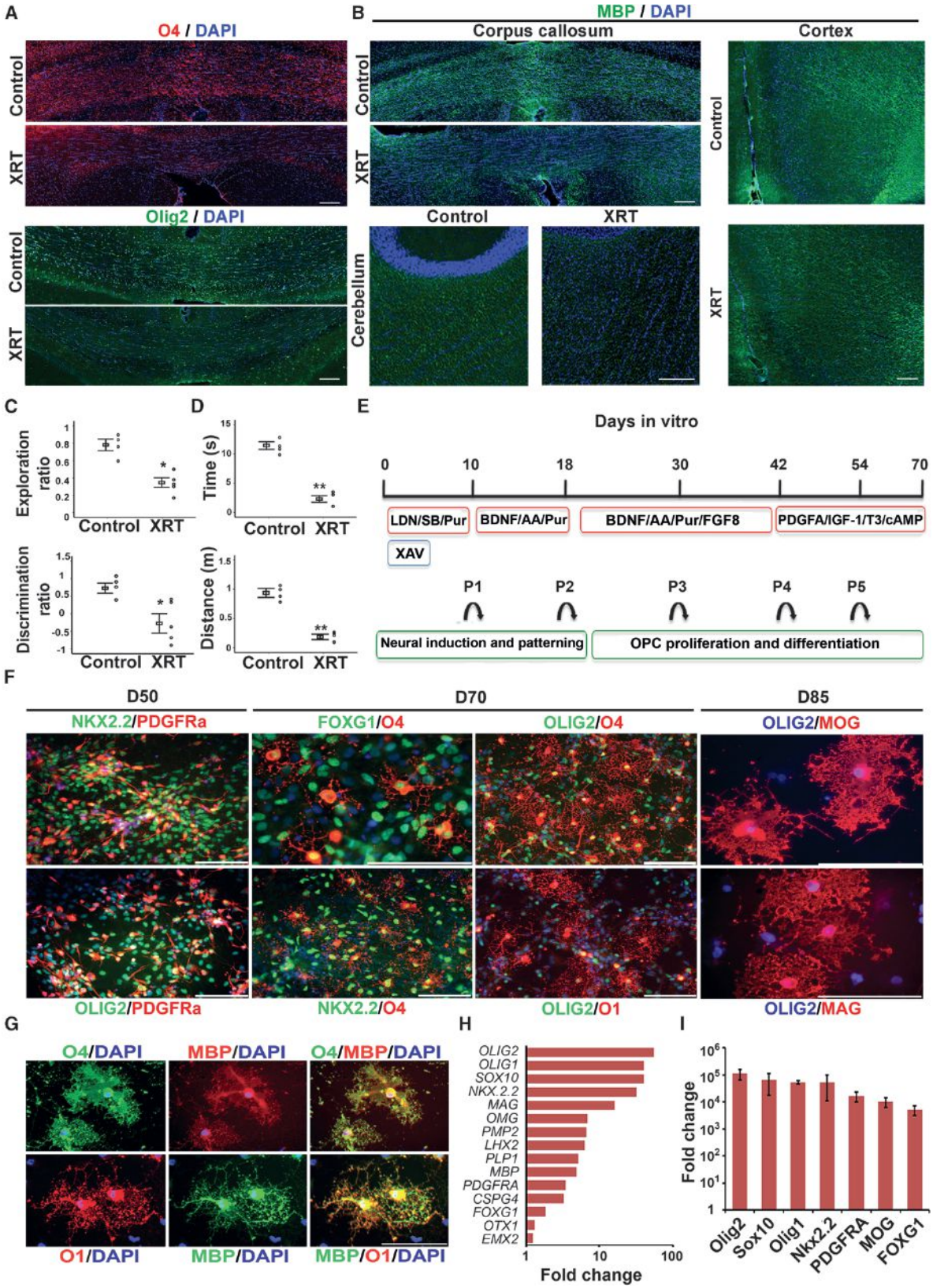

(legend on next page)

fibroblasts of a healthy young donor (J1) and an old donor (J2), and were reprogrammed using Sendai vectors (Miller et al., 2013). All tested lines were capable of oligodendrocyte derivation using the same protocol. Enrichment for $O4^+$ cells on DIV 70 shows a range of 10%–20% $O4^+$ OPC in the cultures. The sorted cells from all three additional lines (H7, J1, and J2) expressed appropriate OPC markers (Olig2, Nkx2.2, Sox10), and exhibited a similar pattern of differentiation and expression of mature markers, e.g., MBP (Figures 2A and 2B). Evidence for myelination of axons was assessed in co-cultures of $O4^+$ OPCs derived from each of the 2 hES and 2 iPSC lines, with human ES-derived neurons or young rat hippocampal neurons (Figure 2C; Figure S3A). After 5 weeks in vitro, the cultures exhibited myelin sheaths along the axons (identified by SMI 312 immunoreactivity); the length of ensheathed/myelinated axons per oligodendrocyte was quantified and found to be similar across the four pluripotent cell lines (Figure 2D). Electron microscopy sections demonstrated the presence of compact myelin sheaths with dense lines (Figure 2E). The cultures did not exhibit any spontaneous or endogenous myelination under control conditions (Figure S3B).

Grafted Human ESC-Derived Oligodendrocytes Remyelinate the Irradiated Brain and Ameliorate Cognitive Function

We then asked whether the human ESC-derived oligodendrocytes could succeed in restoring myelination in the irradiated brains. We thus irradiated a set of 10 nude rats using the same regimen of 50 Gy in 10 fractions, followed by behavioral testing for novel object preference, object location recognition, and rotarod (with acceleration) performance. At 4 weeks post-radiation, the rats (XRT+ graft group) received bilateral stereotactic injections of human ESC-derived oligodendrocytes into the corpus callosum (2 injections per cerebral hemisphere, for a total of 1 million cells). The injected cells were enriched for O4 expression via FACS on DIV 100 (35.7% ± 10.62 of the cells were $O4^+$ pre-sort), immediately prior to grafting. Control groups consisted of non-irradiated animals (control group) and sham injections of Hanks' balanced salt solution (HBSS) into irradiated (XRT group) rats.

Serial behavioral testing was performed on all animals. It consisted of the novel object preference and object location tasks, as well as rotarod testing. While the XRT group continued to exhibit poor performance compared to age-matched normal rats, the irradiated but grafted group demonstrated statistically significant improvements in novel object preference and object location recognition parameters, at 10 weeks after transplantation (Figures 3A and 3B). These tasks reflect multiple cognitive processes related to memory and learning such as preference for novelty and recognition memory (Antunes and Biala, 2012; Barker et al., 2007). However, the animals did not show any improvement in the rotarod task, which involves a challenge to motor balance and coordination (Figure 3C).

Analysis of the grafted brains demonstrated excellent survival of the human cells, which were identified by immunohistochemistry for human nuclear antigen (hNA) or human neural cell adhesion molecule (hNCAM). Cells were found throughout the cerebral hemispheres with many in the corpus callosum where they appeared aligned along the main transverse axis, similar to host cells. Human cells were also distributed along other white matter pathways, including the fimbria of the hippocampus and the commissures, as shown by a series of camera lucida representations and corresponding immunohistochemistry images (Figure 3D). Phenotypic analysis of the surviving human cells by confocal microscopy demonstrated that the majority are oligodendrocytes at various stages of maturity, expressing Olig2, Olig1, O4, myelin-associated glycoprotein (MAG), myelin oligodendrocyte-specific protein (MOSP) (Figures S4A and S4B), and MBP. A detailed analysis of the brain sections demonstrated significant evidence of contribution of the graft cells to remyelination and replenishment of the oligodendrocyte pool. The total number of olig2 cells within the corpus callosum was decreased in the irradiated rats, but replenished to near normal in the grafted animals (control $0.64 \times 10^6 \pm 0.08$; XRT $0.24 \times 10^6 \pm 0.03$; XRT + Graft $0.54 \times 10^6 \pm 0.05$) (Figure 3E). An average of $0.22 \pm 0.01 \times 10^6$ human cells, all expressing olig2, were counted in the corpus callosum and $0.17 \pm 0.05 \times 10^6$ in the hippocampi. These data show that the restoration of olig2 is due in large part to the addition of human cells, rather than the upregulation of olig2 expression in endogenous progenitors. Similarly, a side-by-side comparison of sections from the control, XRT and XRT+ graft brains demonstrates a significant recovery of $O4^+$ progenitors, and evidence of remyelination (Figures 3F and 3G). Imaging-based quantification of the levels of O4 and MBP

Figure 1. Impact of Radiation on the Rat Brain and Derivation of Oligodendrocyte Progenitor Cells from Human Embryonic Stem Cells

(A) Immunohistochemistry shows a decrease in O4 levels and in the number of Olig2+ cells in the corpus callosum in the irradiated (XRT) brain.

(B) A decrease in expression of MBP is noted in various brain regions 14 weeks following radiation compared with normal control.

(C) When compared to age-matched controls (n = 4), irradiated rats (XRT, n = 5) exhibit a decrease in the exploration ratio in the novel object preference task and in the discrimination ratio in the object location task.

(D) The rotarod test also shows a significant decrease in the time spent and the total distance travelled on the accelerating rod.

(E) Schematic protocol for differentiation of human pluripotent stem cells into OPCs.

(F) Immunocytochemical characterization of hES-derived progenitors at progressive stages of differentiation into mature oligodendrocytes. At day 50, early OPCs co-express PDGFRα with Olig2 and Nkx2.2. By day 70, late OPCs emerge, expressing O4 together with Olig2, Nkx2.2, and forebrain specific marker FoxG1. O1 expression also increases as the cells mature; by day 85, they express myelin associated glycoproteins (MOG and MAG).

(G) When placed in differentiation media for 2 weeks, day 70-O4+ cells will mature morphologically and express MBP.

(H) List of selected increased anterior oligospecific genes comparing O4-sorted cell phenotypes versus undifferentiated H9 ESCs, as assessed by microarray analysis.

(I) qRT-PCR analysis of O4 sorted late OPCs at day 70 showed an increase in oligodendrocyte (Olig1, Olig2, Sox10, Nkx2.2, PDGFRα, and MOG) and forebrain-specific markers (FoxG1, OTX1, EMX2) compared to the undifferentiated hES control; $p < 0.01$, n = 3. Fold change is expressed as *log2*.

All panels in (A) and (B) (except for "cerebellum" images) are composites of several low magnification images. All scale bars are 100 μm. Data are mean values ± SEM. (*$p < 0.05$. **$p < 0.01$). Circles in (C) and (D) represent individual scores. All nuclei are counterstained in blue with DAPI. See also Figures S1 and S2.

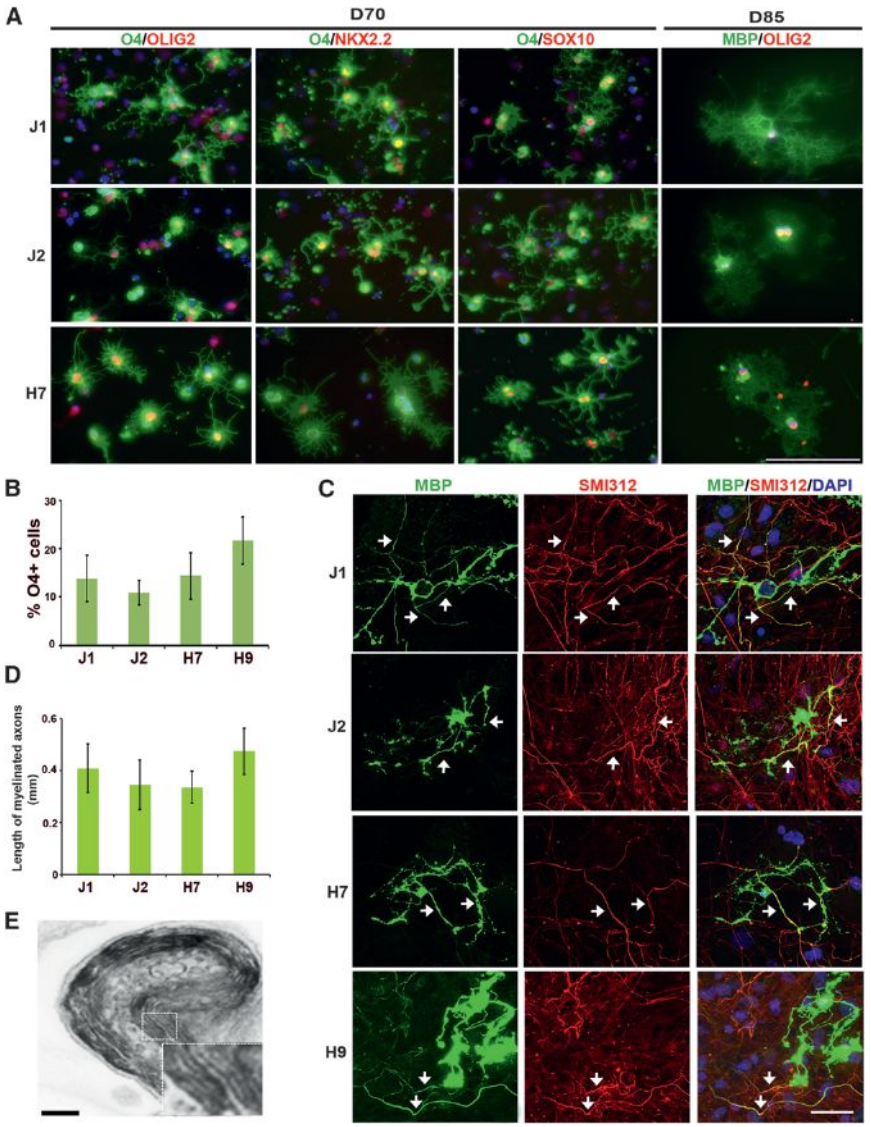

Figure 2. OPCs Can Be Derived from Different Human Pluripotent Stem Cell Lines and Can Myelinate In Vitro

(A) Immunocytochemistry of late OPCs derived from hES line (H7) and 2 iPS lines (J1, J2).The cells co-express Olig2, Nkx2.2, and Sox10 with O4. Day 70 O4+ cells mature into MBP- expressing oligodendrocytes after 2 weeks of differentiation. Scale bar represents 200 μm.

(B) Comparison of the efficiency of OPC derivation by FACS for O4 across four human pluripotent stem cell (hPSC) lines.

(C) In vitro myelination assay: co-culture of O4 sorted cells of different origins with rat hippocampal neurons for 5 weeks. Immunocytochemistry for the axonal marker SMI312 and MBP demonstrates myelination of several axons by a single oligodendrocyte cell. Arrows indicate fibers that co-express both markers. Scale bar represents 50 μm.

(D) Graph represents the total length of axons with myelin sheaths per MBP^+ oligodendrocyte derived from the hPSC lines shown.

(E) Representative electron microscopy (EM) image from a co-culture of OPCs and neurons, showing the formation of multilayered compact myelin sheaths. Scale bar represents 500 nm.

Data are mean values ± SEM. (*$p < 0.05$. **$p < 0.01$). All nuclei are counterstained in blue with DAPI. See also Figure S3, which includes negative control co-cultures.

confirms these observations in a statistically significant manner (Figures 3F and 3G). The decrease in myelin, which followed a patchy pattern, and its recovery are shown in Luxol-stained coronal sections of various areas of the brain (Figure S4C). A stereological volumetric analysis of the corpus callosum also shows recovery to near normal volume in the grafted animals (Figure S4D). We estimated axonal density by immunohistochemistry for SMI312, an axonal marker (Figure S5A), and by electron microscopy and did not note significant differences among the animal groups (axonal density of 149.2 ± 13.55 vs 138.06 ± 11.69 vs 147.15 ± 23.01, per 100 μm^2 in the control, XRT and XRT+ graft groups respectively; $p > 0.05$). Similarly, a stereological estimate of the number of neurons in the cortex did not show changes across the animal groups (11.71 ± 1.78 × 10^6 in the control vs 11.65 ± 1.09 × 10^6 in the XRT group, Figure S5B). However, the proportion of axons that are ensheathed in myelin shows a significant increase in the grafted animals, compared to the sham treated radiation group (53% ± 6% in the XRT+ graft, vs 27% ± 8% in the XRT and 62% ± 7% in the normal control, Figure 4A). These data suggest that the gain in callosal dimensions is likely due to remyelination and recovery of the glial cell population. MBP, a major component of the myelin sheath is a complex structure that is highly conserved across species (Harauz and Boggs, 2013). In view of their significant homology, MBP of rat or human origin cannot be distinguished by any known antibody. Therefore, confirming the human origin of myelin will depend on co-labeling with human markers. Multichannel confocal imaging (Figure 4B) and orthogonal projections (Figure 4C) show co-labeling of human fibers (hNCAM) with MBP (3D reconstruction in Figure 4D; Movie S1). Imaging of the paranodal and juxtaparanodal proteins that define the nodes of Ranvier demonstrates reduced density and loss of architecture following radiation, as is often reported in demyelination conditions (Uchida et al., 2012), but significant recovery after grafting (Figure 4E). 3D reconstruction of confocal optical sections showed the juxtaparanodal protein kv1.2 alternating with the paranodal protein Caspr1, in appropriate ''paranodal'' alignment along a myelinated fiber (Gu and Gu, 2011), with overlay of human NCAM, suggesting contribution of human cells to the reconstruction of a node of Ranvier (Figure 4F; Movie S2). Electron microscopy of brain sections showed areas of significant loss of myelin or degeneration and unraveling of the myelin sheath around the axons in the corpus callosum of the irradiated brains. In contrast, the grafted brains exhibited evidence of structural repair of the demyelinated areas with

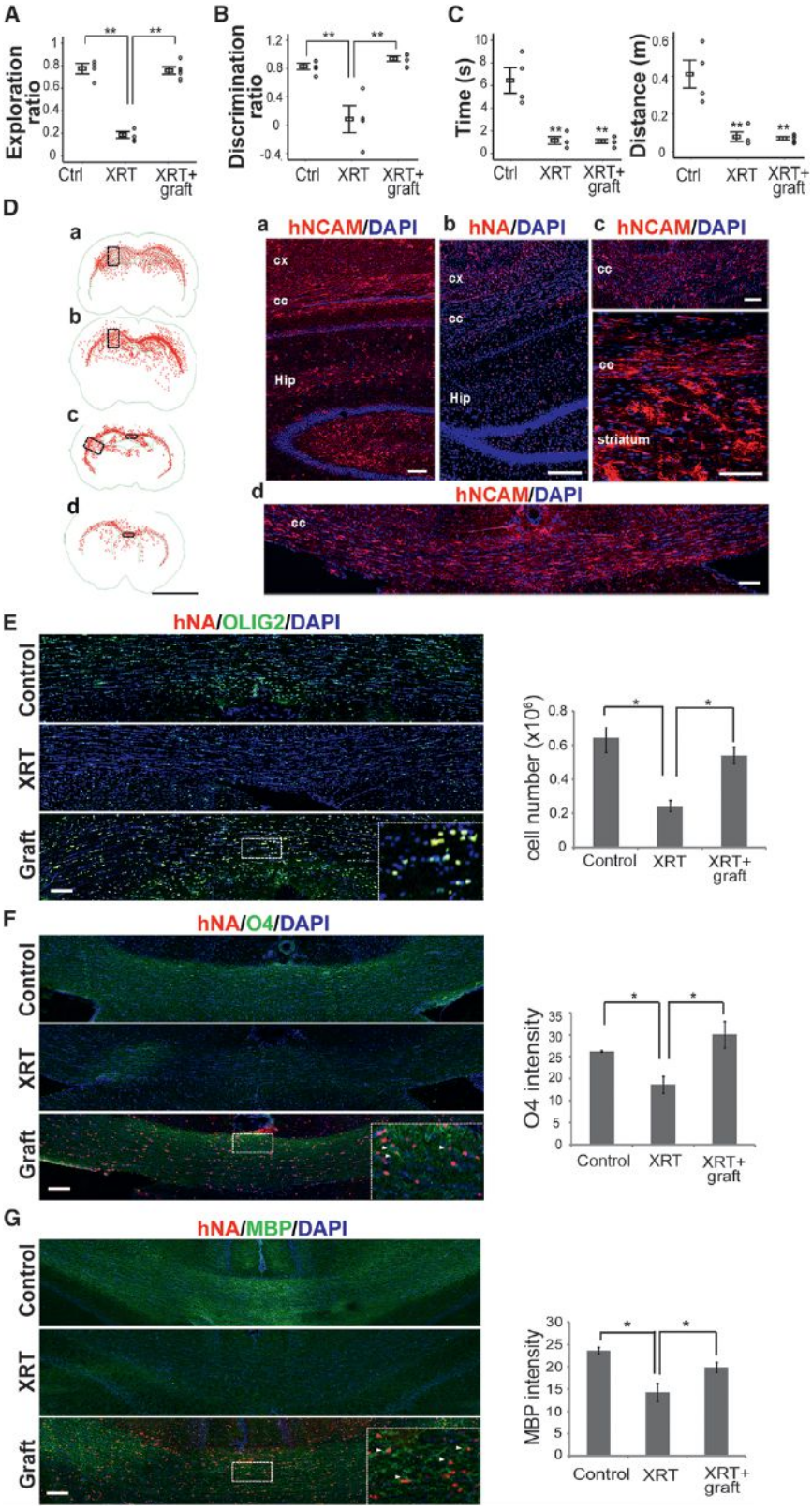

Figure 3. Grafted Human ES-Derived OPCs Remyelinate the Irradiated Brain and Ameliorate Cognitive Function

(A and B) Grafted animals (n = 6) showed significant improvement on the novel object preference (exploration ratio) and object location tasks (discrimination ratio) when compared to sham grafted irradiated animals (n = 4) to normal controls (n = 4).

(C) Grafted animals failed to improve on the rotarod task exhibiting scores that are similar to the irradiated sham injected group (XRT).

(D) Camera lucida representations of the distribution of human cells (marked by human nuclear antigen, hNA, or human NCAM [hNCAM]) in a series of coronal sections (a–d) of the brain; the cells migrate widely along white matter paths. Corresponding immunohistochemistry sections demonstrate the human cells in different regions. Cx, cortex; cc, corpus callosum; Hip, hippocampus. Scale bars represent 5 mm for the camera lucida; 100 μm for immunohistochemistry images.

(E) Immunohistochemistry (IHC) pictures and stereological calculation of the number of $Olig2^+$ cells in the corpus callosum of control, irradiated (XRT), and irradiated and grafted animals (Graft). Selected area of the grafted corpus callosum is shown in inset at higher magnification. Scale bar represents 100 μm.

(F and G) Representative IHC pictures and intensity quantification of O4 and MBP in the CC in control, XRT and XRT + graft rats. Selected areas of the grafted corpus callosum are shown in insets at higher magnification. Scale bar represents 100 μm.

All panels in (D)–(G) are composites of several low magnification images. All nuclei are counterstained in blue with DAPI. Data are reported as mean values ± SEM. (*$p < 0.05$. **$p < 0.01$). Circles (A)–(C) represent individual scores. See also Figures S4 and S6.

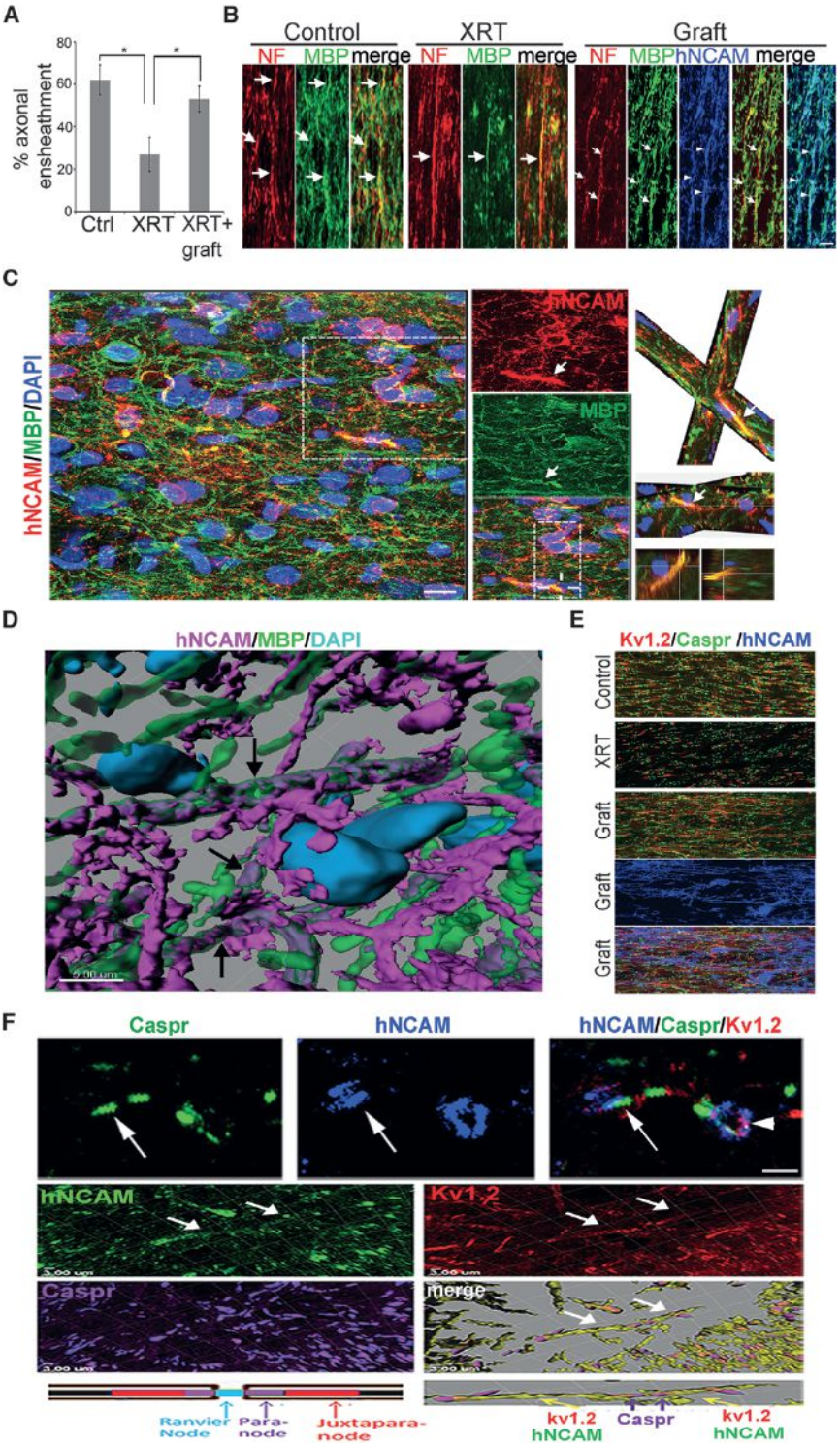

Figure 4. Quantification of Remyelination in the Grafted Irradiated Brains

(A) Quantification of axonal ensheathment demonstrates an increase in the percent myelinated axons after grafting. Data are reported as mean values ± SEM. *$p < 0.05$.

(B) Immunohistochemistry for MBP, neurofilament (NF), and human marker (hNCAM) shows colocalization of NF and MBP fibers and, in the graft group, additional co-labeling of MBP with hNCAM. The arrows point to myelinated axons (co-localization of MBP and NF) and the arrow heads indicate human myelin (co-localization with MBP and hNCAM). Scale bar represents 15 μm.

(C) Confocal imaging of human cells (identified with hNCAM) showing typical oligodendrocyte morphology co-labeled with MBP in cytoplasm and myelin sheath projections. Single channels are displayed in the middle panel, with white arrows identifying myelin from human origin. In the top right panel, two oblique slicers were used on the same field of view as the middle panel to confirm that MBP was expressed by hNCAM-expressing cells. In the right bottom panels, three-dimensional yz and xz orthogonal projections were shown to confirm MBP co-labeling with hNCAM (seen in yellow). Scale bar represents 10 μm.

(D) 3D reconstruction in high magnification of human graft cells projecting hNCAM labeled processes (magenta) that merge with MBP (green) along a probable axon in the cc. The MBP color was rendered semi-transparent to enhance visualization of the overlapping channels (arrows). Scale bar represents 500 μm. See also Movie S1.

(E) Representative confocal IHC images of junxtaparanodal protein kv1.2 and paranodal protein Caspr1 show restoration of nodal architecture in the grafted brain. Scale bar represents 15 μm.

(F) Triple labeling of sections of grafted irradiated brain with hNCAM, Caspr1 (arrows) and Kv1.2 (arrowheads), indicating that human cells associate closely with myelin fibers. Scale bar represents 10 μm. In the middle and lower panels, representative images show co-localization of hNCAM with the juxtaparanodal protein kv1.2 (merge as yellow) and alternating with host Caspr1 (magenta) in appropriate anatomic alignment, likely along a myelinated axon. In the lower right panel, 3D reconstruction performed with Bitplane Imaris software showing the structures in perspective. Scale bar represents 3 μm. The drawing in the lower left panel is a schematic representation to interpret the 3D model shown on the right side. See also Movie S2.

See also Figure S5.

recovery of thin yet compact myelin sheaths wrapped around healthy axons (Figure 5A). These findings are reflected in the quantification (Franklin and Ffrench-Constant, 2008) of the average g-ratio (0.70 in normal group, 0.76 in the XRT group and 0.72 in the XRT+ graft group; Figure 5B). Immunogold electron microscopy showed integration of human NCAM into the myelin sheaths and relatively rare immunogold particles that are not in association with myelin bundles (Figure 5C). Further quantification of myelination by the grafted cells was performed on IHC sections of MBP/hNCAM. The proportion of myelin of human origin in the grafted animals was calculated at ~47% (area of $hNCAM^+MBP^+/MBP^+$). Taken together, these data confirm

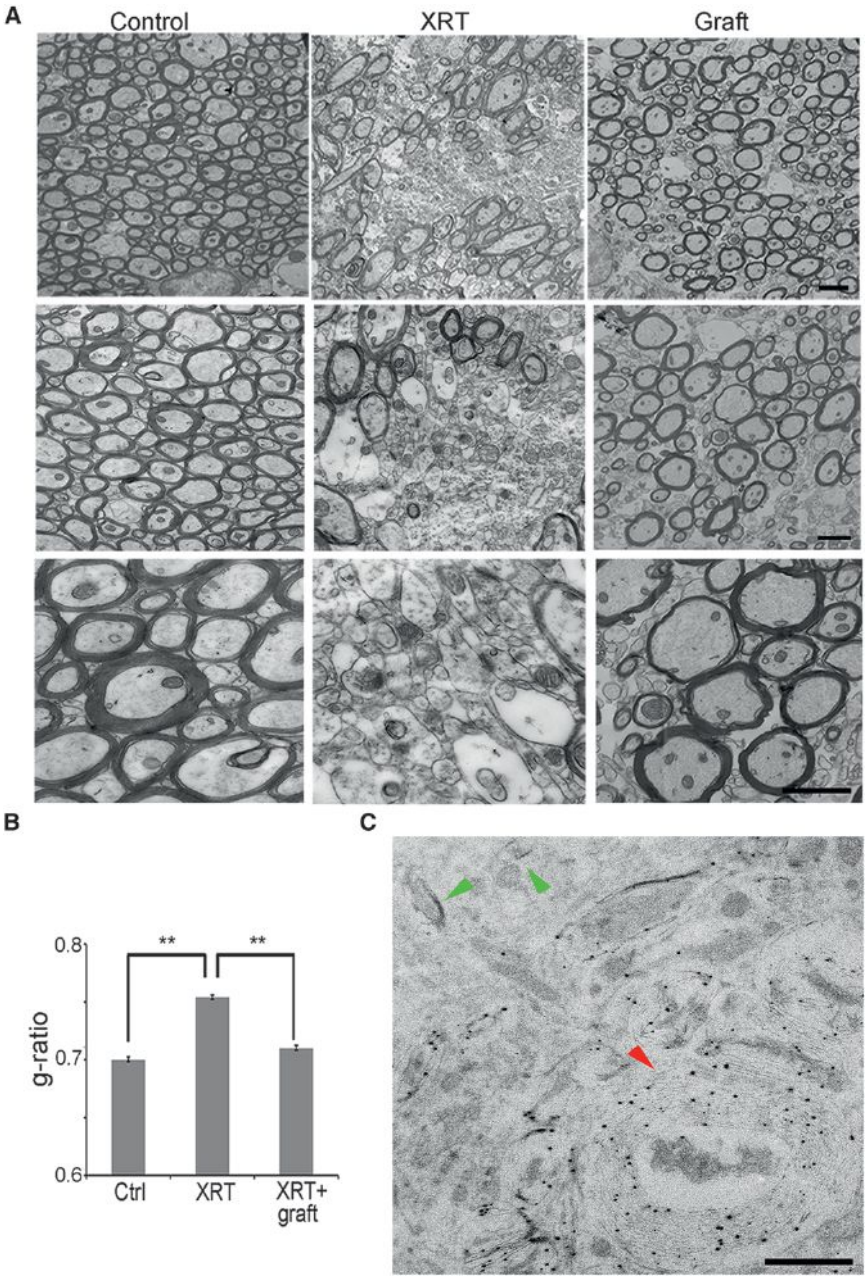

Figure 5. Ultrastructural Analysis of In Vivo Myelination by Human Grafts

(A) Representative EM images of the cc show patchy disruption of the myelin sheath around axons in the irradiated brain. The grafted brains show evidence of recovery of axonal myelination. Recent sheaths are thinner in diameter though they exhibit normal compact anatomy. Scale bar represents 2 μm in the upper panel and 500 nm for the two lower panels.

(B) g-ratios of the axons in corpus callosum in control, irradiated (XRT), and irradiated+graft (XRT+graft) groups. **p<0.01.

(C) Low power view of immuno-electron micrograph of hNCAM. The red arrowhead indicates myelin sheaths of an axonal projection with hNCAM gold labeling (10–25 nm black dots). Green arrows indicate endogenous myelin without immunolabeling. Scale bar represents 2 μm.

that grafted human cells extensively contribute to the structural and functional remyelination in the radiated brain. The transplanted cells did not promote astrogliosis or microglial/macrophage proliferation and activation (Figure S5C). Areas of neurogenesis such as the subventricular zone (SVZ) and hippocampus were impacted by radiation as reported in the literature (Romanko et al., 2004; Monje et al., 2002; Panagiotakos et al., 2007). Specifically there was a loss of doublecortin-expressing neuroblasts and proliferating cells (ki67) in the SVZ and hippocampus. Human cells were found in those regions but none exhibited neuronal differentiation, nor did they promote host-derived neurogenesis (Figures S5D and S5E). There was no evidence of teratomas or other signs of tumor formation, and no graft overgrowth was noted in any of the grafted animals. In fact, a phenotypic analysis of the cells did not demonstrate any Oct4, nestin, or Ki67 co-labeling with a human marker in the grafted brains (data not shown). Astrocytes of human origin were very rare, suggesting that the oligodendrocyte progenitors were either terminally committed or, less likely, that the microenvironment was not supportive of astrocytic differentiation. However, analysis of the cerebellum demonstrated complete absence of human cells and persistent demyelination (Figure S5F), thus possibly explaining the lack of improvement on the rotarod acceleration tasks.

Cerebellar Grafts Rescue Motor Coordination and Remyelinate the Cerebellum

A second group of animals (n = 28) was then subjected to the same radiation regimen, and received human ES-derived oligodendrocytes injected either in the cerebellum alone or in combination with the corpus callosum bilaterally. A total of 1 million cells were injected in the corpus callosum, as in the initial study. The cerebellum received a single injection of 250,000 $O4^+$ sorted cells in the central white matter. Animals were followed and tested behaviorally at two time points, 10 and 14 weeks post-injection. Performance on the novel object preference and object location tasks improved significantly in the group that received callosal and cerebellar grafts when compared to the non-transplanted animals, while the animals with grafts only in the cerebellum did not improve in any of the tests probing cognitive skills (Figure S6A). However, all grafted animals showed improvement in the rotarod task, including those that received cerebellar only injections (Figure 6A). Histological analysis of the brains demonstrated survival and migration of the human cells in the cerebellum (Figure 6B). There was also evidence of remyelination of the cerebellum in

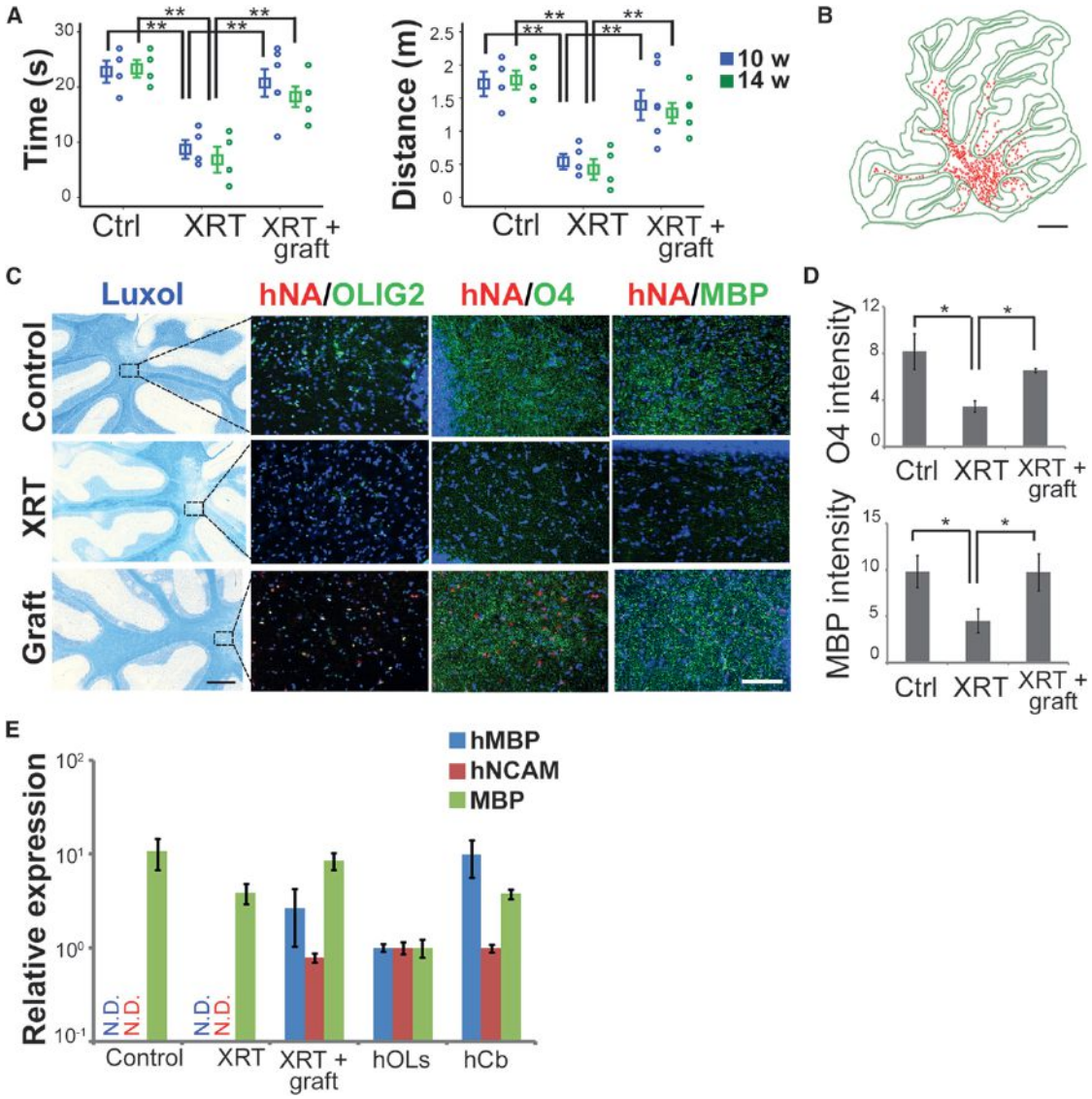

Figure 6. Cerebellar Grafts Rescue Motor Coordination and Remyelinate the Cerebellum

(A) Grafted animals showed improvement on the accelerating rotarod tasks (n = 6).

(B) Representative camera lucida illustration of the distribution of human cells in the cerebellum, detected by IHC for human nuclear antigen (hNA). Scale bar represents 1mm.

(C) Representative Luxol fast blue staining of sagittal sections of the cerebellum and IHC images showing myelin loss in the XRT group and recovery upon grafting. Human cells (hNA) co-label with olig2, O4, and MBP. Scale bar represents 0.5 mm in the luxol images and 100 μm in the IHC images.

(D) Quantification of O4 and MBP image intensity in the white matter of cerebellum.

(E) Human-specific MBP mRNA was detectable in the grafted group, as well as the human ESC-derived oligodendrocytes and the normal human cerebellum tissue (hCb). Expression levels of human NCAM and MBP (human and rat) mRNA are also analyzed as reference. The relative expression of mRNA was normalized to human OPCs. N.D., non detectable.

Data in (A), (D), and (E) are reported as mean values ± SEM with the indicated significance (*$p < 0.05$, **$p < 0.01$). See also Figure S6.

all grafted animals as assessed by Luxol histochemistry and quantitative immunofluorescence for olig2, O4, and MBP (Figures 6C and 6D). Animals that received cell injections in the cerebellum only did not exhibit remyelination in the corpus callosum or elsewhere in the cerebral hemispheres. There was no evidence for endogenous or human astrogliosis, excessive proliferation, or teratomas. To further support the role of human cell-mediated structural repair, we performed qRT-PCR to confirm the presence of myelin of human origin in the grafted tissue. The data demonstrate the expression of a human-specific MBP mRNA isoform in the grafted rat tissue, normal human cerebellum, and human ESC-derived oligodendrocytes, but not in the control or irradiated rat brains (Figure 6E). Expression of human NCAM and MBP (recognizing both human and rat) mRNA were also detected in the same samples as reference. These data provide strong evidence for structural repair of the

demyelinated irradiated brain via human ES-derived oligodendrocytes, leading to behavioral recovery that is specific to the remyelinated region of the brain.

DISCUSSION

As intense efforts in cancer therapies succeed in achieving long periods of remission and hopes of long-term survival, a focus on improving quality of life among survivors is more pressing. Radiation damage to the brain ranks among the major contributors to poor quality of life and is currently untreatable (Van Dongen-Melman et al., 1997; Yabroff et al., 2004). Here we demonstrate that remyelination of the irradiated brain via grafting of human oligoprogenitors can lead to cognitive and motor amelioration. Our model holds particular promise in view of the substantial and clinically relevant dose of fractionated radiation used, 50 Gy. There are reports of repair of radiation-induced demyelination, e.g., in the spinal cord, though the animal models used often received a single dose of radiation (Sun et al., 2013). Here we have focused on modeling whole-brain or large-volume radiation, rather than single high-dose focal radiation. Available clinical regimens are highly variable depending on the disease being treated. Commonly, whole-brain or large-volume partial brain radiation involves the delivery of 30–60 Gy in multiple fractions. It is difficult to fully mimic the human regimens. In particular, the dose per fraction we used is higher than average, largely due to logistical reasons, because the rodents have to be fully anesthesized for each dose of radiation.

Radiation injury is a complex phenomenon with a myriad of direct and indirect consequences, such as an impact on the vascular compartment, glia, local inflammatory systems, neurogenesis, and altered neuronal function (Bentzen, 2006; Greene-Schloesser et al., 2013). Recent reports have shown improvement of cognitive tasks following injection of neural stem cells in the hippocampus of irradiated rats, though the radiation regimen was subtherapeutic (Acharya et al., 2014). It is unclear to what extent rescue of hippocampal neurogenesis would contribute to symptom amelioration in humans. Despite the absence of neuronal differentiation by our cells and the decreased neurogenesis in the hippocampus following radiation, the animals exhibited improvement in cognition and in motor function, suggesting an important role for white matter recovery. The correlation of behavioral amelioration with the site of cell injection and area of remyelination support cell-mediated repair, though the possibility of a favorable paracrine role for the grafted cells cannot be completely excluded.

We also present a robust protocol for the derivation of highly enriched fully committed oligodendrocytes from human ESCs or iPSCs, capable of widespread migration and efficient myelination with near complete absence of other phenotypes and no evidence for proliferative cell types, primitive progeny, or teratomas. Such an approach can be fully GMP-compatible including the sorting step, though further acceleration of the in vitro period would be desirable. Pluripotent stem cells (PSC) are also an attractive cell source given their scalability, at the level of the undifferentiated cells which are readily expandable, as well as during the differentiation process. We estimate based on numerous replications of this protocol, that starting with 10 million undifferentiated hESCs (a few vials), we can obtain about 214 million well characterized $O4^+$ cells at day 100 of culture (assuming an $O4^+$ recovery rate of 35%). A main limiting factor for PSC-based cell therapies is often the ability to direct their differentiation into authentic and stable phenotypes. This is a particularly challenging task if the cells of interest develop late or need to be fully functional prior to transplantation. Here, we present a reliable differentiation strategy with stable phenotypes that closely resemble current definitions of oligodendrocyte progenitors (markers, gene-expression profile). In vivo, the overwhelming majority of the cells develops into mature myelinating oligodendrocytes or remains in the oligoprogenitor stage. We rarely identify any other phenotypes and there were no teratomas or areas of graft overgrowth, though assessments following longer in vivo periods, such as one year or longer, should be performed. Our strategy also includes a sorting step, which not only enriches for the phenotype of interest, but also presents an opportunity for indirectly selecting out undifferentiated ESCs, which are a source of safety concerns. A more aggressive negative selection approach can also be contemplated, but to our knowledge, it has not been a strict prerequisite for FDA approval of pluripotent stem cell based therapies. On the other hand, the differentiation protocol remains rather lengthy and will need to be optimized further for logistical purposes, if GMP manufacturing is planned.

Other human cell sources have been used successfully for remyelination in rodent models, such as fetal or adult white-matter progenitors (Windrem et al., 2004) though access to these cell sources can be difficult, especially because the cells need to be replenished because they are not highly expandable. The FDA has also approved early phase trials of multiply passaged multipotent neural stem cells isolated from fetal brain (Uchida et al., 2012; Gupta et al., 2012). These cells, manufactured to a clinical grade, have been used for a wide range of disorders (Pelizaeus-Merzbacher disease, neuronal ceroid lipofuscinosis, and spinal cord injury; see https://clinicaltrials.gov/). The cells are thought to provide a very beneficial neuroprotective effect.

The requirement for immunosuppression is another important issue in planning for clinical applications, though it remains the subject of debate. The preponderance of available data points towards the need for at least temporary immunosuppression at the time of surgical injection. The specific agents to be used and the total duration of treatment are also highly variable (Tadesse et al., 2014). In the case of radiation injury, immunosuppression could increase the burden of treatment-related morbidities, though most patients already receive far harsher chemotherapeutic agents. On the other hand, the derivation of engraftable oligoprogenitors from iPSCs is robust and feasible, as shown by our group and others; the majority of cancer patients can safely provide genetically normal somatic cells, such as skin, for iPS production, thereby developing a customized autologous cell source. However, there remain significant regulatory hurdles, as well as some scientific concerns, over the clinical use of iPSCs, despite their recent approval in Japan for the treatment of Parkinson's disease.

In summary, our results suggest that countering the cognitive side effects of radiation injury can be achieved safely, using human pluripotent cell-derived oligodendrocytes, thus paving the road towards a clinical trial for a condition that currently has no viable therapeutic options. The protocol could also be readily

adapted to other demyelination disorders and, although further long term data will be required, these results represent a robust first set of preclinical studies, with an eye towards future translation.

EXPERIMENTAL PROCEDURES

Animals, X-Irradiation, and Cell Transplantation

Female Athymic nude rats (RNU rat Crl:NIH-Foxn1rnu, Charles River Laboratories) aged 4 weeks were randomized into three age-matched groups: non-irradiated ("control" rats, n = 16 in total), irradiated rats with sham transplantation of HBSS (XRT, n = 17 in total), and irradiated rats transplanted with human ESC-derived OPCs (XRT + graft, n = 18 in total). Radiation was administered to the cranium using a 250 kV-orthovoltage system. Animals were anesthetized by ketamine (90 mg/kg)/xylazine (4 mg/kg) and placed on a custom-designed positioning platform covered with a protective lead plate with an adjustable aperture, which focuses the radiation delivery to the skull while shielding the rest of the body. A total dose of 50 Gy was administered in 10 fractions (5 Gy/fraction/day), over 2 weeks. One month after irradiation, human cells were transplanted into the corpus callosum, in 2 injections of 250,000 cells in each hemisphere, for a total of 1 million cells (Coordinates: AP −0.40 mm, ML −2.4 mm, VRT −3 mm; AP −0.40 mm, ML 2.4 mm, VRT −3 mm; AP −1.30 mm, ML –2 mm, VRT −3.2 mm; AP −1.30 mm, ML 2 mm, VRT −3.2 mm; tooth bar set at 0). Cerebellar injections were performed unilaterally into the cerebellar white matter and consisted of 250,000 cells delivered stereotactically (Coordinates: AP −12 mm, ML –0.9 mm, VRT −4.2 mm; tooth bar set at 0). The rats were anaesthetized with Ketamine/xylazine during the surgical procedures. Cells were delivered via a Hamilton Syringe (Hamilton Company) on a stereotactic Kopf frame (David Kopf Instruments). All animal procedures and care were performed according to NIH guidelines and following IACUC approval.

Human ESC-Derived Oligodendrocyte Precursor Cell Culture

Human ESCs (WA-09, XX, passages 35–45) were cultured on mouse embryonic fibroblasts (MEFs, GlobalStem) in medium of DMEM/F12 containing 20% knockout serum replacement (Gibco), 0.1 mM β-mercaptoethanol, and 6 ng/ml FGF-2 (R&D Systems). hESCs and iPSCs were used according to institutional ESCRO guidelines and approval.

Neural Induction

For neural induction, a modified version of the dual-SMAD inhibition was used. Undifferentiated hESCs were disaggregated using Accutase (Innovative Cell Technology) and plated on on Matrigel (BD Bioscience)-coated dishes at a density of 40,000 cells/cm2 in MEF conditioned hESC medium supplemented with 10 ng/ml of FGF-2 and Y-27632 (10μM, Tocris Bioscience). When the cells reached a confluent state (2–3 days after plating), they were exposed for 9 days to LDN193189 (200nM, Stemgent) and SB431542 (10 μM, Tocris) in knockout serum replacement medium (KSR) containing DMEM, 15% knockout serum replacement, 2 mM L-glutamine and 10 μM β-mercaptoethanol. Starting from day 5, Purmorphamine (1 μM, Stemgent) was added to differentiation media. KSR medium was gradually replaced with N2 medium (25%, 50%, 75%) starting on day 4 of differentiation as described previously (Chambers et al., 2009).

Patterning and Differentiation of Oligodendrocytes

On day 12, cells were dissociated using Accutase and replated in high-density conditions (300,000 cells per cm2) on dishes precoated with polyornithine (PO; 15 μg/ml), laminin (Lam; 1 μg/ml) and fibronectin (FN; 2 μg/ml) in N2 medium supplemented with brain-derived neurotrophic factor (BDNF; 20 ng/ml, R&D), ascorbic acid (AA; 0.2 mM, Sigma-Aldrich), Purmorphamine (1 uM, Stemgent) and fibroblast growth factor 8 (FGF8; 100 mg/ml, R&D). They are patterned at the P1 stage for 2 weeks. After two weeks of patterning, cells were passaged by mechanical picking of the CNS clusters and re-plated on PO/Lam/FN coated dishes (P2). Starting with P3, neural precursor cells (NPCs) were maintained in N2/B27 medium supplemented with Purmorphamine and FGF8 until day 40 when they were further exposed to glial media containing platelet-derived growth factor (PDGF; 20 ng/ml, R&D), insulin-like growth factor 1 (IGF-1; 20 ng/ml, R&D), triiodothyronine (T3; 20 ng/ml, Sigma-Aldrich) and dibutyryl cAMP (0.1 mM, Sigma-Aldrich). Medium was changed every 2 days, whereas the cultures were passaged every 2 weeks.

Microarray Analysis

For microarray analysis, total RNA from undifferentiated hESCs (control condition) and 70 days old, O4 sorted OPCs was collected using Trizol LS (Invitrogen). Samples were processed by the MSKCC Genomic core facility and hybridized on Illumina Human HT-12 Oligonucleotide arrays (total of 34,694 genes). Gene-expression analysis was done with the Partek Genomics Suite. Genes that had an adjusted p value < 0.05 and a fold change greater than two were considered significant. Raw data for the microarray gene expression reported in this study are available from the public repository of GEO Data Sets (accession number GSE63318). Top enriched gene groups were obtained using Gene Ontology enrichment analysis (DAVID) and are presented as a function of the corresponding Benjamini–Hochberg FDR corrected p values.

In Vitro Myelination Assay

hESC-derived neural stem cells were generated using a modified dual SMAD inhibition protocol (Chambers et al., 2009). Differentiation of neurons from NSCs was achieved by seeding the NSCs at low density in N2 medium without growth factors. Nearly homogenous populations of neurons were generated within 30 days and used for co-culture experiments. Hippocampal neurons were isolated from postnatal day 1 SD rats (Gardner et al., 2012).

Human ES-derived neuronal cells and rat hippocampal neurons were co-cultured with human PSC-derived OPCs sorted for O4 on poly-O-ornithine (50 μg/ml) and laminin (1μg/ml) coated wells in Neurobasal medium (Life Technologies) with B27 (Life Technologies), GlutaMAX-I Supplement (2 mM, Life Technologies), BDNF (20 ng/ml), AA (0.2 mM), T3 (60 ng/ml, Sigma-Aldrich), and cAMP (0.2 mM, Sigma-Aldrich) for 4 weeks and 5 weeks, respectively. Myelination was identified as co-labeling of SMI312 (axons) and MBP (oligodendrocyte processes). The length of axons was measured according to the method described by Deshmukh et al. (2013) with minor modifications. In our experiments, myelination was identified as regions of co-localization between MBP-positive oliogodendrocyte processes and SMI312-positive neuritis, and the length was measured with the NIH ImageJ software. This measurement was analyzed in ten randomly chosen fields from replicate co-culture samples. For the EM studies the co-cultures were maintained for 7 weeks. The differentiation medium was changed twice a week.

Behavioral Testing

We used the novel object-preference task and novel place-recognition tests, modified from Barker et al. (Barker et al., 2007). An open field arena (TSE Systems) was used for testing. During the testing, the time to explore the objects was recorded and analyzed by Videomot2 (TSE Systems). In brief, for novel object-preference task, rats were allowed to habituate twice in the arena with two identical objects for 5 minutes. Then the rats were placed in the arena for 3 minutes with one novel object and one familiar object. The data was presented as exploration ratio or ratio of time spent exploring the novel object versus both objects. For the object-location task, the rats were habituated to two identical objects for 10 minutes. Then they were placed in the arena with one object moved to a new location (novel place) and another identical object remaining in the same position (familiar place) for 3 minutes. The data was presented as discrimination ratio = (time exploring the object in the novel place − the familiar place) / time spent exploring both objects. The Morris water maze test was performed as described by Vorhees et al. (Vorhees and Williams, 2006). An automated rotarod treadmill (7 cm diameter rod, IITC Life Science Inc.) was used in the rotarod analysis. The rats were pre-trained to learn to run on a rotating rod at 5 rpm and 10 rpm prior to testing. The rotarod was accelerated from 15 to 40 rpm over 60 seconds for the analysis. The length of time and distance traveled until the rats fell off the rod were recorded.

Statistics

Results are expressed as the mean ± SEM. The statistical analysis was performed using IBM SPSS Statistics (version 21) software. Normality was tested by Shapiro-Wilk test. Statistical analysis was performed by ANOVA. Homogeneity of variance was tested. $p \leq 0.05$ was considered to denote significance.

ACCESSION NUMBERS

The GEO accession number for the microarray data reported in this paper is GSE63318.

SUPPLEMENTAL INFORMATION

Supplemental Information includes six figures, Supplemental Experimental Procedures, and two movies and can be found with this article online at http://dx.doi.org/10.1016/j.stem.2015.01.004.

AUTHOR CONTRIBUTIONS

J.P. conducted all the in vivo experiments, supervised and/or performed the behavior tests, assisted with the EM images, and co-wrote the manuscript; T.M. conducted all the in vitro studies and co-wrote parts of the manuscript. G.A. and E.P. assisted with behavioral testing and radiation experiments; J.M. and L.D. performed many technical tasks; P.G. consulted on overall plans and experimental design; K.U. performed and /or supervised the EM experiments; J.T. provided the hES derived neurons; D.S. assisted with confocal imaging, 3D rendering, animations, and graphics; and V.T. contributed to overall plan, experimental design and setups, data interpretation, and manuscript writing.

ACKNOWLEDGMENTS

The work was supported by a grant from the NINDS (R01NS054009), the New York State Stem Cell Board (NYSTEM), and the Tri-Institutional Stem Cell Initiative (Tri-Sci). T.M. was supported in part by a Fellowship from the Tri-Sci. D.S. is a Research Scholar from Le Fonds de Recherche du Québec - Santé (FRQ-S) and holds a Junior 1 Career Award. We would like to thank Alexander Lucaci and Rebecca Chen for help with the behavior experiments, Tom Losasso with the radiation dosimetry, Katia Manova, Vitaly Boyko, Fujisawa Sho, and Ke Xu at the Molecular Cytology Core Facility, and Nina Lampen at The Electron Microscopy facility, all at Memorial Sloan Kettering Cancer Center. We are grateful to William Stallcup for the gift of PDGFRα antibody and to Steve Goldman for O4 antibody aliquots.

Received: December 15, 2013
Revised: November 24, 2014
Accepted: January 13, 2015
Published: February 5, 2015

REFERENCES

Acharya, M.M., Christie, L.-A., Hazel, T.G., Johe, K.K., and Limoli, C.L. (2014). Transplantation of human fetal-derived neural stem cells improves cognitive function following cranial irradiation. Cell Transplant. *23*, 1255–1266.

Antunes, M., and Biala, G. (2012). The novel object recognition memory: neurobiology, test procedure, and its modifications. Cogn. Process. *13*, 93–110.

Barker, G.R.I., Bird, F., Alexander, V., and Warburton, E.C. (2007). Recognition memory for objects, place, and temporal order: a disconnection analysis of the role of the medial prefrontal cortex and perirhinal cortex. J. Neurosci. *27*, 2948–2957.

Bentzen, S.M. (2006). Preventing or reducing late side effects of radiation therapy: radiobiology meets molecular pathology. Nat. Rev. Cancer *6*, 702–713.

Chambers, S.M., Fasano, C.A., Papapetrou, E.P., Tomishima, M., Sadelain, M., and Studer, L. (2009). Highly efficient neural conversion of human ES and iPS cells by dual inhibition of SMAD signaling. Nat. Biotechnol. *27*, 275–280.

Deshmukh, V.A., Tardif, V., Lyssiotis, C.A., Green, C.C., Kerman, B., Kim, H.J., Padmanabhan, K., Swoboda, J.G., Ahmad, I., Kondo, T., et al. (2013). A regenerative approach to the treatment of multiple sclerosis. Nature *502*, 327–332.

Douvaras, P., Wang, J., Zimmer, M., Hanchuk, S., O'Bara, M.A., Sadiq, S., Sim, F.J., Goldman, J., and Fossati, V. (2014). Efficient generation of myelinating oligodendrocytes from primary progressive multiple sclerosis patients by induced pluripotent stem cells. Stem Cell Reports *3*, 250–259.

Duffner, P.K., Cohen, M.E., Thomas, P.R., and Lansky, S.B. (1985). The long-term effects of cranial irradiation on the central nervous system. Cancer *56*, 1841–1846.

Franklin, R.J.M., and Ffrench-Constant, C. (2008). Remyelination in the CNS: from biology to therapy. Nat. Rev. Neurosci. *9*, 839–855.

Gardner, A., Jukkola, P., and Gu, C. (2012). Myelination of rodent hippocampal neurons in culture. Nat. Protoc. *7*, 1774–1782.

Gibbs, I.C., Tuamokumo, N., and Yock, T.I. (2006). Role of radiation therapy in pediatric cancer. Hematol. Oncol. Clin. North Am. *20*, 455–470.

Greene-Schloesser, D., Robbins, M.E., Peiffer, A.M., Shaw, E.G., Wheeler, K.T., and Chan, M.D. (2012). Radiation-induced brain injury: A review. Front Oncol *2*, 73.

Greene-Schloesser, D., Moore, E., and Robbins, M.E. (2013). Molecular pathways: radiation-induced cognitive impairment. Clin. Cancer Res. *19*, 2294–2300.

Gu, C., and Gu, Y. (2011). Clustering and activity tuning of Kv1 channels in myelinated hippocampal axons. J. Biol. Chem. *286*, 25835–25847.

Gupta, N., Henry, R.G., Strober, J., Kang, S.M., Lim, D.A., Bucci, M., Caverzasi, E., Gaetano, L., Mandelli, M.L., Ryan, T., et al. (2012). Neural stem cell engraftment and myelination in the human brain. Sci Transl Med. *4*, 155ra137.

Harauz, G., and Boggs, J.M. (2013). Myelin management by the 18.5-kDa and 21.5-kDa classic myelin basic protein isoforms. J. Neurochem. *125*, 334–361.

Hu, B.Y., Du, Z.W., Li, X.J., Ayala, M., and Zhang, S.C. (2009). Human oligodendrocytes from embryonic stem cells: conserved SHH signaling networks and divergent FGF effects. Development *136*, 1443–1452.

Kurita, H., Kawahara, N., Asai, A., Ueki, K., Shin, M., and Kirino, T. (2001). Radiation-induced apoptosis of oligodendrocytes in the adult rat brain. Neurol. Res. *23*, 869–874.

Mabbott, D.J., Noseworthy, M.D., Bouffet, E., Rockel, C., and Laughlin, S. (2006). Diffusion tensor imaging of white matter after cranial radiation in children for medulloblastoma: correlation with IQ. Neuro-oncol. *8*, 244–252.

Miller, J.D., Ganat, Y.M., Kishinevsky, S., Bowman, R.L., Liu, B., Tu, E.Y., Mandal, P.K., Vera, E., Shim, J.W., Kriks, S., et al. (2013). Human iPSC-based modeling of late-onset disease via progerin-induced aging. Cell Stem Cell *13*, 691–705.

Monje, M.L., Mizumatsu, S., Fike, J.R., and Palmer, T.D. (2002). Irradiation induces neural precursor-cell dysfunction. Nat. Med. *8*, 955–962.

Monje, M.L., Toda, H., and Palmer, T.D. (2003). Inflammatory blockade restores adult hippocampal neurogenesis. Science *302*, 1760–1765.

Oi, S., Kokunai, T., Ijichi, A., Matsumoto, S., and Raimondi, A.J. (1990). Radiation-induced brain damage in children—histological analysis of sequential tissue changes in 34 autopsy cases. Neurol. Med. Chir. (Tokyo) *30*, 36–42.

Panagiotakos, G., Alshamy, G., Chan, B., Abrams, R., Greenberg, E., Saxena, A., Bradbury, M., Edgar, M., Gutin, P., and Tabar, V. (2007). Long-term impact of radiation on the stem cell and oligodendrocyte precursors in the brain. PLoS ONE *2*, e588.

Paumier, A., Cuenca, X., and Le Péchoux, C. (2011). Prophylactic cranial irradiation in lung cancer. Cancer Treat. Rev. *37*, 261–265.

Ringborg, U., Bergqvist, D., Brorsson, B., Cavallin-Ståhl, E., Ceberg, J., Einhorn, N., Frödin, J.-E., Järhult, J., Lamnevik, G., Lindholm, C., et al. (2003). The Swedish Council on Technology Assessment in Health Care (SBU) systematic overview of radiotherapy for cancer including a prospective survey of radiotherapy practice in Sweden 2001—summary and conclusions. Acta Oncol. *42*, 357–365.

Romanko, M.J., Rola, R., Fike, J.R., Szele, F.G., Dizon, M.L., Felling, R.J., Brazel, C.Y., and Levison, S.W. (2004). Roles of the mammalian subventricular zone in cell replacement after brain injury. Prog. Neurobiol. *74*, 77–99.

Sano, K., Morii, K., Sato, M., Mori, H., and Tanaka, R. (2000). Radiation-induced diffuse brain injury in the neonatal rat model—radiation-induced

apoptosis of oligodendrocytes. Neurol. Med. Chir. (Tokyo) *40*, 495–499, discussion 499–500.

Saxe, M.D., Battaglia, F., Wang, J.-W., Malleret, G., David, D.J., Monckton, J.E., Garcia, A.D., Sofroniew, M.V., Kandel, E.R., Santarelli, L., et al. (2006). Ablation of hippocampal neurogenesis impairs contextual fear conditioning and synaptic plasticity in the dentate gyrus. Proc. Natl. Acad. Sci. USA *103*, 17501–17506.

Schatz, J., Kramer, J.H., Ablin, A., and Matthay, K.K. (2000). Processing speed, working memory, and IQ: a developmental model of cognitive deficits following cranial radiation therapy. Neuropsychology *14*, 189–200.

Sun, Y., Xu, C.C., Li, J., Guan, X.Y., Gao, L., Ma, L.X., Li, R.X., Peng, Y.W., and Zhu, G.P. (2013). Transplantation of oligodendrocyte precursor cells improves locomotion deficits in rats with spinal cord irradiation injury. PLoS ONE *8*, e57534.

Tabar, V., and Studer, L. (2014). Pluripotent stem cells in regenerative medicine: challenges and recent progress. Nat. Rev. Genet. *15*, 82–92.

Tadesse, T., Gearing, M., Senitzer, D., Saxe, D., Brat, D.J., Bray, R., Gebel, H., Hill, C., Boulis, N., Riley, J., et al. (2014). Analysis of graft survival in a trial of stem cell transplant in ALS. Ann Clin Transl Neurol *1*, 900–908.

Uchida, N., Chen, K., Dohsa, M., Hansen, K.D., Dean, J., Buser, J.R., Riddle, A., Beardsley, D., Wan, Y., Gong, X., et al. (2012). Human neural stem cells induce functional myelination in mice with severe dysmyelination. Sci. Transl. Med. *4*, 155ra136.

Uh, J., Merchant, T.E., Li, Y., Feng, T., Gajjar, A., Ogg, R.J., and Hua, C. (2013). Differences in brainstem fiber tract response to radiation: a longitudinal diffusion tensor imaging study. Int. J. Radiat. Oncol. Biol. Phys. *86*, 292–297.

Van Dongen-Melman, J.E., De Groot, A., Van Dongen, J.J., Verhulst, F.C., and Hählen, K. (1997). Cranial irradiation is the major cause of learning problems in children treated for leukemia and lymphoma: a comparative study. Leukemia *11*, 1197–1200.

Vorhees, C.V., and Williams, M.T. (2006). Morris water maze: procedures for assessing spatial and related forms of learning and memory. Nat. Protoc. *1*, 848–858.

Wang, S., Bates, J., Li, X., Schanz, S., Chandler-Militello, D., Levine, C., Maherali, N., Studer, L., Hochedlinger, K., Windrem, M., and Goldman, S.A. (2013). Human iPSC-derived oligodendrocyte progenitor cells can myelinate and rescue a mouse model of congenital hypomyelination. Cell Stem Cell *12*, 252–264.

Windrem, M.S., Nunes, M.C., Rashbaum, W.K., Schwartz, T.H., Goodman, R.A., McKhann, G., 2nd, Roy, N.S., and Goldman, S.A. (2004). Fetal and adult human oligodendrocyte progenitor cell isolates myelinate the congenitally dysmyelinated brain. Nat. Med. *10*, 93–97.

Yabroff, K.R., Lawrence, W.F., Clauser, S., Davis, W.W., and Brown, M.L. (2004). Burden of illness in cancer survivors: findings from a population-based national sample. J. Natl. Cancer Inst. *96*, 1322–1330.

Cell Stem Cell
Clinical Progress

Sustained Mobilization of Endogenous Neural Progenitors Delays Disease Progression in a Transgenic Model of Huntington's Disease

Abdellatif Benraiss,[1,2,*] Michael J. Toner,[1,2] Qiwu Xu,[2,3] Elodie Bruel-Jungerman,[1,3] Eloise H. Rogers,[1] Fushun Wang,[2,3] Aris N. Economides,[4] Beverly L. Davidson,[5] Ryoichiro Kageyama,[6] Maiken Nedergaard,[2,3] and Steven A. Goldman[1,2,3,*]
[1]Department of Neurology
[2]Department of Neurosurgery
[3]Center for Translational Neuromedicine
University of Rochester Medical Center, Rochester, NY 14642, USA
[4]Regeneron Pharmaceuticals, Tarrytown, NY 10591, USA
[5]Department of Medicine, University of Iowa, Iowa City, IA 52242 USA
[6]Institute for Virus Research, Kyoto University, Shogoin-Kawahara, Sakyo-ku, Kyoto 606-8507, Japan
*Correspondence: abdellatif_benraiss@urmc.rochester.edu (A.B.), steven_goldman@urmc.rochester.edu (S.A.G.)
http://dx.doi.org/10.1016/j.stem.2013.04.014

SUMMARY

Huntington's disease (HD) is a neurodegenerative disease characterized in part by the loss of striatopallidal medium spiny projection neurons (MSNs). Expression of BDNF and noggin via intracerebroventricular (ICV) delivery in an adenoviral vector triggers the addition of new neurons to the neostriatum. In this study, we found that a single ICV injection of the adeno-associated viruses AAV4-BDNF and AAV4-noggin triggered the sustained recruitment of new MSNs in both wild-type and R6/2 mice, a model of HD. Mice treated with AAV4-BDNF/noggin or with BDNF and noggin proteins actively recruited subependymal progenitor cells to form new MSNs that matured and achieved circuit integration. Importantly, the AAV4-BDNF/noggin-treated R6/2 mice showed delayed deterioration of motor function and substantially increased survival. In addition, squirrel monkeys given ICV injections of adenoviral BDNF/noggin showed similar addition of striatal neurons. Induced neuronal addition may therefore represent a promising avenue for disease amelioration in HD.

INTRODUCTION

Huntington's disease (HD) is an autosomal-dominant neurodegenerative disorder characterized by progressive impairment of motor function and cognition and an invariably fatal outcome. HD is characterized by the progressive loss of both cortical and subcortical neurons, as most markedly reflected in the loss of striatal medium spiny neurons (MSNs) and consequent striatal atrophy. In previous studies in adult rodents, we found that new MSNs may be generated from resident subependymal neural stem cells by concurrent overexpression of BDNF and noggin (Benraiss et al., 2001; Chmielnicki et al., 2004). The newly generated MSNs established axonal projections to their normal targets in the globus pallidus and proved able to temporarily slow disease progression and extend life span in R6/2 mice, a murine model of HD (Cho et al., 2007). Yet these prior studies had demonstrated neither the functional integration of these new neurons nor their sustained therapeutic value. Furthermore, the practical therapeutic value of the adenoviral approach used for BDNF and noggin delivery was limited by the transient expression and immunogenicity of adenoviral vectors (Dai et al., 1995). To overcome these limitations, we used adeno-associated virus serotype 4 (AAV4), a vector that is neither immunogenic nor neurotoxic, to achieve sustained BDNF and noggin expression. Using two AAV4s constructed to overexpress BDNF and the ΔB2 mutein of noggin (Paine-Saunders et al., 2002), we found that their combined delivery resulted in the sustained ependymal overexpression of BDNF and noggin, which in turn led to persistent neuronal addition to the rat neostriatum for at least 4 months (Benraiss et al., 2012).

On the basis of these studies, in the present study we asked whether AAV4-BDNF and AAV4-noggin (AAV4-BDNF/noggin) coexpression might be used to drive the sustained addition of new MSNs to the neostriata of R6/2 huntingtin mutant mice. We found that bilateral intraventricular injections of AAV4-BDNF/noggin indeed triggered substantial and sustained MSN addition to the striata of R6/2 mice and that mice so treated exhibited a delay in disease progression, as manifested by both improved motor coordination and significantly extended life span. Furthermore, using inducible nestin-CreERT2/ROSA26/EYFP mice crossed to R6/2 mice and injected with a retrograde tracer to investigate the origin and connectivity of the newly generated neurons, we found that the cells expressed prototypic markers of mature MSNs and successfully extended projections to the globus pallidus. Using this model, we then assessed the electrophysiological properties of the newly generated neurons and found that they matured as typical MSNs, which were physiologically indistinguishable from resident striatal neurons. Thus, intraventricular delivery of AAV4-BDNF/noggin, and its associated induction of sustained striatal neuronal recruitment, may comprise a promising therapeutic treatment for HD.

RESULTS

AAV4 Drives Transgene Expression Limited to the Ventricular Wall of the Adult Forebrain

To achieve the long-term expression of BDNF and noggin in the brain, we used an AAV4-based transfer vector, based upon AAV4's predilection for ependymal cells within the adult brain (Liu et al., 2005). In normal adult mice, we first used immunofluorescence to identify AAV4-EGFP (AAV4-Null)-transduced cells 8 weeks after intracerebroventricular (ICV) viral injection. The GFP^+ cells were restricted to the ependymal wall of the lateral ventricle (Figure S1 available online), reproducing the expression pattern noted after ICV injection into adult rats (Benraiss et al., 2012). No parenchymal EGFP expression was noted, nor did we find any evidence of $EGFP^+$ cells in the olfactory bulb, suggesting that the neural stem cells of the subventricular zone (SVZ) were not transduced; rather, transgene expression appeared limited to the ependymal cell layer lining the ventricular lumen. Accordingly, immunostaining for BDNF protein revealed that BDNF overexpression in AAV4-BDNF/noggin-treated striata was both strong and largely limited to the ventricular lining (Figure S1).

To assess the levels of BDNF/noggin released into the CSF, 4-week-old mice received bilateral injections of either AAV4-BDNF/noggin, AAV4-Null, or saline (n = 6/group). Eight weeks later, the mice were sacrificed with CSF withdrawal via cisternal tap, and their BDNF and noggin levels were quantified by ELISA. Among the AAV4-BDNF/noggin-treated mice, CSF BDNF levels averaged 1 ± 0.1 ng/ml CSF (0.7 ± 0.05 ng/μg protein; mean ± SEM), while noggin achieved 8.4 ± 0.2 ng/ml CSF (6.2 ± 0.2 ng/μg protein; mean ± SEM). In contrast, neither BDNF nor noggin were detectable in the CSF of any AAV4-Null or saline-treated animals (Table S1). These data indicated that AAV4-mediated intracerebral delivery was sufficient to drive the sustained CSF production of BDNF and noggin in the adult mouse brain at levels previously demonstrated (Chmielnicki et al., 2004; Cho et al., 2007) to be sufficient for the induction of striatal neuronal addition.

AAV4-BDNF/Noggin-Treated R6/2 Mice Recruited New Striatal Neurons

We next asked if intraventricular injection of AAV4-BDNF/noggin was sufficient to induce the addition of new neurons in R6/2 mice. We gave bilateral ICV injections of AAV4-BDNF/noggin (n = 13), AAV4-EGFP (AAV4-Null, n = 16), or saline (n = 15) to 4-week-old R6/2 mice. The viral titer was adjusted to 1.3×10^{12} viral genomes (vg)/ml, and 1.5 μl of viral suspension containing 1.85×10^9 vg was then injected into each ventricle. Beginning 2 weeks after viral injection, all mice were given daily BrdU injections (75 mg/kg) for 4 weeks. The mice were then sacrificed 2 weeks after the last BrdU injection, at 12 weeks of age, to permit sufficient time for the maturation and integration of newly generated neurons. Immunostained cryosections of AAV4-BDNF/noggin-treated brains revealed striatal $BrdU^+$ neurons, which expressed the early neuronal markers doublecortin (Dcx) and ßIII-tubulin (TuJ1). In addition, many $BrdU^+$ striatal neurons coexpressed the mature neuronal antigens NeuN and DARPP-32, the latter indicating their maturation as MSNs (Figure 1).

Stereological analysis revealed that AAV4-BDNF/noggin-treated R6/2 mice harbored significantly more $Dcx^+/BrdU^+$ cells than either their AAV4-Null or saline-treated controls (228 ± 42.8, versus 43 ± 14.5 and 31 ± 9.2 $Dcx^+/BrdU^+$ cells/mm^3, respectively; mean ± SEM, $p < 0.001$ by one-way ANOVA with Bonferroni post hoc tests) (Figure 1A). Similarly, ßIII-tubulin/$BrdU^+$ neurons were found in significantly higher numbers in R6/2 mice treated with AAV4-BDNF/noggin compared to those treated with AAV4-Null or saline (AAV4-BDNF/noggin: 194 ± 30.8; AAV4-Null: 16 ± 7.0; saline: 5 ± 5.0 ßIII-tubulin+/$BrdU^+$ cells/mm^3; mean ± SEM; $p < 0.001$) (Figure 1B). Importantly, whereas small numbers of immature neurons were noted in the striata of AAV4-Null or saline-treated R6/2 mice, no newly generated neurons progressed to mature phenotype in these control mice. Thus, AAV4-BDNF/noggin-treated mice harbored significantly more $NeuN^+/BrdU^+$ striatal neurons than did their AAV4-Null or saline controls (58.5 ± 14.2 versus 0 ± 0 and 0 ± 0 $NeuN^+/BrdU^+$ cells/mm^3, respectively; mean ± SEM; $p < 0.01$) (Figure 1C). Similarly, $DARPP\text{-}32^+/BrdU^+$ neurons were found only in AAV4-BDNF/noggin-treated R6/2 mice, and not in their AAV4-Null or saline-treated R6/2 controls (53 ± 15.5, 0 ± 0, and 0 ± 0 $DARPP\text{-}32^+/BrdU^+$ cells/mm^3, respectively; mean ± SEM, $p < 0.01$) (Figure 1D and Table S2). It is worth noting that $Dcx^+/BrdU^+$ cells were much more abundant than $NeuN^+/BrdU^+$ or $DARPP\text{-}32^+/BrdU^+$ cells. This may be in part due to the expression of Dcx by glial progenitor cells (Sim et al., 2006; Tamura et al., 2007). More broadly though, our data suggest that not all newly generated neuroblasts survive to maturity in these mice, and the fraction of newly generated neurons that do so is a dynamic and regulated function of their exposure to BDNF and noggin.

We next asked whether treatment with AAV4-BDNF/noggin affected striatal neuronal number or morphometrics. To this end, AAV4-BDNF/noggin or AAV4-Null-treated R6/2 mice and their wild-type littermates (four groups; n = 7/group) were injected at 4 weeks and sacrificed at 12 weeks. Cryosections of their striata were immunostained for neuronal NeuN, and both $NeuN^+$ neuronal counts and striatal volumes were then stereologically estimated (Figure S2). No differences were noted in total striatal neuronal numbers across groups, including between our R6/2-105 CAG repeat mice and their wild-type controls, reflecting previous reports that R6/2-150 CAG mice undergo little if any striatal neuronal loss (Cho et al., 2007; Davies et al., 1997; Turmaine et al., 2000). In addition, no effect of AAV4-BDNF/noggin treatment was noted on the terminal neuronal counts of either R6/2 mice or their wild-type controls ($p > 0.05$, two-way ANOVA with Bonferroni post hoc tests) (Figure S2A). This was not surprising, given the relatively small fraction of the whole represented by the newly generated population, and the unclear fate of diseased resident neurons when joined by newly generated cells.

Despite their stable neuronal numbers, the R6/2-105 CAG mice used in this study exhibited significant striatal involution relative to their wild-type littermates; this too has previously been noted in R6/2-150 CAG mice (Cho et al., 2007; Davies et al., 1997; Turmaine et al., 2000). As a result, the AAV4-Null-treated R6/2 mice displayed higher neuronal densities than did their wild-type counterparts ($21.1 \times 10^4 \pm 1.9 \times 10^4$ versus $14.1 \times 10^4 \pm 1.1 \times 10^4$ neurons/mm^3, respectively; mean ± SEM, $p < 0.05$, two-way ANOVA with post hoc Bonferroni post

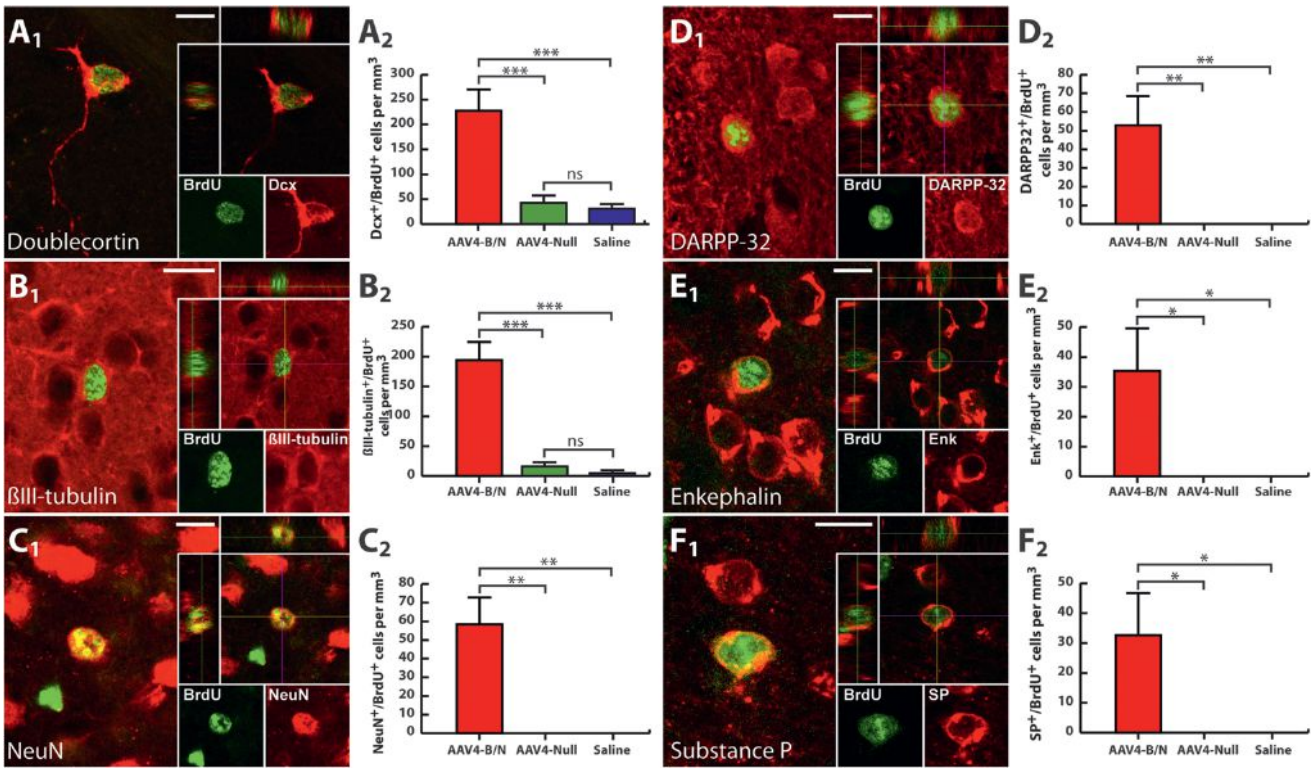

Figure 1. Newly Generated Neurons Mature into Medium Spiny Neurons

Striatal sections of AAV4-BDNF/noggin-treated R6/2 mice, sacrificed 8 weeks after viral injection. Sections were immunostained for BrdU (green) and one of the following neuronal markers: Doublecortin (A_1), βIII-tubulin/TuJ1 (B_1), NeuN (C_1), DARPP-32 (D_1), enkephalin (E_1), or substance P (F_1) (all in red). Double-immunolabeled cells were confirmed as such by confocal imaging, with orthogonal views in the x-z and y-z planes. Stereological counts of newly generated neurons defined by their expression of BrdU along with doublecortin (A_2), βIII-tubulin/TuJ1 (B_2), NeuN (C_2), DARPP-32 (D_2), enkephalin (E_2), or substance P (F_2). One-way ANOVA with Bonferroni post hoc tests; mean ± SEM. *$p < 0.05$, **$p < 0.01$, ***$p < 0.001$. Scale bar: 10 μm. See also Figure S1 and Tables S1 and S2.

test). The higher densities of the R6/2 mice appeared to be a product of neuronal atrophy and involution of the R6/2 neuropil, which yielded higher packing densities for surviving cells. Importantly, this higher density was reversed by AAV4-BDNF/noggin-treatment, such that the striatal neuronal densities of treated R6/2 mice did not significantly differ from those of the AAV4-Null-treated wild-type mice ($18.9 \times 10^4 \pm 1.8 \times 10^4$ versus $14.1 \times 10^4 \pm 1.1 \times 10^4$ neurons/mm^3, respectively; mean ± SEM, $p > 0.05$, one-way ANOVA with post hoc Bonferroni test) (Figure S2B).

Newly Generated MSNs Expressed Markers of Both Striatal Output Pathways

MSNs expressing substance P project to the globus pallidus interna (GPi) and comprise the direct output pathway of the basal ganglia. In contrast, enkephalin-expressing neurons project to the globus pallidus externa (GPe) and thereby comprise the indirect pathway. To determine the extent to which each of these MSN phenotypes were represented among AAV4-BDNF/noggin-induced striatal neurons, we immunostained sections of treated mice for BrdU together with either substance P or enkephalin. We found that new enkephalin$^+$/BrdU$^+$ and substance-P$^+$/BrdU$^+$ neurons were both abundant and roughly equally represented in AAV4-BDNF/noggin-treated R6/2 striata (35 ± 14.3 enkephalin$^+$/BrdU$^+$ and 33 ± 14.1 substance P$^+$/BrdU$^+$ cells/mm^3, respectively; mean ± SEM, $p < 0.05$ by one-way ANOVA with Bonferroni post hoc t test) (Figures 1E and 1F and Table S2). This neuropeptide expression data suggested that newly generated MSNs integrate into the direct and indirect striatal output pathways with roughly equal probability.

AAV4-BDNF/Noggin Treatment Delayed Disease Progression and Extended Survival

We next asked whether AAV4-BDNF/noggin administration and its associated induction of striatal neuronal replacement were associated with either an amelioration of disease or a delay in disease progression. To do so, we assessed the effects of treatment on both the motor performance and survival of R6/2 HD mice. The AAV4-BDNF/noggin-treated mice exhibited more sustained motor performance through at least the third month post-injection, relative to both AAV4-Null- and saline-treated controls. The two sets of controls did not significantly differ from one another at any time point (Figure 2A). ANOVA confirmed that the rate of deterioration of motor performance was significantly slowed by AAV4-BDNF/noggin treatment ($F [2,187] = 15.49$; $p < 0.0001$; two-way ANOVA with Bonferroni post hoc tests).

To assess the survival benefit of AAV4-BDNF/noggin administration, and inferentially of induced MSN addition, we next evaluated the effects of treatment upon the net life span of HD

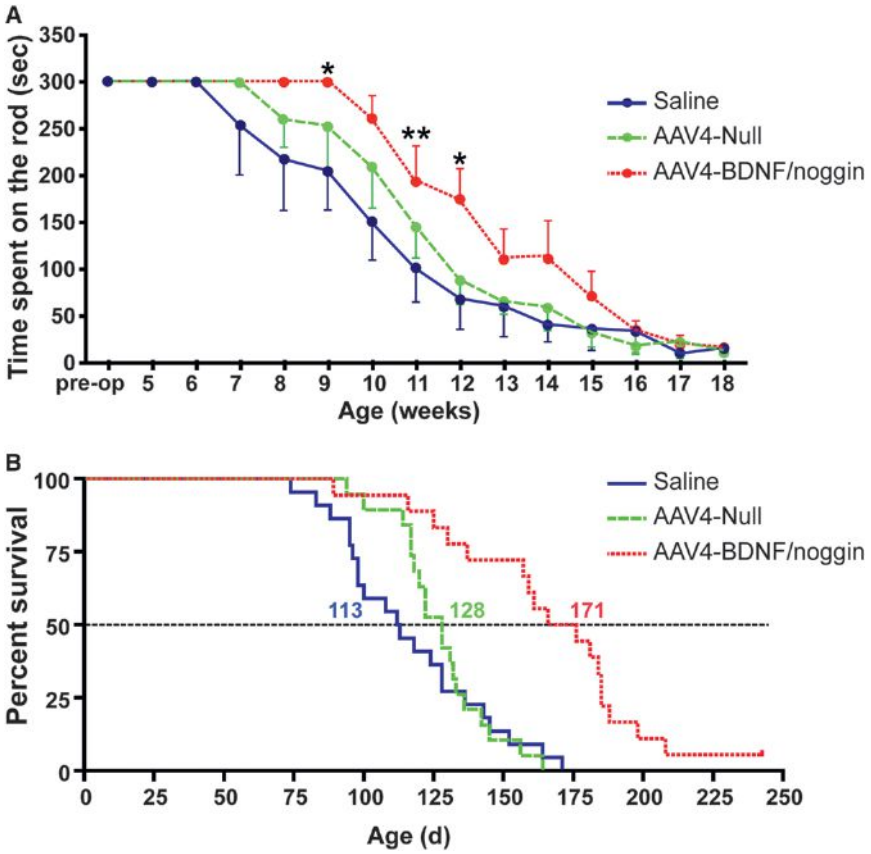

Figure 2. AAV4-BDNF/Noggin Treatment Delayed Motor Deficits and Extended Survival in R6/2 Mice

(A) AAV4-BDNF/noggin-treated R6/2 mice (n = 13) exhibited slower deterioration of motor performance than did AAV4-Null (n = 11) or saline-treated (n = 10) controls. (A) plots the duration of rotarod performance as a dual function of age and treatment, using a 14 rpm challenge. ANOVA of rotarod endurance versus weeks posttreatment confirmed that the rate of deterioration of motor performance was slowed significantly by AAV4-BDNF/noggin ($F [2,187] = 15.49$; $p < 0.0001$; two-way ANOVA with Bonferroni post hoc tests; mean ± SEM; $^*p < 0.05$, $^{**}p < 0.01$).

(B) This plot illustrates the survival curves of AAV4-BDNF/noggin-treated and untreated R6/2 mice. AAV4-BDNF/noggin (n = 18), AAV4-Null (n = 19), or saline-treated R6/2 mice (n = 21) were allowed to live among wild-type littermates. Kaplan-Meier survival analysis showed that the AAV4-BDNF/noggin-treated R6/2 mice lived a median of 171 days, while AAV4-Null-treated and saline controls survived only 128 and 113 days, respectively.

See also Figure S2.

transgenic mice. AAV4-BDNF/noggin (n = 18), AAV4-Null (n = 19), or saline (n = 21) injections were administered into the lateral ventricles of 4-week-old R6/2 mice (Figure 2B). AAV4-BDNF/noggin treatment significantly extended the survival of these mice, relative to the AAV4-Null or saline control animals; ANOVA with post hoc comparisons confirmed the difference in mean survival between AAV4-BDNF/noggin-treated R6/2 mice, AAV4-Null-treated mice, and saline controls (Log-rank test, $p < 0.0001$ for each). In contrast, no significant difference was noted in survival between the saline and AAV4-Null control groups (Log-rank test, $p = 0.69$). Thus, AAV4-BDNF/noggin treatment yielded both a slower rate of motor deterioration and substantially improved survival. Of note, treatment was not associated with any worsening of weight loss of R6/2 mice, which tends to occur as disease progress (Mangiarini et al., 1996). As such, we observed no significant difference in body weight that could be attributed to AAV4-BDNF/noggin treatment at the well-tolerated doses and transgene expression levels achieved in this study (age effect: $F[14,312] = 7.43$, $p < 0.0001$; treatment effect: $F[2,312] = 0.71$, $p > 0.05$; two-way ANOVA with Bonferroni post hoc tests; Figure S3).

Newly Generated MSNs Arise from Nestin-Expressing Subependymal Cells

To establish whether AAV4-BDNF/noggin-induced newly generated MSNs functionally integrate into the existing striatopallidal circuits, we asked whether these cells extend projection fibers to the globus pallidus. Specifically, we used a fate-tracking reporter mouse to establish the origin and fate of newly generated neurons. In brief, nestin-CreERT2/ROSA-EYFP mice (Imayoshi et al., 2006) express a Cre recombinase-estrogen receptor fusion protein under the control of the promoter and second intronic enhancer of nestin, which is expressed by neural stem cells and their immediate transit-amplifying progeny (Keyoung et al., 2001; Lendahl et al., 1990; Mignone et al., 2004; Zimmerman et al., 1994). Upon tamoxifen administration to adult mice, nestin-expressing cells begin to constitutively express the EYFP reporter, thereby permanently labeling both neural stem and progenitor cells and all of their progeny generated after the period of tamoxifen treatment (Figure S4).

Next, we then sought to specifically label newly generated neurons to characterize their connectivity and functional phenotype. To this end, 3-week-old nestin-CreERT2/ROSA-EYFP bigenic mice were treated with tamoxifen to activate nestin-driven Cre recombinase; the mice then received intraventricular injections of AAV4-BDNF/noggin and were examined 8 weeks later, to allow sufficient time for the migration and differentiation of newly generated neurons (Figure S5A). We found that BDNF/noggin overexpression resulted in the robust recruitment of new $EYFP^+$ striatal neurons, all presumably derived from nestin-expressing stem or progenitor cells. The $EYFP^+$ cells also coexpressed both NeuN and DARPP-32 (Figures 3A and 3C), indicating that newly generated MSNs are the progeny of nestin-expressing subependymal cells. Stereological analysis revealed that the striata of AAV4-BDNF/noggin-treated nestin-CreERT2/ROSA-EYFP mice harbored significantly more $EYFP^+/DARPP\text{-}32^+$ cells than did AAV4-Null controls (139 ± 40.3 versus 14.9 ± 4.5 $EYFP^+/DARPP\text{-}32^+$ cells/mm^3, respectively; mean ± SEM; $p < 0.05$) (Table S3).

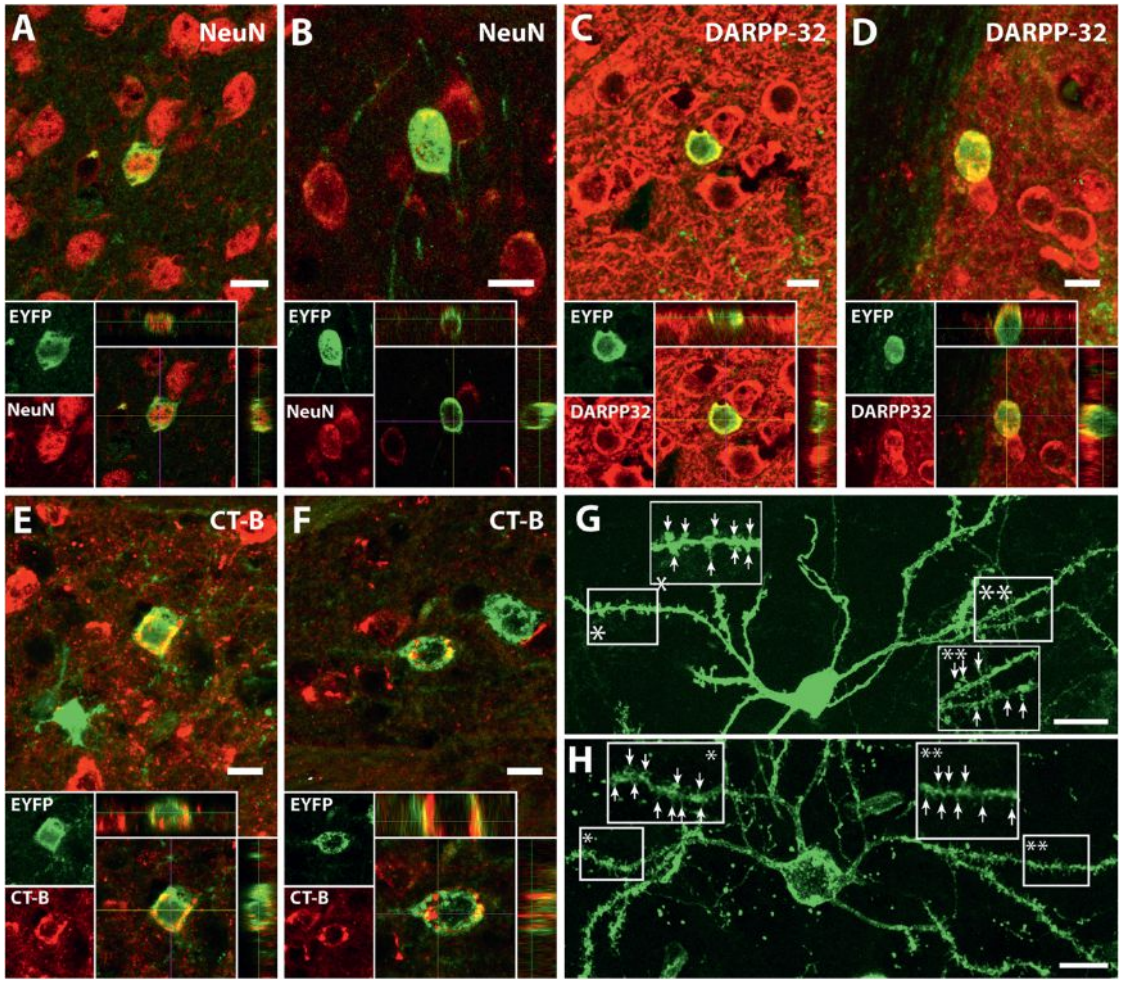

Figure 3. Fate-Mapping Reveals the Origin and Morphologies of BDNF/Noggin-Induced MSNs

Tamoxifen-induced nestin-CreERT2/ROSA-EYFP (A, C, and E) or nestin-CreERT2/ROSA-EYFP/R6/2 (B, D, and F) transgenic mice received bilateral, intraventricular injections of AAV4-BDNF/noggin at 4 weeks of age. Newly generated neurons expressed the mature and medium-spiny neuronal markers NeuN (A and B) and DARPP-32 (C and D), respectively. (E and F) New EFYP^{+} neurons also integrated into the striatopallidal circuitry as revealed by their incorporation of the retrograde tracer cholera toxin subunit B (CT-B; Alexa Fluor 555-conjugated) following receipt of intrapallidal injections. (G and H) To visualize the fine morphologies of AAV4-BDNF/noggin-induced MSNs, 3-week-old nestin-CreERT2/ROSA-mEGFP (membrane-targeted EGFP) mice were treated with tamoxifen for 5 days followed by intraventricular AAV4-BDNF/noggin. The mice were sacrificed 8 weeks later (see Figure S4 for design). The expression of mEGFP by new striatal neurons revealed their complex dendritic networks (G), which mimicked those of resident neurons expressing mEGFP following intrastriatal injection of Lenti-CMV-mEGFP (H). Arrows indicate dendritic spines. Scale bars: (A)–(F): 10 μm; (G) and (H): 20 μm. See also Figure S4 and Tables S3A and S3B.

Newly Generated MSNs Acquired Phenotypically Appropriate Dendritic Arbors

To investigate the morphology of newly generated striatal neurons, and to assess their acquisition of medium spiny neuronal phenotype, we used conditionally expressed membrane-linked EGFP (mEGFP) to visualize newly generated neurons and viral labeling to visualize existing resident neurons. Conditional targeting of newly generated neurons was done by crossing the nestin-CreERT2 to ROSA26-mEGFP mice; this reporter expresses mEGFP upon tamoxifen-triggered Cre-dependent removal of an upstream floxed-stop. This was followed by treatment with AAV4-BDNF/noggin, as described above in Figure S5A. In addition, in order to target preexisting neurons, 10-week-old wild-type mice received intrastriatal injections of lentivirus constitutively expressing the same membrane-tagged mEGFP reporter; the mice were sacrificed 2 weeks after viral injection. In both cases, striatal neurons could be identified by their expression of mEGFP-reported fluorescence, which revealed that newly generated neurons shared with their preexisting counterparts the prototypic morphologies of MSNs. We found that the dendritic spine morphologies and densities of new and preexisting resident neurons were indistinguishable from one another (Figures 3G and 3H). Statistical analysis did not reveal any difference in spine numbers on dendrites (11.7 ± 0.9 and 11.2 ± 0.5 spines/10 μm dendritic length, for newly generated and preexisting neurons, respectively; mean ± SEM; n = 7 neurons each; $p > 0.5$, $t = 0.55$). Thus, newly generated neurons are morphologically indistinguishable from preexisting MSNs, in both their gross morphology and dendritic spine densities.

Newly Generated MSNs in the R6/2 Mice Arise from SVZ Nestin$^+$ Cells

Having demonstrated the origins and maturation of newly generated MSNs in wild-type nestin-CreERT2/ROSA-EYFP reporter mice, we next asked whether these mice could be crossed to R6/2 mice to allow the tracking of newly generated neurons in the adult diseased brain. We found that the resultant triple transgenic mice, after receiving a 10 day regimen of tamoxifen beginning at 3 weeks of age and injected with AAV4-BDNF/noggin (n = 4) or AAV4-Null (n = 3) at 4 weeks of age, exhibited the robust neostriatal addition of tagged neurons when assessed at 12 weeks of age. In particular, the AAV4-BDNF/noggin-treated triple transgenic mice showed substantial recruitment of new EYFP$^+$ MSNs, as evidenced by their coexpression of EYFP together with either NeuN or DARPP-32 (Figures 3B and 3D). Importantly, AAV4-BDNF/noggin-associated neuronal addition was at least as pronounced in nestin-CreERT2/ROSA-EYFP/R6/2 trigenic mice as in healthy wild-type nestin-CreERT2/ROSA-EYFP controls (212.6 ± 60.8 EYFP$^+$/DARPP-32$^+$ versus 139 ± 40.2 cells/mm^3, respectively; mean ± SEM; $p < 0.05$). Statistical analysis confirmed the significant effect of AAV4-BDNF/noggin in inducing neuronal addition and that R6/2 mice exhibited this effect as strongly as their wild-type counterparts (treatment effect: $F [1,8] = 23.70$, $p < 0.01$; genotype effect: $F [1,8] = 2.11$, $p > 0.05$; two-way ANOVA with Bonferroni post hoc tests) (Table S3). Of note, we reproducibly detected evidence of neuronal addition in AAV4-Null R6/2 mice, which exhibited 48.5 ± 10.7 EYFP$^+$/DARPP-32$^+$ cells/mm^3 (mean ± SEM; Table S3); this appeared to reflect an element of compensatory neuronal addition in the HD environment, as we have previously noted in adenoviral Null-treated R6/2 mice (Cho et al., 2007), and which has been similarly reported in human autopsy samples (Curtis et al., 2003).

Newly Generated MSNs Extend Axonal Projections to the Globus Pallidus

In previous studies, we noted that newly generated MSNs recruited in response to adenoviral BDNF and noggin overexpression can extend projections to their pallidal targets. To confirm that AAV4-BDNF/noggin-induced neurons similarly develop pallidal axonal projections, virally treated bigenic nestin-CreERT2/ROSA-EYFP and trigenic nestin-CreERT2/ROSA-EYFP/R6/2 mice (n = 4 each) were all given intrapallidal injections of a retrograde tracer, Alexa Fluor 555-conjugated cholera toxin subunit B (CT-B), 1 week before their sacrifice at 12 weeks of age (Figures S5A and S5B). Many newly generated EYFP$^+$ neurons incorporated the CT-B retrograde tracer after receiving intrapallidal injections, indicative of their successful projection to the globus pallidus, as typical of medium spiny phenotype (Figures 3E and 3F). To rule out any labeling of striatal MSNs by diffusion of the tracer rather than a retrograde incorporation, we also stained for choline acetyltransferase (ChAT), a marker for cholinergic nonprojecting striatal interneurons. Confocal analysis showed no CT-B accumulation within the cell bodies of ChAT-immunoreactive neurons of the striatum, underscoring the lack of diffusion of the tracer from the site of injection (Figure S5C).

New Striatal Neurons Mature as Physiologically Active Projection Neurons

To investigate the ability of newly generated neurons to functionally integrate into the striatopallidal circuitry, we next asked if they developed afferent synaptic input and were competent to generate action potentials. To this end, we performed whole-cell electrophysiological recording. Due to the attenuated visibility of EYFP within live tissue, we crossed the nestin-CreER^{T2} mice with a ROSA-CAG-EYFP reporter mouse in which the EYFP is directed by the relatively strong CAG (chicken β-actin) promoter; this yields more intense EYFP expression upon removal of the floxed stop (Madisen et al., 2010). Three-week-old nestin-CreERT2/ROSA-CAG-EYFP mice received daily tamoxifen injections for 5 days; 2 days later, and at 4 weeks of age, an osmotic micropump that continuously infused BDNF and noggin protein over the ensuing 14 days through the end of their sixth week of age was implanted into the lateral ventricle. One week later, the mice were given an intrapallidal injection of Alexa Fluor 594-conjugated CT-B as a retrograde tracer in order for us to identify those new neurons that successfully integrated into the striatopallidal circuitry. The mice were then sacrificed at 8 weeks of age, and two-photon-assisted patch-clamp recordings were performed on 300 μm coronal vibratome sections, as described (Bekar et al., 2008; Kang et al., 1998) (Figure 4A). New projection neurons (EYFP$^+$) that incorporated the red fluorescent tracer (CT-B$^+$) were subjected to whole patch-clamp in current-clamped configuration, and their responses to increased current steps were recorded and compared to that of CT-B$^+$/EYFP$^-$ single-labeled or unlabeled resident striatal neurons. We found that newly generated striatopallidal projection neurons (EYFP$^+$/CT-B$^+$ neurons; n = 4) exhibited electrophysiological characteristics analogous to those of existing MSNs that had similarly incorporated the retrograde tracer (EYFP$^-$/CT-B$^+$; n = 5) and to unlabeled striatal neurons defined only by their morphology (n = 10) (Figures 4B and 4C). Analysis of the resting membrane potential, the frequency of action potentials, and the maximal amplitude of action potentials revealed no significant differences among the three different groups of cells recorded in 8-week-old wild-type mice (Figure 4D and Table S4). Thus, the newly generated MSNs developed functional striatopallidal projections and exhibited electrophysiological responses analogous to those of preexisting resident MSNs.

Newly Generated Neurons in R6/2 HD Mice Integrate As Functional Striatopallidal Neurons

To assess the functional integration as evidenced by the electrophysiological competence of newly generated neurons in HD mice, nestin-CreERT2/ROSA-EYFP mice were crossed with R6/2 mice. These mice were then subjected to the same experimental paradigm as their bigenic wild-type counterparts (Figure 4A). As with the wild-type mice, electrophysiological recordings of newly generated EYFP$^+$/CT-B$^+$ neurons that successfully extended pallidal projections (n = 6 recorded) were compared both to neurons that had incorporated the retrograde tracer (EYFP$^-$/CT-B$^+$; n = 4) and to unlabeled neurons (EYFP$^-$/CTB$^-$; n = 7). The resting membrane potential, as well as the action potential thresholds and maximal amplitudes thereof, were similar in R6/2 and wild-type mice. Interestingly though, the newly generated EYFP$^+$/CT-B$^+$ neurons of R6/2 mice

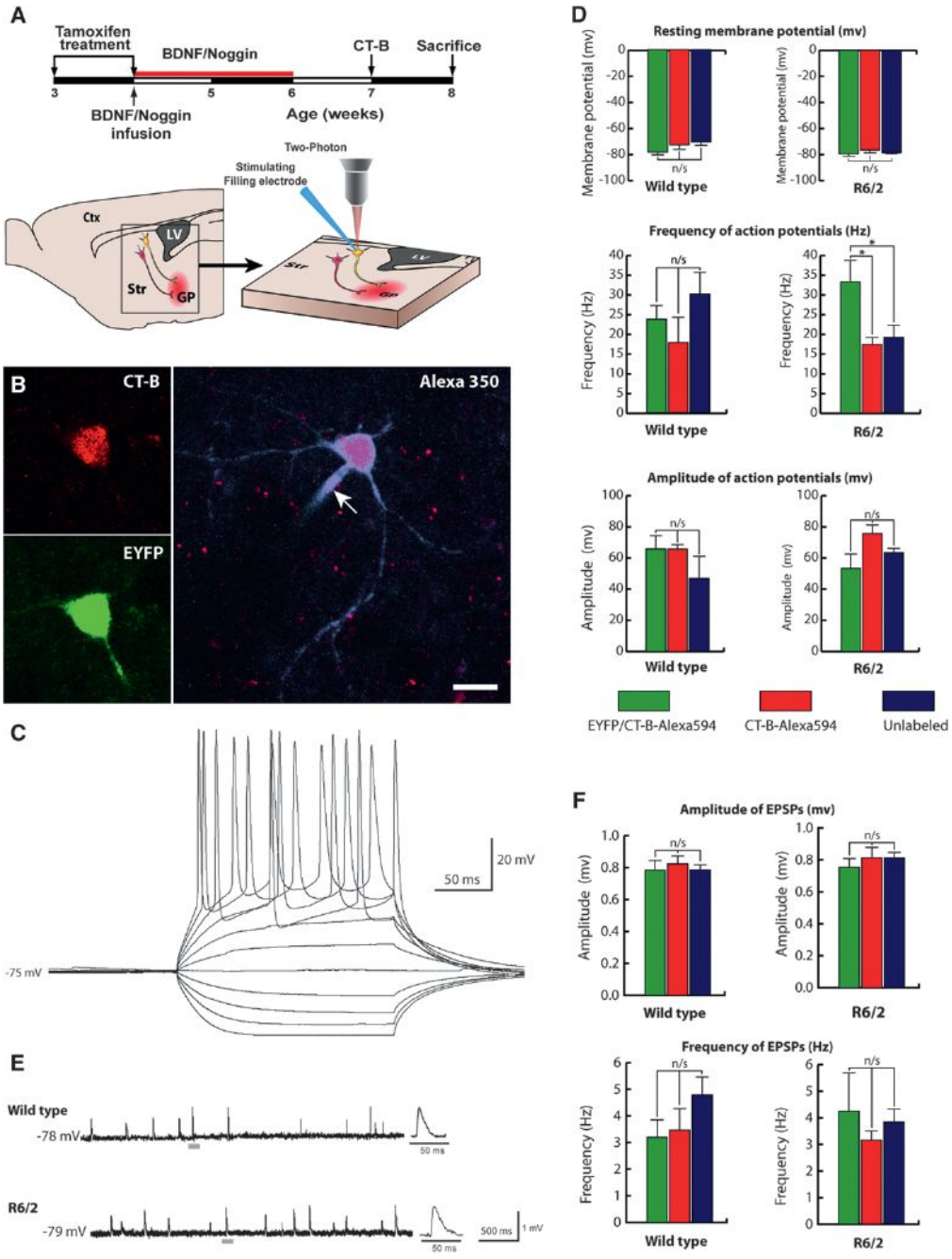

Figure 4. BDNF/Noggin-Induced MSNs Functionally Integrate into the R6/2 Striatum

(A) Experimental design: 4-week-old tamoxifen-pretreated nestin-CreER^{T2}/ROSA26-CAG-EYFP (wild-type) or nestin-CreERT2/ROSA-CAG-EYFP/R6/2 (R6/2) mice were given 2 week intraventricular infusions of BDNF and noggin proteins, followed 1 week later by intrapallidal injection of the retrograde tracer Alexa Fluor 594-conjugated CT-B. (B) Example of EYFP$^+$/CT-B$^+$ double-labeled neuron targeted for recording of field potentials. Arrow indicates the pipette used for whole-cell patch-clamp recording and filled with Alexa Fluor 350 for subsequent confirmation of the analyzed cells. (C) Representative action potentials recorded from a newly generated neuron (EYFP$^+$/CT-B$^+$) that had incorporated the retrograde cholera toxin-B tracer. (D) Comparisons of membrane potential, firing frequency, and amplitude in all three categories of recorded striatal neurons, in both wild-type and R6/2 mice. One-way ANOVA with Bonferroni post hoc t tests; mean ± SEM; n/s, not significant; *$p < 0.05$. (E) Excitatory postsynaptic potentials (EPSPs) were also recorded on patched neurons of both wild-type and R6/2 mice. (F) No significant differences were noted in the amplitude or frequency of EPSPs of newly recruited neurons (EYFP$^+$/CT-B$^+$), when they were compared to either preexisting MSNs that incorporated the retrograde tracer (EYFP$^-$/CT-B$^+$) or resident unlabeled neurons. One-way ANOVA with Bonferroni post hoc t tests; mean ± SEM; n/s, not significant; *$p < 0.05$. Scale bar: (B), 10 μm. See also Figure S3 and Tables S4A and S4B.

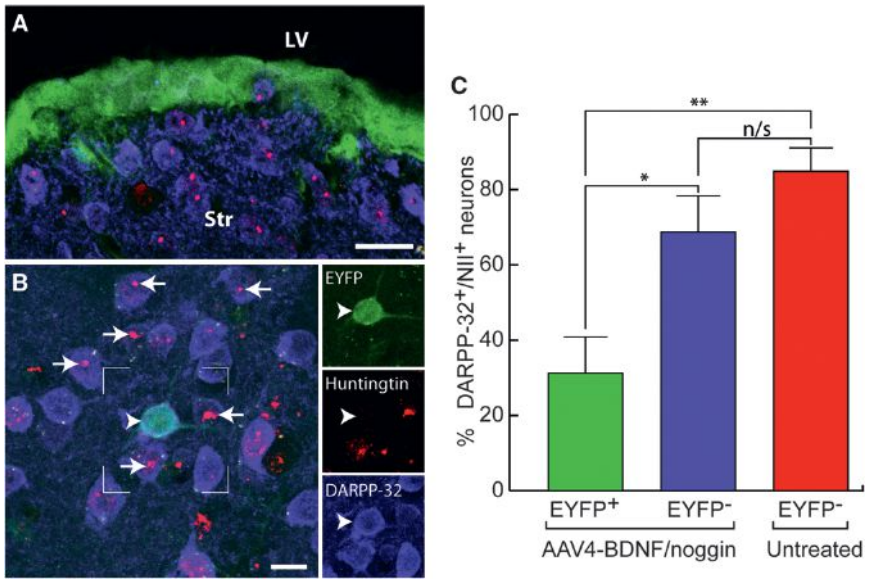

Figure 5. Newly Recruited MSNs Have Reduced Neuronal Intranuclear Inclusions

Serial brain sections from a 12-week-old tamoxifen- and AAV4-BDNF/noggin-treated nestin-CreERT2/ROSA-EYFP/R6/2 mouse were immunostained with anti-huntingtin EM48 antibodies (red), identifying neuronal intranuclear inclusions, and DARPP-32 (blue) and EYFP (green). (A) Inclusions were absent from *nestin*-EYFP$^+$ progenitor cells of the subventricular zone. Str, neostriatum; LV, lateral ventricle. (B) New neurons (arrows), arising from the SVZ, do not initially harbor nuclear inclusions (arrowhead). (C) Stereological counts of neuronal intranuclear inclusions (NII) showed that less than one-third of newly generated neurons harbored NII when assessed, whereas over two-thirds of EYFP$^-$ stable MSNs did so, whether in AAV4-BDNF/noggin-treated or untreated R6/2 mice. One-way ANOVA with Bonferroni post hoc tests; mean ± SEM; *$p < 0.05$, **$p < 0.01$. Scale bars: (A), 25 μm; (B), 10 μm. See also Figure S4.

exhibited a significantly higher frequency of action potentials during current injection than did preexisting (EYFP$^-$/CT-B$^\pm$) neurons (33.3 ± 5.4 Hz for EYFP$^+$/CT-B$^+$ neurons, versus 17.5 ± 1.7 Hz and 19.3 ± 3.0 Hz for EYFP$^-$/CT-B$^+$ and unlabeled neurons, respectively; mean ± SEM; $p < 0.05$ by one-way ANOVA with Bonferroni post hoc tests) (Figure 4D and Table S4A). Since we noted no such difference in action potential frequency between newly generated and preexisting MSNs in wild-type mice, it would seem unlikely that this is either a fundamental distinction of newly generated adult neurons or a function of their relative immaturity. Rather, these data suggest that the higher action potential frequency among the recorded new neurons may reflect some difference in their membrane properties compared to those of established resident neurons of the R6/2 striatum, even at this relatively early 8 week time point. Together, these data indicate that BDNF/noggin-induced, newly generated striatopallidal neurons extended axons to the globus pallidus and were fully capable of generating trains of action potentials in both wild-type and R6/2 mice.

To further establish whether AAV4-BDNF/noggin-recruited new neurons fully integrated in the R6/2 brain, we next asked if they received afferent input. We found that adult-generated EYFP$^+$/CT-B$^+$ striatopallidal neurons indeed exhibited excitatory postsynaptic potentials (EPSPs) and that they did so in both wild-type and R6/2 mice. In both the wild-type and R6/2 mice, the EPSPs of newly generated EYFP$^+$/CT-B$^+$ neurons were indistinguishable from those of both EYFP$^-$/CT-B$^+$ and unlabeled stable resident striatal neurons (Figures 4E and 4F and Table S4B). These observations suggest that the excitatory synaptic input to newly generated MSNs is indistinguishable from that of resident MSNs and further confirm that these new neurons effectively integrate into the existing striatopallidal circuitry.

Newly Generated Striatal Neurons in Adult R6/2 Mice Contain Fewer Intranuclear Inclusions

Neuronal intranuclear inclusions (NIIs) are aggregates of mutant huntingtin, the abundance of which correlates with cellular atrophy and death in HD (Bates, 2003; Becher et al., 1998; Hickey and Chesselet, 2003). Using an antibody (EM48) that recognizes the N-terminal portion of huntingtin protein, NIIs were first visualized in both the striatum and cortex of R6/2 mice at 3.5 weeks of age (Meade et al., 2002). This finding suggests that NIIs are not present at birth in R6/2 mice and instead only appear after a period of postnatal differentiation. This was similarly evident within the young neuronal progeny of SVZ neural stem cells, in which we noted an absence of nuclear inclusions (Figure 5A). Since newly generated neurons arise from mitotic SVZ progenitors, and since mutant huntingtin preferentially accumulates as a function of postmitotic cellular age (Gutekunst et al., 2002), we postulated that new neurons might arise without preexisting NIIs. To test this hypothesis, serial brain sections from tamoxifen-pretreated AAV4-BDNF/noggin-treated nestin-CreERT2/ROSA-EYFP/R6/2 mice were immunostained with EM48 antibody (see Figure S5A for design). Stereological analysis showed that newly generated MSNs, coexpressing DARPP-32 and EYFP, contained significantly fewer EM48$^+$ NIIs than did stable EYFP$^-$/DARPP-32$^+$ resident neurons in the same animals (31.0% ± 9.6% versus 68.7% ± 9.6%, respectively; mean ± SEM; $p < 0.05$ by one-way ANOVA with Bonferroni tests; Figures 5B and 5C). Indeed, less than one-third of adult-generated striatal neurons contained inclusions by 12 weeks, a time point by which over two-thirds of resident neurons had already developed inclusion pathology. Thus, BDNF/noggin-induced adult-generated MSNs first developed intranuclear inclusions only after several months of postmitotic ontogeny, suggesting the relative (if transient) protection of newly generated neurons from mutant huntingtin-associated pathology.

New Neurons Can Be Generated in the Neostriatum of the Adult Squirrel Monkey

The ability of AAV4-BDNF/noggin treatment to induce and sustain the addition of new neurons to the HD neostriatum, and to extend both motor performance and survival in affected mice, suggested the potential for using this strategy as a

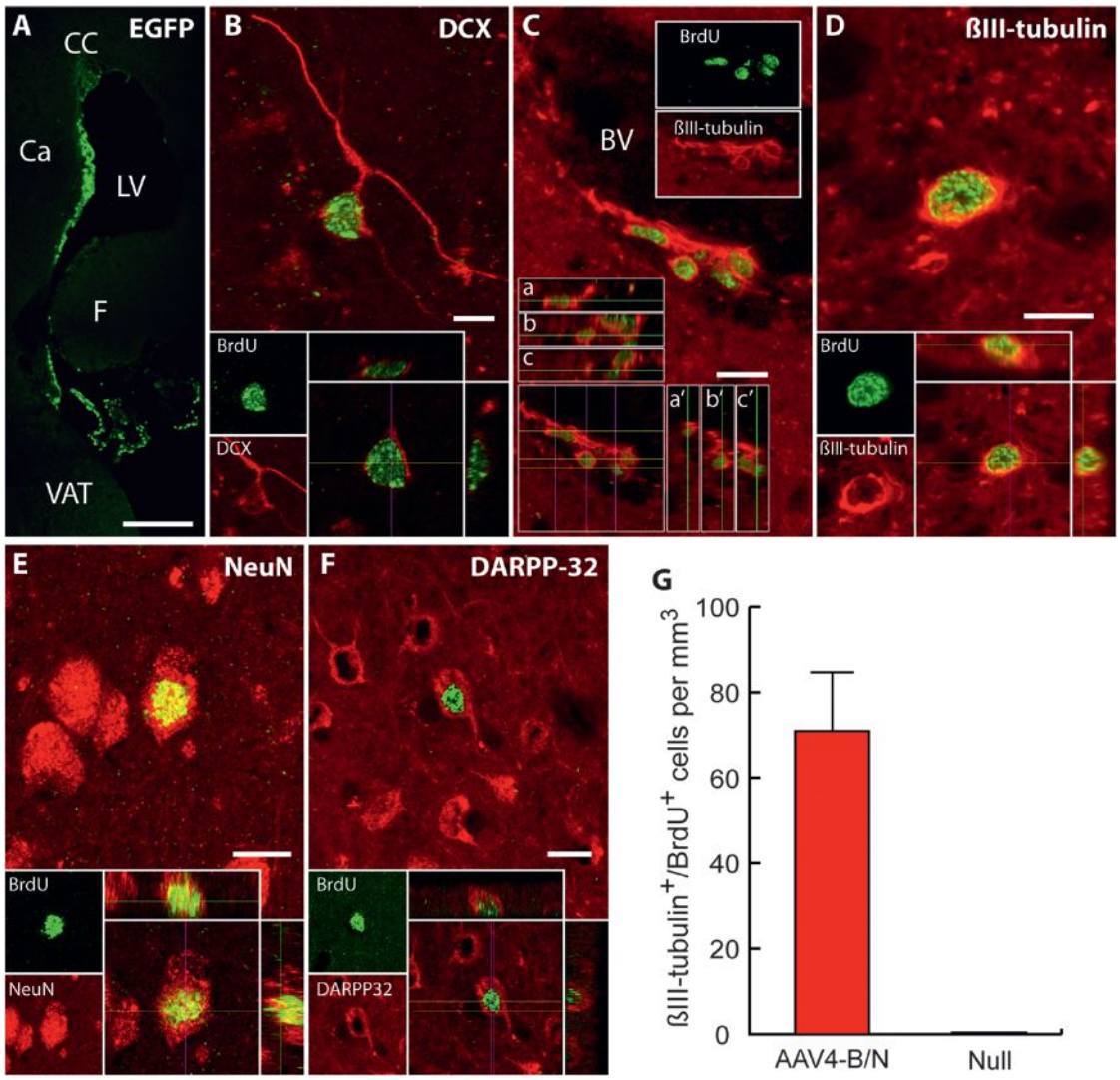

Figure 6. Adenoviral BDNF/Noggin Triggered Neuronal Addition to the Adult Monkey Striatum

(A) Sections of a squirrel monkey brain, from an animal killed 8 weeks after intraventricular injection of adenoviral EGFP, revealed EGFP expression limited to the ependymal cell layer of the lateral ventricle; no parenchymal expression of EGFP was noted.

(B–F) Striatal sections of an AdBDNF/Adnoggin-treated monkey were coimmunolabeled for BrdU (green) together with the neuronal markers Dcx (B), ßIII-tubulin (C and D), NeuN (E), and DARPP-32 (F) (red). In (C), many $BrdU^+$ apparent neuronal migrants were found abutting the adluminal surfaces of striatal blood vessels.

(G) Newly generated $ßIII\text{-}tubulin^+$ neurons, identified by their incorporation of BrdU, were abundant yet limited to the striata of AdBDNF/noggin-treated animals (mean ± SEM). No evidence of striatal neurogenesis was noted in AdNull-treated controls.

LV, lateral ventricle; F, fimbria; Ca, Caudate; Cc, corpus callosum; VAT, ventral anterior thalamus. Scale bars: (A): 500 μm, (C): 50 μm, (B), (D), (E), and (F): 10 μm. See also Figure S5.

treatment approach in clinical HD. On that basis, we next asked whether nonhuman primates might also have sufficient numbers of accessible subependymal progenitors to similarly respond to BDNF and noggin with heterotopic striatal neuronal addition (Bedard et al., 2005). To that end, we injected adult squirrel monkeys with adenoviral overexpression vectors for BDNF and noggin. We used adenovirus rather than AAV for this small study so as to maximize the levels of CSF BDNF and noggin; our question here was whether we could induce significant striatal neuronal addition in primates, as opposed to whether we could sustain it for maximal therapeutic benefit.

To transduce adult monkeys to overexpress ventricular BDNF and noggin, we used CT (computed tomography) guidance to deliver either an AdBDNF/AdNoggin mixture (20 μl/injection, containing AdBDNF 1.73×10^{13} particles/ml and AdNoggin 1.9×10^{13} particles/ml, 1:1) or AdEGFP (AdNull, in similar volume and titer) into each lateral ventricle (n = 3 monkeys). Beginning 1 week later, the animals received BrdU injections (75 mg/kg) for 15 days. Eight weeks after the viral injection, the monkeys were sacrificed and their brains were processed for histology. Control animals injected with AdNull (n = 3) showed marked expression in the ependymal walls of the lateral ventricles (Figure 6A). In AdBDNF/noggin-treated animals, CSF BDNF was

measured by ELISA at 820.7 ± 120 pg/ml CSF (0.95 ± 0.2 pg/μg protein; mean ± SEM), while noggin measured 1.1 ± 0.2 ng/ml (0.8 ± 0.05 pg/μg protein; mean ± SEM). These levels are within the dose range appropriate for eliciting BDNF-induced striatal neurogenesis, as we have previously shown in rodents (Chmielnicki et al., 2004).

In the AdBDNF/noggin-treated monkey striata, confocal microscopy demonstrated abundant BrdU-incorporating neurons; these newly generated neurons coexpressed Dcx, ßIII-tubulin, NeuN, and/or DARPP-32, and colabeling for each marker was confirmed as such by confocal imaging with orthogonal views (Figures 6B–6F). Many $BrdU^+/Dcx^+$ and $BrdU^+/\beta III\text{-}tubulin^+$ cells in particular were noted as apparent migrants along striatal blood vessels (Figures 6B and 6C). Importantly, $BrdU^+$ neurons were found only in the striata of AdBDNF/noggin-treated animals (70.9 ± 13.7 $ßIII\text{-}tubulin^+/BrdU^+$ cells/mm^3 mean ± SEM); no $BrdU^+$ neurons were noted in any AdNull-treated monkey striata (Figure 6G). Thus AdBDNF/noggin stimulated the addition of new cells that expressed antigenic markers of both migrating neuroblasts and mature MSNs, thereby highlighting the potential use of BDNF/noggin-induced striatal neurogenesis as a therapeutic strategy for HD.

DISCUSSION

In this study, we found that the intraventricular delivery of AAV4-BDNF and AAV4-noggin was sufficient to induce and sustain striatal neuronal recruitment from endogenous neural progenitor cells in R6/2 huntingtin mutant mice, that the newly generated neurons developed as MSNs and became both anatomically and functionally integrated into striatopallidal circuits, and that their production slowed disease progression and extended the survival of these HD mice. The newly generated neurons included both enkephalin and substance-P-expressing cells, which define neurons of the indirect and direct striatofugal pathways, respectively; these were added in roughly equal proportions, suggesting the reconstitution of each major pool of striatal projection neurons. By fate-mapping subependymal neural stem and progenitor cells using nestin-$CreER^{T2}$/ROSA26/EYFP bigenic and nestin-CreERT2/ROSA-EYFP/R6/2 trigenic mice, we then confirmed that the newly generated MSNs arose from nestin-derived progeny in both wild-type and HD mice. By combining this strategy with intrapallidal injection of a retrograde tracer, and then using two-photon microscopy of striatal slices to identify adult-generated striatopallidal neurons for patch-clamp analysis, we further confirmed that AAV4-BDNF/noggin-induced nestin-CreERT2/ROSA-EYFP-tagged neurons successfully extended projections to the globus pallidus and functionally integrated into the existing striatopallidal circuitry. On the basis of these findings, we then assessed the utility of this strategy in mediating neuronal addition to the adult primate striatum, using adenoviral delivery to overexpress BDNF and noggin in the ventricular walls of adult squirrel monkeys. We found that just as in mice, monkeys harbor a progenitor population able to respond to local noggin and BDNF overexpression with heterotopic neuronal addition to the normal adult neostriatum.

AAV4 proved an appropriate and effective long-term expression vector, with widespread yet phenotype-specific ependymal transduction in both wild-type and R6/2 mice, as previously noted in other systems (Benraiss and Goldman, 2011; Benraiss et al., 2012; Davidson et al., 2000; Dodge et al., 2010; Liu et al., 2005). Importantly, AAV4's restricted tropism toward ependymal cells permitted the sustained exposure of subependymal neural stem cells and their progeny to BDNF and noggin, without themselves being directly transduced. This exquisite phenotypic and regional specificity proved critical; indeed, we have observed that neuronal recruitment to the olfactory bulb falls when BDNF expression vectors are injected directly into the subependyma (data not shown), an approach that transduces the progenitors themselves to overexpress the transgenes of interest (Henry et al., 2007; Reumers et al., 2008). The distinct results achieved using ependymal versus subependymal transduction by BDNF expression vectors suggests that such autocrine expression may have very different effects on neural stem and progenitor cell fate than the transient "next-door neighbor" exposure provided by ependymal transduction.

To directly visualize those neurons generated in response to BDNF and noggin, we used tamoxifen-inducible nestin-CreERT2/ROSA-EYFP reporter mice to label subependymal neural stem and progenitor cells and their progeny; these mice exhibit permanent reporter gene expression by all cells derived from those cells that were nestin-expressing at the time of tamoxifen exposure. As such, they allow the specific identification, lineage tracing, and anatomical tracking of those neurons newly generated in adulthood. By inducing Cre recombination and then treating with BDNF and noggin (delivered by AAV4, as well as proteins in separate experiments using osmotic minipump), we found that newly generated striatal $EYFP^+$ neurons coexpressed a combination of markers that typify MSNs, including βIII-tubulin, NeuN, and DARPP-32. Thus, our nestin-CreERT2/ROSA-EYFP/R6/2 trigenic HD reporter mice confirmed that BDNF and noggin treatment induced the striatal recruitment of new neurons from nestin-expressing neural stem and progenitor cells.

Our functional data suggest that these newly added neurons may be able to functionally complement those lost in HD. In particular, our electrophysiological analysis of newly generated $EYFP^+$ MSNs in both 60-day-old wild-type and R6/2 mice revealed that these new projection neurons were functionally competent and integrated, receiving afferent input as well as generating both spontaneous and stimulus-evoked trains of action potentials. Interestingly, previous studies have similarly shown that MSNs of presymptomatic HD mouse models—including R6/2—have electrophysiological profiles identical to wild-type mice, although they diverge at terminal stages of the disease (90 days) (André et al., 2011; Klapstein et al., 2001). Our analysis confirmed that the electrophysiological properties and network integration of existing unlabeled MSNs at 60 days were comparable in wild-type and R6/2 mice. In addition, the identification of striatal nestin-$EYFP^+$ MSNs backfilled by CT-B injected into the globus pallidus also enabled us to compare the electrophysiological properties of newly generated neurons with those of their preexisting, stably resident counterparts. This analysis suggested that newly generated MSNs in both wild-type and R6/2 mice received functional inputs—as reflected in their EPSPs—and generated action potentials in a manner virtually indistinguishable from that of existing MSNs.

In this study, we only used R6/2 mice with 105 ± 5 CAG repeats, which we verified in all mice using PCR across the repeat region. In these mice, symptom onset begins as early as 8–9 weeks; by 12 weeks, affected mice manifest a resting tremor and ataxia, startle myoclonus, and seizures, and they typically die by 16–17 weeks of age. In contrast, our AAV4-BDNF/noggin-treated mice just began to exhibit deteriorating motor skills by that age, and lived an average of 33.5% longer than did their controls, with outliers living as long as twice the maximal life span of any controls. The survival advantage associated with induced neuronal production may be limited by the effective functional life span of the newly generated neurons, which also express the polyglutamine expansion of mutant huntingtin. Yet our data indicate that subependymal progenitors do not express neuronal intranuclear inclusions and that newly generated neurons only slowly accumulate these markers of cytopathology. Thus, whereas most resident MSNs manifested pronounced intranuclear inclusions by 12 weeks of age, less than one-third of newly generated neurons did so by that point (Figure 5). These observations suggest that newly generated neurons have a discrete window of time during which they may functionally integrate and compensate for impaired resident neurons before they themselves succumb to HD pathology. This in turn suggests the potential utility of a long-lasting and/or repetitive induction of striatal neuronal addition as a means of long-term disease management. This may be accomplished through the use of long-term expression vectors, such as AAV4, or by the intermittent delivery of BDNF and noggin proteins; in this paper, we have reported examples of both delivery strategies, each of which effectively stimulated neuronal recruitment.

Thus, the sustained AAV4-mediated delivery of BDNF and noggin to the adult R6/2 brain was associated with both enhanced neurogenesis and delayed disease progression. The neurons generated from this approach arose from subependymal progenitors and extended axons to their normal developmental targets, achieving electrophysiological network integration and compensating for the function of neurons lost to the disease process. The extended functional competence and survival of the AAV4-BDNF/noggin-treated R6/2 mice thus presents a unique example of induced compensatory neuronal replacement as a means of treating an adult neurodegenerative disorder. R6/2 is but a single model, though, which manifests only mutant exon 1 expression and may then recapitulate HD pathology differently than do full-length mutant huntingtin models. Clinical translation of this approach thus demands its validation in other models of HD and, in particular, in transgenic models of full-length mutant huntingtin (Gray et al., 2008; Southwell et al., 2013; Yu-Taeger et al., 2012), especially those with shorter, more clinically representative CAG repeat expansions than the 105 CAG repeats borne by the R6/2 mice used in our present study. Nonetheless, given the persistence of competent neural stem and progenitor cells in the adult human brain (Kirschenbaum et al., 1994; Pincus et al., 1998; Sanai et al., 2004), and the apparent responsiveness to BDNF and noggin of these progenitors in the adult nonhuman primate brain (Figure 6), paired with the favorable safety profile of AAV vectors in several human clinical trials (Christine et al., 2009; LeWitt et al., 2011; Mueller and Flotte, 2008), we believe that our data suggest the feasibility of induced striatal neuronal addition as a viable therapeutic strategy for HD.

EXPERIMENTAL PROCEDURES

Animals and Viral Injection

This study was approved by the University Committee on Animal Resources of the University of Rochester. Wild-type females with ovary transplants from R6/2^{+} (105 CAG) mice were purchased from Jackson Laboratories. Mice were genotyped after weaning; we analyzed those that were R6/2 transgenic positive to determine their CAG repeat number by PCR, with primers encoding a product spanning the repeat region (forward primer 5′-ATGAAGGCCTTC GAGTCCCTCAAGTCCTTC-3′ and reverse 5′-GGCGGCTGAGGAAGCTG AGGA-3′). Only mice with confirmed 105 ± 5 CAG repeats were used for this study.

Adeno-associated viruses (AAV4) expressing BDNF and noggin were produced at the University of Iowa Gene Transfer Vector Core, as described (Benraiss et al., 2012). For all experiments, R6/2 mice received bilateral intraventricular 1.5 μl injections of a 1:1 mixture of AAV4-BDNF and AAV4-ΔB2noggin (referred to as AAV4-BDNF/noggin), AAV4-Null, or saline at 4 weeks of age. Beginning 2 weeks later, mice were treated with BrdU (75 mg/kg, i.p.) for 30 days, then killed 2 weeks later for histological analysis. Both our stereotaxic injection and BrdU labeling protocols are further detailed in the Supplemental Experimental Procedures.

Six male adult squirrel monkeys, weighing between 700 and 1,200 g, were injected with 20 μl of either an adenoviral-BDNF/adenoviral-noggin mixture or a control adenoviral-EGFP into the lateral ventricles (n = 3 monkeys each), using stereotaxic coordinates determined through computerized tomography scanning of each animal. Beginning 1 week following adenoviral injection, the monkeys received daily intravenous injections of BrdU (75 mg/kg, IV) for 15 days, to label newly generated neurons. Five weeks later, the animals were killed and their brains were dissected, cryosectioned, and immunostained for analysis.

Identifying Newly Generated Neurons in Nestin-CreER^{T2}/ROSA26-EYFP Mice

Nestin-CreER^{T2}/ROSA26-EYFP bigenic mice were used experimentally or bred (Imayoshi et al., 2006, 2008) with females with ovary transplants from R6/2^{+} (105 CAG) mice. At three weeks of age, the mice received daily injections of tamoxifen (2.5 mg i.p., or 125 mg/kg) for 10 days. The tamoxifen stock solution was prepared by suspending 250 mg tamoxifen (Sigma; T5648) in 1 ml of ethanol followed by the addition of 9 ml peanut oil. The mice were injected with AAV4 1 day after their last tamoxifen injection, when 4 weeks old. A subset of these nestin bigenic or trigenic mice (n = 4 each) also received a stereotaxic intrapallidal injection of the fluorescent-conjugated retrograde tracer CT-B, conjugated to Alexa Fluor 555 (0.5 μl; Invitrogen; C-34776). The injections were given 1 week prior to sacrifice at 12 weeks, at the following coordinates relative to bregma: AP −0.8 mm; ML ± 2.25 mm; DV −3.6 mm.

Analogous bigenic and trigenic reporter mice established with mEGFP were established to permit whole-cell visualization of both newly generated and resident MSNs. The construction of these mice, and of corresponding lentiviral-mEGFP vectors, is described in the Supplemental Experimental Procedures.

Immunolabeling

Immunophenotyping of newly generated and resident MSNs was accomplished using a panel of antigenic markers that included Dcx, ßIII-tubulin, NeuN, DARPP-32, and substance P and enkephalin, typically colabeled with one another or for BrdU; detailed protocols for each of these immunostains are provided in the Supplemental Experimental Procedures.

Electrophysiological Assessment

Physiological recordings of newly generated neurons in slice preparations of *nestin*-EYFP bigenic wild-type and crossed R6/2 trigenic mice were performed as described in detail in the Supplemental Experimental Procedures.

Confocal Imaging

In striatal sections, cells that were double-labeled with BrdU or GFP and markers described were selected for confocal analysis. Images were acquired using an Olympus Fluoview confocal microscope and an argon-krypton laser and analyzed as previously described (Benraiss et al., 2001; Chmielnicki et al., 2004; Cho et al., 2007). More detailed methods and scoring criteria are described in the Supplemental Experimental Procedures.

Scoring and Quantification

Counts of striatal $BrdU^+$ cells were scored by antigenic phenotype using stereological methodology for unbiased estimation across the striatal volume as detailed in the Supplemental Experimental Procedures.

Rotarod Performance

Motor coordination and balance were measured using rotarod analysis as previously described (Cho et al., 2007) and as detailed in the Supplemental Experimental Procedures.

Survival

The viabilities of AAV4-BDNF/noggin, AAV4-Null, or saline-treated R6/2 mice were assessed twice daily throughout the entire length of the experiment. At least one wild-type littermate was provided in each experimental cage, and no mice entered into the survival study were subjected to behavioral tests so as to exclude the possibility of any confounding effects of such tests upon net life span. Survival data were analyzed by Kaplan-Meier survival curves.

SUPPLEMENTAL INFORMATION

Supplemental Information for this article includes Supplemental Experimental Procedures, six figures, and four tables and can be found with this article online at http://dx.doi.org/10.1016/j.stem.2013.04.014.

ACKNOWLEDGMENTS

This work was supported by NINDS R01NS52534 and R37NS29813, the Hereditary Disease Foundation, CHDI, and the New York State Stem Cell Research Program (NYSTEM). Work in the Davidson laboratory was supported by DK54759, NS34568, and HD3353. We thank Dr. Louis DiVincenti, Jr. for his veterinary expertise and assistance with the squirrel monkey arm of this project. We also thank the referees for their consistently helpful critiques and suggestions during the progression of this study. Dr. Goldman and colleagues have received the following patents relevant to this study: "Gene-therapy-mediated induction of neurogenesis in the adult brain," U.S. Patent 7,037,493, and "Enhancing neurotrophin-induced neurogenesis by endogenous neural progenitor cells by concurrent overexpression of BDNF and an inhibitor of a progliogenic bone morphogenetic protein," U.S. Patent 7,576,065. These patents are owned by the Cornell University Center for Technology Enterprise; neither Dr. Goldman nor any coauthors have received income from these patents.

Received: February 9, 2012
Revised: February 23, 2013
Accepted: April 16, 2013
Published: June 6, 2013

REFERENCES

André, V.M., Cepeda, C., Fisher, Y.E., Huynh, M., Bardakjian, N., Singh, S., Yang, X.W., and Levine, M.S. (2011). Differential electrophysiological changes in striatal output neurons in Huntington's disease. J. Neurosci. *31*, 1170–1182.

Bates, G. (2003). Huntingtin aggregation and toxicity in Huntington's disease. Lancet *361*, 1642–1644.

Becher, M.W., Kotzuk, J.A., Sharp, A.H., Davies, S.W., Bates, G.P., Price, D.L., and Ross, C.A. (1998). Intranuclear neuronal inclusions in Huntington's disease and dentatorubral and pallidoluysian atrophy: correlation between the density of inclusions and IT15 CAG triplet repeat length. Neurobiol. Dis. *4*, 387–397.

Bedard, A., Gravel, C., and Parent, A. (2005). Chemical characterization of newly generated neurons in the striatum of adult primates. Exp. Brain Res. *170*, 501–512.

Bekar, L., Libionka, W., Tian, G.F., Xu, Q., Torres, A., Wang, X., Lovatt, D., Williams, E., Takano, T., Schnermann, J., et al. (2008). Adenosine is crucial for deep brain stimulation-mediated attenuation of tremor. Nat. Med. *14*, 75–80.

Benraiss, A., and Goldman, S.A. (2011). Cellular therapy and induced neuronal replacement for Huntington's disease. Neurotherapeutics *8*, 577–590.

Benraiss, A., Chmielnicki, E., Lerner, K., Roh, D., and Goldman, S.A. (2001). Adenoviral brain-derived neurotrophic factor induces both neostriatal and olfactory neuronal recruitment from endogenous progenitor cells in the adult forebrain. J. Neurosci. *21*, 6718–6731.

Benraiss, A., Bruel-Jungerman, E., Lu, G., Economides, A.N., Davidson, B., and Goldman, S.A. (2012). Sustained induction of neuronal addition to the adult rat neostriatum by AAV4-delivered noggin and BDNF. Gene Ther. *19*, 483–493.

Chmielnicki, E., Benraiss, A., Economides, A.N., and Goldman, S.A. (2004). Adenovirally expressed noggin and brain-derived neurotrophic factor cooperate to induce new medium spiny neurons from resident progenitor cells in the adult striatal ventricular zone. J. Neurosci. *24*, 2133–2142.

Cho, S.R., Benraiss, A., Chmielnicki, E., Samdani, A., Economides, A., and Goldman, S.A. (2007). Induction of neostriatal neurogenesis slows disease progression in a transgenic murine model of Huntington disease. J. Clin. Invest. *117*, 2889–2902.

Christine, C.W., Starr, P.A., Larson, P.S., Eberling, J.L., Jagust, W.J., Hawkins, R.A., VanBrocklin, H.F., Wright, J.F., Bankiewicz, K.S., and Aminoff, M.J. (2009). Safety and tolerability of putaminal AADC gene therapy for Parkinson disease. Neurology *73*, 1662–1669.

Curtis, M.A., Penney, E.B., Pearson, A.G., van Roon-Mom, W.M., Butterworth, N.J., Dragunow, M., Connor, B., and Faull, R.L. (2003). Increased cell proliferation and neurogenesis in the adult human Huntington's disease brain. Proc. Natl. Acad. Sci. USA *100*, 9023–9027.

Dai, Y., Schwarz, E.M., Gu, D., Zhang, W.W., Sarvetnick, N., and Verma, I.M. (1995). Cellular and humoral immune responses to adenoviral vectors containing factor IX gene: tolerization of factor IX and vector antigens allows for long-term expression. Proc. Natl. Acad. Sci. USA *92*, 1401–1405.

Davidson, B.L., Stein, C.S., Heth, J.A., Martins, I., Kotin, R.M., Derksen, T.A., Zabner, J., Ghodsi, A., and Chiorini, J.A. (2000). Recombinant adeno-associated virus type 2, 4, and 5 vectors: transduction of variant cell types and regions in the mammalian central nervous system. Proc. Natl. Acad. Sci. USA *97*, 3428–3432.

Davies, S.W., Turmaine, M., Cozens, B.A., DiFiglia, M., Sharp, A.H., Ross, C.A., Scherzinger, E., Wanker, E.E., Mangiarini, L., and Bates, G.P. (1997). Formation of neuronal intranuclear inclusions underlies the neurological dysfunction in mice transgenic for the HD mutation. Cell *90*, 537–548.

Dodge, J.C., Treleaven, C.M., Fidler, J.A., Hester, M., Haidet, A., Handy, C., Rao, M., Eagle, A., Matthews, J.C., Taksir, T.V., et al. (2010). AAV4-mediated expression of IGF-1 and VEGF within cellular components of the ventricular system improves survival outcome in familial ALS mice. Mol. Ther. *18*, 2075–2084.

Gray, M., Shirasaki, D.I., Cepeda, C., André, V.M., Wilburn, B., Lu, X.H., Tao, J., Yamazaki, I., Li, S.H., Sun, Y.E., et al. (2008). Full-length human mutant huntingtin with a stable polyglutamine repeat can elicit progressive and selective neuropathogenesis in BACHD mice. J. Neurosci. *28*, 6182–6195.

Gutekunst, C.-A., Norflus, F., and Hersch, S.M. (2002). The neuropathology of Huntington's Disease. In Huntington's Disease, G. Bates, P. Harper, and L. Jones, eds. (Oxford: Oxford), pp. 251–275.

Henry, R.A., Hughes, S.M., and Connor, B. (2007). AAV-mediated delivery of BDNF augments neurogenesis in the normal and quinolinic acid-lesioned adult rat brain. Eur. J. Neurosci. *25*, 3513–3525.

Hickey, M.A., and Chesselet, M.F. (2003). Apoptosis in Huntington's disease. Prog. Neuropsychopharmacol. Biol. Psychiatry *27*, 255–265.

Imayoshi, I., Ohtsuka, T., Metzger, D., Chambon, P., and Kageyama, R. (2006). Temporal regulation of Cre recombinase activity in neural stem cells. Genesis *44*, 233–238.

Imayoshi, I., Sakamoto, M., Ohtsuka, T., Takao, K., Miyakawa, T., Yamaguchi, M., Mori, K., Ikeda, T., Itohara, S., and Kageyama, R. (2008). Roles of continuous neurogenesis in the structural and functional integrity of the adult forebrain. Nat. Neurosci. *11*, 1153–1161.

Kang, J., Jiang, L., Goldman, S.A., and Nedergaard, M. (1998). Astrocyte-mediated potentiation of inhibitory synaptic transmission. Nat. Neurosci. *1*, 683–692.

Keyoung, H.M., Roy, N.S., Benraiss, A., Louissaint, A., Jr., Suzuki, A., Hashimoto, M., Rashbaum, W.K., Okano, H., and Goldman, S.A. (2001). High-yield selection and extraction of two promoter-defined phenotypes of neural stem cells from the fetal human brain. Nat. Biotechnol. *19*, 843–850.

Kirschenbaum, B., Nedergaard, M., Preuss, A., Barami, K., Fraser, R.A., and Goldman, S.A. (1994). In vitro neuronal production and differentiation by precursor cells derived from the adult human forebrain. Cereb. Cortex *4*, 576–589.

Klapstein, G.J., Fisher, R.S., Zanjani, H., Cepeda, C., Jokel, E.S., Chesselet, M.F., and Levine, M.S. (2001). Electrophysiological and morphological changes in striatal spiny neurons in R6/2 Huntington's disease transgenic mice. J. Neurophysiol. *86*, 2667–2677.

Lendahl, U., Zimmerman, L.B., and McKay, R.D. (1990). CNS stem cells express a new class of intermediate filament protein. Cell *60*, 585–595.

LeWitt, P.A., Rezai, A.R., Leehey, M.A., Ojemann, S.G., Flaherty, A.W., Eskandar, E.N., Kostyk, S.K., Thomas, K., Sarkar, A., Siddiqui, M.S., et al. (2011). AAV2-GAD gene therapy for advanced Parkinson's disease: a double-blind, sham-surgery controlled, randomised trial. Lancet Neurol. *10*, 309–319.

Liu, G., Martins, I.H., Chiorini, J.A., and Davidson, B.L. (2005). Adeno-associated virus type 4 (AAV4) targets ependyma and astrocytes in the subventricular zone and RMS. Gene Ther. *12*, 1503–1508.

Madisen, L., Zwingman, T.A., Sunkin, S.M., Oh, S.W., Zariwala, H.A., Gu, H., Ng, L.L., Palmiter, R.D., Hawrylycz, M.J., Jones, A.R., et al. (2010). A robust and high-throughput Cre reporting and characterization system for the whole mouse brain. Nat. Neurosci. *13*, 133–140.

Mangiarini, L., Sathasivam, K., Seller, M., Cozens, B., Harper, A., Hetherington, C., Lawton, M., Trottier, Y., Lehrach, H., Davies, S.W., and Bates, G.P. (1996). Exon 1 of the HD gene with an expanded CAG repeat is sufficient to cause a progressive neurological phenotype in transgenic mice. Cell *87*, 493–506.

Meade, C.A., Deng, Y.P., Fusco, F.R., Del Mar, N., Hersch, S., Goldowitz, D., and Reiner, A. (2002). Cellular localization and development of neuronal intranuclear inclusions in striatal and cortical neurons in R6/2 transgenic mice. J. Comp. Neurol. *449*, 241–269.

Mignone, J.L., Kukekov, V., Chiang, A.S., Steindler, D., and Enikolopov, G. (2004). Neural stem and progenitor cells in nestin-GFP transgenic mice. J. Comp. Neurol. *469*, 311–324.

Mueller, C., and Flotte, T.R. (2008). Clinical gene therapy using recombinant adeno-associated virus vectors. Gene Ther. *15*, 858–863.

Paine-Saunders, S., Viviano, B.L., Economides, A.N., and Saunders, S. (2002). Heparan sulfate proteoglycans retain Noggin at the cell surface: a potential mechanism for shaping bone morphogenetic protein gradients. J. Biol. Chem. *277*, 2089–2096.

Pincus, D.W., Keyoung, H.M., Harrison-Restelli, C., Goodman, R.R., Fraser, R.A., Edgar, M., Sakakibara, S., Okano, H., Nedergaard, M., and Goldman, S.A. (1998). Fibroblast growth factor-2/brain-derived neurotrophic factor-associated maturation of new neurons generated from adult human subependymal cells. Ann. Neurol. *43*, 576–585.

Reumers, V., Deroose, C.M., Krylyshkina, O., Nuyts, J., Geraerts, M., Mortelmans, L., Gijsbers, R., Van den Haute, C., Debyser, Z., and Baekelandt, V. (2008). Noninvasive and quantitative monitoring of adult neuronal stem cell migration in mouse brain using bioluminescence imaging. Stem Cells *26*, 2382–2390.

Sanai, N., Tramontin, A.D., Quiñones-Hinojosa, A., Barbaro, N.M., Gupta, N., Kunwar, S., Lawton, M.T., McDermott, M.W., Parsa, A.T., Manuel-García Verdugo, J., et al. (2004). Unique astrocyte ribbon in adult human brain contains neural stem cells but lacks chain migration. Nature *427*, 740–744.

Sim, F.J., Lang, J., Waldau, B., Roy, N.S., Schwartz, T., Chandross, K., Natesan, S., Merrill, J., and Goldman, S.A. (2006). Complementary patterns of gene expression by human oligodendrocyte progenitor cells and their environment predict determinants of progenitor maintenance and differentiation. Annals Neurol. *59*, 763–779.

Southwell, A.L., Warby, S.C., Carroll, J.B., Doty, C.N., Skotte, N.H., Zhang, W., Villanueva, E.B., Kovalik, V., Xie, Y., Pouladi, M.A., et al. (2013). A fully humanized transgenic mouse model of Huntington disease. Hum. Mol. Genet. *22*, 18–34.

Tamura, Y., Kataoka, Y., Cui, Y., Takamori, Y., Watanabe, Y., and Yamada, H. (2007). Multi-directional differentiation of doublecortin- and NG2-immunopositive progenitor cells in the adult rat neocortex in vivo. Eur. J. Neurosci. *25*, 3489–3498.

Turmaine, M., Raza, A., Mahal, A., Mangiarini, L., Bates, G.P., and Davies, S.W. (2000). Nonapoptotic neurodegeneration in a transgenic mouse model of Huntington's disease. Proc. Natl. Acad. Sci. USA *97*, 8093–8097.

Yu-Taeger, L., Petrasch-Parwez, E., Osmand, A.P., Redensek, A., Metzger, S., Clemens, L.E., Park, L., Howland, D., Calaminus, C., Gu, X., et al. (2012). A novel BACHD transgenic rat exhibits characteristic neuropathological features of Huntington disease. J. Neurosci. *32*, 15426–15438.

Zimmerman, L., Parr, B., Lendahl, U., Cunningham, M., McKay, R., Gavin, B., Mann, J., Vassileva, G., and McMahon, A. (1994). Independent regulatory elements in the nestin gene direct transgene expression to neural stem cells or muscle precursors. Neuron *12*, 11–24.

CellPress

Cell Stem Cell
Article

Cardiac Repair in a Porcine Model of Acute Myocardial Infarction with Human Induced Pluripotent Stem Cell-Derived Cardiovascular Cells

Lei Ye,[1,2] Ying-Hua Chang,[3] Qiang Xiong,[1] Pengyuan Zhang,[1] Liying Zhang,[1] Porur Somasundaram,[1] Mike Lepley,[2,4] Cory Swingen,[1] Liping Su,[1] Jacqueline S. Wendel,[5] Jing Guo,[1] Albert Jang,[6] Daniel Rosenbush,[1] Lucas Greder,[2] James R. Dutton,[2] Jianhua Zhang,[7] Timothy J. Kamp,[3,7] Dan S. Kaufman,[2,4] Ying Ge,[3,8] and Jianyi Zhang[1,2,5,6,*]

[1]Division of Cardiology, Department of Medicine
[2]Stem Cell Institute
University of Minnesota, Minneapolis, MN, 55455, USA
[3]Department of Cell and Regenerative Biology, University of Wisconsin, Madison, WI, 53705, USA
[4]Division of Hematology, Oncology, and Transplantation, Department of Medicine
[5]Department of Biomedical Engineering
[6]Department of Electrical and Computer Engineering
University of Minnesota, Minneapolis, MN, 55455, USA
[7]Department of Medicine, University of Wisconsin, Madison, WI, 53705, USA
[8]Department of Chemistry, University of Wisconsin, Madison, WI, 53706, USA
*Correspondence: zhang047@umn.edu
http://dx.doi.org/10.1016/j.stem.2014.11.009

SUMMARY

Human induced pluripotent stem cells (hiPSCs) hold promise for myocardial repair following injury, but preclinical studies in large animal models are required to determine optimal cell preparation and delivery strategies to maximize functional benefits and to evaluate safety. Here, we utilized a porcine model of acute myocardial infarction (MI) to investigate the functional impact of intramyocardial transplantation of hiPSC-derived cardiomyocytes, endothelial cells, and smooth muscle cells, in combination with a 3D fibrin patch loaded with insulin growth factor (IGF)-encapsulated microspheres. hiPSC-derived cardiomyocytes integrated into host myocardium and generated organized sarcomeric structures, and endothelial and smooth muscle cells contributed to host vasculature. Trilineage cell transplantation significantly improved left ventricular function, myocardial metabolism, and arteriole density, while reducing infarct size, ventricular wall stress, and apoptosis without inducing ventricular arrhythmias. These findings in a large animal MI model highlight the potential of utilizing hiPSC-derived cells for cardiac repair.

INTRODUCTION

Human induced pluripotent stem cells (hiPSCs) are promising therapeutic agents that can potentially generate an unlimited range and quantity of clinically relevant cell types that are not rejected by the patient's immune system. Several studies have reported generation of cardiomyocytes from hiPSCs (Burridge et al., 2012), and transplantation of these cells into rodent models of MI have suggested that they may provide functional benefit (Caspi et al., 2007; Laflamme et al., 2007; Shiba et al., 2012; van Laake et al., 2008). In a guinea pig model of cardiac injury, transplanted human embryonic stem cell-derived cardiomyocytes (hESC-CMs) showed electric coupling to native myocardium (Shiba et al., 2012). However, preclinical studies in large animal models of MI are necessary to fully evaluate the therapeutic potential of this approach and to empirically determine the optimal combination of cell types, supplementary factors, and delivery methods to maximize efficacy and stringently assess safety (Cibelli et al., 2013). To this end, Chong et al. utilized a nonhuman primate model of myocardial ischemia, injecting one billion hESC-CMs into the hearts of macaques with MI injury, and finding extensive evidence of engraftment, remuscularization, and electromechanical synchronization 2 to 7 weeks after transplantation (Chong et al., 2014). Despite these promising findings, telemetric electrocardiographic (ECG) evaluation demonstrated ventricular arrhythmias in some treated animals, suggesting further investigation of optimal cell quantities and delivery approaches is warranted.

Currently, poor engraftment of transplanted cardiomyocytes presents a significant barrier to transplantation-based approaches for myocardial cell therapy. In vitro studies strongly suggest that myocytes survive better when cocultured with endothelial cells (ECs) than when cultured alone (Xiong et al., 2012). Coadministration of ECs could enhance CM survival and benefit left ventricular (LV) myocardial perfusion, metabolism, and contractile activity through release of signaling molecules such as nitric oxide, vascular endothelial growth factor (VEGF), and insulin growth factor (IGF), which has also been shown to inhibit apoptosis (Davis et al., 2006; Brutsaert, 2003; Hsieh et al., 2006). Consistent with this hypothesis, we recently demonstrated that transplantation of hiPSC-derived ECs (hiPSC-ECs) and smooth muscle cells (hiPSC-SMCs) into ischemic porcine myocardial tissue contributes to

improvements in perfusion, wall stress, and cardiac performance (Xiong et al., 2012); however, myocardial repair and functional improvements may be even more extensive if primary force-producing myocardial cells are included in the population of transplanted cells.

In the present study, we injected three hiPSC-derived cell types (hiPSC-CMs, hiPSC-ECs, and hiPSC-SMCs) directly into injured hearts in a porcine large animal model of acute myocardial infarction. Cells were coinjected through an epicardial fibrin patch that provided prolonged release of the prosurvival factor insulin-like growth factor 1 (IGF-1), and cell engraftment and functional outcomes were evaluated. Our results show engraftment of cells from all three lineages at the site of injury, for at least 4 weeks after injection. This was accompanied by improvements in myocardial wall stress, metabolism, and contractile performance, and, importantly, did not lead to the development of ventricular arrhythmias. Together, these findings show that coadministration of multiple hiPSC-cardiovascular lineage cell populations promotes myocardial repair in large-animal models of MI.

RESULTS

Differentiation of hiPSCs into Cardiac-Lineage CMs, ECs, and SMCs

hiPSCs were reprogrammed from human dermal fibroblasts and engineered to express eGFP (Figure S1 available online) and differentiated into CMs via the Sandwich method (Zhang et al., 2012). Isolated areas of contracting cells typically appeared on day 7 of differentiation (Movies S1, S2, and S3) and were collected 1 week later for purification via a microdissection and preplating method. Expression of cardiac-specific proteins in differentiated hiPSC-CMs was evaluated on day 30 after cells started contracting. Nearly all hiPSC-CMs expressed slow myosin heavy chain, α-sarcomeric actin (Figure 1A), and the cardiac-specific myofilament cTnT (Figure 1B). Approximately 20%–30% of the hiPSC-CMs expressed the 2v isoform of myosin light chain (MLC2v) (Figure 1B, middle), which is found only in ventricular CMs, and cardiac connexin-43 was present at numerous points of contact between adjacent cells (Figure 1C). The purity of the final hiPSC-CM population was as high as 93% when evaluated via flow cytometry analysis of cTnT expression (Figures 1D and 1E) and >90% when evaluated via fluorescence immunostaining for cTnT expression (Figure 1F). hiPSC-ECs and hiPSC-SMCs were generated via established differentiation protocols (Hill et al., 2010; Woll et al., 2008) and expressed EC- and SMC-specific proteins (Figures 1G–1L).

hiPSC-Derived Cardiac Cells Engraft and Survive after Transplantation into a Porcine Model of Myocardial Infarction

We then tested our hypothesis that transplantation of three hiPSC-derived cardiac cell types would improve recovery after ischemic myocardial injury in a large-animal model (swine) of ischemia-reperfusion (IR) injury. A total of 92 pigs underwent the IR protocol; 89 pigs survived and were divided into five groups (Table S1). Animals receiving CMs, EC, and SMCs (Cell group) or CMs, ECs, SMC, and the fibrin/IGF-1 patch (Cell+Patch group) were injected with two million hiPSC-CMs, two million hiPSC-ECs, and two million hiPSC-SMCs (six million cells total) directly into the injured myocardium; for animals in the Cell+Patch group, the needle was inserted through an IGF-1-containing fibrin scaffold patch (Figure S2) that had been created over the site of injury. Animals in the Patch group were treated with scaffold patch alone, and both the patch and the cells were withheld from animals in the MI group. Animals in the Sham group underwent all surgical procedures for induction of IR injury, except for the ligation step, and recovered without any experimental treatments.

We then evaluated the engraftment and survival rates of the transplanted cells. Since the transplanted cells were genetically male and engineered to express GFP, while the recipient pigs were female, we performed quantitative PCR (qPCR) assessments for the human Y chromosome. Lineages of surviving cells were determined by staining for expression of the human-specific EC marker CD31 (hiPSC-ECs), for coexpression of GFP and α-smooth-muscle actin (SMA) (hiPSC-SMCs), and for coexpression of GFP and cTnT (hiPSC-CMs).

At 4 weeks after injury, 4.2% ± 1.1% of transplanted cells survived in animals in the Cells group while 8.97% ± 1.8% survived in the hearts of Cell+Patch animals. In contrast, 3.2% ± 0.4% of the two million cells administered to the CM group survived. Substantial proportions of all three transplanted cell types were observed in Cell+Patch hearts: 27.1% ± 5% of surviving transplanted cells were hiPSC-CMs, 34.2% ± 10% were hiPSC-ECs, and 40.5% ± 1% were hiPSC-SMCs. These observations suggest that the IGF-1-containing fibrin patch may have substantially improved the engraftment of all three hiPSC-derived cell lineages. Furthermore, GFP-expressing cells were present in cardiac muscle fibers (Figures 2A), but rarely in fibers composed of porcine cardiomyocytes (Figures S3A–S3D), suggesting that the transplanted hiPSC-CMs may have developed into new muscle fibers rather than incorporating into existing host cardiac muscle. GFP^+ cells were also identified in capillaries and arterioles (Figures 2B and 2C), although the proportion of vessels apparently generated directly from transplanted cells was less than 0.1%.

Transplantation of hiPSC-Derived Cardiac Cells Improves Cardiac Function and Bioenergetics after MI

Measurements of cardiac function were evaluated 1 and 4 weeks after injury and cell transplantation. Left-ventricular ejection fraction (LVEF) was significantly better in Cell+Patch group animals than in MI and Patch animals (Figure 3A) at 4 weeks. Systolic thickening fractions that reflect regional myocardial contractility were significantly greater in the infarct zone (IZ) and at the border zone (BZ) of the infarct in hearts from Cell+Patch animals than in MI hearts at both week 1 and week 4 time points (Figure 3B). Infarct size was significantly smaller in Cell+Patch hearts than in MI hearts ($p < 0.05$) at week 1, while the difference between Cell+Patch and Patch hearts approached statistical significance ($p = 0.051$) (Figure 3C). Measurements of regional wall stress performed 4 weeks after injury were significantly lower in Cell+Patch hearts than in Patch hearts (Figure 3D). Together, these results show that transplantation of multiple hiPSC-derived cardiac lineages, in combination with IGF-1/fibrin patch, improves cardiac function after MI.

We then determined whether these functional improvements in Cell+Patch animals were accompanied by improved

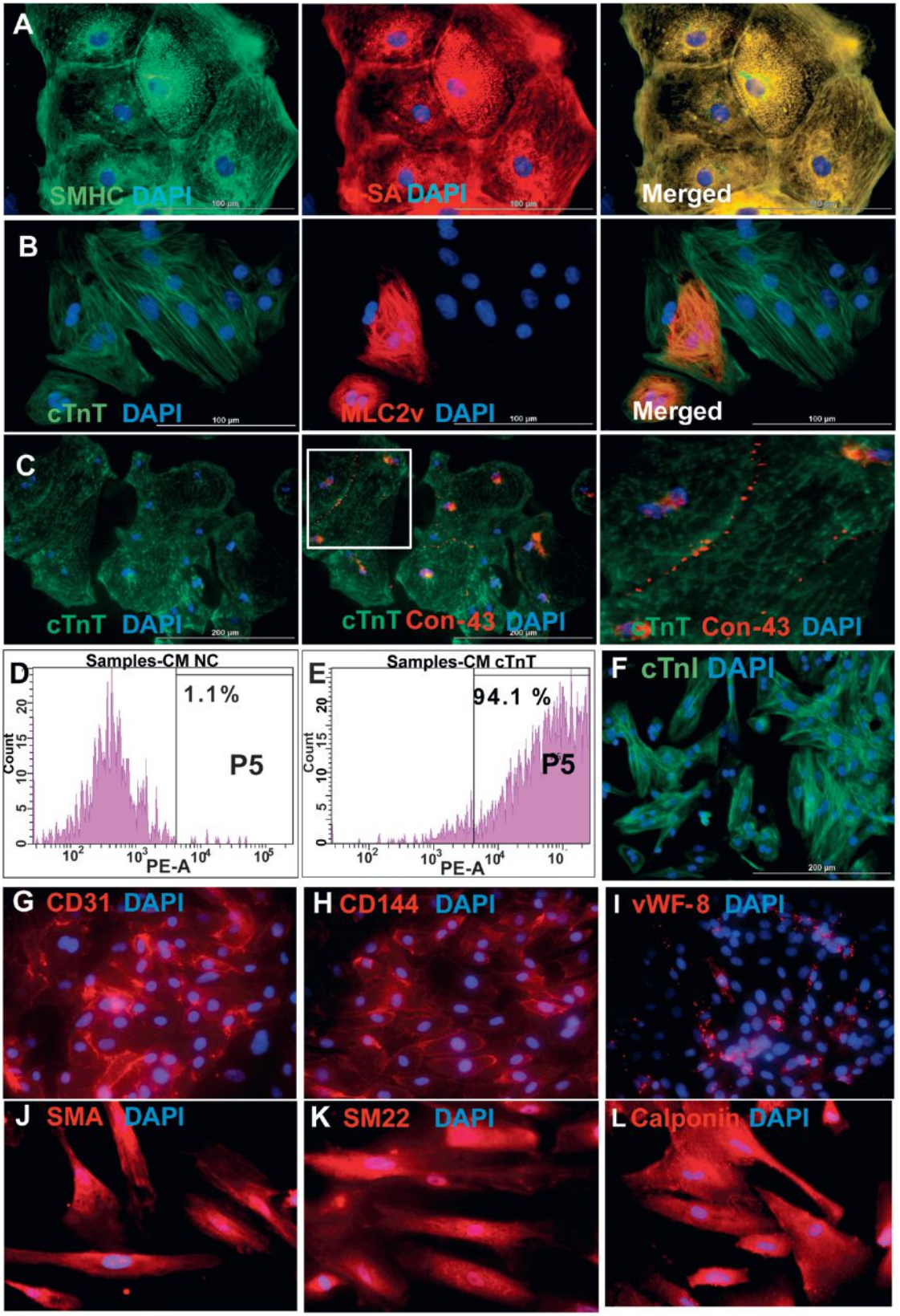

(legend on next page)

myocardial bioenergetics and efficient ATP utilization. Myocardial ATP hydrolysis rates were measured in vivo with the ^{31}P MRS-MST method (Xiong et al., 2013). Measurements were performed at the BZ of the infarct under both baseline and elevated cardiac work states in response to catecholamine stimulation. Myocardial PCr/ATP ratios that reflect mitochondrial energetic efficiency, were significantly higher in animals from the Cell+Patch group than in MI animals under baseline conditions (Figure 3E), while the rate of ATP hydrolysis was significantly higher in Cell+Patch group hearts than in MI and Patch hearts during high cardiac workload (Figure 3F); measurements in Patch and MI animals were similar under both conditions. Collectively, these observations indicate that the transplantation of hiPSC-derived cardiovascular cells improved LV pump function and myocardial energy metabolism while reducing infarct size.

Combined hiPSC-CM and Patch Treatment Does Not Induce Ventricular Arrhythmias

Arrhythmogenesis is a primary risk associated with pluripotent cell-derived CM therapy for treatment of cardiac disorders. In a recent study, significant ventricular arrhythmias were detected after transplantation of hESC-CMs in a nonhuman primate model of MI (Chong et al., 2014). Thus, we examined whether the hiPSC-CM patch transplantation protocol used here might be associated with onset of cardiac arrhythmia. Ischemia-reperfusion injury was induced in 16 pigs who then received the fibrin/IGF-1 patch alone (Patch group), the patch and ten million hiPSC-CMs (Patch+CMs), or neither experimental treatment (Table S1). ECGs were recorded continuously for 4 weeks afterward using an implantable loop recorder. Severe arrhythmias and ST elevations were observed in all animals during coronary artery occlusion and reperfusion, but no animal in any treatment group developed spontaneous arrhythmia during the 4-week follow-up period. Furthermore, no evidence of ventricular tachycardia (VT) or ventricular fibrillation (VF) was induced in response to programmed electrical stimulation (PES) in hearts of Patch+CM group animals, even when the most aggressive stimulation protocol was applied. Thus, the combined Patch+hiPSC-CM administration protocol used for the experiments described in this report does not appear to impair the electromechanical stability of swine hearts.

Transplantation of hiPSC-Derived Cardiac Cells Reduces Cardiomyocyte Apoptosis and Stimulates Nkx2.5 Expression after IR Injury

We next assessed how Cell+Patch treatment improves cardiac function. One possibility is through induction of cytoprotective mechanisms. To evaluate this possibility, we measured apoptosis in the hearts of animals sacrificed 3 days after IR injury and treatment (Figures 4A–4G). At the BZ of the infarct, apoptotic (i.e., TUNEL$^+$) cells were significantly less common in animals from the Cell+Patch group than in MI and Patch animals, both in the total cell population (Figure 4F) and specifically among CMs (i.e., cTnI$^+$ cells) (Figure 4G). Furthermore, the proportion of CMs that expressed Nkx2.5 (Figures 4H–4N), which has been shown to protect CMs from oxidative stress (Toko et al., 2002), was significantly greater in Cell+Patch animals than in MI animals at week 4 ($p < 0.05$), and the difference between Cell+Patch and Patch animals approached statistical significance ($p = 0.056$), at week 1 after IR injury (Figure 4N). Nkx2.5 expression in MI hearts increased at week 4 but remained significantly lower than in Cell+Patch hearts. Thus, transplantation of hiPSC-derived cells increased cell survival during the first few days after IR injury and is associated with upregulation of Nkx2.5 expression. The decline in apoptosis could also result from improvements in wall stress and decreased fibrosis. Consistently, examination of Masson-Trichrome-stained heart sections from animals sacrificed at week 4 showed thicker subepicardium in the region where the patch was applied (~2.44 mm) than in animals from the Sham (0.16 mm) or MI (0.88 mm) groups (Figure S4).

Transplantation of hiPSC-Derived Cardiac Cells Enhance the Vasculogenic Response to IR Injury

Increased angiogenesis could also contribute to improved ventricular function. We therefore assessed whether transplantation of hiPSC-derived cardiac cells promotes angiogenesis in peri-infarct border zone (BZ) of MI hearts. Four weeks after injury, CD31+vascular structures and arterioles that coexpressed CD31 and SMA were significantly greater in the BZ of Cell and Cell+Patch hearts than in the corresponding regions of MI and Patch hearts (Figure 5). Additionally, vascular density was significantly greater in the CM group than in the MI group. Thus, transplantation of the hiPSC-derived cardiac cells promoted neovascularization, probably by inducing paracrine mechanisms in recipient myocardial tissue (Table S2).

The cell and patch treatments may also have delayed the immune response to IR injury. While infiltration of cells expressing the inflammatory marker CD11b (Figures S5A–S5F) peaked 3 days after injury in the MI group, this was significantly delayed in the IZ and BZ regions of hearts from Cell+Patch animals (Figure S5G). CD11b$^+$ cells were significantly more common in Cell+Patch hearts than in MI hearts at week 1 but not at week 4, while the CM, Cells, and Patch groups showed a statistically nonsignificant

Figure 1. Differentiation of Human iPSCs into Cardiomyocytes, Endothelial Cells, and Smooth Muscle Cells

(A–C) hiPSCs were differentiated into CMs via the Sandwich method (Zhang et al., 2012), and the lineage of the differentiated hiPSC-CMs was confirmed via the expression of (A) slow myosin heavy chain (SMHC) and α-sarcomeric actin (α-SA); (B) cardiac troponin T (cTnT) and the ventricular- specific cardiomyocyte protein myosin light chain 2v (MLC2v); and (C) cTnT and the gap-junction protein connexin-43 (Con-43); nuclei were counterstained with DAPI. The boxed region in the second panel of (C) is shown at higher magnification.

(D–F) The purity of the hiPSC-CM population was evaluated via flow cytometry analysis of cTnT expression in (D) isotype controls and (E) purified hiPSC-CMs, and by (F) immunofluorescence analysis of cardiac troponin I (cTnI) expression; nuclei were counterstained with DAPI. Scale bar represents 100 μm in (A) and (B) and 200 μm in (C) and (F). (See also Movies S1, S2, and S3.) hiPSCs were differentiated into ECs and SMCs as described previously (Hill et al., 2010; Woll et al., 2008).

(G–L) The lineage of the differentiated hiPSC-ECs was confirmed via the expression of (G) CD31, (H) CD144, and (I) vWF-8; and (J–L) the lineage of the differentiated hiPSC-SMCs was confirmed via the expression of (J) smooth-muscle actin (SMA), (K) SM22, and (L) calponin. Nuclei were counterstained with DAPI. Magnification (G)–(L) = 200×. (See also Figure S1.)

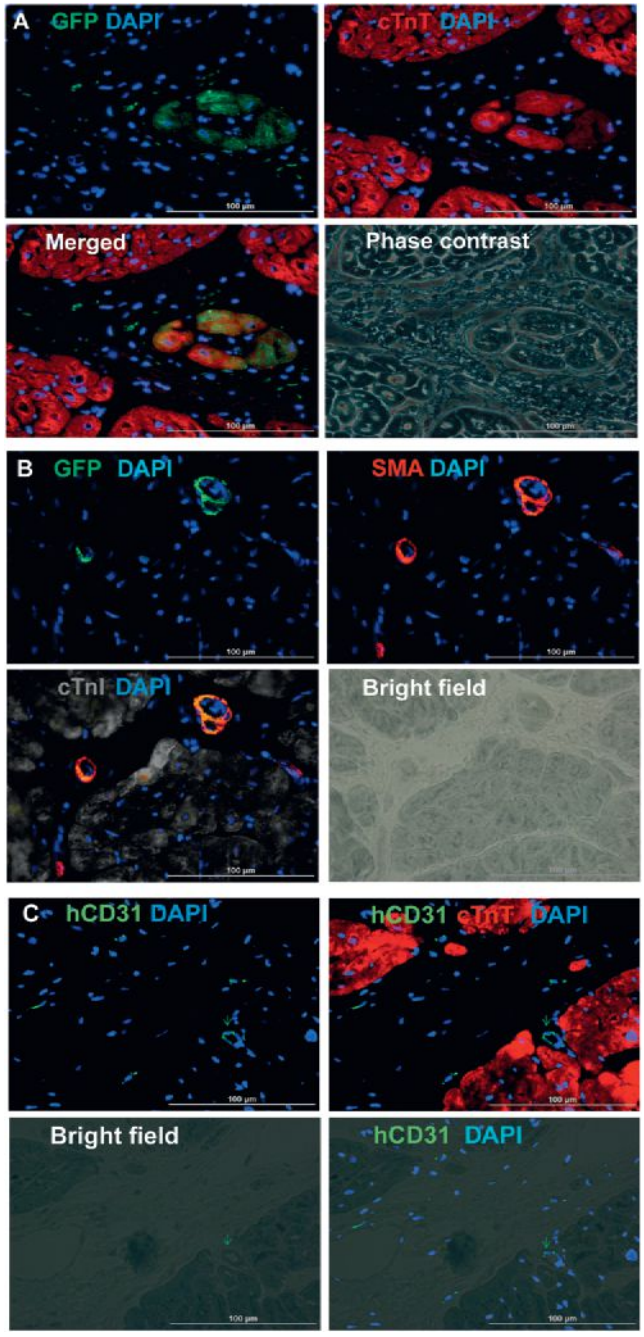

Figure 2. hiPSC-Derived Cardiac Cells Engraft and Survive after Transplantation into the Hearts of Swine with MI

(A) Engraftment of the injected cells was evaluated in sections stained for the presence of GFP; muscle fibers were visualized via fluorescent immunostaining for cTnT, and nuclei were counterstained with DAPI. The sections displayed in the first three panels were imaged with a phase-contrast microscope.

(B) Engrafted cells were identified in arterioles via immunofluorescent staining for the coexpression of GFP and SMA; muscle fibers were visualized via immunofluorescent staining for cTnI and nuclei were counterstained with DAPI.

(C) Engrafted cells were identified in blood vessels (i.e., capillaries and arterioles) via immunofluorescent staining for the human-specific isoform of CD31; muscle fibers were visualized via cTnT staining and nuclei were counterstained with DAPI. Scale bar represents 100 μm. (See also Figure S3.)

increase at weeks 1 and 4, suggesting a delayed host immune response following cell transplantation, possibly reducing immune rejection and increasing engraftment and survival of hiPSC-derived cells.

Paracrine Factor Release from the hiPSC-Derived Cells

This increase in angiogenesis observed after Cell+Patch treatment could be due to release of paracrine factors, as suggested by studies showing that endothelial cells promote cardiomyocyte survival (Xiong et al., 2012). To determine whether hiPSC-derived vascular cells possess cytoprotective effects similar to those previously reported in similar cell types, we cultured hiPSC-CMs under hypoxic conditions in media collected from the hiPSC-derived vascular cells (i.e., conditioned media) or with unconditioned (basal) media. hiPSC-CMs tended to shrink when cultured with unconditioned media but not when cultured with the conditioned media (Figures 5I and 5J). Culture in conditioned media was also associated with significant declines in hiPSC-CM apoptosis (Figures 5K, 5L, and 5N) and in the amount of cytoplasmic leakage of lactate dehydrogenase (LDH) from hiPSC-CMs (Figure 5M). Thus, hiPSC-derived vascular cells appear to release paracrine factors that protect hiPSC-CMs from hypoxic injury.

We then performed protein array analysis to identify paracrine factors that may be responsible for these in vitro cytoprotective effects and that might induce repair mechanisms in injured myocardial tissue. A total of 21 factors were detected, and their expression was confirmed in hiPSC-CMs, as well as hiPSC-derived vascular cells (Table S2). Several of the identified factors are known to impede apoptosis (angiogenin, angiopoietin, IL-6, MMP-1, PDGF-BB, TIMP-1, uPAR, and VEGF), induce cell migration or homing (angiogenin, angiopoietin, IL-8, MCP-1, MCP-3, MMP-9, uPAR, and VEGF), and promote cell division (angiogenin, angiopoietin, PDGF-BB, and VEGF), suggesting multiple paracrine mechanisms through which hiPSC-ECs and hiPSC-SMCs could promote CM survival and cardiac repair.

Myocardial Protein Expression after IR Injury and Cell Therapy

Understanding changes in the expression profile of myocardial proteins will help reveal the molecular mechanisms underlying improvements in left ventricular function associated with cell therapy. To provide further insights into these mechanisms, we performed a quantitative proteomics analysis on LV tissues from SHAM hearts and from MI hearts that were treated with or without hiPSC-derived vascular cells (which have both hiPSC-ECs and hiPSC-SMCs) after IR injury (Figure S6). We confidently identified 66 proteins whose expression pattern was altered in MI hearts but fully or partially restored to normal after cell transplantation (Figure 6). Thus, the functional benefits associated with cell therapy appear to be accompanied by a recovery of the myocardial protein expression profile of the recipient hearts.

DISCUSSION

The present study is among the first to evaluate the combined administration of three hiPSC-derived cardiovascular lineage cells in a large-animal model of ischemic myocardial injury. Our

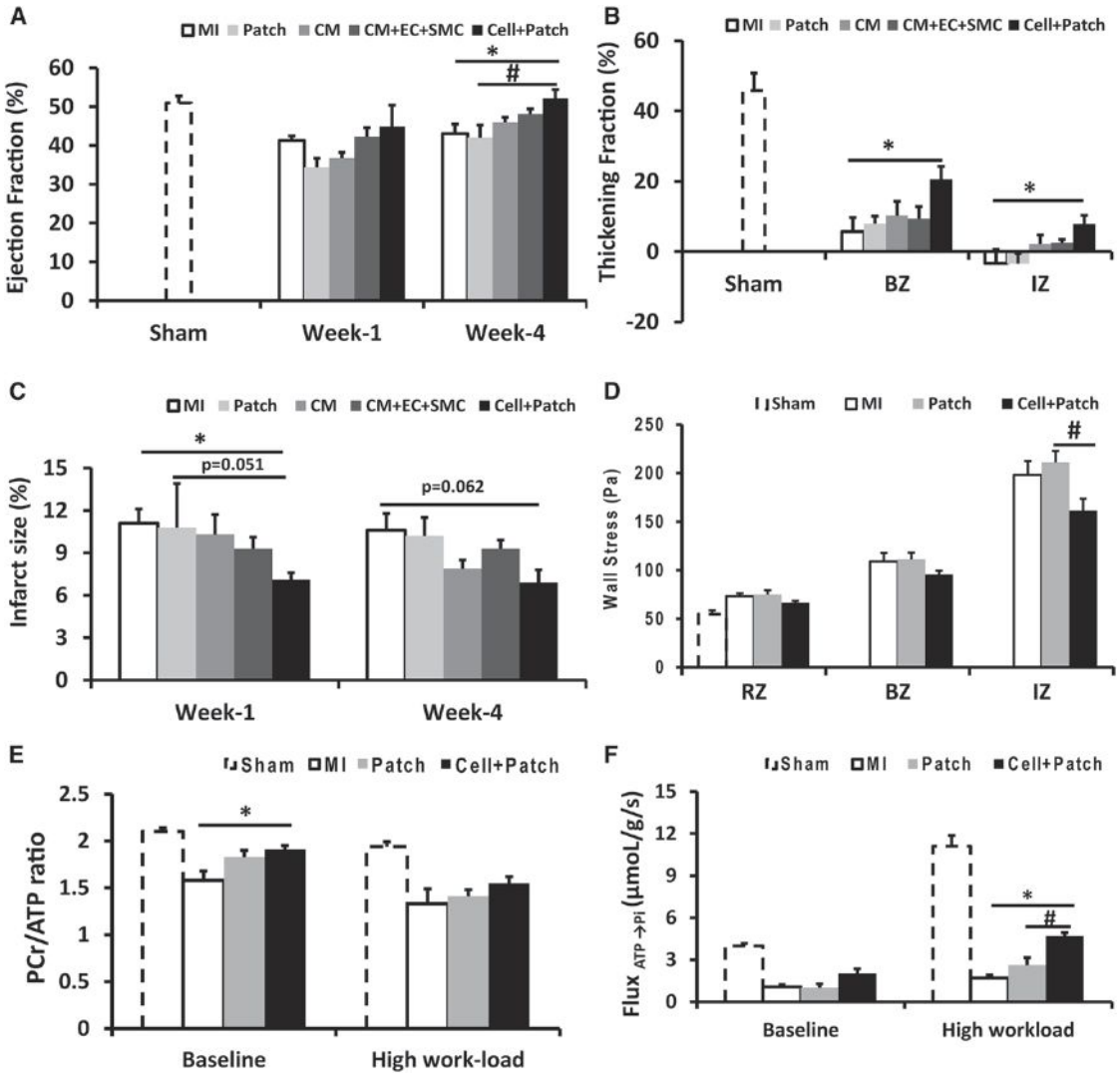

Figure 3. Transplanted hiPSC-Derived Cardiac Lineage Cells Improve Cardiac Function

(A) LV ejection fractions were evaluated at week 1 and week 4 after MI injury and treatment.

(B) LV wall systolic thickening fractions in the infarct zone (IZ) and at the border zone (BZ) of ischemia were evaluated at week 4.

(C) Infarct sizes were evaluated at week 1 and week 4 and expressed as a percentage of the LV surface area.

(D) LV wall stress in the IZ, in the BZ, and in uninjured regions of the myocardium (i.e., the remote zone [RZ]) was evaluated at week 4.

(E and F) Four weeks after MI injury and treatment, (E) PCr/ATP ratios and (F) the ATP hydrolysis rate were determined in the BZ under both baseline conditions and after a high cardiac workload was induced via catecholamine administration; measurements were obtained via a double-saturation ^{31}P MRS-MST protocol. For (B), (D), (E), and (F), measurements in Sham animals were performed in regions that corresponded to the site of injury in the other experimental groups. Data are presented as mean ± SEM, *$p < 0.05$ versus MI; #$p < 0.05$ versus Patch. (See also Figures S2 and S4 and Table S1.)

results indicate that when hiPSC-CM, hiPSC-SMC, and hiPSC-EC injection is performed through a fibrin patch that has been created over the injection site and contains gelatin microspheres that release IGF-1 into the surrounding tissue, the engraftment rate of the transplanted cells can be as high as 8.97% ± 1.8% 4 weeks after transplantation, which is ~20-fold greater than the engraftment rate observed when adult swine progenitor cells were evaluated in the same animal model (Zeng et al., 2007). Our results also demonstrate that the transplanted cells developed into functioning CMs and vascular cells and that the combination of hiPSC-CM, hiPSC-EC, and hiPSC-SMC injection with patch application led to significant improvements in LV wall stress, infarct size, systolic thickening fraction, vascular density, and ATP turnover rate. These findings are consistent with the concept that the severity of LV functional decline and structural remodeling is proportional to scar size (Pfeffer and Braunwald, 1990) and that LV dilatation and hypertrophy are exacerbated as increases in systolic wall stress propagate from the IZ and BZ to the adjacent myocardium (Pfeffer and Braunwald, 1990).

Previous attempts to isolate hiPSC- or hESC-derived CMs have been only moderately successful. Xu et al. (2006) used a method based on Percoll separation and cardiac body formation

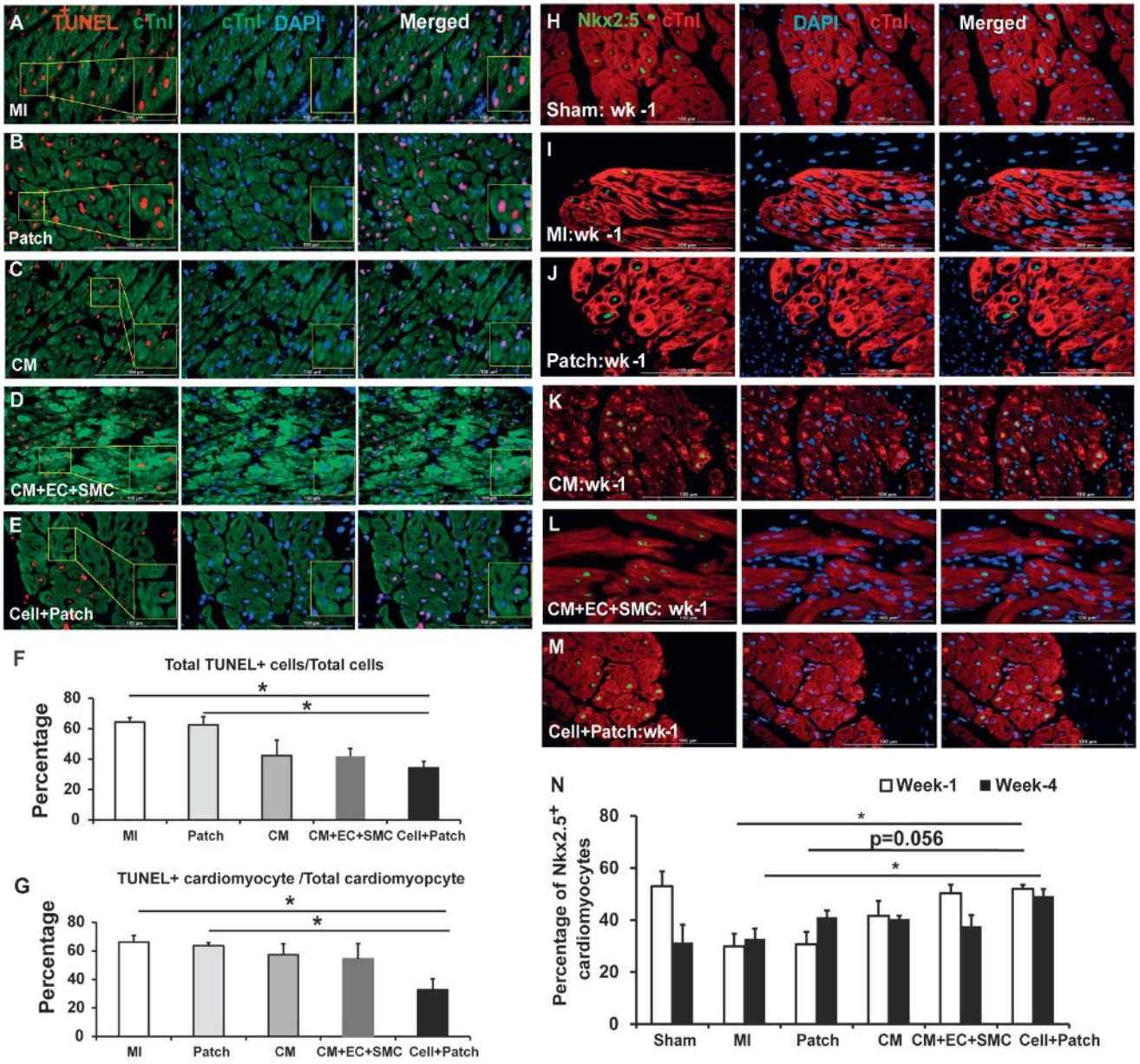

Figure 4. Transplantation of hiPSC-Derived Cardiac Cells Reduces Cardiomyocyte Apoptosis and Enhances Endogenous Cell Survival

(A–G) Apoptotic cells were identified in sections from the border zone of infarct in hearts from animals in the (A) MI, (B) Patch, (C) CM, (D) CM+EC+SMC, and (E) Cell+Patch groups with the TUNEL assay. Muscle fibers were visualized via fluorescent immunostaining for cTnI, and nuclei were counterstained with DAPI; the boxed regions toward the left of (A), (B), (C), (D), and (E) are displayed at higher magnification in the boxes at the right of the images. (F) Apoptosis was quantified as the percentage of cells that were positive for TUNEL staining. (G) Cardiomyocyte apoptosis was quantified as the percentage of cTnI-positive cells that were also positive for TUNEL staining.

(H–N) NkX2.5 expression was evaluated in sections from the border zone of infarct hearts that compared to Sham operated-normal hearts: (H) Sham, (I) MI, (J) Patch, (K) CM, (L) CM+EC+SMC, and (M) Cell+Patch. The immunofluorescent staining positives with anti-Nkx2.5 antibody are shown in green; muscle fibers were visualized via fluorescent immunostaining for cTnI, and nuclei were counterstained with DAPI. (N) The percentage of cardiomyocytes that expressed Nkx2.5 was determined at week 1 and week 4 after injury. Data are presented as mean ± SEM. *$p < 0.05$; scale bar represents 100 μm. (See also Table S2.)

to obtain hESC-CMs, but just 35%–66% of the isolated cells expressed slow myosin heavy chain or cTnT, suggesting that the purity of the obtained population would not be sufficient for use in large-animal models. With the differentiation protocol (Zhang et al., 2012) used here, 68% of the differentiated cells expressed cTnT, and the purity was subsequently increased to >90% via microdissection and preplating, yielding a total of three to four million hiPSC-CMs per well. This yield and purity is sufficient for experiments in large animal models and supports the feasibility of potential clinical trials.

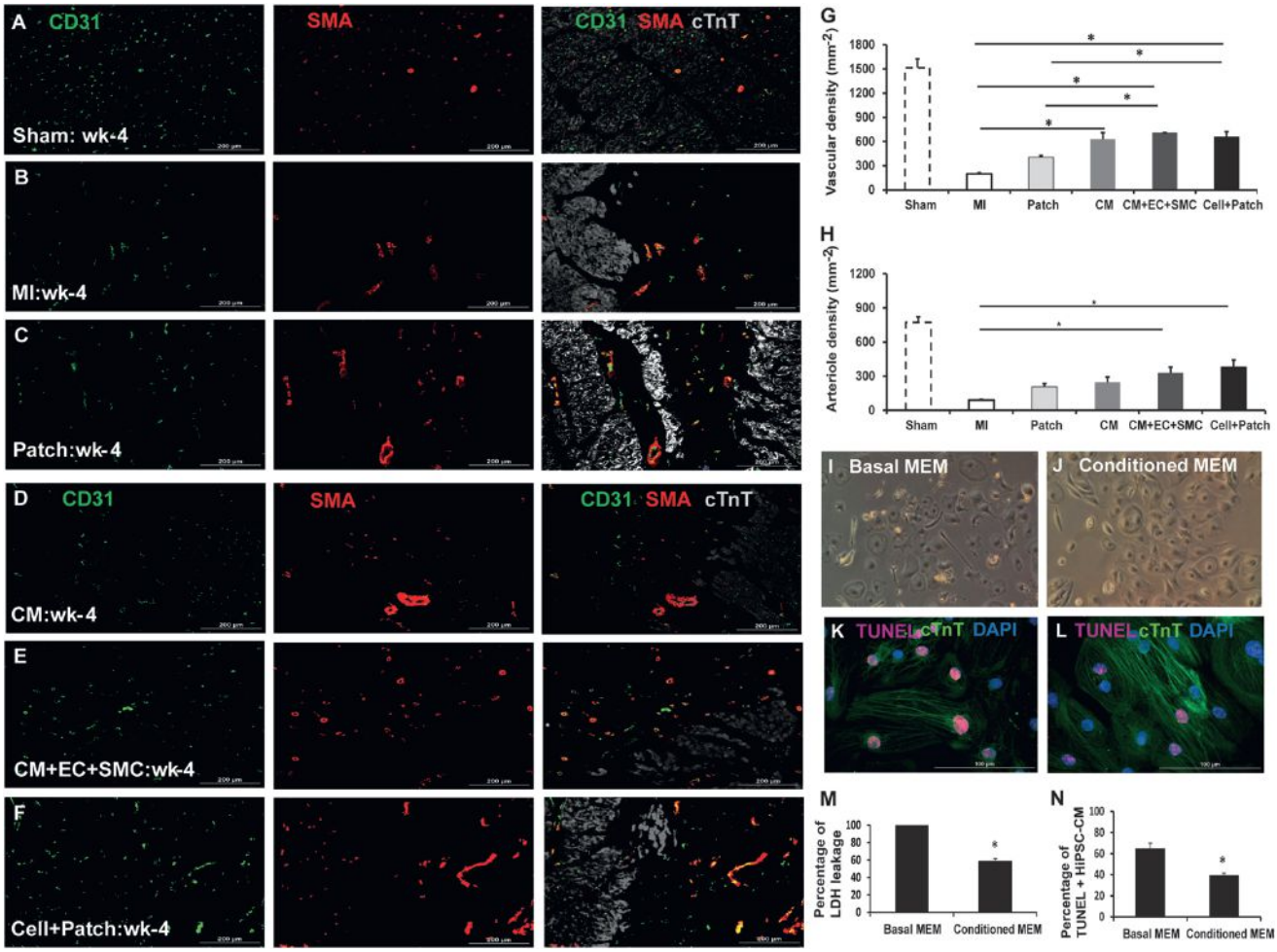

Figure 5. The hiPSC-Derived Cardiac Cells Enhance the Angiogenic Response and Inhibit Apoptosis

Vascular density and arteriole density at week 4 after MI were evaluated in sections from the border zone of infarct in the hearts of animals from the (A) Sham, (B) MI, (C) Patch, (D) CM, (E) CM+EC+SMC, and (F) Cell+Patch groups via immunofluorescent staining for CD31 and SMA; muscle fibers were visualized via cTnT staining. (G) Vascular density was determined by counting CD31+ vascular structures, and (H) arteriole density was determined by counting vascular structures that expressed both CD31 and SMA. *$p < 0.05$; scale bar represents 200 μm.

(I–N) hiPSC-CMs were cultured under hypoxic conditions in (I) basal media (Basal MEM) or (J) media collected from the hiPSC-derived vascular cells (Conditioned MEM) for 48 hr; then, (K and L) apoptotic cells were identified via the TUNEL assay, (M) cytotoxicity was quantified via the intensity of lactate dehydrogenase fluorescence observed in the media, and (N) apoptosis was quantified as the percentage of cells that were positive for TUNEL staining. *$p < 0.05$ versus basal MEM; magnification: 100× for (I) and (J); scale bar represents 100 μm. Data are presented as mean ± SEM. (See also Figure S5 and Table S2.)

One of the primary factors limiting the effectiveness of cell therapy is the low proportion of transplanted cells that survive in the recipient heart a few weeks after transplantation (Beauchamp et al., 1999; Qu et al., 1998; Tang et al., 2010; Zeng et al., 2007). Coadministration of a cytoprotective agent, such as IGF-1, can improve cell survival rate (Davis et al., 2006; Li et al., 1997; Wang et al., 1998), but the administered cells may still be lost after reestablishment of blood flow or be forced out of the myocardium along the needle track by high pressure during systolic contraction. Notably, a considerably higher rate of engraftment was observed in hearts from the Cell+Patch group, which was 2-fold greater than the rate observed in Cell group hearts, ~2.5-fold greater than observed in CMs hearts, and ~4-fold greater than when only hiPSC-derived ECs and SMCs were incorporated into a growth-factor-enriched patch (Shimizu et al., 2002; Xiong et al., 2013). This can be partially attributed to the fibrin patch itself, as the patch forms a physical barrier preventing ejection of the cells into the epicardial space while providing a prolonged IGF-1 supply to promote cell survival.

The overall engraftment rate for the three cell populations administered to Cell+Patch animals was ~9% and the proportion of cells that expressed EC-, SMC-, or CM-specific markers are ~34%, ~40%, and ~27%, respectively. Substantial engraftment of stem cell-derived CMs has also been observed in a primate model of postinfarction LV remodeling (Chong et al., 2014): ~2% of the LV was composed of engrafted cells, but the precise engraftment rate could not be calculated because the engrafted cells were not counted. However, macaque hearts are

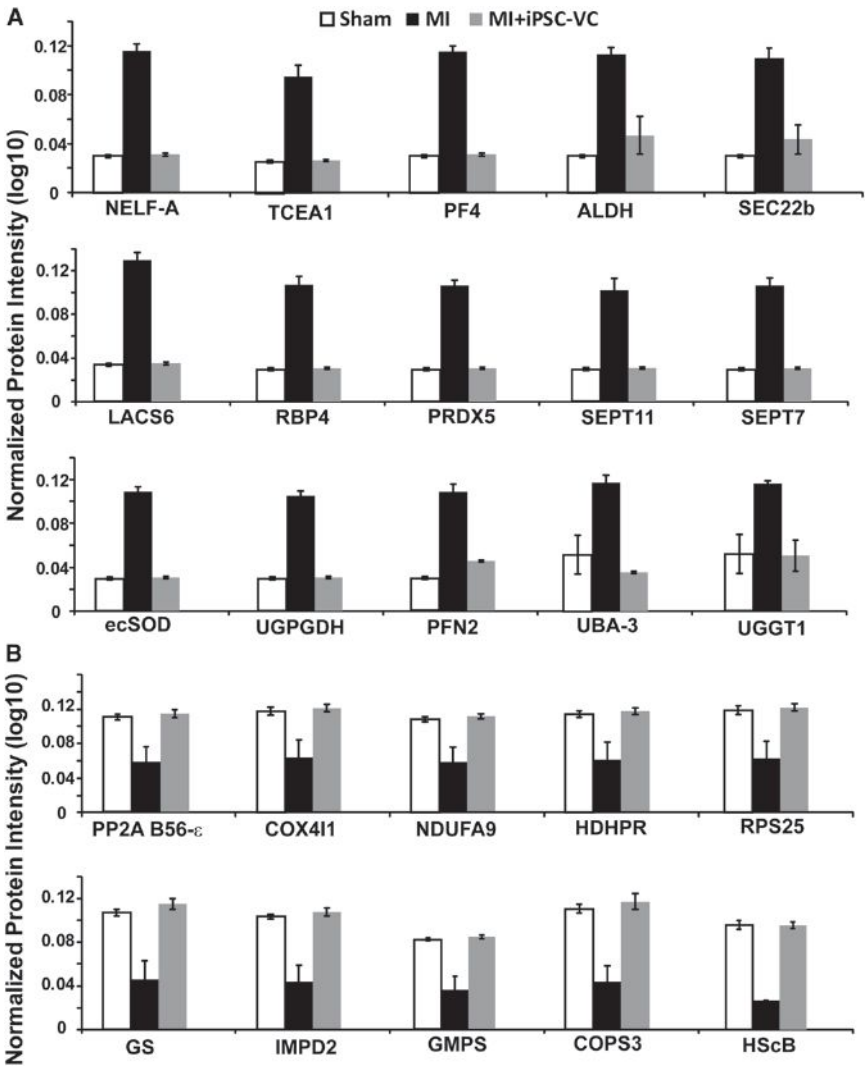

Figure 6. Protein Expression Levels Are Significantly Altered in MI and Partially Restored by Cell Transplantation

Myocardial protein expression profiles were evaluated in animals that had been treated with (MI+iPSC-VC) or without (MI) hiPSC-VC transplantation after experimentally induced MI; control assessments were performed in animals that underwent all surgical procedures for the induction of MI except for the ligation step (SHAM); results are displayed for 25 proteins whose expression levels (A) increased or (B) decreased after MI and were restored to normal levels by cell therapy. NELF-A, negative elongation factor A; TCEA1, transcription elongation factor A protein 1; PF4, platelet factor 4; ALDH, aldehyde dehydrogenase (mitochondrial); SEC22b, vesicle-trafficking protein SEC22b; LACS6, long-chain-fatty-acid-CoA ligase 6; RBP4, retinol-binding protein 4; PRDX5, peroxiredoxin-5 (mitochondrial); SEPT11, septin-11; SEPT7, septin-7; ecSOD, extracellular superoxide dismutase (Cu-Zn); UGPGDH, UDP-glucose-6-dehydrogenase; PFN2, profiling-2; UBA-3, NEDD8-activating enzyme E1 catalytic subunit; UGGT1, UDP-glucose:glycoprotein glucosyltransferase 1; PP2A B56-ε, serine/threonine-protein phosphatase 2A 56 kDa regulatory subunit ε isoform; COX4I1, cytochrome C oxidase subunit 4 isoform 1, mitochondrial; NDUFA9, NADH dehydrogenase (ubiquinone) 1 α subcomplex subunit 2; HDHPR, dihydropteridine reductase; RPS25, 40S ribosomal protein S25; GS, glutamine synthetase; IMPD2, inosine-5′-monophosphate dehydrogenase 2; GMPS, GMP synthase (glutamine-hydrolyzing); COPS3, COP9 sinalosome complex subunit 3; HScB, iron-sulfur cluster co-chaperone protein HScB (mitochondrial). Data are presented as mean ± SEM. (See also Figures S6 and S7.)

approximately one-sixth the size of human hearts (37–52 g versus ~300 g), which contain approximately three billion CMs, and ~70% of cardiac mass is contained in the LV; thus, the LVs of the animals used in the primate study probably contained ~350 million CMs, approximately seven million of which (i.e., 2% of 350 million) were the transplanted hESC-CMs. Since one billion hiPSC-CMs were administered to each macaque, the engraftment rate appears to have been ~0.7%, which is consistent with other rates reported in the literature (Zeng et al., 2007) and ~10-fold lower that the rate of hiPSC-CM engraftment observed in the Cell+Patch animals in the present study.

One of the most critical concerns associated with cardiac cell therapy is the development of arrhythmogenic complications. The study by Chong et al. (2014) illustrates that transplantation of human CMs to large animal post-MI models can unmask potential arrhythmic complications that are not observed in comparable small animal models (Shiba et al., 2012). All the monkeys studied by Chong et al. (2014) that received hESC-CMs developed spontaneous arrhythmia during the EKG follow-up evaluations. In the present study, we used a strategy of a smaller cell dose and aiming at mobilization of the endogenous cardiac progenitors, which we have reported earlier (Zeng et al., 2007; Xiong et al., 2013). We used a 100-fold lower dose of hiPSC-CMs compared to Chong's report and found no increase of spontaneous or PES-induced arrhythmia in any of the animals that received cell therapy. The remarkably better electrical stability achieved with our approach may be attributable, in part, to the smaller cell dose used (ten million versus one billion) and targeting the cytokine-associated mobilization of the endogenous progenitors (Xiong et al., 2013; Zeng et al., 2007). Electromechanical connectivity may be more extensive between native tissues and tissues generated through endogenous repair mechanisms than between native tissues and large piece of cardiac tissue that develop directly from the engrafted cells. Coadministration of ECs has been linked to the regulation of cardiovascular physiology (Brutsaert, 2003; Hsieh et al., 2006) and could have further improved myocardial recovery primarily through the enhancement of cytokine-associated mechanisms. These data also indicate that strategies designed to promote the paracrine effect of transplanted CMs and ECs maybe be more desirable in cardiac cell therapy.

Transplantation of hiPSC-derived cells was also associated with increases in the expression of Nkx2.5 in host cardiomyocytes,

which is known to protect cardiomyocytes from oxidative damage (Toko et al., 2002). Furthermore, myocardial perfusion is maintained by the regulatory activity of small resistant vessels (Frame and Sarelius, 1993), so the significant increase in myocardial arteriole density observed in the BZ of Cell+Patch-treated hearts also probably contributed to declines in apoptosis and to the preservation of contractile function. The increase in arteriole density appears to have occurred through the sprouting of preexisting microvessels in the BZ of the treated hearts, because nearly all of the vessels were GFP negative. The increase in arteriole density was also accompanied by a significant improvement in the myocardial ATP turnover rate (Figure 3F). The calculated rate, which incorporates the rates associated with all enzymatic processes that support contraction and relaxation as well as the rates generated by rapid near-equilibrium enzymes, was markedly reduced at the BZ of infarction in MI hearts, while measurements under high workload conditions were significantly greater in Cell+Patch animals than in animals from either the MI or Patch group.

Cyclosporine was administered to animals from all treatment groups to reduce the likelihood of immune rejection in animals treated with the hiPSC-derived cells. Nevertheless, assessments of $CD11b^+$ cell density suggest that the immune response was both elevated and delayed in Patch, CM, CM+EC+SMC, and Cell+Patch animals (though the increase was significant in only the Cell+Patch group). Both the patch and the transplanted cells could have contributed to this increase, because the patch was created by combining fibrin with thrombin, which is known to amplify the inflammation induced by ischemia (Chen and Dorling, 2009), and because the transplanted cells released inflammatory cytokines such as MCP-1 and IL-6. Notably, IL-6 production was 8-fold and 20-fold higher in hiPSC-ECs than in hiPSC-CMs or hiPSC-SMCs, respectively. Future study may be required to find an optimal dosage of cyclosporine or addition of other immunosuppression regimen, such as FK506, to minimize the immune rejection and achieve higher cell engraftment rate.

In conclusion, the studies described in this report evaluate the combined use of hiPSC-ECs, hiPSC-SMCs, and hiPSC-CMs in a porcine model of ischemia reperfusion myocardial injury. Our results demonstrate that when the enhanced cell delivery was achieved by an IGF-1-containing fibrin patch, the engraftment rate was remarkably greater than achieved with any other delivery method used in the porcine IR model (Zeng et al., 2007). Furthermore, the combination of all three cell types with extended, patch-mediated IGF-1 administration was associated with significant improvements in myocardial wall stress, apoptosis, arteriole density, metabolism, and contractile function. Collectively, these observations support the feasibility of future mechanistic studies of hiPSC-derived cardiac cells in large animal models. Studies with longer follow-up periods will also be needed to ensure that the benefits of treatment are maintained and to fully characterize any potential adverse effects that may be associated with this promising therapeutic modality.

EXPERIMENTAL PROCEDURES

Generation and Characterization of hiPSC-Derived Cardiac Cells

The hiPSC-CMs, hiPSC-SMCs, and hiPSC-ECs used in this study were generated from two hiPSC lines: DriPS16 (Cell+Patch group) and GRiPS (for the CM and CM+EC+SMC groups). Both hiPSC lines were reprogrammed from male, human, neonatal, dermal fibroblasts by transfecting cells with either lentivirus (DriPS16) or Sendai virus (GRiPS) coding for OCT4, SOX2, KLF4, and C-MYC and then engineered to constitutively express GFP. Cells were cultured in hiPSC growth medium with irradiated mouse embryonic fibroblasts and passaged every 6–7 days (Wilber et al., 2007).

hiPSCs were differentiated into ECs and SMCs as described previously (Hill et al., 2010; Woll et al., 2008). hiPSC-ECs were characterized via the expression of CD31, CD144, and vWF-8 (Xiong et al., 2012). hiPSC-SMCs were characterized via the expression of α-smooth muscle actin (SMA), SM22, and calponin.

In vitro cytoprotection assays are detailed in Supplemental Experimental Procedures

Paracrine Factor Release from Cultured hiPSC-CMs, ECs, and SMCs

hiPSC-CMs (3.5×10^5) and hiPSC-SMCs (3.5×10^5) were cultured in 6-well plates, washed three times with DPBS, and then cultured in 1 ml RPMI basal medium; hiPSC-ECs (4×10^5) were cultured in 1 ml EBM2 basal medium. The medium was collected 48 hr later and analyzed with the Human Angiogenesis Antibody Array G1 Array (RayBiotech). Measurements were corrected for background signals via control assessments with basal media that had been exposed to identical conditions.

Synthesis of IGF-containing microspheres and patch manufacture are detailed in Supplemental Experimental Procedures.

Porcine IR Injury Model and Treatment

Experiments were performed in female Yorkshire swine (~13 kg, 45 days of age, Manthei hog farm, Elk River, MN) (Xiong et al., 2012). The experimental protocol was approved by the IACUC of the University of Minnesota, and all experimental procedures were performed in accordance with the Animal Use Guidelines of the University of Minnesota and consistent with the National Institutes of Health *Guide for the Care and Use of Laboratory Animals* (NIH publication No 85-23).

A total of 108 pigs underwent the ischemia reperfusion (IR) protocol (Table S1). Ninety-two pigs were used in the first part of the study: two pigs died of ventricular fibrillation during occlusion, and one died of cardiac arrhythmia 1 week after IR injury while the MRI data were being collected. The remaining 89 pigs were divided into six groups. Animals in the CM+EC+SMC and Cell+Patch groups were treated by injecting two million hiPSC-CMs, two million hiPSC-ECs, and two million hiPSC-SMCs (six million cells total) directly into the injured myocardium; for animals in the Cell+Patch group, the needle was inserted through an IGF-1-containing fibrin patch that had been created over the site of injury. Animals in the Patch group were treated with the patch alone, and both the patch and the cells were withheld from animals in the MI group. Animals in the SHAM group underwent all surgical procedures for the induction of IR injury except for the ligation step and recovered without any of the experimental treatments. Sixteen pigs were used in loop recorder study. The Patch+CM group used in the arrhythmogenesis experiments exposed to a protocol of fibrin patch enhanced delivery of ten million hiPSC-CMs on surface of the injured myocardium (Table S1).

Patch application was performed by suspending 5 mg of microspheres (loaded with 2.5 μg IGF-1) in 1 ml fibrinogen solution (25 mg/ml); then, the fibrinogen solution was coinjected with 1 ml thrombin solution (80 NIH units/ml, supplemented with 2 μl 400 mM $CaCl_2$ and 200 mM Ɛ-aminocaproic acid) into a 2.3-cm-diameter plastic ring that had been placed on the epicardium of the infarcted region to serve as a mold for the patch; the mixture usually solidified within 30 s (Xiong et al., 2012). Cells were suspended in 1 ml MEM and administered via ten intramyocardial injections (0.1 ml/injection).

Cardiac MRI and MR Spectroscopy are detailed in Supplemental Experimental Procedures

The ECG Monitoring and Programmed Electrostimulation Physiology Studies

The implantable loop recorders (Medtronic-Reveal) were placed in the left paraspinal area inferior to the angle of the scapula in the subcutaneous plane. It was sutured in the place where the best electrograms were obtained and there was no evidence of myopotential noise. It was programmed in the conventional manner to document VT and asystole. The loop recorder was

interrogated at the time of explantation when the animals were sacrificed 4 weeks after the cell therapy.

The programmed electrostimulation physiology studies (PES study) were done at the time of sacrifice in 4 weeks. The PES study was done from the epicardium in an open-chest fashion. The PES study was done from two sites: one close to the infarct and one remote from the infarct. The study was done with a Medtronic screw lead in the epicardium and the Bard system was used for stimulation. It was done at two cycle lengths at 400 ms and 300 ms drive trains. Four additional stimuli were given till effective refractory period (ERP) was reached or 160 ms.

hiPSC-EC, hiPSC-SMC, and hiPSC-CM engraftment rate and immunohistochemical evaluations are detailed in Supplemental Experimental Procedures.

Experimental Procedures for proteomics are detailed in Supplemental Experimental Procedures.

Statistical Analysis

Results are presented as mean ± SEM. Comparisons among groups were analyzed for significance with one-way ANOVA. A value of $p < 0.05$ was considered significant. Results identified as significant via ANOVA were reanalyzed with the Tukey correction. Statistical analyses were performed with SPSS software (version 20).

SUPPLEMENTAL INFORMATION

Supplemental Information includes Supplemental Experimental Procedures, six figures, two tables, and three movies and can be found with this article online at http://dx.doi.org/10.1016/j.stem.2014.11.009.

ACKNOWLEDGMENTS

The authors would like to thank W. Kevin Meisner, Ph.D., E.L.S., for his editorial assistance. This work was supported by US Public Health Service grants NIH RO1s, HL UO1 100407, HL UO1 099773, and P41RR08079.

Received: April 21, 2013
Revised: March 24, 2014
Accepted: November 12, 2014
Published: December 4, 2014

REFERENCES

Beauchamp, J.R., Morgan, J.E., Pagel, C.N., and Partridge, T.A. (1999). Dynamics of myoblast transplantation reveal a discrete minority of precursors with stem cell-like properties as the myogenic source. J. Cell Biol. *144*, 1113–1122.

Brutsaert, D.L. (2003). Cardiac endothelial-myocardial signaling: its role in cardiac growth, contractile performance, and rhythmicity. Physiol. Rev. *83*, 59–115.

Burridge, P.W., Keller, G., Gold, J.D., and Wu, J.C. (2012). Production of de novo cardiomyocytes: human pluripotent stem cell differentiation and direct reprogramming. Cell Stem Cell *10*, 16–28.

Caspi, O., Huber, I., Kehat, I., Habib, M., Arbel, G., Gepstein, A., Yankelson, L., Aronson, D., Beyar, R., and Gepstein, L. (2007). Transplantation of human embryonic stem cell-derived cardiomyocytes improves myocardial performance in infarcted rat hearts. J. Am. Coll. Cardiol. *50*, 1884–1893.

Chen, D., and Dorling, A. (2009). Critical roles for thrombin in acute and chronic inflammation. J. Thromb. Haemost. *7* (1), 122–126.

Chong, J.J., Yang, X., Don, C.W., Minami, E., Liu, Y.W., Weyers, J.J., Mahoney, W.M., Van Biber, B., Cook, S.M., Palpant, N.J., et al. (2014). Human embryonic-stem-cell-derived cardiomyocytes regenerate non-human primate hearts. Nature *510*, 273–277.

Cibelli, J., Emborg, M.E., Prockop, D.J., Roberts, M., Schatten, G., Rao, M., Harding, J., and Mirochnitchenko, O. (2013). Strategies for improving animal models for regenerative medicine. Cell Stem Cell *12*, 271–274.

Davis, M.E., Hsieh, P.C., Takahashi, T., Song, Q., Zhang, S., Kamm, R.D., Grodzinsky, A.J., Anversa, P., and Lee, R.T. (2006). Local myocardial insulin-like growth factor 1 (IGF-1) delivery with biotinylated peptide nanofibers improves cell therapy for myocardial infarction. Proc. Natl. Acad. Sci. USA *103*, 8155–8160.

Frame, M.D., and Sarelius, I.H. (1993). Regulation of capillary perfusion by small arterioles is spatially organized. Circ. Res. *73*, 155–163.

Hill, K.L., Obrtlikova, P., Alvarez, D.F., King, J.A., Keirstead, S.A., Allred, J.R., and Kaufman, D.S. (2010). Human embryonic stem cell-derived vascular progenitor cells capable of endothelial and smooth muscle cell function. Exp. Hematol. *38*, 246–257, e1.

Hsieh, P.C., Davis, M.E., Lisowski, L.K., and Lee, R.T. (2006). Endothelial-cardiomyocyte interactions in cardiac development and repair. Annu. Rev. Physiol. *68*, 51–66.

Laflamme, M.A., Chen, K.Y., Naumova, A.V., Muskheli, V., Fugate, J.A., Dupras, S.K., Reinecke, H., Xu, C., Hassanipour, M., Police, S., et al. (2007). Cardiomyocytes derived from human embryonic stem cells in pro-survival factors enhance function of infarcted rat hearts. Nat. Biotechnol. *25*, 1015–1024.

Li, Q., Li, B., Wang, X., Leri, A., Jana, K.P., Liu, Y., Kajstura, J., Baserga, R., and Anversa, P. (1997). Overexpression of insulin-like growth factor-1 in mice protects from myocyte death after infarction, attenuating ventricular dilation, wall stress, and cardiac hypertrophy. J. Clin. Invest. *100*, 1991–1999.

Pfeffer, M.A., and Braunwald, E. (1990). Ventricular remodeling after myocardial infarction. Experimental observations and clinical implications. Circulation *81*, 1161–1172.

Qu, Z., Balkir, L., van Deutekom, J.C., Robbins, P.D., Pruchnic, R., and Huard, J. (1998). Development of approaches to improve cell survival in myoblast transfer therapy. J. Cell Biol. *142*, 1257–1267.

Shiba, Y., Fernandes, S., Zhu, W.Z., Filice, D., Muskheli, V., Kim, J., Palpant, N.J., Gantz, J., Moyes, K.W., Reinecke, H., et al. (2012). Human ES-cell-derived cardiomyocytes electrically couple and suppress arrhythmias in injured hearts. Nature *489*, 322–325.

Shimizu, T., Yamato, M., Isoi, Y., Akutsu, T., Setomaru, T., Abe, K., Kikuchi, A., Umezu, M., and Okano, T. (2002). Fabrication of pulsatile cardiac tissue grafts using a novel 3-dimensional cell sheet manipulation technique and temperature-responsive cell culture surfaces. Circ. Res. *90*, e40.

Tang, X.L., Rokosh, G., Sanganalmath, S.K., Yuan, F., Sato, H., Mu, J., Dai, S., Li, C., Chen, N., Peng, Y., et al. (2010). Intracoronary administration of cardiac progenitor cells alleviates left ventricular dysfunction in rats with a 30-day-old infarction. Circulation *121*, 293–305.

Toko, H., Zhu, W., Takimoto, E., Shiojima, I., Hiroi, Y., Zou, Y., Oka, T., Akazawa, H., Mizukami, M., Sakamoto, M., et al. (2002). Csx/Nkx2-5 is required for homeostasis and survival of cardiac myocytes in the adult heart. J. Biol. Chem. *277*, 24735–24743.

van Laake, L.W., Passier, R., Doevendans, P.A., and Mummery, C.L. (2008). Human embryonic stem cell-derived cardiomyocytes and cardiac repair in rodents. Circ. Res. *102*, 1008–1010.

Wang, L., Ma, W., Markovich, R., Chen, J.W., and Wang, P.H. (1998). Regulation of cardiomyocyte apoptotic signaling by insulin-like growth factor I. Circ. Res. *83*, 516–522.

Wilber, A., Linehan, J.L., Tian, X., Woll, P.S., Morris, J.K., Belur, L.R., McIvor, R.S., and Kaufman, D.S. (2007). Efficient and stable transgene expression in human embryonic stem cells using transposon-mediated gene transfer. Stem Cells *25*, 2919–2927.

Woll, P.S., Morris, J.K., Painschab, M.S., Marcus, R.K., Kohn, A.D., Biechele, T.L., Moon, R.T., and Kaufman, D.S. (2008). Wnt signaling promotes hematoendothelial cell development from human embryonic stem cells. Blood *111*, 122–131.

Xiong, Q., Ye, L., Zhang, P., Lepley, M., Swingen, C., Zhang, L., Kaufman, D.S., and Zhang, J. (2012). Bioenergetic and functional consequences of cellular therapy: activation of endogenous cardiovascular progenitor cells. Circ. Res. *111*, 455–468.

Xiong, Q., Ye, L., Zhang, P., Lepley, M., Tian, J., Li, J., Zhang, L., Swingen, C., Vaughan, J.T., Kaufman, D.S., and Zhang, J. (2013). Functional consequences

of human induced pluripotent stem cell therapy: myocardial ATP turnover rate in the in vivo swine heart with postinfarction remodeling. Circulation *127*, 997–1008.

Xu, C., Police, S., Hassanipour, M., and Gold, J.D. (2006). Cardiac bodies: a novel culture method for enrichment of cardiomyocytes derived from human embryonic stem cells. Stem Cells Dev. *15*, 631–639.

Zeng, L., Hu, Q., Wang, X., Mansoor, A., Lee, J., Feygin, J., Zhang, G., Suntharalingam, P., Boozer, S., Mhashilkar, A., et al. (2007). Bioenergetic and functional consequences of bone marrow-derived multipotent progenitor cell transplantation in hearts with postinfarction left ventricular remodeling. Circulation *115*, 1866–1875.

Zhang, J., Klos, M., Wilson, G.F., Herman, A.M., Lian, X., Raval, K.K., Barron, M.R., Hou, L., Soerens, A.G., Yu, J., et al. (2012). Extracellular matrix promotes highly efficient cardiac differentiation of human pluripotent stem cells: the matrix sandwich method. Circ. Res. *111*, 1125–1136.

Cell Stem Cell
Clinical Progress

Human iPSC-Derived Oligodendrocyte Progenitor Cells Can Myelinate and Rescue a Mouse Model of Congenital Hypomyelination

Su Wang,[1] Janna Bates,[1] Xiaojie Li,[1] Steven Schanz,[1] Devin Chandler-Militello,[1] Corri Levine,[1] Nimet Maherali,[2] Lorenz Studer,[3] Konrad Hochedlinger,[2] Martha Windrem,[1] and Steven A. Goldman[1,*]
[1]Center for Translational Neuromedicine and Department of Neurology, University of Rochester Medical Center, Rochester, NY, 14642, USA
[2]Massachusetts General Hospital Center for Regenerative Medicine and Harvard Stem Cell Institute, 42 Church Street, Cambridge, MA, 02138, USA
[3]Developmental Biology Program, Sloan-Kettering Institute, 1275 York Avenue, New York, NY, 10065, USA
*Correspondence: steven_goldman@urmc.rochester.edu
http://dx.doi.org/10.1016/j.stem.2012.12.002

SUMMARY

Neonatal engraftment by oligodendrocyte progenitor cells (OPCs) permits the myelination of the congenitally dysmyelinated brain. To establish a potential autologous source of these cells, we developed a strategy by which to differentiate human induced pluripotent stem cells (hiPSCs) into OPCs. From three hiPSC lines, as well as from human embryonic stem cells (hESCs), we generated highly enriched OLIG2$^+$/PDGFRα^+/NKX2.2$^+$/SOX10$^+$ human OPCs, which could be further purified using fluorescence-activated cell sorting. hiPSC OPCs efficiently differentiated into both myelinogenic oligodendrocytes and astrocytes, in vitro and in vivo. Neonatally engrafted hiPSC OPCs robustly myelinated the brains of myelin-deficient shiverer mice and substantially increased their survival. The speed and efficiency of myelination by hiPSC OPCs was higher than that previously observed using fetal-tissue-derived OPCs, and no tumors from these grafts were noted as long as 9 months after transplant. These results suggest the potential utility of hiPSC-derived OPCs in treating disorders of myelin loss.

INTRODUCTION

A number of strategies have been developed for the cell-based repair of demyelinated lesions of both the brain and spinal cord (Ben-Hur and Goldman, 2008; Franklin and Ffrench-Constant, 2008; Goldman et al., 2012). In particular, human glial progenitor cells capable of oligodendrocytic maturation and myelination have been derived from both fetal and adult human brain tissue (Dietrich et al., 2002; Roy et al., 1999; Windrem et al., 2004), as well as from human embryonic stem cells (hESCs) (Hu et al., 2009b; Izrael et al., 2007; Keirstead et al., 2005), and have proven effective in experimental models of both congenitally dysmyelinated (Sim et al., 2011; Windrem et al., 2004; Windrem et al., 2008) and adult demyelinated (Windrem et al., 2002) brain and spinal cord. Yet these successes in immunodeficient mice notwithstanding, immune rejection has thus far hindered the use of allogeneic human cells as transplant vectors. Concern for donor cell rejection has been especially problematic in regards to adult demyelinating diseases such as multiple sclerosis, in which the inflammatory processes underlying the disorders can present an intrinsically hostile environment to any allogeneic graft (Keyoung and Goldman, 2007).

To address this issue, we sought to develop a robust protocol for the scalable production of myelinogenic oligodendrocytes (OLs) from skin-derived human induced pluripotent stem cells (hiPSCs). By constructing hiPSCs from skin or blood derived from a particular patient, one may hope to generate sufficient oligodendrocyte progenitor cells (OPCs) to provide that patient with myelinogenic autografts largely, though perhaps not completely, free of rejection risk. To this end, in this study we developed protocols by which we have generated highly enriched populations of human OPCs from multiple lines of both hiPSCs and hESCs. These cells reliably progress through the serial stages of neural stem cell, glial progenitor cell, and both oligodendrocytic and astrocytic differentiation in vitro. On that basis, we assessed the myelination competence of the hiPSC-derived OPCs (hiPSC OPCs) in a genetic model of congenital hypomyelination, the shiverer mouse, and established their ability to efficiently and robustly myelinate the hypomyelinated shiverer brain with no evidence of either tumorigenesis or heterotopic nonglial differentiation. The transplanted animals survived significantly longer than their untreated counterparts, and many were spared early death, a striking clinical rescue from a fatal hereditary disorder via an iPSC-based strategy. These data thus strongly support the utility of hiPSCs as a feasible and effective source of both OPCs and their derived myelinogenic central OLs and suggest the potential of these cells as therapeutic vectors in disorders of central myelin.

RESULTS

Human iPSCs Can Be Efficiently Directed to Glial Progenitor Cell Fate

We used four different iPSC lines from three different sources for this study; these included WA09/H9 hESCs (Thomson et al., 1998); keratinocyte-derived K04 hiPSCs (Maherali et al., 2008); and fibroblast-derived C14 and C27 hiPSCs (Chambers et al., 2009). We selected specific features of several published

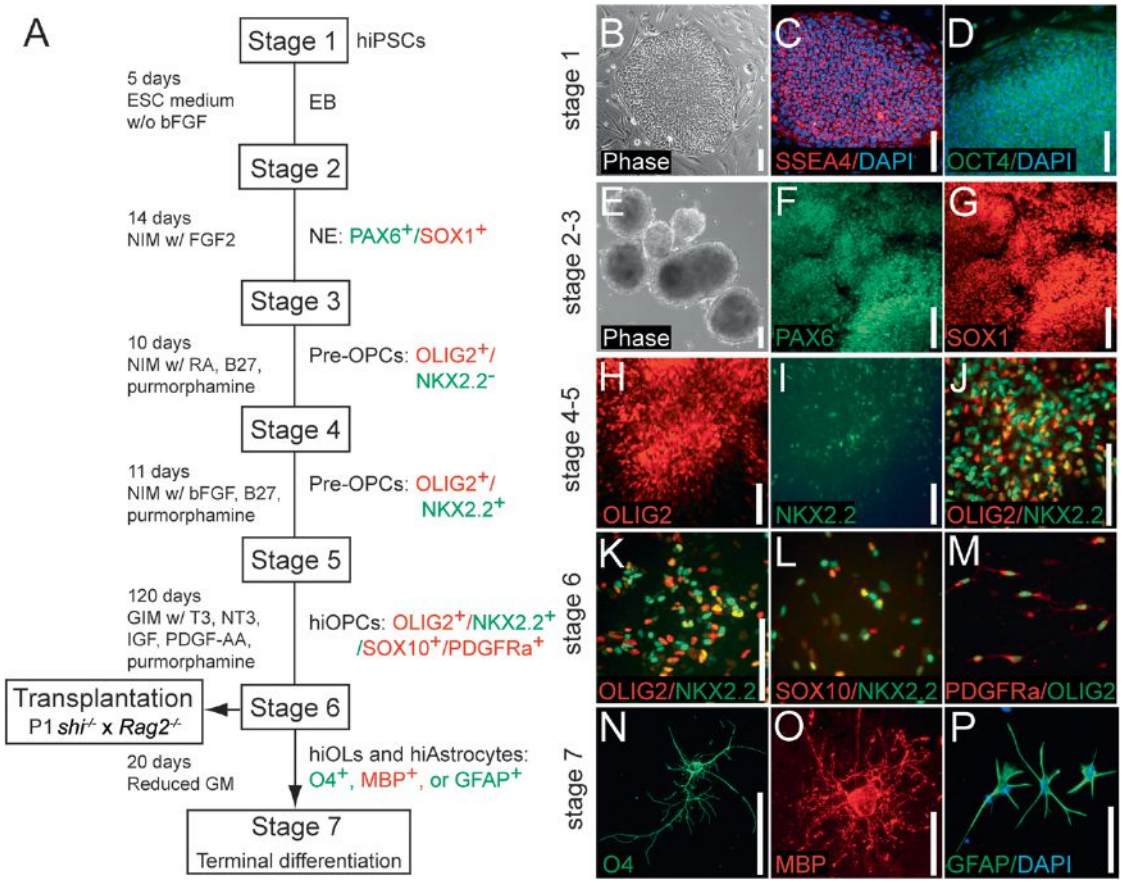

Figure 1. hiPSCs Can Be Directed into OPC Fate

(A) A schematic protocol for directed differentiation of hiPSCs into OPCs. Embryoid bodies (EBs) were differentiated from undifferentiated hiPSCs (stage 1) from DIV 0–5. EBs were then differentiated as neuroepithelial (NE) cells in neural induction media (NIM; see Experimental Procedures) with bFGF.

(B–D) Undifferentiated hiPSCs (stage 1) and hiPSC colonies expressed the pluripotency markers SSEA4 and OCT4. (B) Phase contrast. (C) SSEA4 (red); DAPI (blue). (D) OCT4 (green); DAPI (blue).

(E–G) EBs (E) and neuroepithelial cells (F and G) could be generated from hiPSCs (stages 2 and 3). hiPSC-derived neuroepithelial cells at this stage expressed the neuroepithelial markers PAX6 and SOX1. (E) Phase contrast. (F) PAX6 (green). (G) SOX1 (red).

(H and I) $OLIG2^+$ and $NKX2.2^-$ early glial progenitor cells appeared under the influence of retinoic acid (RA) and purmorphamine, a small-molecule agonist of sonic hedgehog signaling. By stage 4, OLIG2 was expressed in early pre-OPCs, which then serially developed NKX2.2 expression. (H) OLIG2 (red). (I) NKX2.2 (green).

(J) $OLIO2^+/NKX2.2^-$ early pre-OPCs were differentiated into later-stage $OLIG2^+/NKX2.2^+$ pre-OPCs when RA was replaced by bFGF at stage 5. OLIG2 (red); NKX2.2 (green).

(K–M) Pre-OPCs were further differentiated into bipotential OPCs in GIM (glial induction media; see Experimental Procedures) supplemented with PDGF-AA, T3, NT3, and IGF. Stage 6 was extended as long as 3–4 months for maximization of the production of myelinogenic OPCs. By the time of transplant, these cells expressed not only OLIG2 and NKX2.2 (K), but also SOX10 (L) and PDGFRα (M). By the end of stage 6, hiPSC OPCs could be identified as $OLIG2^+/NKX2.2^+/SOX10^+/PDGFR\alpha^+$. (K) OLIG2 (red); NKX2.2 (green). (L) SOX10 (red); NKX2.2 (green). (M) PDGFRα (red), OLIG2 (green).

(N–P) In vitro terminal differentiation of hiPSC OPCs into hiPSC-derived OLs (hiOLs), identified by $O4^+$ (N) and MBP^+ (O). OLs and $GFAP^+$ astrocytes (P) arose with reduction in glial mitogens. (N) O4 (green). (O) MBP (red). (P) GFAP(green); DAPI (blue).

Scale: 100 μm (B–N, P) and 25 μm (O). See also Figure S1.

protocols for the production of glial progenitor cells from hESCs (Hu et al., 2009b; Izrael et al., 2007) and then optimized the resultant hybrid protocol for use with WA09/H9 hESCs. We then modified the resultant protocol to further optimize its efficiency with the three hiPSC lines, which were derived in different labs, from different cell sources, and using different reprogramming protocols (Chambers et al., 2009; Maherali et al., 2008) (Figure S1 available online). We found that the resultant six-stage OPC differentiation protocol, which spans a range of 110–150 days in vitro as detailed in the Supplemental Experimental Procedures and schematized in Figure 1, efficiently generated human OPCs (hOPCs) as well as their mature progeny, including both astrocytes and OLs, from hESCs and hiPSCs alike (Figures 1B–1P). Its efficiency of OPC production, as defined by the incidence of $OLIG2^+/NKX2.2^+$ gliogenic (Qi et al., 2001; Zhou et al., 2001; Zhou et al., 2000) cell clusters in stage 6, ranged from 45.4 ± 20.3% in WA09/H9-derived hESCs to 73.8 ± 8.7%, 78.9 ± 6.1%, and 79.5 ± 8.5% in K04-, C14-, and C27-derived OPCs, respectively (all data are provided as means ± SEM; Figures 2A and S2). Thus, each of the hiPSC and hESC lines could be directed into highly enriched preparations of $OLIG2^+/PDGFR\alpha^+/NKX2.2^+/SOX10^+$ OPCs. Indeed, the efficiencies of

A

Stage	Markers	H9	K04	C14	C27
3	PAX6$^+$	80 ± 9.9%	51 ± 8.4%	79 ± 6.5%	79 ± 9.6%
	SOX1$^+$	76 ± 8.4%	62 ± 10.9%	92 ± 3.8%	94 ± 2.7%
	PAX6$^+$/SOX1$^+$	75 ± 8.8%	52 ± 7.5%	78 ± 4.7%	76 ± 7.0%
4	OLIG2$^+$	75 ± 13.5%	85 ± 11.1%	94 ± 5.6%	100 ± 0%
	NKX2.2$^+$	54 ± 7.6%	73 ± 8.5%	75 ± 5.8%	44 ± 6.3%
	OLIG2$^+$/NKX2.2$^+$	62 ± 3.0%	71 ± 10.0%	72 ± 5.6%	44 ± 6.3%
5	OLIG2$^+$	90 ± 3.2%	92 ± 3.4%	84 ± 7.5%	95 ± 2.9%
	NKX2.2$^+$	83 ± 5.7%	89 ± 2.3%	75 ± 8.8%	68 ± 8.2%
	OLIG2$^+$/NKX2.2$^+$	84 ± 5.0%	88 ± 3.1%	75 ± 8.8%	68 ± 7.8%
6	OLIG2$^+$	83 ± 10.6%	95 ± 2.3%	91 ± 4.0%	87 ± 6.1%
	NKX2.2$^+$	45 ± 20.3%	74 ± 8.7%	80 ± 6.1%	80 ± 8.5%
	OLIG2$^+$/NKX2.2$^+$	45 ± 20.3%	74 ± 8.7%	80 ± 6.1%	80 ± 8.5%

n=3-6/cell line

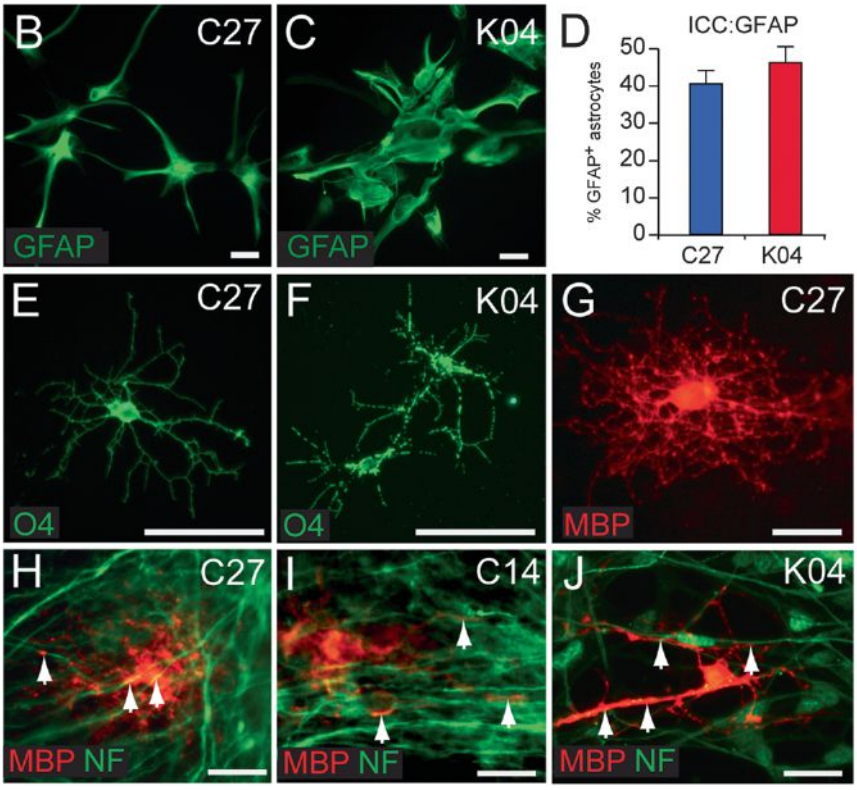

Figure 2. Both Astrocytes and OLs Are Efficiently Generated from hiPSC OPCs

(A) Expression of neural markers during induction of oligodendroglial-lineage hiPSC-derived neuroepithelial cells in stage 3, pre-OPCs in stages 4 and 5, and OPCs in stage 6. Cultures were immunostained for PAX6 and SOX1, or OLIG2 and NKX2.2, respectively. The proportion of immunopositive clusters for each marker set were scored for each hiPSC line. At least three repeats in each group were performed; data are provided as means ± SEM. In stage 6, gliogenic clusters were dissociated to single-cell suspensions and plated in GIM, resulting in the terminal differentiation of both astrocytes and myelinogenic OLs.

(B and C) GFAP$^+$ astrocytes were evident in cultures of hiPSC OPCs by 95 DIV; C27-derived (B) and K04-derived (C) astrocytes are shown here.

(D) Proportion of GFAP$^+$ astrocytes among all cultured cells at 95 DIV; the remainder expressed oligodendroglial lineage markers (means ± SEM; see Figure S2I). ICC, immunocytochemistry.

(E–J) Later in stage 6 (160 DIV), hiPSC-derived OPCs differentiated as both O4$^+$ (F and G) and MBP$^+$ (G) OLs. (H–J) When cocultured with human fetal cortical neurons, hiPSC OPCs derived from C27 (H), C14 (I), and K04 (J) hiPSCs all generated MBP$^+$ myelinogenic OLs that engaged NF$^+$ axons (MBP, red; NF, green).

Scale: 50 μm. See also Figure S2.

OPCs' differentiation from hiPSCs, whether induced from keratinocytes (K04 cells) or fibroblasts (C14 and C27 cells), were consistently higher than that of WA09/H9 hESCs.

Both Astrocytes and OLs Are Efficiently Derived from hiPSC-Derived hOPCs

Both in vitro and in vivo, hiPSC OPCs readily differentiated into astrocytes as well as OLs. GFAP-defined astroglia first appeared by 70 days in vitro (DIV), significantly earlier than OLs did. By late stage 6, at 120 DIV, GFAP$^+$ astrocytes were found to be abundant when gliogenic spheres were plated onto a polyornithine/laminin-coated surface (Figures 2B–2D). By that time, GFAP$^+$ cells comprised 40%–50% of cells in OPC-induced cultures, across all cell lines (Figure 2D). Quantitative RT-PCR (qRT-PCR) confirmed the upregulation of *GFAP* messenger RNA (mRNA) expression during OPC differentiation in all cell lines (Table S1A).

The production of OLs from hESC- and hiPSC-derived OPCs was triggered by the withdrawal of gliogenic growth factors to half-normal levels (see Experimental Procedures). When hiPSC OPCs were exposed to those conditions for 2 weeks, a proportion matured into O4$^+$ and/or myelin basic protein (MBP)$^+$ OLs (Figures 2E–2G). According to flow cytometry, O4$^+$ OLs in C27, C14, and K04 hiPSC-derived OPC cultures respectively comprised 11.9 ± 3.8%, 4.1 ± 0.9%, and 7.6 ± 1.5% of all cells (at 194 ± 15, 186 ± 14, and 205 ± 14 DIV, respectively; means ± SEM) (Figure 3A; Table S1B). Of note, our culture conditions favored initial oligodendrocytic differentiation, but not postmitotic oligodendrocytic survival, because our focus was on preparing populations of transplantable lineage-biased progenitors and immature oligodendroglia rather than more mature—but less transplantable—process-bearing OLs.

OPCs Could Be Isolated from hiPSC Cultures by CD140a- and CD9-Directed Fluorescence-Activated Cell Sorting

Flow cytometry for A2B5, CD140a/PDGFαR, and the tetraspanin CD9 (Berry et al., 2002; Terada et al., 2002) was next used for identifying and quantifying hiPSC OPCs in stage 6 culture

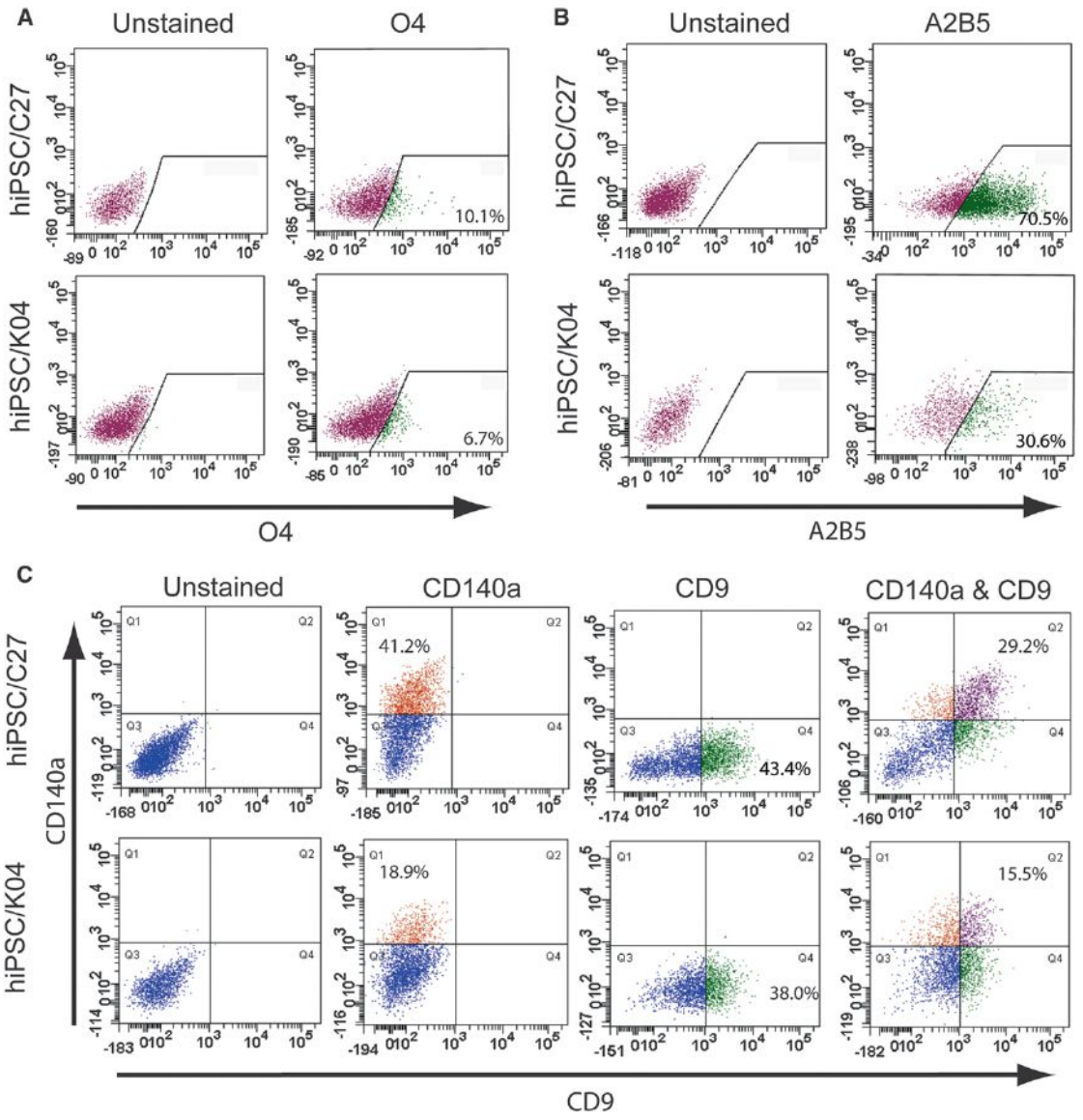

Figure 3. OPCs Can Be Isolated from Mixed hiPSC Culture by CD140a- and CD9-Directed FACS

(A) hiPSC OPC-derived OLs were recognized and isolated by FACS using monoclonal antibody O4, which recognizes oligodendrocytic sulfatide. The incidence of $O4^+$ oligodendroglia varied across different hiPSC lines, from 4% to 12% (see Table S1; n = 4–7 experiments).

(B) OPCs derived from hiPSCs (C27 and K04) were readily recognized with the cell-surface marker A2B5.

(C) OPCs derived from either hiPSCs (C27 and K04) or hESCs (WA09/H9) were readily recognized with cell-surface markers, PDGFRα (CD140a), and CD9 by FACS analysis. The relative proportions of CD140a, CD9, and CD140a/CD9 double-labeled cells varied across the different cell-line-derived OPCs (n = 4–7 experiments).

See also Tables S1A and S1B.

(Figures 3B and 3C). $CD140a^+$ OPCs derived from C27, C14, and K04 hiPSCs respectively comprised 33.0 ± 10.3%, 32.8 ± 12.0%, and 41.1 ± 6.1% of all cells, compared to 37.5 ± 10.2% of H9-derived cells (Figure 3C; Table S1C). The $CD9^+$ fraction of $CD140a^+$ cells, which defined a later-stage pool of OPCs, comprised 24.0 ± 8.0% and 12.4 ± 2.3% of cells in stage 6 C27 and K04 hiPSC cultures, respectively; matched cultures of H9-derived OPCs included 15.0 ± 4.9% $CD9^+/CD140a^+$ cells (Figure 3C; Table S1C; n = 4–7 repeats each). Thus, hiPSC OPCs could be identified and isolated at different stages of lineage restriction, which were serially represented by A2B5, CD140a, CD9, and O4. Selection based on these epitopes permits the isolation of relatively pure populations of hiPSC OPCs while removing residual undifferentiated cells from the isolate.

hiPSC-Derived OLs Generated MBP in Contact with Human Axons In Vitro

We next sought to examine the ability of hiPSC OLs to myelinate axons in vitro. hiPSC OPCs from each cell line were cocultured

with human fetal cortical neurons isolated from 20 week gestational age (g.a.) fetal brain using polysialyted neural cell adhesion molecule (PSA-NCAM)-directed selection (Windrem et al., 2008). The neurons were cultured on laminin for 10–14 days to allow phenotypic maturation and fiber extension and were confirmed to be free of tissue-derived OLs by O4 immunolabeling. hiPSC OPCs were then prepared as clusters of 50–100 μm in diameter and cocultured with the fetal neurons for 4 weeks; the cultures were then immunolabeled for MBP and neurofilament (NF). Confocal imaging revealed abundant MBP^+ processes that contacted axons and initiated ensheathment (Figures 2H–2J), though unambiguous myelin formation was not noted at the time points imaged. Thus, to better assess myelinogenesis by hiPSC OPCs, we next evaluated their engraftment and myelination in vivo.

hiPSC OPCs Efficiently and Functionally Myelinated the Shiverer Brain

To definitively establish the myelination competence of hiPSC OPCs, we transplanted them into newborn homozygous shiverer (*shi*/*shi*) × *rag2*$^{-/-}$ immunodeficient mice. For this experiment, the mice were implanted with 100,000 hiPSC-derived OPCs bilaterally into the corpus callosum (n = 4–7 mice per hiPSC line for K04, C27, and C14 hiPSC-derived OPCs), using previously described methods (Windrem et al., 2008). At 3 or 4.5 months of age, the mice were killed and their brains were analyzed in terms of donor cell distribution and density, myelin production and the proportion of myelinated axons, and nodal reconstitution. All three of the hiPSC line-derived OPCs were able to robustly myelinate the recipient brains; from each line, high donor cell densities and widespread dispersal were observed throughout the forebrain white matter (Figures 4A and 4B). C27, C14, and K04 hiPSC OPC-derived oligodendrocytic differentiation and myelination were analogous in extent, with robust myelination of the corpus callosum and capsules (Figures 4C, 4E, 4H, 5B, 5G, and 5J). As a result of the superior initial neuralization of these two lines relative to C14, we achieved higher net yields of OPCs with C27 and K04 hiPSCs and hence only pursued quantitative assessment of myelination in recipients of C27 or K04 hiPSC OPCs.

Quantitative histology revealed that within the corpus callosa of 3 month (13 week)-old shiverer recipients, C27 and K04 hiPSC-derived OPCs and oligodendroglia, defined as human nuclear antigen $(hNA)^+/OLIG2^+$, achieved densities of 29,498 ± 13,144 and 37,032 ± 8,392 cells/mm^3, respectively. Among these, 7,298 ± 2,659 (C27) and 2,328 ± 650 (K04) cells/mm^3 expressed MBP; these comprised 10.9 ± 5.1% (C27) and 4.7 ± 1.1% (K04) of all donor cells within the sampled midline of the corpus callosum at the 13 week time point. To assess the myelination efficiency in terms of the proportion of axons myelinated, we next used confocal analysis to quantify the fraction of callosal axons ensheathed by hiPSC oligodendroglia in the three mice engrafted with C27 hiPSC-derived OPCs. At the 13 week time point analyzed, 17.2 ± 7.2% of host mouse axons were ensheathed within the three sampled callosa (Figure 5B). Remarkably, the density of hiPSC-OPC donor-derived myelination and the proportion of ensheathed axons at 13 weeks proved as high as, and perhaps exceeded, those achieved by OPCs derived from second-trimester fetal brain tissue, whether isolated as $A2B5^+/PSA\text{-}NCAM^-$ or $CD140a^+$ cells (Sim et al., 2011; Windrem et al., 2004; Windrem et al., 2008).

hiPSC OPCs Efficiently Generated Astrocytes and OLs In Vivo

Besides the large numbers of hiPSC OPCs that differentiated as myelinogenic OLs in the shiverer mouse brain, large numbers also remained as resident $OLIG2^+$ and $NG2^+$ progenitor cells, and many OPCs of all three hiPSC lines differentiated as astrocytes as well, particularly as fibrous astrocytes of the white matter (Figures 4D, 4F, and 4I). When hiPSC-OPC-transplanted mice were assessed at 13 weeks after neonatal graft, most donor cells persisted as progenitors or had initiated oligodendroglial differentiation; by that time point, the net proportion of $OLIG2^+$ cells, which included both OPCs and oligodendroglia, arising from all K04 and C27 transplanted cells was 78.7 ± 2.4%, whereas the remainder were largely donor-derived $GFAP^+$ astroglia (Table S2).

Interestingly, despite the widespread infiltration of the recipient brains by hiPSC OPCs, substantial astrocytic differentiation was noted by those cells within the presumptive white matter, within which the donor cells differentiated as morphologically apparent fibrous astrocytes, in close association with hiPSC-derived OLs. These hiPSC-derived astrocytes might have been generated from lineage-restricted hiPSC-derived astrogliogenic precursors or by astrocytic differentiation in situ from still-bipotential hOPCs. In either case, by 3 months after neonatal transplant, the callosal and capsular white matter of shiverer recipients of OPC grafts derived from all three hiPSC lines manifested human astrocytic scaffolds harboring densely engrafted myelinogenic OLs, in each case yielding substantially reconstructed and densely myelinated central white matter (Figures 4D, 4F, and 4I).

Neonatal Engraftment with hiPSC OPCs Could Rescue the Shiverer Mouse

We next asked whether the robust engraftment and myelination noted in transplanted shiverer mice were sufficient to ameliorate neurological deterioration and prolong the survival of shiverer mice, which typically die by 20 weeks of age. To this end, we transplanted a set of 22 neonatal homozygous shiverer × *rag2* nulls with 300,000 C27-derived hiPSC OPCs using a five-site forebrain and brainstem injection protocol that achieves whole-neuraxis engraftment via transplanted OPCs (Figures 6A–6D) (Windrem et al., 2008). A matched set of 19 littermate controls were injected only with saline, and both sets were housed without further manipulation. Predictably, the 19 unimplanted shiverer controls died before 5 months of age, with a median survival of 141 days. In contrast, 19 of the 22 implanted mice lived longer than the longest-lived control mouse. The transplanted mice exhibited greatly prolonged survival (Figure 6E), with reduced death over our 9 month period of observation, after which the experiment was terminated so that surviving mice could be processed for both immunohistochemical assessment of late-stage myelination and nodal reconstitution and for ultrastructural analysis (see next section). Comparison of the Kaplan-Meier survival plots of transplanted and control mice revealed a highly significant difference (chi

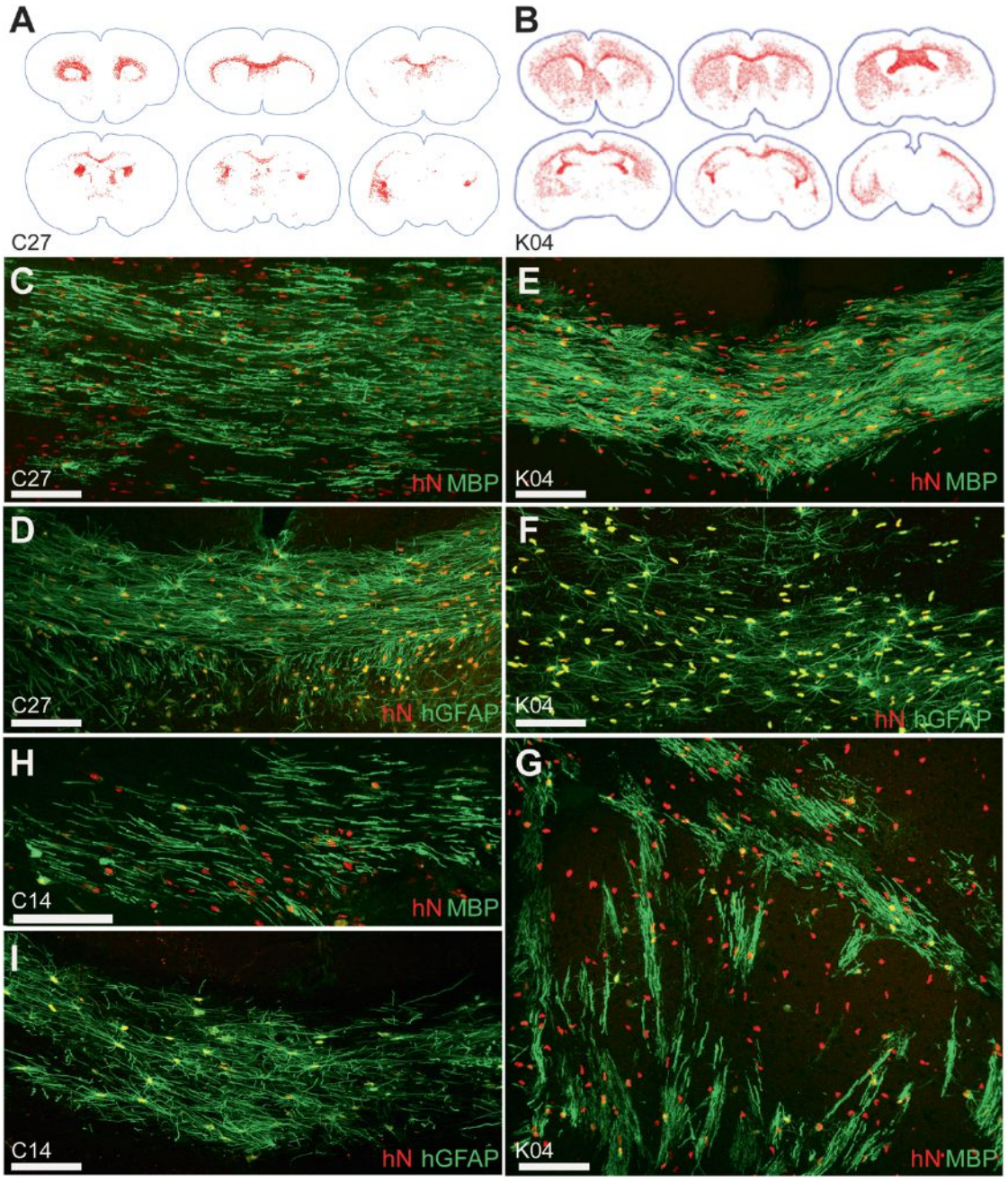

Figure 4. hiPSCs Migrate Widely and Differentiate as Astroglia and Myelinogenic OLs

hiPSC OPCs generated from all three hiPSC lines migrated throughout the shiverer brain, engrafting most densely in white matter. Distributions of C27 (A) and K04 (B) hiPSC-derived OPCs are shown (hNA^+, red, mapped in Stereo Investigator). By 13 weeks of age, C27 hiPSC OPCs (C), K04 hiPSC OPCs (E and G), and C14 hiPSC OPCs (H) matured into MBP-expressing oligodendroglia (green) throughout the subcortical white matter, including callosal and capsular (C, E, and H) as well as striatal (G) tracts. In these 13-week-old shiverer mouse recipients, C27 (D), K04 (F), and C14 (I) hiPSC-derived OPCs also differentiated as astroglia (human-specific GFAP, green), especially as fibrous astrocytes in the central white matter.
Scale: 100 μm (C–I). See also Table S2.

square = 17.95 by the Gehan-Breslow-Wilcoxon test; $p < 0.0001$) (Figure 6E). Those transplanted mice that survived beyond 6 months uniformly exhibited substantial myelination of the brain, brainstem, and cerebellum (Figures 6A–6D and S3). Remarkably, the time-point-matched degree of cerebral myelination, as well as the proportion of shiverers alive at any given time point, was greater in hiPSC-OPC-engrafted mice than in mice previously engrafted with fetal-human-tissue-derived, A2B5-sorted OPCs (Windrem et al., 2008), which had otherwise been treated identically.

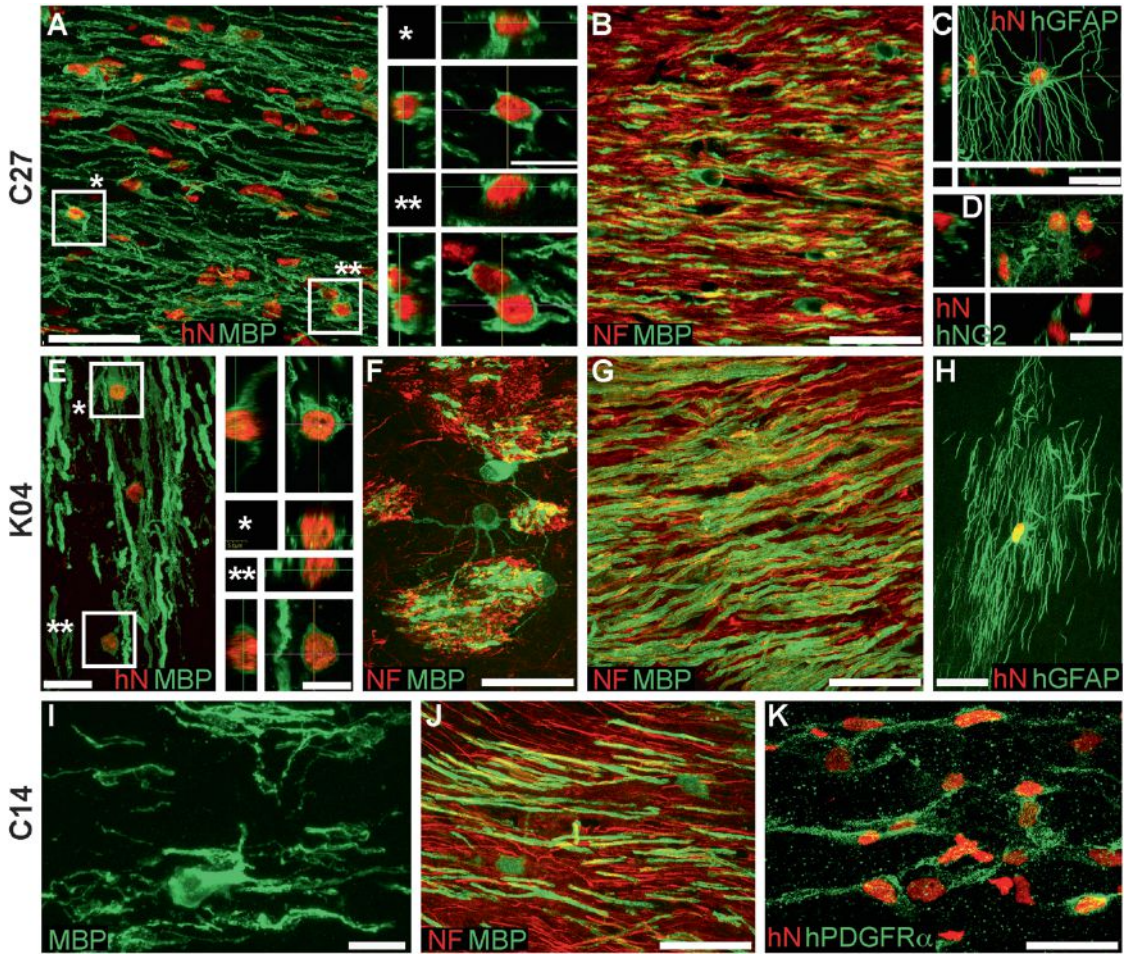

Figure 5. hiPSC OPCs Robustly Myelinate In Vivo

Confocal images of the callosal and capsular white matter of mice engrafted with hiPSC OPCs derived from all three tested hiPSC lines demonstrate dense donor-derived myelination: (A and B) C27-derived, (E–G) K04-derived, and (I and J) C14-derived. (A), (G), and (J) show abundant, donor-derived MBP expression (green) by C27, K04, and C14 hiPSC OPCs (hNA, red), respectively. Representative z stacks of individual hNA^+ OLs are shown as asterisks in (A) and (E). By the 19 week time point assessed here, C27 (B), K04 (F and G), and C14 (J) hiPSC oligodendroglia robustly myelinated axons (NF, red). hiPSC-derived oligodendroglial morphologies are exemplified in panels (F) (K04) and (I) (C14); (F) shows multiaxon myelination by single OLs in the striatum.

hiPSC OPCs also generated astroglia (C, C27; H, K04), which exhibited the complex fibrous morphologies typical of human astrocytes (human-specific GFAP, green). Many cells also remained as progenitors, immunostaining for NG2 (D, C27) and human-specific PDGFRα (K, C14).

Scale: 50 μm (A–C, G, J); 20 μm (C–F, H, K); and 10 μm (I, insets to A and E).

hiPSC OPCs Generated Ultrastructurally Mature Myelin with Nodal Reconstitution

In light of the markedly extended survival of hiPSC-OPC-transplanted mice, we next sought to confirm that this was associated with the formation of ultrastructurally compact myelin around host axons by hiPSC OLs. To this end, we used electron microscopy on samples of corpus callosum derived from 22- to 36-week-old engrafted shiverers (n = 3). These mice comprised animals that had been subjected to the five-site injection protocol and survived significantly longer than their unengrafted controls; these apparently rescued mice were killed after relatively long survival time points to permit assessment of their myelin integrity and quality. We found that their recipient callosa were densely myelinated by mature compact myelin characterized by concentrically organized major dense lines (Figures 7A–7E) and interlaminar tight junctions (Figures 7F, 7G, and S4C); the engrafted callosa were quite unlike those of their untransplanted shiverer controls, which failed to exhibit major dense lines or any other evidence of myelin compaction (Figures S4B, S4D, and S4E).

Anatomic reconstitution of nodes of Ranvier was also noted in these mice, as determined by immunolabeling of Caspr and ßIV spectrin, which respectively identified paranodal and nodal segments of newly myelinated axons (Figures 7H and 7I). In past studies, we correlated the anatomic and antigenic reconstitution of nodal architecture with the restoration of both rapid conduction and functional competence (Windrem et al., 2008). The rapid and robust reacquisition of nodal architecture in these mice suggests that hiPSC-derived OLs generate the cues necessary for the nodal organization of axonal proteins, upon which the formation of functional nodes of Ranvier depends.

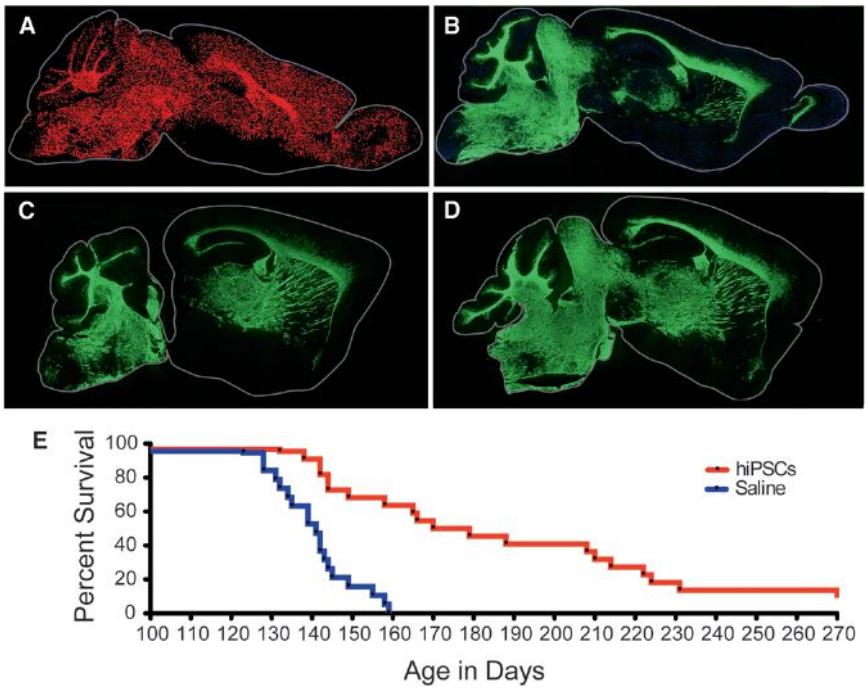

Figure 6. hiPSC OPCs Myelinate Widely to Greatly Extend the Survival of Hypomyelinated Mice

(A) Dot map indicating the distribution of hiPSC-derived donor cells (C27) at 7 months of age, following neonatal engraftment in a shiverer mouse brain. Widespread dispersal and chimerization by hiPSC OPCs is evident (hNA, red).

(B) hiPSC-OPC-derived myelination in a shiverer forebrain at 7 months; section 1 mm lateral to (A). MBP immunoreactivity (green) is all donor derived.

(C and D) Myelination in sagittal sections taken at different mediolateral levels from two additional 7-month-old mice, each engrafted with C27 hiPSC OPCs at birth.

(E) Kaplan-Meier plot of the survival of C27 iPSC-OPC-implanted (n = 22) versus saline-injected (n = 19) control mice. Remaining engrafted mice sacrificed for electron microscopy at 9–10 months (≥270 days).

Scale: 2 mm (A and B). See also Figure S3.

Together, these data indicate that hiPSC-derived OPCs can efficiently generate OLs, which in turn can robustly myelinate the hypomyelinated shiverer forebrain, and that the myelin thereby generated is able to restore nodal architecture as well as to ensheath axons as efficiently as purified isolates of fetal-tissue-derived OPCs.

hiPSC OPCs Were Nontumorigenic In Vivo

The persistence of undifferentiated pluripotent stem cells may cause either teratomas or neuroepithelial tumors in graft recipients (Roy et al., 2006). To assess whether any pluripotent or incompletely differentiated hESCs or hiPSCs remained in nominally fully differentiated OL cultures, we used both immunolabeling and qRT-PCR to assess the expression of pluripotent markers by late-stage hiPSC-derived OPCs. By 100 DIV, no detectable OCT4, NANOG, or SSEA4 protein could be found in OPCs derived from any of the hESC and hiPSC lines used in this study. Similarly, qRT-PCR revealed that transcripts of *OCT4* and human telomerase reverse transcriptase (*hTERT*) were downregulated to essentially undetectable levels by 95 or more DIV (Figures S2J and S2K). We also examined the in vivo expression of OCT4, NANOG, and SSEA4 by engrafted OPCs 3 months after transplantation. As noted, only a small minority of hNA^+ donor cells were unstained by OLIG2, MBP, or GFAP. Many donor-derived cells expressed nestin or SOX2, suggesting their persistence as neural progenitors, but no persistent expression of OCT4, NANOG, or SSEA4 was detectable in any of these cells, from any of the lines assessed.

Accordingly, we found no evidence of teratoma formation in any of the 16 *shi/shi* × *rag2*$^{-/-}$ mice examined for this purpose, which included mice transplanted neonatally with 100,000 cells and killed either 3 (n = 11) or 4.5 (n = 5) months later. We also examined available mice in our survival series, all of whom had been transplanted at five sites with a total of 300,000 cells and had died between 4 and 9 months of age (n = 10); none had any evidence of teratomas, heterotopias, or any type of tumor formation. In addition, we transplanted hiPSCs into normally myelinated *rag2*-null mice to assess tumorigenicity in the wild-type myelin environment as well. Of five mice examined 6 months after transplantation, none showed any evidence of tumor formation, heterotopias, or even foci of undifferentiated expansion. Of note, persistent expression of *SOX2*, *KLF4*, and c-*MYC* mRNA was noted by qPCR in the hiPSC-derived cells, reflecting some level of unsilenced expression of the lentivirally inserted reprogramming genes; nonetheless, the expression of the these transcripts was not associated with tumorigenesis by cells transplanted at the end of stage 6.

The lack of tumor formation in hiPSC-OPC-engrafted mice was associated with a significant decrease in the mitotic fraction of the implanted hiPSC OPCs as a function of time after graft. hiPSC OPC proliferation in vivo was measured as Ki67 expression by all human donor cells, which was noted to decrease linearly from 3 months (13.6 ± 0.6%) to 6 months (4.3 ± 0.04%) of age (R^2 = 0.9; p = 0.001; n = 7).

To establish the role of our differentiation protocol in diminishing the risk of tumorigenesis, we also transplanted *rag2*-null mice with both C27 and K04 hiPSCs at the end of stages 1 and 3. This was also done as a positive control for tumor detection, given our lack of observed tumors in the hiPSC OPC (stage 6)-engrafted mice, as much as 9 months after transplant. Yet in contrast to the hiPSC-OPC-engrafted mice, which were entirely tumor-free, *every* animal engrafted with earlier-stage hiPSCs manifested histologically overt tumor formation by 3 months (n = 8 mice engrafted with stage 1 hiPSCs; n = 6 with stage 3 cells). Thus, our differentiation protocol appeared to effectively deplete the donor cell pool of persistent undifferentiated cells; the resultant grafts of hiPSC OPCs proved uniformly nontumorigenic when studied as long as 9 months after transplant.

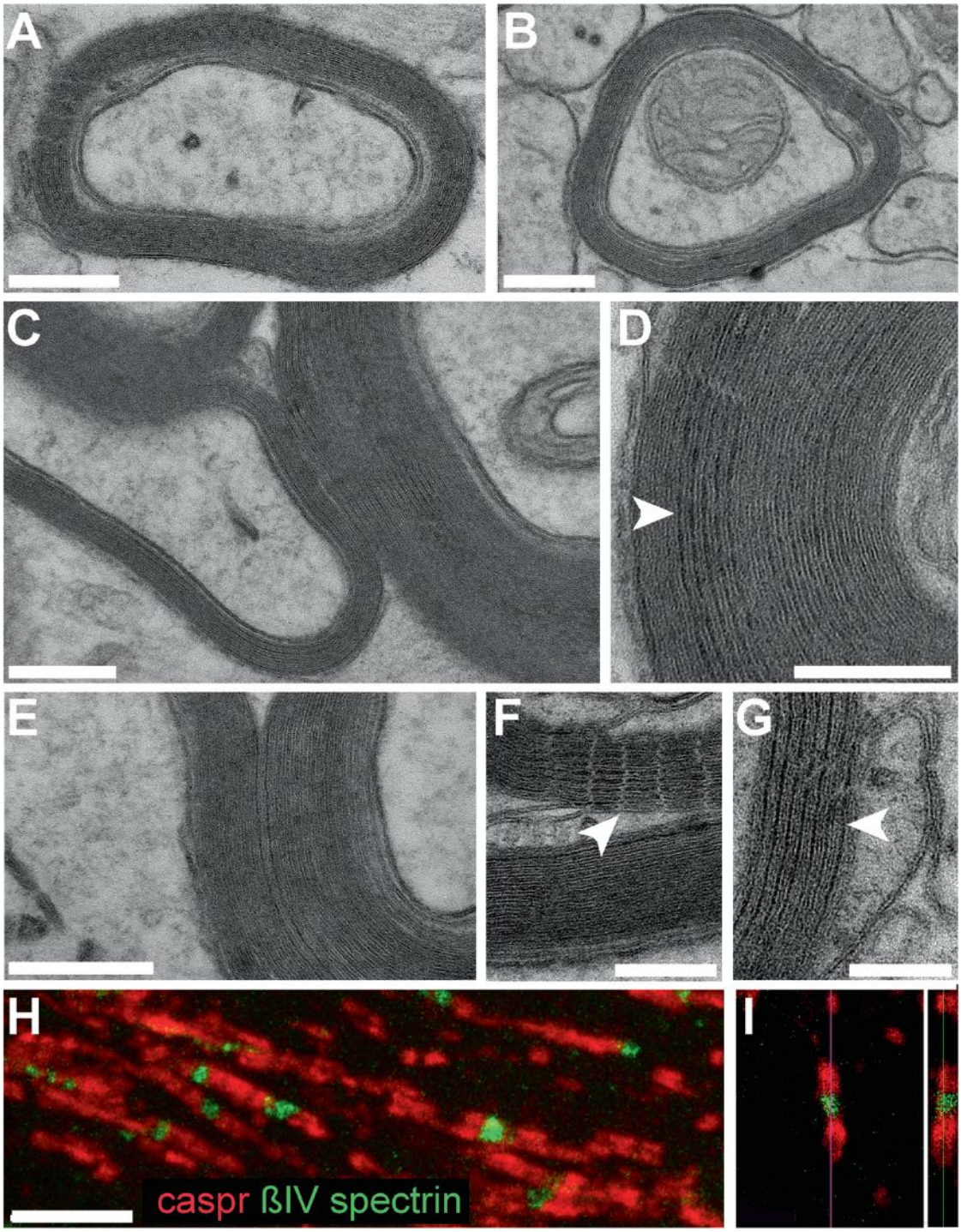

Figure 7. hiPSC-Derived OLs Produce Compact Myelin and Induce Nodes of Ranvier

Representative electron microscopic images of sections through the corpus callosum (A and B) and ventral pons (C) of a 40-week-old shiverer mouse neonatally engrafted with C27 hiPSC OPCs, showing donor-derived compact myelin with evident major dense lines, ensheathing mouse axons.

(D–G) Higher-power images of donor-derived myelin in the corpus callosum, also at 40 weeks. (D and E) The alternating major dense (arrowheads) and intraperiod lines, characteristic of mature myelin, are evident. (F and G) Myelin sheaths in the corpus callosum ensheathing central axons are shown, their maturation manifested by parallel arrays of tight junctions (F, arrowhead) and major dense lines (G, arrowhead).

This mature myelination permitted the organization of architecturally appropriate nodes of Ranvier by hiPSC oligodendroglia. In (H) and (I), nodal reconstitution in transplanted shiverers is demonstrated by immunostaining of oligodendrocytic paranodal Caspr protein (red), seen flanking nodes of Ranvier identified here by ßIV spectrin (green). An isolated node is shown in confocal cross-section in (I).

Scale: 200 nm (A–E); 100 nm (F and G); and 5 μm (H and I). See also Figure S4.

DISCUSSION

In this study, we established the feasibility of using hiPSCs to generate highly enriched populations of both astrocytes and myelinogenic central OLs, with high efficiency and yield. The success of our protocol in all four lines used in this study, which include WA09/H9 hESCs and K04, C14, and C27 iPSCs, suggests its broad applicability, and the highly efficient gliogenesis afforded by this strategy indicates its robust nature. Most importantly, the robust myelination that we noted in vivo, which compared favorably to that previously demonstrated by tissue-derived fetal human glial progenitors, suggested the probable functional integration and utility of these grafts. Accordingly, we noted that myelination-deficient shiverers engrafted neonatally with hiPSC OPCs survived substantially longer than did both their untransplanted and saline-injected controls; indeed, over three-fourths of hiPSC-OPC-transplanted mice survived over 6 months, long after all untreated control mice had died. As a result, we can now reliably produce hiPSC OPCs from single-patient skin samples in sufficient numbers to provide myelinogenic autografts largely, though perhaps not completely (Zhao et al., 2011), free of rejection risk.

Importantly, the myelination efficiency of the implanted iPSC-derived OPCs, defined as the proportion of central axons myelinated as a function of time after graft, proved as high as that which we had previously achieved using tissue-derived, CD140a-sorted OPCs (Sim et al., 2011). Indeed, it was remarkable to note that the proportion of axons ensheathed was as high in enriched but unsorted hiPSC-OPC grafts as in fetal-tissue-derived OPC grafts that had been sorted for $CD140a^+$ cells prior to transplant. Indeed, the hiPSC-OPCs grafts myelinated more axons more rapidly than did A2B5/PSA-NCAM-sorted fetal-tissue-derived cells, probably reflecting the higher proportion of bipotential glial progenitor cells in the hiPSC-OPC populations by the time of their harvest and transplantation.

In light of the robust myelination afforded by hiPSC-OPC grafts, we asked whether neonatal transplantation of hiPSC OPCs might be sufficient to rescue the phenotype and survival of recipient shiverer homozygotes, as we had previously observed in a minority of shiverers transplanted with fetal-human-brain-derived OPCs. We found that the hiPSC-OPC-transplanted mice indeed exhibited markedly improved survival; death was both delayed and reduced overall in the transplanted group over the 9 month period of observation. As we had previously documented with fetal-brain-tissue-derived OPC grafts, the rescued mice manifested progressive resolution of their neurological deficits (Windrem et al., 2008). Remarkably, however, the proportion of animals whose survival benefitted from hiPSC-OPC transplantation was substantially higher than that which we previously reported using tissue-derived human OPCs: whereas we had observed that only one-quarter of shiverer mice transplanted with tissue-derived OPCs survived beyond 6 months of age (Windrem et al., 2008), in our present study over half of the hiPSC-OPC-engrafted mice did so (Figure 6E). Nonetheless, some later deaths beyond 7 months of age were still noted; this may reflect an inhomogeneous dispersal of hiPSC OPCs that we observed in some animals, the nature of which we continue to investigate. Those late deaths notwithstanding, at least one-fifth of the mice appeared to represent outright clinical rescues, though we sacrificed these survivors at $\geq$ 9 months for histological and ultrastructural analysis. These provocative data suggest the superiority of hiPSC OPCs as therapeutic vectors, perhaps by virtue of their more rapid myelinogenesis, which may be a function of the prolonged differentiation conditions that we employed in our OPC induction protocol.

Interestingly, we observed no evidence of tumorigenesis from implanted hiPSC-derived glial progenitors, at time points as long as 9 months after transplant. This was surprising, given that previous studies had provided ample evidence for the risk of tumor formation from either residual undifferentiated cells (Pruszak et al., 2009) or from partially differentiated neuroepithelial cells in hESC-derived transplants (Roy et al., 2006). It is possible that the prolonged differentiation protocols that we employed to produce OPCs are robust enough to effectively eliminate any residual undifferentiated cells prior to transplantation. It is similarly possible that epigenetic marks persisting in reprogrammed hiPSCs effectively lowered the later risk of tumorigenesis by their differentiated derivatives. In any case, even longer survival time points will be needed, with more animals and an intensive search for any residual undifferentiated and/or potentially tumorigenic cells in vivo, before we can confidently state the safety of these grafts. Should tumorigenesis at any point be a concern, then hiPSC OPCs may be sorted to purity before transplantation, on the basis of the high incidence of definitively pro-oligodendrocytic $CD9^+/CD140a^+$ cells in our cultures, and our ability to isolate these cells by fluorescence-activated cell sorting (FACS) based upon these coexpressed epitopes (Sim et al., 2011).

These findings indicate that high-efficiency in vivo oligodendrocytic differentiation and myelination can be achieved from hiPSCs, suggesting the potential utility of iPSC-derived autografts in treating acquired disorders of myelin. Yet it is also important to note the efficient, context-dependent generation of both fibrous and protoplasmic astrocytes from engrafted hiPSC OPCs. Besides the importance of astroglia in effecting the structural and physiological reconstitution of dysmyelinated tracts, astrocytic engraftment may be of particular importance in correcting dysmyelinating disorders of enzyme deficiency, given that astrocytic lysosomal enzymes have been found to readily transit from wild-type to deficient glia within brain tissue, in a manner potentially sufficient to rescue enzyme-deficient hosts (Lee et al., 2007). In addition, hiPSC-derived astrocytes may prove to be critically important therapeutic vectors for diseases of primarily astrocytic pathology (Krencik et al., 2011), such as Alexander disease and the vanishing white-matter disorders (Bugiani et al., 2011), in which myelin loss occurs but may be secondary to astrocytic dysfunction. In each of these cases, however, the therapeutic use of iPSC-derived astroglia will need to be paired with methods for the ex vivo correction of the genetic defects characteristic of these disorders.

Human iPSC OPCs might thus be attractive vectors for restoring or replacing glial populations in a variety of disease settings. Most critically, our data suggest the preferential use of hiPSC-derived OPCs to restore lost myelin in disorders such as multiple sclerosis and traumatic demyelination, in which no genetic abnormalities might complicate the use of a patient's own somatic cells as the iPSC source. iPSC OPCs may similarly prove of great therapeutic value in genetic disorders of myelin,

such as Pelizaeus-Merzbacher disease, recognizing that the underlying genetic defect must first be repaired in the donor somatic cells before glial progenitor induction and implantation. Our present study thus establishes the technical feasibility and efficacy of generating myelinogenic OLs from hiPSCs and suggests the clinical situations in which this approach might be most appropriate. We may now reasonably contemplate the clinical application of patient-specific, somatic cell-derived glial progenitor cell transplants for the treatment of acquired disorders of myelin, as well as of the broader spectrum of human glial pathologies.

EXPERIMENTAL PROCEDURES

hESC and hiPSC Culture

We used four distinct lines of pluripotent cells in this study. These included hESCs (WA09/H9; WiCell, Madison, WI, USA) and hiPSCs of both keratinocyte (K04; K. Hochedlinger) and fibroblast origin (C14 and C27 hiPSCs; L. Studer). The experiments described were approved by the University of Rochester Embryonic Stem Cell Research Oversight committee.

OPC Production

OPCs were induced from hESCs and iPSCs using our modifications of published protocols (Hu et al., 2009a; Hu et al., 2009b; Izrael et al., 2007), as schematized in Figure 1 and described in detail in the Supplemental Experimental Procedures.

Directed Astrocytic or Oligodendrocytic Maturation

hiPSC- or hESC-derived gliogenic spheres at 120–170 DIV were cultured in suspension in GIM supplemented with platelet-derived growth factor-AA (PDGF-AA; 10 ng/ml), insulin growth factor-1 (IGF-1; 10 ng/ml) and Neurotrophin-3 (NT3; 10 ng/ml). To differentiate these OPCs into mature OLs or astrocytes, the spheres were dissected into small cell clusters (around 50–100 μm in diameter) mechanically with a Sharpoint blade (Surgimed-MLB). The dissected OPC clusters were plated onto polyornithine/laminin-coated 12-well plates and cultured in GIM for 1–2 weeks. For induction of astrocytes, the OPC clusters were cultured either in GIM supplemented with PDGF-AA (10 ng/ml), IGF-1 (10 ng/ml), and NT3 (10 ng/ml) or in GIM supplemented with 10% fetal bovine serum (FBS; HyClone) for 1–2 weeks. For directing the maturation of OLs, the cultures were switched to half GIM supplemented with PDGF-AA (5 ng/ml), IGF-1 (5 ng/ml), and NT3 (5 ng/ml) plus half neurobasal (NB) media (Invitrogen) supplemented with B27 (1X) and brain-derived neurotrophic factor (BDNF; 10 ng/ml) and grown for 2–4 weeks. The mature astrocytes were recognized with immunostaining of anti-GFAP or anti-CD44. Oligodendroglia were identified using O4 and MBP antibodies.

In Vitro Immunocytochemistry

All in vitro fixation and immunolabeling protocols are detailed in the Supplemental Experimental Procedures.

Isolation of Human Fetal Neuronal Progenitor Cells for Coculture

Human fetal forebrain tissue was obtained from second-trimester aborted fetuses of 20 weeks g.a. Tissues were obtained as deidentified tissue, as approved by the Research Subjects Review Board of the University of Rochester Medical Center. The tissue samples were washed 2–3 times with sterile Hank's balanced salt solution with Ca^{2+}/Mg^{2+} ($HBSS^{+/+}$). Cortical plate tissue was separated from the ventricular zone/subventricular zone, then dissociated with papain (Worthington Biochemical) as described (Keyoung et al., 2001; Wang et al., 2010). The cells were resuspended at 2–4 × 10^6 cells/ml in Dulbecco's modified Eagle's medium (DMEM)/F12 supplemented with N-2 supplement (Life Technologies) and basic fibroblast growth factor (bFGF; 20 ng/ml) and plated in suspension culture dishes. A day later, the cells were recovered and neurons isolated by magnetic-activated cell sorting (Windrem et al., 2008). In brief, the recovered neural progenitor cells were incubated with PSA-NCAM (Chemicon) at 1:100 for 30 min, then washed and labeled with rat anti-mouse immunoglobulin M microbeads (Miltenyi Biotech). The bound PSA-$NCAM^+$ neurons were eluted, spun, washed with DMEM/F12, and then cultured in DMEM/F12 with N2, 0.5% PD-FBS, and bFGF (20 ng/ml) for 4–6 days. For coculture with hiPSC OPCs, the fetal cortical neurons were dissociated into single cells and then plated onto either poly-L-ornithine/laminin-coated 24-well plates or poly-L-ornithine/fibronectin-coated coverslips (50,000–100,000 cells per well or coverslip). The replated neurons were then switched to NB media with B27 (1X) and BDNF (10 ng/ml; Invitrogen) for an additional 6–10 days prior to coculture.

Coculture of hiPSC-Derived OPCs with Human Fetal Cortical Neurons In Vitro

Gliogenic OPC spheres derived from either K04 or C27 hiPSCs were induced up to 130 DIV prior to coculture. These were dissected into small pieces of <1 mm^3 and cultured for 2–3 weeks to allow the OPCs to expand as a monolayer surrounding the core clusters. The OPC clusters and their monolayer surrounds were then recollected with cold $HBSS^{-/-}$ from the culture dishes and manually dissected into smaller fragments of 100–200 μm in diameter. Small aliquots were fully dissociated into single cells with Accutase (Chemicon) for 5 min at room temperature, then assessed by hemocytometry. For coculture, the hiPSC OPCs were then seeded at 200,000 cells/ml, either with or without human cortical neurons, and cultured in a 1:1 mixture of NB/B27/BDNF and GIM/NT3/IGF-1/PDGF-AA media. The cultures of cortical neurons alone, hiPSC OPCs alone, or both populations together were allowed to grow 2–4 additional weeks before fixation and immunolabeling for O4, MBP, GFAP, and ßIII-tubulin.

Flow Cytometry

Flow-cytometric methods, by which hESC- and hiPSC-derived OPCs were analyzed for A2B5, CD140a, CD9, and O4 immunoreactivities, as well as the cell preparation methods antecedent to cytometry and sorting, are described in detail in the Supplemental Experimental Procedures.

RNA Extraction and RT-PCR

Total RNA was extracted from undifferentiated hESCs and hiPSCs, or hESC- and hiPSC-derived OPCs, using RNeasy mini kit (QIAGEN). The first of strand of complementary DNA was transcribed using the TaqMan Reverse Transcription kit (Roche #N808-0234). The primer sequences are given in the Supplemental Experimental Procedures. The relative abundance of transcript expression of mRNAs was measured with the ABI PRISM 7000 system. The resultant expression data were normalized to the expression level of glyceraldehyde-3-phosphate dehydrogenase (*GAPDH*) mRNA. Statistical analysis was performed on transformed data. The means and SEM were calculated following a paired t test.

Neonatal Xenograft into Shiverer Mice

Homozygous shiverer mice (The Jackson Laboratory, Bar Harbor, ME, USA) were crossed with homozygous *rag2*-null immunodeficient mice (Shinkai et al., 1992) on the C3H background (Taconic, Germantown, NY, USA) for generation of *shi/shi* × $rag2^{-/-}$ myelin-deficient, immunodeficient mice. The hiPSC-derived OPCs were prepared for transplantation as described for in vitro coculture. Neonatal pups were either transplanted bilaterally in the corpus callosum with a total of 100,000 cells, as described in Windrem et al., 2004, or with 300,000 cells, using the procedure described in Windrem et al., 2008. At 3 months of age, transplanted mice were anesthetized with pentobarbital, then perfusion fixed with cold $HBSS^{+/+}$ followed by 4% paraformaldehyde. All procedures were approved by the University Committee on Animal Resources. Brains were extracted and postfixed for 2 hr in cold paraformaldehyde. Brains processed for electron microscopy were perfused in 4% paraformaldehyde and 0.25% glutaraldehyde.

Immunohistochemistry of Tissue Sections

Human cells were identified with mouse anti-hNA, clone 235-1 (MAB1281 at 1:800; Millipore, Billerica, MA, USA). Phenotypes were identified with human-specific NG2 (MAB2029 at 1:200; Millipore), rat anti-MBP (Ab7349 at 1:25), rabbit anti-OLIG2 (Ab33427 at 1:1000; Abcam, Cambridge, MA, USA), human-specific mouse anti-GFAP (SMI-21 at 1:500), mouse anti-NF (SMI-311 and SMI-312 at 1:1,000; Covance, Princeton, NJ, USA), and rabbit anti-Ki67 (RM-9106 at 1:200; Thermo-Fisher, Freemont, CA, USA). Alexa Fluor

secondary antibodies, including goat anti-mouse, -rat, and -rabbit antibodies conjugated to 488, 568, 594, and 647 nm fluorophores, were used at 1:400 (Invitrogen, Carlsbad, CA, USA). PAX6, NKX2.2, OCT4, NANOG, and SOX2 antibodies were employed using the same conditions as in vitro.

Morphometrics

Myelinated Axon Counts

Regions of dense engraftment with human cells were selected for NF and MBP staining; a 1 μm stack of ten superimposed optical slices taken at 0.1 μm intervals (Olympus FluoView 300) was made for each of three fields of view in the corpus callosum. Three parallel, equidistant lines were laid over the images perpendicular to the axons. Axons were scored at intersections with the lines as either myelinated (closely apposed to MBP on both sides) or unmyelinated.

Mapping of Human Cell Engraftment

The positions of all anti-human nuclei$^+$ cells were mapped on 20 μm coronal sections at 160 μm intervals from −3.2 to 1.2 bregma anterior-posterior.

Cell Counting

Three unilateral, equally spaced samples of corpus callosum, from −0.4 to 1.2 bregma, were counted for cells expressing hNA together with either MBP, hGFAP, OLIG2, or Ki67. White matter was also assessed for the presence of any hNA$^+$ cells coexpressing HuC/HuD, OCT4, or NANOG. All data are provided as means ± SEM.

Electron Microscopy

Samples of human iPSC-derived glial chimeric white matter were taken from mice killed at 22–40 weeks of age, perfused with half-strength Karnovsky's fixative, then processed for ultrastructural analysis of myelin morphology and quality using previously described techniques (Windrem et al., 2008).

SUPPLEMENTAL INFORMATION

Supplemental Information includes four figures, two tables, and Supplemental Experimental Procedures and can be found with this article online at http://dx.doi.org/10.1016/j.stem.2012.12.002.

ACKNOWLEDGMENTS

This work was supported by New York State Stem Cell Science (NYSTEM); the National Multiple Sclerosis Society; NIH grants R01NS75345 and R01NS39559; the G. Harold and Leila Y. Mathers Charitable Foundation; and the Dr. Miriam and Sheldon G. Adelson Medical Research Foundation. We thank Karen Bentley and Gayle Schneider for their assistance in electron microscopy.

Received: June 23, 2012
Revised: October 4, 2012
Accepted: December 5, 2012
Published: February 7, 2013

REFERENCES

Ben-Hur, T., and Goldman, S.A. (2008). Prospects of cell therapy for disorders of myelin. Ann. N Y Acad. Sci. *1142*, 218–249.

Berry, M., Hubbard, P., and Butt, A.M. (2002). Cytology and lineage of NG2-positive glia. J. Neurocytol. *31*, 457–467.

Bugiani, M., Boor, I., van Kollenburg, B., Postma, N., Polder, E., van Berkel, C., van Kesteren, R.E., Windrem, M.S., Hol, E.M., Scheper, G.C., et al. (2011). Defective glial maturation in vanishing white matter disease. J. Neuropathol. Exp. Neurol. *70*, 69–82.

Chambers, S.M., Fasano, C.A., Papapetrou, E.P., Tomishima, M., Sadelain, M., and Studer, L. (2009). Highly efficient neural conversion of human ES and iPS cells by dual inhibition of SMAD signaling. Nat. Biotechnol. *27*, 275–280.

Dietrich, J., Noble, M., and Mayer-Proschel, M. (2002). Characterization of A2B5+ glial precursor cells from cryopreserved human fetal brain progenitor cells. Glia *40*, 65–77.

Franklin, R.J.M., and Ffrench-Constant, C. (2008). Remyelination in the CNS: from biology to therapy. Nat. Rev. Neurosci. *9*, 839–855.

Goldman, S.A., Nedergaard, M., and Windrem, M.S. (2012). Glial progenitor cell-based treatment and modeling of neurological disease. Science *338*, 491–495.

Hu, B.Y., Du, Z.W., Li, X.J., Ayala, M., and Zhang, S.C. (2009a). Human oligodendrocytes from embryonic stem cells: conserved SHH signaling networks and divergent FGF effects. Development *136*, 1443–1452.

Hu, B.Y., Du, Z.W., and Zhang, S.C. (2009b). Differentiation of human oligodendrocytes from pluripotent stem cells. Nat. Protoc. *4*, 1614–1622.

Izrael, M., Zhang, P., Kaufman, R., Shinder, V., Ella, R., Amit, M., Itskovitz-Eldor, J., Chebath, J., and Revel, M. (2007). Human oligodendrocytes derived from embryonic stem cells: Effect of noggin on phenotypic differentiation in vitro and on myelination in vivo. Mol. Cell. Neurosci. *34*, 310–323.

Keirstead, H.S., Nistor, G., Bernal, G., Totoiu, M., Cloutier, F., Sharp, K., and Steward, O. (2005). Human embryonic stem cell-derived oligodendrocyte progenitor cell transplants remyelinate and restore locomotion after spinal cord injury. J. Neurosci. *25*, 4694–4705.

Keyoung, H.M., and Goldman, S.A. (2007). Glial progenitor-based repair of demyelinating neurological diseases. Neurosurg. Clin. N. Am. *18*, 93–104, x.

Keyoung, H.M., Roy, N.S., Benraiss, A., Louissaint, A., Jr., Suzuki, A., Hashimoto, M., Rashbaum, W.K., Okano, H., and Goldman, S.A. (2001). High-yield selection and extraction of two promoter-defined phenotypes of neural stem cells from the fetal human brain. Nat. Biotechnol. *19*, 843–850.

Krencik, R., Weick, J.P., Liu, Y., Zhang, Z.J., and Zhang, S.C. (2011). Specification of transplantable astroglial subtypes from human pluripotent stem cells. Nat. Biotechnol. *29*, 528–534.

Lee, J.-P., Jeyakumar, M., Gonzalez, R., Takahashi, H., Lee, P.J., Baek, R.C., Clark, D., Rose, H., Fu, G., Clarke, J., et al. (2007). Stem cells act through multiple mechanisms to benefit mice with neurodegenerative metabolic disease. Nat. Med. *13*, 439–447.

Maherali, N., Ahfeldt, T., Rigamonti, A., Utikal, J., Cowan, C., and Hochedlinger, K. (2008). A high-efficiency system for the generation and study of human induced pluripotent stem cells. Cell Stem Cell *3*, 340–345.

Pruszak, J., Ludwig, W., Blak, A., Alavian, K., and Isacson, O. (2009). CD15, CD24, and CD29 define a surface biomarker code for neural lineage differentiation of stem cells. Stem Cells *27*, 2928–2940.

Qi, Y., Cai, J., Wu, Y., Wu, R., Lee, J., Fu, H., Rao, M., Sussel, L., Rubenstein, J., and Qiu, M. (2001). Control of oligodendrocyte differentiation by the Nkx2.2 homeodomain transcription factor. Development *128*, 2723–2733.

Roy, N.S., Wang, S., Harrison-Restelli, C., Benraiss, A., Fraser, R.A., Gravel, M., Braun, P.E., and Goldman, S.A. (1999). Identification, isolation, and promoter-defined separation of mitotic oligodendrocyte progenitor cells from the adult human subcortical white matter. J. Neurosci. *19*, 9986–9995.

Roy, N.S., Cleren, C., Singh, S.K., Yang, L., Beal, M.F., and Goldman, S.A. (2006). Functional engraftment of human ES cell-derived dopaminergic neurons enriched by coculture with telomerase-immortalized midbrain astrocytes. Nat. Med. *12*, 1259–1268.

Shinkai, Y., Rathbun, G., Lam, K.P., Oltz, E.M., Stewart, V., Mendelsohn, M., Charron, J., Datta, M., Young, F., Stall, A.M., et al. (1992). RAG-2-deficient mice lack mature lymphocytes owing to inability to initiate V(D)J rearrangement. Cell *68*, 855–867.

Sim, F.J., McClain, C.R., Schanz, S.J., Protack, T.L., Windrem, M.S., and Goldman, S.A. (2011). CD140a identifies a population of highly myelinogenic, migration-competent and efficiently engrafting human oligodendrocyte progenitor cells. Nat. Biotechnol. *29*, 934–941.

Terada, N., Baracskay, K., Kinter, M., Melrose, S., Brophy, P.J., Boucheix, C., Bjartmar, C., Kidd, G., and Trapp, B.D. (2002). The tetraspanin protein, CD9, is expressed by progenitor cells committed to oligodendrogenesis and is linked to beta1 integrin, CD81, and Tspan-2. Glia *40*, 350–359.

Thomson, J.A., Itskovitz-Eldor, J., Shapiro, S.S., Waknitz, M.A., Swiergiel, J.J., Marshall, V.S., and Jones, J.M. (1998). Embryonic stem cell lines derived from human blastocysts. Science *282*, 1145–1147.

Wang, S., Chandler-Militello, D., Lu, G., Roy, N.S., Zielke, A., Auvergne, R., Stanwood, N., Geschwind, D., Coppola, G., Nicolis, S.K., et al. (2010). Prospective identification, isolation, and profiling of a telomerase-expressing subpopulation of human neural stem cells, using sox2 enhancer-directed fluorescence-activated cell sorting. J. Neurosci. *30*, 14635–14648.

Windrem, M.S., Roy, N.S., Wang, J., Nunes, M., Benraiss, A., Goodman, R., McKhann, G.M., 2nd, and Goldman, S.A. (2002). Progenitor cells derived from the adult human subcortical white matter disperse and differentiate as oligodendrocytes within demyelinated lesions of the rat brain. J. Neurosci. Res. *69*, 966–975.

Windrem, M.S., Nunes, M.C., Rashbaum, W.K., Schwartz, T.H., Goodman, R.A., McKhann, G., 2nd, Roy, N.S., and Goldman, S.A. (2004). Fetal and adult human oligodendrocyte progenitor cell isolates myelinate the congenitally dysmyelinated brain. Nat. Med. *10*, 93–97.

Windrem, M.S., Schanz, S.J., Guo, M., Tian, G.F., Washco, V., Stanwood, N., Rasband, M., Roy, N.S., Nedergaard, M., Havton, L.A., et al. (2008). Neonatal chimerization with human glial progenitor cells can both remyelinate and rescue the otherwise lethally hypomyelinated shiverer mouse. Cell Stem Cell *2*, 553–565.

Zhao, T., Zhang, Z.N., Rong, Z., and Xu, Y. (2011). Immunogenicity of induced pluripotent stem cells. Nature *474*, 212–215.

Zhou, Q., Wang, S., and Anderson, D.J. (2000). Identification of a novel family of oligodendrocyte lineage-specific basic helix-loop-helix transcription factors. Neuron *25*, 331–343.

Zhou, Q., Choi, G., and Anderson, D.J. (2001). The bHLH transcription factor Olig2 promotes oligodendrocyte differentiation in collaboration with Nkx2.2. Neuron *31*, 791–807.

Cell Stem Cell
Clinical Progress

Expandable Megakaryocyte Cell Lines Enable Clinically Applicable Generation of Platelets from Human Induced Pluripotent Stem Cells

Sou Nakamura,[1] Naoya Takayama,[1] Shinji Hirata,[1] Hideya Seo,[1] Hiroshi Endo,[1] Kiyosumi Ochi,[1] Ken-ichi Fujita,[1] Tomo Koike,[1] Ken-ichi Harimoto,[1] Takeaki Dohda,[1] Akira Watanabe,[2] Keisuke Okita,[2] Nobuyasu Takahashi,[3] Akira Sawaguchi,[3] Shinya Yamanaka,[2] Hiromitsu Nakauchi,[4] Satoshi Nishimura,[5,6] and Koji Eto[1,4,*]
[1]Department of Clinical Application, Center for iPS Cell Research and Application (CiRA), Kyoto University, 606-8507, Japan
[2]Department of Reprogramming Science, CiRA, Kyoto University, 606-8507, Japan
[3]Department of Anatomy, Ultrastructural Cell Biology, Faculty of Medicine, University of Miyazaki, Miyazaki 889-1692, Japan
[4]Laboratory of Stem Cell Therapy, Center for Stem Cell Biology and Regenerative Medicine, Institute of Medical Science, The University of Tokyo, Tokyo 108-8639, Japan
[5]Department of Cardiovascular Medicine, The University of Tokyo, Tokyo 113-8655, Japan
[6]Department of Cell and Molecular Medicine, Center for Molecular Medicine, Jichi Medical University, Tochigi 329-0498, Japan
*Correspondence: kojieto@cira.kyoto-u.ac.jp
http://dx.doi.org/10.1016/j.stem.2014.01.011

SUMMARY

The donor-dependent supply of platelets is frequently insufficient to meet transfusion needs. To address this issue, we developed a clinically applicable strategy for the derivation of functional platelets from human pluripotent stem cells (PSCs). This approach involves the establishment of stable immortalized megakaryocyte progenitor cell lines (imMKCLs) from PSC-derived hematopoietic progenitors through the overexpression of BMI1 and BCL-XL to respectively suppress senescence and apoptosis and the constrained overexpression of c-MYC to promote proliferation. The resulting imMKCLs can be expanded in culture over extended periods (4–5 months), even after cryopreservation. Halting the overexpression of c-MYC, BMI1, and BCL-XL in growing imMKCLs led to the production of CD42b$^+$ platelets with functionality comparable to that of native platelets on the basis of a range of assays in vitro and in vivo. The combination of robust expansion capacity and efficient platelet production means that appropriately selected imMKCL clones represent a potentially inexhaustible source of hPSC-derived platelets for clinical application.

INTRODUCTION

Platelets generated from megakaryocyte (MK) precursors are vital for the treatment of many hematological diseases and traumas. Currently, platelets can only be obtained through blood donation. Fresh single-donor platelets have a short shelf life and must be maintained with plasma at 20°C –24°C; they readily lose clotting activity when pooled from multiple donors and frozen or warmed to 37°C (Bergmeier et al., 2003; Nishikii et al., 2008). Moreover, repeated transfusion induces the production of antibodies against allogenic human leukocyte antigen (HLA) or human platelet antigen (HPA) on the transfused platelets (Schiffer, 2001), which renders the patient unresponsive to platelet transfusion therapy. These supply logistics and practical limitations represent barriers to the widespread application of platelets as a resource for patients. In that context, human induced pluripotent stem cells (hiPSCs) (Takahashi et al., 2007) could represent a potent alternative source of platelet production. Because platelets do not contain nuclei, gamma irradiation before transfusion could be used to eliminate any residual contaminating hiPSCs and their derivatives, reducing the risk of tumorigenesis. Thus, the application of iPSC-based technology could potentially yield a consistent supply of HLA- and/or HPA-matched or even autologous platelets in a way that would address some of the major roadblocks in the current clinical approaches to platelet-based therapy.

Our group and another recently demonstrated that hiPSCs derived from human skin fibroblasts or blood cells or from human embryonic stem cells (hESCs) can be used to generate platelets in vitro and that these platelets appeared to function normally when transfused into mouse models (Takayama et al., 2010; Lu et al., 2011). However, the yield of platelets was still far below what would be required to generate even 1 u of platelet concentrate for patient transfusion. Recent studies have shown that self-replicating MK progenitors can be directly generated from murine hematopoietic stem cells (HSCs) within bone marrow (BM) in vivo (Yamamoto et al., 2013), but there was no evident way to sustain long-term self-replication of MK progenitors in vitro. We previously showed that the activation of c-MYC to a restricted level below that associated with senescence and apoptosis induction appears to lead to an increase in platelet generation (Takayama et al., 2010). In the present study, we show that co-overexpression of c-MYC and BMI1, a polycomb complex component that represses the *INK4A/ARF* gene locus (Oguro et al., 2006), enables megakaryocytic cell lines (MKCLs) derived from hiPSCs or hESCs to grow continuously for up to 2 months. A destabilization domain (DD) vector system (Banaszynski et al., 2006) enabled us to control exogenous c-MYC within the appropriate range, leading to successful induction of

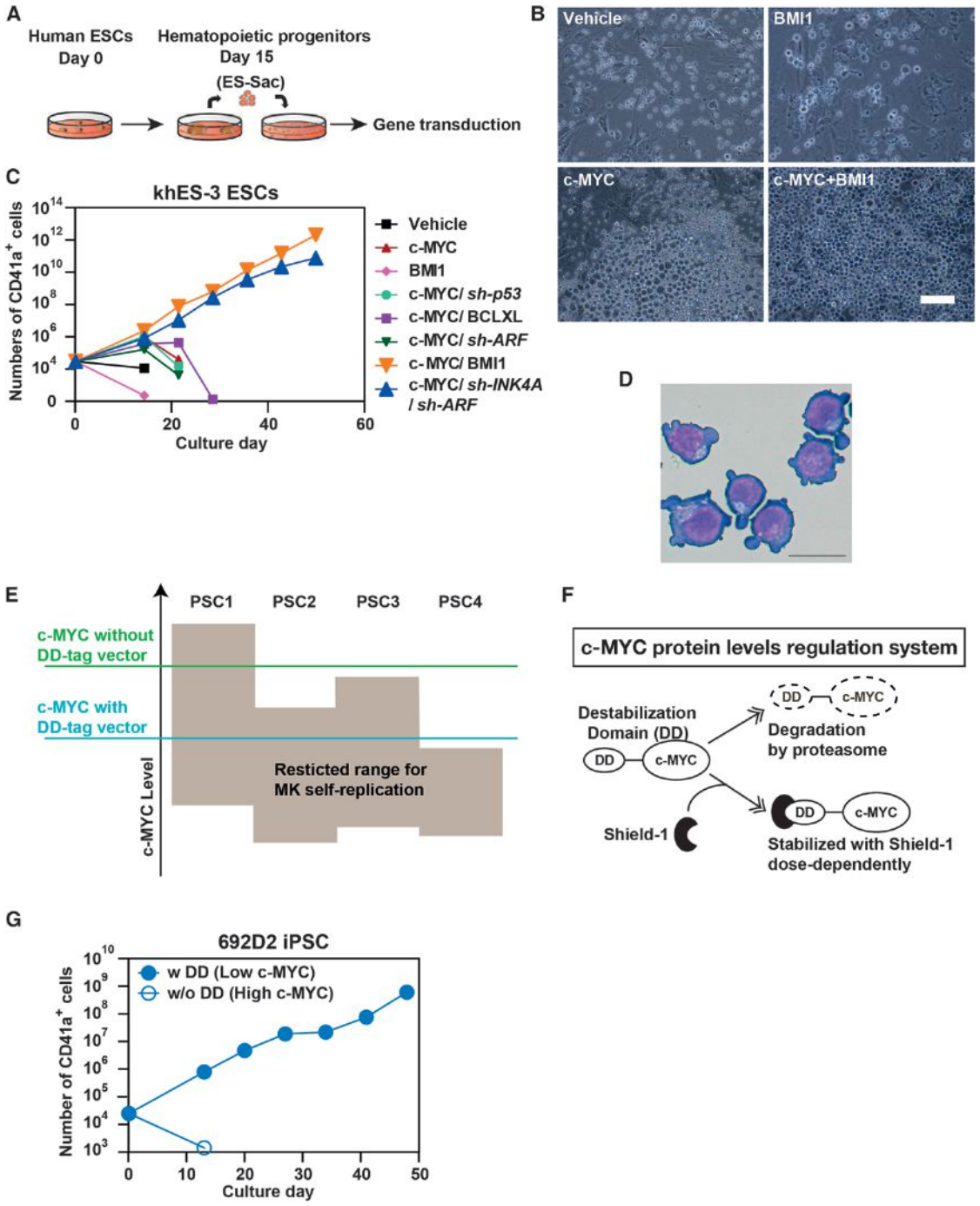

Figure 1. Induction of a Megakaryocyte Progenitor Cell Line from Human Embryonic Stem Cells and Induced Pluripotent Stem Cells Was Induced by Restricted Range of c-MYC Overexpression along with BMI1 Overexpression

(A) Scheme for inducing megakaryocyte progenitor cell lines (MKCLs) from human PSCs. The targets for gene transduction are hematopoietic progenitors, including the $CD34^+$ population.

(B) Representative photomicrograph of cells transduced with vector alone, c-MYC alone, BMI1 alone, or a combination of c-MYC and BMI1 (200×). The scale bar represents 100 μm.

(C) Numbers of $CD41a^+$ cells after gene manipulation. Hematopoietic progenitor cells (HPCs) within human embryonic stem cell (hESC; KhES-3 clone) sacs were collected and transduced with noninducible retroviral vectors with vector alone (GFP alone), c-MYC alone, BMI1 alone, or combinations of c-MYC plus *p53* knockdown, c-MYC plus *ARF* knockdown, c-MYC plus BCL-XL, c-MYC plus *INK4A*/*ARF* knockdown (blue), or c-MYC plus BMI1 (orange). The combinations of c-MYC plus BMI1 and c-MYC plus *INK4A*/*ARF* knockdown induced exponential growth in $CD41a^+$ megakaryocytes (MKs). Results are expressed as means from two to three independent experiments.

(D) Representative image of May-Giemsa-stained MKCLs. The scale bar represents 20 μm.

(legend continued on next page)

MKCLs. The addition of BCL-XL made it possible to obtain immortalized MKCLs (imMKCLs) that can be grown for more than 5 months and thus function as candidate cell banks. When the expression of c-MYC, BMI1, and BCL-XL is turned off, imMKCLs produce functional CD42b (glycoprotein Ib α [GPIbα] and receptor for von Willebrand factor [vWF])$^+$ platelet particles. The expression of CD42b on platelets is required for the initiation of clotting (Ware et al., 2000) and bacterial clearance in vivo (Wong et al., 2013). Although previous studies have reported that CMK, Meg01, and K562 cells, three well-known MK lineage leukemia cell lines, can become polyploid and release CD41a$^+$ particles in the presence of agonist stimulation, they do not provide a suitable source for a platelet supply because the particles are CD42b$^-$ (Isakari et al., 2009; Sato et al., 1989; Terui et al., 1998). In this report, we describe a strategy that involves MKCLs with long-term self-renewal capacity and the potential to provide an inexhaustible supply of CD42b$^+$ platelets; in that respect, they resemble endogenous self-replicating MK progenitors identified in vivo (Yamamoto et al., 2013). Clinical application of this technology could provide a plentiful supply of platelets from suitably screened and selected imMKCL clones to serve as cell bank stocks with minimal risk of adverse side effects.

RESULTS

Induction of Expandable MK Progenitor Cells from Human PSCs with c-MYC and BMI1

We previously showed that, when expressed at an appropriate level, c-MYC acts as a growth mediator in normal megakaryopoiesis and thrombopoiesis from hESCs or hiPSCs, whereas excessive c-MYC expression in hematopoietic progenitor cells (HPCs) induces the activation of the INK4A and ARF pathways, leading to senescence and apoptosis (Takayama et al., 2010). Therefore, we hypothesized that c-MYC activation might contribute to self-replication at the MK progenitor stage. When we assessed the effects of c-MYC overexpression alone, BMI1 overexpression alone, c-MYC overexpression plus *p53* knockdown, c-MYC plus BCL-XL overexpression, and c-MYC plus BMI1 overexpression in CD34$^+$CD43$^+$-containing HPCs derived from the KhES-3 hESC line, we found that c-MYC overexpression alone or the combination of c-MYC and BMI1 overexpression increased numbers of large cells expressing megakaryocytic CD41a$^+$CD42a (GPIX)$^+$CD42b$^+$CD9$^+$ markers over a 2-week period (Figures 1A–1C; Figure S1A available online). With c-MYC and BMI1 overexpression (Figure 1C, orange triangles) or c-MYC overexpression and *INK4A/ARF* knockdown (Figure 1C, blue triangles), but none of the other aforementioned conditions, proliferation of this cell population was maintained at an exponential level for 2 months (MK progenitor cell line; Figure 1C, orange triangles) and was dependent upon the presence of thrombopoietin (TPO) with the help of stem cell factor (SCF). This suggests that the effect of BMI1 may be to at least inhibit INK4A/ARF-dependent senescence and apoptosis during the initiation of self-replication, as confirmed by quantitative PCR (qPCR) analysis, which revealed BMI1 represses c-MYC-induced the upregulation of *INK4A/ARF* (Figure S1B). The CD41a$^+$ MKCLs derived from hESCs showed monoblastic morphology with basophilic cytoplasm (Figure 1D) and generated aberrant platelet-like particles expressing normal levels of CD41a but reduced levels of CD42b (Figure S1C). This is consistent with the requirement for the downregulation of c-MYC for maturation of MKs (Takayama et al., 2010).

A Defined c-MYC Expression Level Is Important for MKCL Induction and Robust Expansion

Our ability to induce MKCLs with c-MYC and BMI1 overexpression and then grow the cells for more than 2 weeks varied among individual PSC clones (data not shown). Therefore, we suspected that individual PSC clones require different levels of c-MYC. When we prepared an inducible all-in-one vector harboring c-MYC and BMI1 (Ohmine et al., 2001) (Figure S1D), we obtained clearer evidence that c-MYC levels are crucial for the sustained growth of MKCL, given that we saw different results with c-MYC-2A-BMI1 and BMI1-2A-c-MYC gene sequences in this vector (Figures S1E and S1F). Furthermore, to confirm the hypothesis that, in some individual PSC clones, the effective c-MYC expression level may be restricted to a specific range (Figure 1E), we used a vector tagged with a DD (Banaszynski et al., 2006) in order to reduce the level of c-MYC protein (Figure 1F). This system regulates protein stability, and thus the level of c-MYC expression, in a manner that depends on the Shield1 concentration (NIH 3T3 cells in Figure S1G). When we used this DD-tagged vector system to establish iPSC (692D2)-derived MKCLs, we found that 692D2 iPSCs showed no self-replication when transduced with c-MYC-2A-BMI1 overexpression without a DD tag, but transduction of the DD tag vector without the addition of Shield1 allowed clone 692D2 to grow for up to 50 days in culture (Figure 1G). This self-replication was inhibited by 100 or 1,000 nM Shield1 (Figure 2Ai), suggesting the total c-MYC level most likely blocked stable self-replication. This result was not due to nonspecific cell toxicity (Figure S2A) or activation of the *INK4A/ARF* gene locus by the high level of c-MYC, given that levels of *p14* and *p16* mRNA (derived *INK4A/ARF* locus gene) did not differ in the presence or absence of 1,000 nM Shield1 (Figure S2B).

Given that BMI1, which is also overexpressed in our system, represses the *INK4A/ARF* gene locus, the mechanism underlying the MYC-dependent failure of continuous self-replication was unclear. However, the well-known involvement of c-MYC in caspase-dependent apoptosis (Juin et al., 2002) prompted us to assess caspase activity in the MKCL clone. Caspase assays revealed that the activation of caspases 3 and 7 in DD

(E) Schematic diagram illustrating the hypothesis that there is an association between c-MYC levels and MK self-replication. Individual human PSC clones (hESCs or hiPSCs) define the c-MYC activation window (restricted range) needed to induce MK self-replication.
(F) Scheme for a c-MYC regulation system using a destabilization domain (DD). Proteins with a DD are rapidly destroyed via the ubiquitin-proteasome pathway. Administration of Shield1 putatively inhibits DD-mediated degradation in a concentration-dependent manner.
(G) Numbers of CD41a$^+$ MKs determined by flow cytometry. MKs were derived from iPSCs (692D2) transduced with inducible c-MYC-DD-2A-BMI1 (with [w] DD) or inducible c-MYC-2A-BMI1 retroviral vector (without [w/o] DD; see Figure S2A).

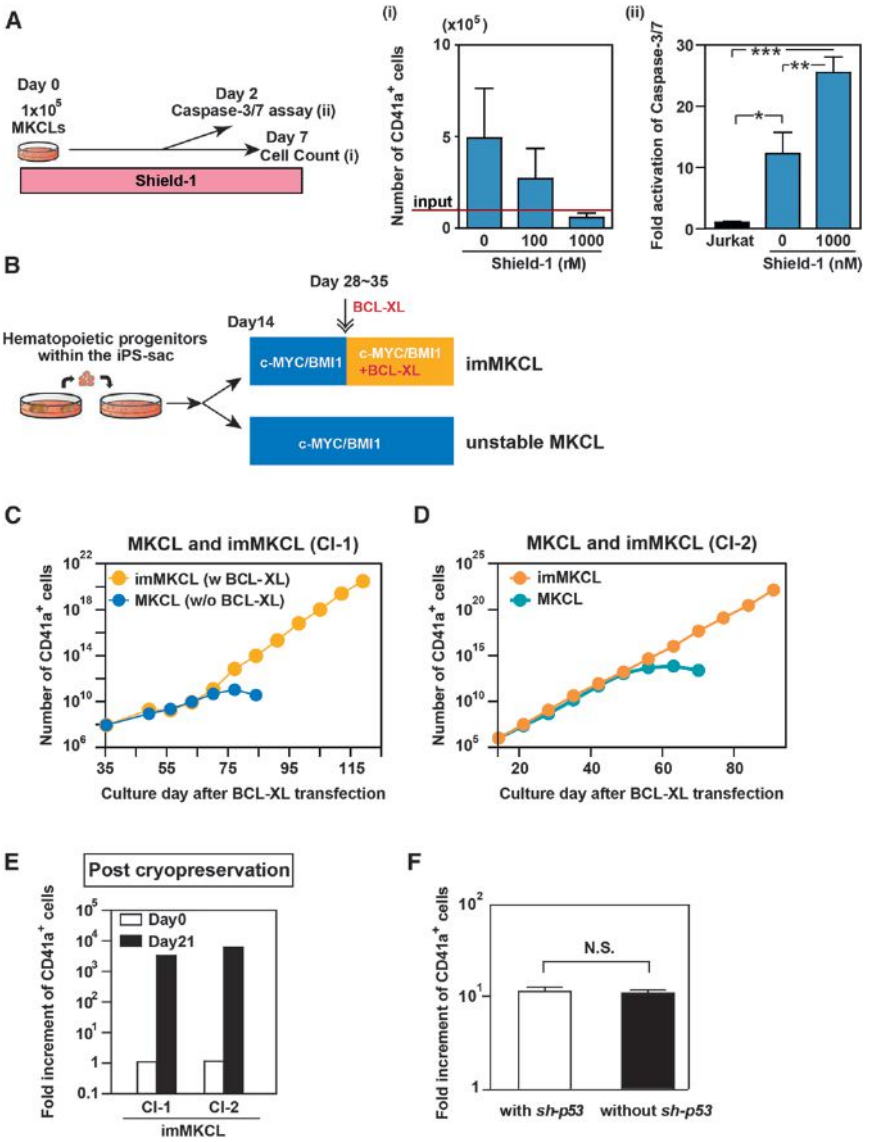

Figure 2. Later Expression of BCL-XL Inhibited Caspase Activation Induced by Excessive c-MYC, Stabilizing Cell Growth and Contributing to the Establishment of imMKCLs

(A) Relationship between the c-MYC expression level, cell viability, and caspase activity. (i) Numbers of live CD41a$^+$ MKs derived from hiPSC (692D2)-based MKCLs generated with an inducible DD vector in the absence or presence of the indicated concentrations of Shield1. (ii) Caspase 3 and 7 activity in samples of Jurkat cells (control, fold = 1, black bar) or hiPSC (692D2)-derived MKCLs on day 2 of culture after transduction with a DD system in the absence or presence of 1,000 nM Shield1. *p < 0.05; **p < 0.01; ***p < 0.001. Results are expressed as means ± SE from five independent experiments.

(B) Scheme for generating unstable MKCLs with c-MYC and BMI1 (2F) or imMKCLs with c-MYC, BMI1, and BCL-XL (3F).

(C and D) Additional transduction of *BCL-XL* gene improved the growth curve for CD41a$^+$ MKs derived from hiPSC (692D2)-derived MKCLs with a DD system (C; clone 1 [Cl-1]) and from hESCs (KhES3)-derived MKCLs (D; Cl-2). Yellow circles indicate the numbers of cells obtained with 3F, and blue circles indicate 2F. Cell numbers were calculated cumulative values.

(E) Increment in CD41a$^+$ cells derived from Cl-1 and Cl-2 after cryopreservation. Results were an average of two independent experiments.

(F) The additional effect of *p53* knockdown on immortalization of MKCLs. Results are expressed as means ± SE from three independent experiments.

self-replicable MKCLs derived from iPSC clone 692D2 was 2-fold higher in the presence of 1,000 nM Shield1 than in its absence. This increased caspase activation was also associated with reduced cell viability (Figures 2Ai and 2Aii), confirming that restricting caspase activation may be key to successfully establishing expandable MKCLs (Figure S2B). Notably, caspase activation in the absence of Shield1 was still 12.2× higher than in Jurkat cells (Figure 2Aii). Some apoptotic events are transcriptionally determined (Chen et al., 2007; Kumar and Cakouros, 2004). Therefore, to further address the mechanism by which excessive c-MYC represses self-replication and induces apoptosis, we carried out a microarray analysis with iPSC-derived MKCLs treated with or without 1,000 nM Shield1. Gene ontology classification of genes differentially expressed in the presence and absence of Shield1 indicated a correlation between higher levels of c-MYC (1,000 nM Shield1) and the expression of the proapoptotic factors *BMF* and *BBC3* (*PUMA*), which can contribute to the release of cytochrome-c from mitochondria via mitochondrial outer membrane permeabilization. High levels of c-MYC also influenced cell-cycle-related genes, increasing the expression of cyclin-dependent kinase inhibitors (*CDKN1B*, *p27*, and *Kip1*), which could arrest MKCL growth. These changes were also confirmed by qPCR analysis (Figures S2C and S2D). Thus, high c-MYC expression can lead to caspase-dependent MKCL apoptosis (Figure 2A), despite the suppression of the INK4A/ARF pathway by BMI1 (Figure S2B). These data again indicate that alternative apoptosis pathways, as well as the INK4A/ARF pathways, are independently induced by excessive c-MYC in individual PSC-derived MKCL clones.

Suppression of Caspase Activation through BCL-XL Expression Promotes Immortalization

We noticed that MKCLs obtained from either ESC clone KhES3 or iPSC clone 692D2 with c-MYC plus BMI1 (Figure 2B, bottom line) exhibited limited growth potential and discontinuous cell growth that ceased at about 60 days, potentially reflecting an increase in caspase activation (692D2 cell growth in Figure 2C; KhES3 cell growth in Figure 2D; 0 nM Shield1for 692D2 in Figure 2Ai and KhES-3 in Figure S2E). Thus, it appears that the expression of c-MYC and BMI1 alone are not suitable for

generation of an immortalized cell line. We therefore sought to examine the effect of BCL-XL on days 14–21 after transduction of c-MYC plus BMI1 (Figure 2B). We found that BCL-XL overexpression induced exponential growth of CD41a$^+$ cells derived from either 692D2 or KhES3 cells. This growth persisted for over 5 months, and we therefore deemed these cells to be self-renewing imMKCLs (Figures 2C and 2D for 692D2 [imMKCL clone 1, Cl-1], and Figure 2D for KhES-3 ESCs [Cl-2]; yellow circles). These two imMKCLs also showed comparable growth after cryopreservation (Figure 2E) as well as somewhat larger cell size and expression of CD41a, CD42a, CD42b, and CD9 (Figure S2F). Growth of these imMKCLs was sustained even with higher c-MYC expression in the presence of 100 or 1,000 nM Shield1 (Figures S2G–S2I), and the cells exhibited comparatively low levels of caspase 3 and 7 activation, similar to that of Jurkat cells (Figure S2I).

To further validate the function of BCL-XL in caspase regulation, we tested the effect of the caspase inhibitor Z-VAD FMK on proliferation. Caspase inhibition increased proliferation about 21-fold, whereas BCL-XL expression elicited a 64-fold increase. In contrast, the vehicle control (DMSO) enhanced apoptosis (Figures S3A–S3C). Altogether, these findings again confirm that BCL-XL inhibits apoptosis through caspase 3 and 7 inactivation and that c-MYC, BMI1, and BCL-XL are all required for the induction of imMKCLs from PSC clones. In addition, because it is well known that activation of p53 and p21 is also associated with c-MYC-dependent apoptosis (Hotti et al., 2000), we assessed the effect of inhibiting p53 on cell growth with imMKCL Cl-1. Our results show no involvement of p53 in cells expressing c-MYC, BMI1, and BCL-XL (Figure 2F), and a similar result was obtained with KhES-3-imMKCL (Cl-2; data not shown).

Next, we asked whether the simultaneous overexpression of c-MYC, BMI1, and BCL-XL was more suitable for establishing imMKCLs than overexpression of c-MYC plus BMI1 followed by later expression of BCL-XL. To address that question, we used four individual PSC clones to compare two protocols: simultaneous overexpression of all three genes or overexpression of c-MYC and BMI1 followed by BCL-XL 14–21 days later, counting from the HPC stage (days 28–35 from the hESC or iPSC stage; Figure 2B, top). Simultaneous addition of all three genes promoted maximal proliferation for only up to 40–50 days, whereas stepwise addition of c-MYC and BMI1 followed by BCL-XL consistently showed more sustained proliferation with all clones examined (Figure S3D–S3G).

One potential caveat to this approach is that long-term cultivation might lead to imMKCLs becoming oncogenic. Interestingly, after cultivation for 5 months, two of three imMKCLs, Cl-1 and Cl-2 but not Cl-7, consistently showed a specific karyotypic abnormality: chromosomal translocation that included chromosome +1 or −5 (Figure S4A). When these two clones were separately infused into immunodeficient mice, one (n = 5) displayed leukemogenesis contributing to early death, but the other did not (Figure S4B). These results highlight the importance of transplantation studies with imMKCLs for clone selection. Interestingly, Cl-7 exhibited no karyotypic abnormality (Figure S4A) and consistently showed no abnormalities in transplantation studies (up to 16 weeks; Figure S4B). Therefore, we suggest that combined analysis, including both karyotypic examination and transplantation of individual imMKCL clones, would be useful for selecting imMKCLs as cell bank stock candidates.

Differentiation Phase of imMKCLs for Upregulation of CD42b during Maturation

The GPIb-V-IX complex, particularly CD42b (GPIbα), on platelets is a key binding site for vWF and is required for the initial adhesion of platelets to an injured vessel wall (Ware et al., 2000) as well as normal circulation after transfusion (Leytin et al., 2004). Platelets lacking CD42b expression are quickly cleared from the circulation in vivo, leading to insufficient numbers of circulating platelets after transfusion (Nishikii et al., 2008). Assuming that the downregulation of c-MYC would be required for the generation of CD42b$^+$ platelets (Takayama et al., 2010), we turned off the expression of all three inducers (c-MYC, BMI1, and BCL-XL). Five days after these genes were turned off under serum-free conditions (Figure 3A), the iPSC-derived imMKCLs had changed to exhibit MK polyploidization (Figure 3B; on, 5.5% [left]; off, 20.2% [right]) as well as proplatelet formation (Figure 3C and Movie S1) with increased CD42b expression. This is exemplified by the two imMKCL clones in Figure 3D. Along with those changes, after turning off the expression of the exogenous inducing genes, both endogenous and exogenous *c-MYC*, *BMI1*, and *BCL-XL* expression declined (Figure S5A), and transcription factors associated with MK maturation, *GATA1*, *FOG1*, *NFE2*, and *β1-tubulin* increased to levels comparable to or higher than those seen in cord blood (CB)-derived MKs (Figure 3E).

Induction of Efficient Yield of CD41a$^+$CD42b$^+$ Platelets

Turning *c-MYC*, *BMI1*, and *BCL-XL* off with a doxycycline-regulated system increased the CD42b$^+$ platelet yield from imMKCLs and upregulated CD42b expression in CD41a$^+$ platelets (Figures 4A and 4B), in comparison to maintaining the overexpression of the three factors or *BCL-XL* alone (Figure S5B). In addition, whereas imMKCLs generated significant numbers of CD41a$^+$ CD42b$^+$ particles that closely resembled endogenous platelets, the well-known MKCLs Meg01, CMK, and K562, produced mostly CD41a$^+$, but CD42b$^-$, platelet-like particles (Figure S5C). We estimated production to be three CD42b$^+$ platelets per Cl-2 imMKCL-MK and 10 platelets per Cl-7 imMKCL-MK after the induction of differentiation (5 days after exogenous expression was turned off; Figure S5D) under serum-free conditions, which is a suitable level for clinical application. In a 10-cm dish scale (10 ml), 4×10^6 and 2×10^6 platelets per ml were obtained from imMKCL Cl-7 and Cl-2, respectively (Figure 4C). Therefore, our proposed system could theoretically yield 10^{11} platelets (equivalent to one transfusion) within 5 days with 25–50 l medium.

Characterization of platelet yields using flow cytometry revealed that the expression levels of platelet-functional molecules, including CD42b, CD61 (β3 integrin), protease-activated receptor 1 (PAR1; thrombin receptor), CD49b (α2 integrin), and CD29 (β1 integrin), were mostly comparable to those seen in fresh human peripheral blood (PB)-derived platelets and higher than in human endogenous pooled platelets, although the expression of GPVI (GP6) was a little weaker than it was in fresh PB (Figure 4D), possibly because of receptor shedding at 37°C (Gardiner et al., 2012). At the ultrastructural level, transmission

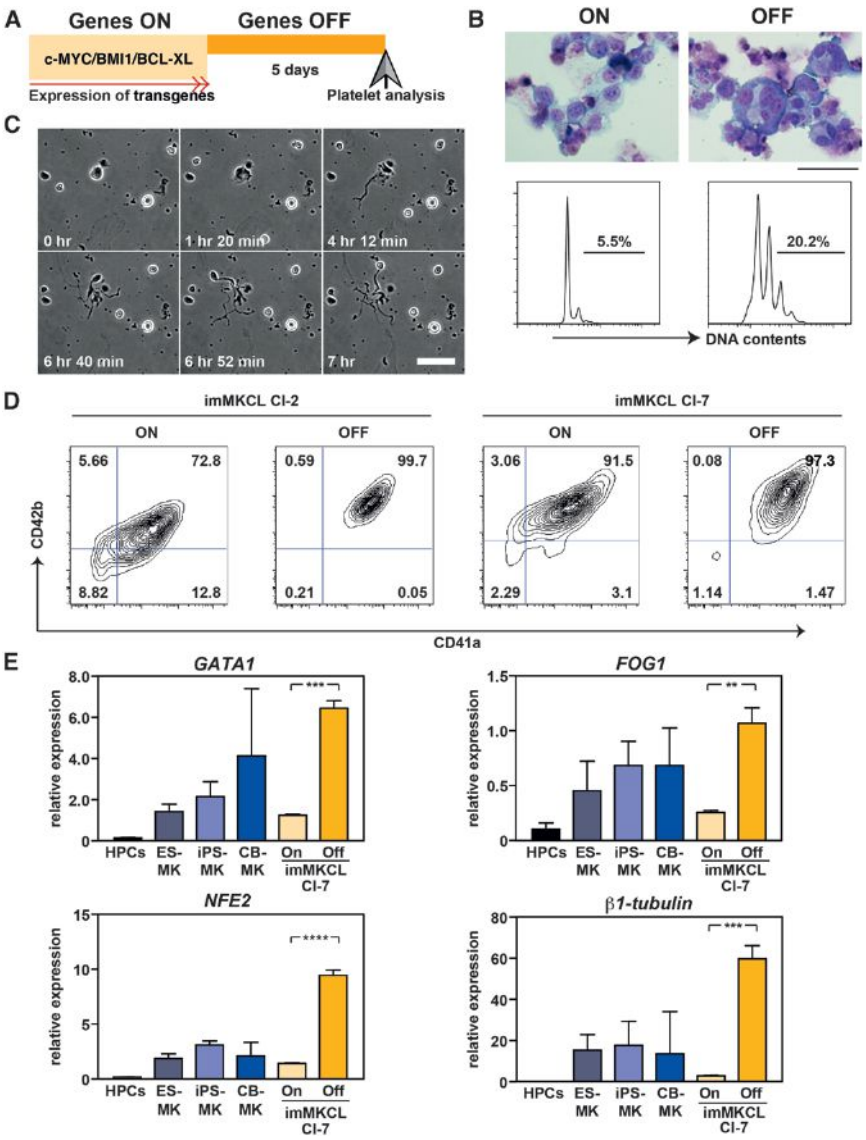

Figure 3. Turning Off 3F Transgenes Promoted the Maturation of MKs from imMKCLs

(A) MKs and platelets were analyzed 5 days after turning off 3F (cMYC, BMI1, and BCL-XL) expression.

(B) Giemsa staining (top pictures) and flow cytometric analysis of ploidy among imMKCLs with and without 3F expression (genes on or genes off). The scale bar represents 50 μm.

(C) imMKCL Cl-7 examined with time-lapse microscopy 4 days after genes were turned off. Sequential images showing proplatelet formation. The scale bar represents 50 μm.

(D) Representative contour plots for imMKCL Cl-2 and Cl-7 (MK populations are shown in side and forward scatter contour plots in a flow cytometer) derived from ESCs and iPSCs (KhES3 and DN-SeV2, respectively).

(E) qPCR analysis of *GATA1*, *p45 NF-E2*, *FOG1*, and *β1-tubulin* gene expression. Samples were obtained from hiPSC-derived $CD34^+/CD43^+/CD41a^-/GPA^-$ HPCs (Sac-HPCs), Sac-dependent MKs from ESCs and iPSCs, MKs derived from cord blood (CB)-$CD34^+$ cells, and imMKCL Cl-7 (DN-SeV2 iPSC clone) in the presence (on) or absence (off) of 3F. Gene expression was normalized to GAPDH expression. 3F was transduced into Sac-HPCs as described in the Experimental Procedures. Results are expressed as means ± SE from three independent experiments.

electron microscopy revealed frequent generation of platelets through cytoplasmic fragmentation (Figure S6A) and proplatelets in the culture dish (Figure 3C and Movie S1). Individual imMKCL-derived platelets showed normal microtubules but fewer granules when compared to fresh human donor platelets (Figure 5A and S6A). To explore the functionality of imMKCL-derived platelets, we used flow cytometry to examine integrin αIIβ3 activation (inside-out signaling) or platelet aggregation after stimulation with platelet agonists (De Cuyper et al., 2013). Agonist stimulation increased PAC-1 binding mean fluorescent intensity, given that this antibody binds to the activated form of αIIbβ3 integrin (Figures 5B and 5C) as well as platelet aggregation (Figure 5D), clot retraction (Figure 5E), actin cytoskeletal changes (Figure S6B), and vWF or ADP secretion (Figure S6C). Collectively, most in vitro functional parameters indicated that imMKCL platelets gave less robust responses than fresh human platelets, but, comparison to pooled human endogenous platelets (Figures 5C and 5D) or iPSC-derived platelets generated with a direct differentiation method (data not shown; Takayama et al., 2010) indicated their functionality was still sufficient to be useful. We also used an ex vivo flow chamber system within which human vWF (10 μg/ml) was immobilized and a shear rate of 1,600 s^{-1} was applied. imMKCL platelets showed 62.3% (Cl-2) and 75.8% (Cl-7) of the CD42b-dependent binding of fresh human platelets, and human CD42b blocking antibody reversed this adhesion (Figure 5F). With our current protocol, final platelet collection takes place during the final 5 days in the absence of serum at 37°C. Altogether, these two conditions may account for the relatively low granule content (Figure S6C) and diminished aggregation (Figure 5D).

imMKCL-Derived Platelets Show Thrombogenic Activity in Mouse Models of Thrombocytopenia

Next, we evaluated the in vivo circulation of imMKCL platelets with previously optimized transfusion models (Takayama et al., 2010). Using NOD/SCID/IL-2Rg-null (NOG) mice with irradiation-induced thrombocytopenia, flow cytometric analyses were carried out 30 min, 2 hr, and 24 hr after transfusion (1 or 6 × 10^8 platelets per mouse). The posttransfusion kinetics of imMKCL-derived platelets were nearly the same as those obtained with fresh human platelets (n = 4 individual groups in two independent experiments; Figures 6A and 6B). To further assess the functionality of imMKCL platelets in vivo, we used

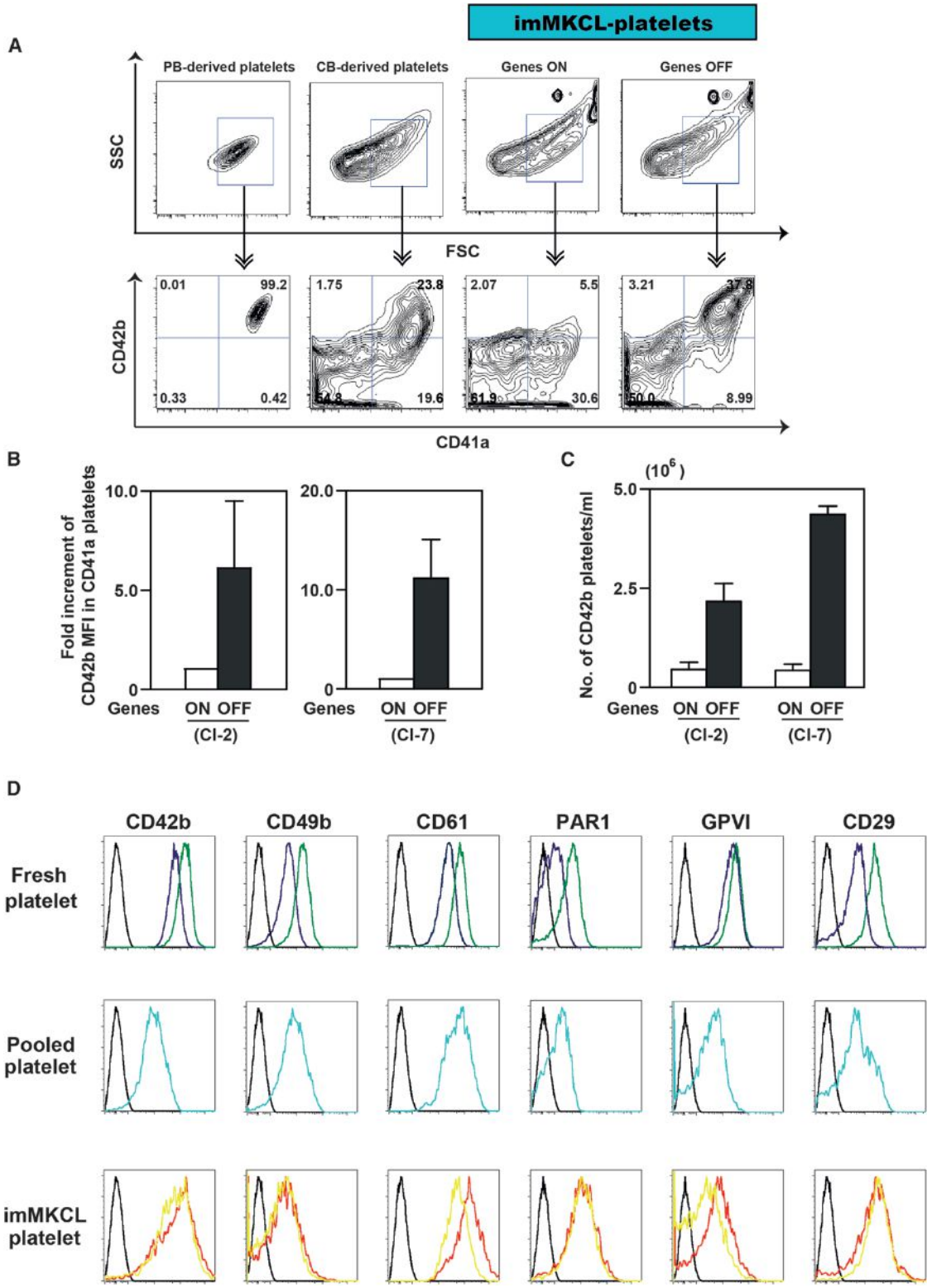

Figure 4. imMKCL-Derived Mature MKs Generated CD41a$^+$CD42b$^+$ Platelets upon Turning Off 3F Transgenes

(A) Representative contour plots for human peripheral blood (PB)-, CB-CD34$^+$HS/PC-, and imMKCL (3F on and off)-derived platelets (platelet population are shown in side and forward scatter contour plots).

(B) Fold increment in CD42b$^+$ mean fluorescent intensity (MFI) among CD41a$^+$ imMKCL Cl-2 (KhES3)- and Cl-7 (DN-SeV2)-derived platelets. White bars, genes on; black bars, genes off. Results are expressed as means± SE from three independent experiments. The mean value of the samples with genes on is assigned as 1.0.

(legend continued on next page)

thrombocytopenic NOG mice and high-spatiotemporal-resolution confocal laser microscopy to visualize the initial adhesion of individual platelets to laser-exposed vessel walls and the subsequent thrombus formation under flow conditions without apparent endothelial disruption (Takizawa et al., 2010; Nishimura et al., 2012). Using fresh human platelets or imMKCL-derived platelets labeled with carboxyfluorescein diacetate and succinimidyl ester, along with injection of Texas Red dextran to visualize blood cell kinetics, we calculated the numbers of platelets adhering to the endothelium after laser injury in the NOG system (Movie S2). We confirmed that single imMKCL-derived platelets adhere to the vessel without forming aggregates with host platelets. AK4 antibody (antihuman P-selectin) partly reversed the platelet adhesion (i.e., >60% for Cl-2 platelets; Figure 6C), indicating that P-selectin contributed to the initial adhesion of the imMKCL platelets and that endothelial-derived vWF and P-selectin are relevant in our mouse models (Nishimura et al., 2012). We also confirmed the contribution of these platelets to thrombi in vivo. We found that platelets from four different imMKCL clones differentially contributed to the developing thrombi to a degree that was at a minimum better than human endogenous pooled platelets ($n = 40$ vessels from three to five animals individually, $p < 0.0001$; Figures 6D and 6E and Movie S3), suggesting that transfer to in vivo conditions may further improve the functionality of imMKCL platelets, perhaps through rejuvenation via endocytosis of granules. Accordingly, our results suggest that, although imMKCL platelets display a smaller capacity for adhesion and aggregation than fresh donor platelets in vitro and in vivo, the functional capacity observed is at a useful level and could potentially be improved by further optimization of the culture conditions and/or the collection method.

DISCUSSION

For successful clinical application of hiPSC technology to platelet transfusion, it will be necessary to produce very large quantities of platelets. To achieve this goal, we will need to boost production efficiency at two stages: the transition from HSCs or myeloid lineage HPCs to MKs and the transition from MKs to platelets (Fuentes et al., 2010; Lu et al., 2011; Takayama et al., 2010; Lambert et al., 2013; Yamamoto et al., 2013). In the present report, we focused on a strategy of generating self-renewing immortalized MKs (Yamamoto et al., 2013), and we have succeeded in establishing imMKCLs with in vitro long-term expansion capacity from human ESCs or iPSCs with three defined factors (c-MYC, BMI1, and BCL-XL) with a temporally hierarchical overexpression protocol (Figures 2 and S3D–S3G). Sustained expansion of these imMKCLs relied on carefully regulated expression of the inducing genes to balance proliferative and apoptotic signals and optimize consistent proliferation. These self-replicating MKs may be applicable in the clinic as a source for a continuous and virtually inexhaustible supply of platelets.

We also showed that the INK4A/ARF and caspase 3 and 7 pathways are activated at the MK progenitor stage when c-MYC levels are too high. The DD derived from mutant human FKBP12 contributes to instability of the tagged protein, but the effect is attenuated by addition of Shield1 (Banaszynski et al., 2006). By using a DD tag vector system as a tool for investigating the impact of restricted c-MYC levels (Figures 1E–1G and S1G), we confirmed the importance of reducing caspase activity during immortalized self-replication of the MK lineage in the presence of TPO and SCF, which suggests that caspase activity plays a role in the previously observed unstable proliferation of MKs in vitro (Figures 7A–7C). This ''constrained protein expression'' system could also be useful for studying genes that must be strictly regulated. These findings also suggest the existence of a regulatory pathway distinct from the INK4A/ARF and p53 pathways that exerts a protective effect against oncogenic stress in the MK lineage (Figure 2F).

Exogenous overexpression of *BCL-XL* contributed to long-term self-replication by attenuating caspase 3 and 7 activation, even in the presence of higher c-MYC levels (Figure 7C), and endogenous BCL-XL may be required for the survival of imMKCLs yielding platelets (Figures S5A and S5B). Consistent with that idea, results obtained with BCL-XL-deficient mice indicate that this protein is required for MK survival and platelet release (Josefsson et al., 2011). By contrast, sustained BCL-XL overexpression reportedly has a negative effect on the development of demarcation membranes in MKs and on platelet production (Kaluzhny et al., 2002). However, c-MYC-dependent MK proliferation was also TPO-dependent and required BMI1 to be present prior to BCL-XL (Figures 1C, 2C, 2D, and S3D–S3G). Interestingly, we recently showed that the combination of c-MYC and BCL-XL overexpression in $CD34^+CD43^+$-containing HPCs leads to stable erythroblast self-replication induced by erythropoietin (Hirose et al., 2013) but not MK lineage growth (Figure 1C). Thus, distinct combinations of c-MYC and BCL-XL and c-MYC and BMI1 appear to provide context-dependent expansion capacity for erythroblast or MK lineages, respectively (Hirata et al., 2013; Yamamoto et al., 2013). It has also been reported that BMI1 directly binds to RUNX1 and core binding transcriptional factor β and acts as a regulator during megakaryopoiesis (Yu et al., 2012), suggesting that BMI1 may have an alternative function in imMKCL development. The MK proliferation program may be disrupted when the effects of BCL-XL dominate before the MK proliferation program is fully established.

For clinical application, the quality of expandable imMKCLs must be strictly validated, and they must be cryopreserved as master cell banks (MCBs) matched to the required HLA and HPA type. After thawing, MCB-derived working cells would be expected to grow within an appropriate and sufficient term and

(C) Numbers of $CD41a^+CD42b^+$ platelets generated from imMKCL Cl-2 (KhES3) and Cl-7 (DN-SeV2) in a 1 ml culture volume. White bars, genes on; black bars, genes off. Results are expressed as means ± SE from three independent experiments.
(D) Histograms show CD42b, CD49b, CD61, PAR1, GPVI, and CD29 expression on platelets (fresh and pooled) derived from normal donors (two different donors) and imMKCL Cl-2 and Cl-7. Donor-derived pooled platelets were pooled at 37°C for 5 days. Fresh human platelets were from donors 1 (purple) or 2 (green). Pooled platelets were from donor 1. imMKCL platelets were from Cl-2 (yellow) and Cl-7 (red). Black lines in all panels indicate IgG control. x axes, MFI (log scale); y axes, counts.

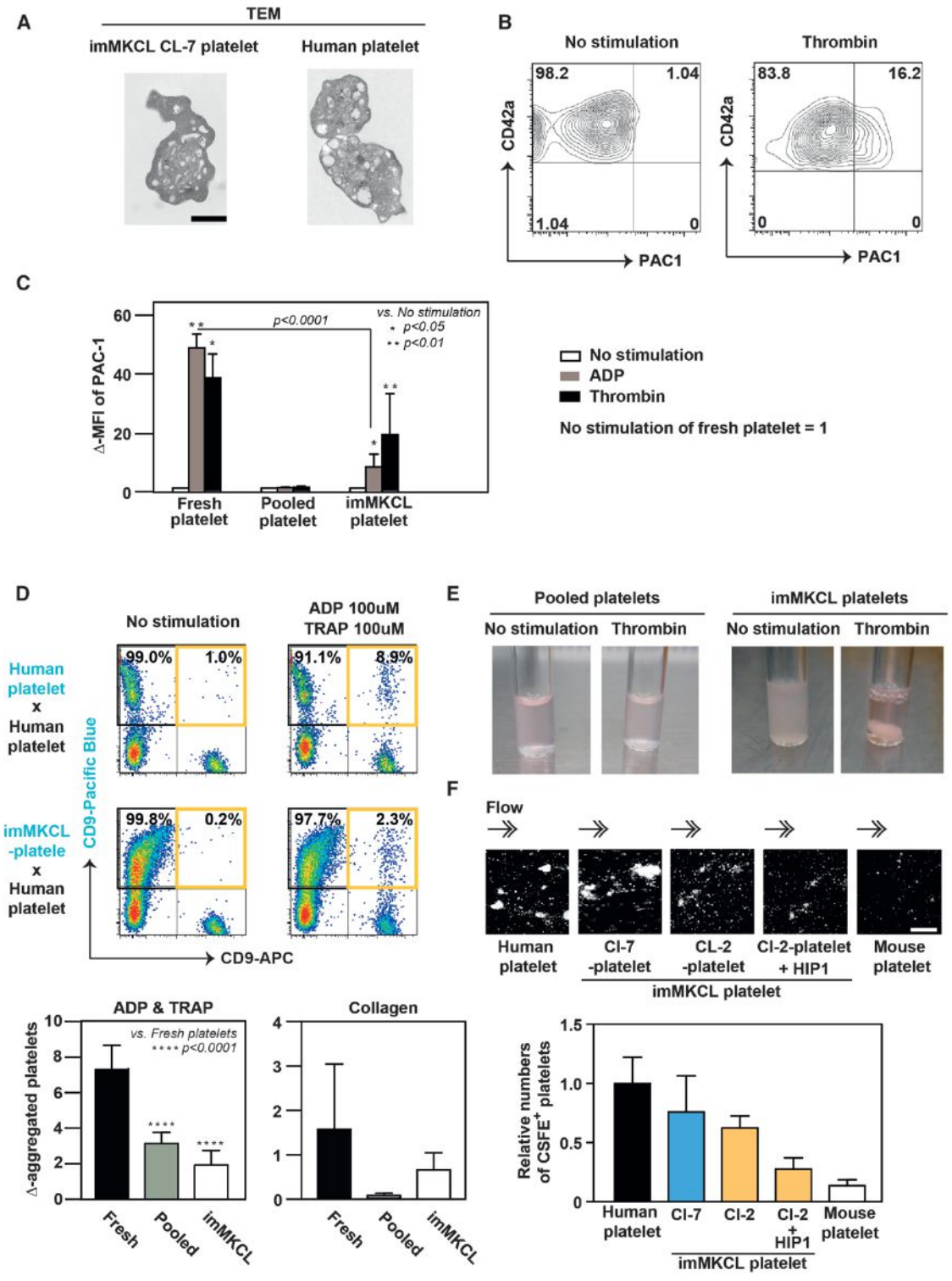

Figure 5. Characterization of imMKCL-Derived Platelets In Vitro

(A) Transmission electron micrographs of an imMKCL CI-7-derived platelet 5 days after genes off (left) and two fresh donor platelets (right). The imMKCL platelet shows fewer a-granules and dense granules than fresh platelets. The scale bar represents 1 μm.

(B) Representative contour plots for imMKCL platelets showing CD42a (GPIX) and PAC1 bound in the absence or presence of thrombin (1 u/ml).

(C) PAC1 binding to human fresh platelets, human pooled platelets, or imMKCL platelets was quantified by flow cytometry. Data depict means (± SEM) from three independent experiments. y axis indicates ΔMFI calculated as agonist (+) minus no agonist (−). The MFI of agonist (−) was 1.0 in individual samples. ADP (200 μM) or thrombin (1 u/ml) was the agonist.

(legend continued on next page)

generate large numbers of platelets. In this context, continuous culture after cryopreservation (Figure 2E) may enable a continuous supply of platelets through gene manipulation (i.e., a drug-induced genes-off condition). Furthermore, after we had established stably expandable imMKCLs in the presence of serum, we identified two clones that were capable of growing well in liquid culture after adaptation to serum- and feeder-free conditions (Figure S6D). This development suggests that it may well be feasible to use this type of system to generate platelets on the type of industrial scale that can be achieved with tanks.

We compared our current imMKCL/MCB system with our earlier strategy (Takayama et al., 2010). Figure S7 depicts the advantages of the current strategy and its feasibility in terms of three parameters: manipulation, duration, and culture scale. For each parameter in the figure, the top panels show our current protocol, and the bottom panels show the earlier protocol (Takayama et al., 2010). It is important to consider the need to prepare and provide more than 10^{11} platelets, given that 3×10^{11} platelets are required for 1 u of platelet concentrate for transfusion in the United States. We suggest using 10^8 imMKCL cells per vial as a MCB-derived working cell stock, which will produce 2.5×10^{10} MKs in around 14 days (Figures 2C, 2D, and S3D–S3G). In addition, much less medium is required in the current system (Figure S7), and there might be no requirement for mouse feeder cells or serum (Figure S6D). However, when looking at the similarity between human endogenous platelets and imMKCL platelets, there were several discrepancies between the functional parameters in vitro and in vivo (Figures 6C and 6D). In general, platelet concentrate is supplied in highly concentrated serum for transfusion. This suggests that supplementing with serum or a serum replacement could help to increase the functional capacity of imMKCL-derived platelets. Our data already suggest that this approach could be helpful; for example, serum supplementation improved clot retraction with imMKCL-derived platelets (Figure 5E). This is in contrast to endogenous pooled platelets, which did not form clots at all, even with serum supplementation. Therefore, although further optimization of this final step is needed (e.g., through the induction of differentiation at room temperature (20°C –24°C) before imMKCL platelets are clinically useful, we conclude that an imMKCL system could potentially provide useful platelets in large quantities.

As mentioned, another area for further optimization is the platelet yield per MK, the improvement of which would contribute to further reducing the volume. Several earlier reports on in vitro platelet production systems documented similarly limited efficiency of platelet production from single MKs (Ono et al., 2012; Takayama et al., 2008, 2010). In contrast, it is thought that each MK generates several thousand platelets in vivo (Patel et al., 2005). One approach could be to use a bioreactor that mimics the conditions within BM (Patel et al., 2005), where shear stress from blood flow might accelerate platelet biogenesis from MKs (Junt et al., 2007). On the basis of that idea, we recently demonstrated the feasibility of an artificially produced bioreactor with 2D microfluid circulation and biodegradable scaffolds, which increased platelet yield from hESC- and hiPSC-derived MKs (Nakagawa et al., 2013).

In conclusion, the technology outlined in this study sheds light on an exciting avenue for potential iPSC-based platelet supply. This protocol is also being developed for an Investigational New Drug Application to the United States Food and Drug Administration. To achieve that, further optimization of MK maturation and the efficiency of platelet release in a liquid culture system will help to improve the technology as it develops toward clinical application. Ultimately, we believe that, through the integration of a broad range of technologies, it will be feasible through to achieve clinically effective platelet transfusion without a requirement for donor blood.

EXPERIMENTAL PROCEDURES

Ethical Review

KhES-3 hESC clone (Institute for Frontier Medical Science, Kyoto University) was used with approval from the Ministry of Education, Culture, Sports, Science and Technology of Japan. Collection of PB from healthy volunteers was approved by the ethics committee of the Institute of Medical Science at the University of Tokyo and the Kyoto University Committee for Human Sample-Based Experiments. All studies involving the use of human samples were conducted in accordance with the Declaration of Helsinki.

Cells, Reagents, and Mice

KhES-3 hESCs from H. Suemori (Suemori et al., 2006) and human iPSC clones (585A1, 585B1, 606A1, 648B1, 692D2, and DNSeV-2) were used (Okita et al., 2013). Six-week-old NOG mice were purchased from the Central Institute for Experimental Animals. The mice were irradiated at 2.4 Gy in order to induce thrombocytopenia 9 days before transfusion. Then, selected mice (platelets = 5–20 $\times 10^4/\mu l$) were used for studies of posttransfusion platelet kinetics and in vivo imaging of thrombogeneity.

The following vectors were used: pMXs retroviral vector, pGCDNsam retroviral vector, modified pMXs Tet off-inducible retroviral vector (Ohmine et al., 2001), and CSII-based all-in-one inducible lentiviral vector (Ai-LV) (Takayama et al., 2010). Retrovirus production with a 293 Gag, Pol, VSV-G (vesicular stomatitis virus G) system and lentiviral production were as described previously

(D) Flow cytometric detection of aggregated platelets as a double-positive population among human fresh donor platelets stained with CD9-APC or among human fresh donor platelets (top panel in the dot plot) or with imMKCLs platelets (bottom panel in the dot plot) stained with CD9 Pacific Blue after agonist stimulation. In the absence of agonist stimulation, the double-positive population was small. The lower graph contains summarized results showing the percent double-positive platelets (human fresh platelets, pooled platelets, or imMKCL platelets). y axis indicates D-aggregated percentage calculated as agonist (+) minus agonist (−).Results are expressed as means ± SE from seven independent experiments for ADP&TRAP (left) or four independent experiments for collagen (right).

(E) Pictures of clot retraction. Human endogenous pooled or imMKCL (Cl-7) platelets were suspended in 20% platelet-depleted human plasma containing Iscove's modified Dulbecco's medium (1.6×10^8 platelets/ml). Even when supplemented with human plasma, pooled platelets stored without serum showed no clot retraction, whereas imMKCL platelets did.

(F) Ex vivo flow chamber system within which human vWF (10 μg/ml) was immobilized, and the shear rate was 1,600 s^{-1}. Human and mouse PB platelets and imMKCL Cl-2 and Cl-7 platelets were stained with carboxyfluorescein diacetate, succinimidyl ester (CSFE) and analyzed. Top: representative immunofluorescence micrograph of the chamber. Bottom: relative number of $CSFE^+$ platelets adhering to human vWF. HIP-1, human CD42b antibody. The scale bar represents 100 μm. Results are expressed as means ± SE of a total of 20 trials from three independent experiments. The mean value of human platelets is assigned as 1.0.

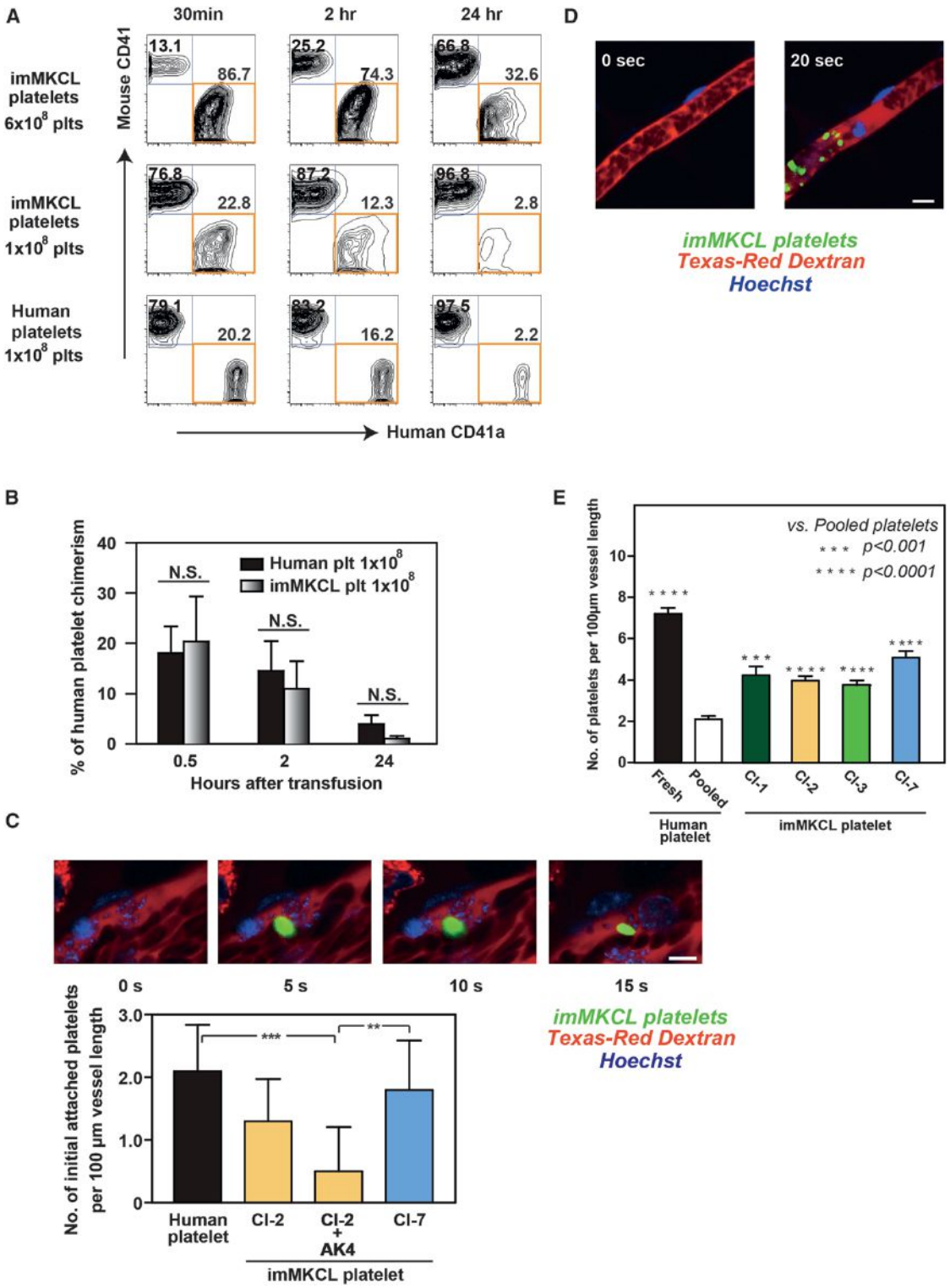

Figure 6. imMKCL-Derived Platelets Show Circulation Potential and Intact In Vivo Functionality in a Thrombocytopenic Mouse Model

(A) Platelet transfusion model in which NOG mice were irradiated (2.4 Gy) in order to induce thrombocytopenia. Nine days later, imMKCL-derived platelets (6×10^8 or 1×10^8) and human PB-derived platelets (1×10^8) were injected via the tail vein. Shown are representative contour plots of samples from a transfused mouse. Detected are mouse $CD41^+$ and human $CD41a^+$ cells 30 min, 2 hr, and 24 hr after transfusion.

(B) Platelet chimerism was quantified by flow cytometry. Circulation of injected platelets was evaluated after 30 min, 2 hr, and 24 hr. N = 4 individual groups from two independent experiments.

(legend continued on next page)

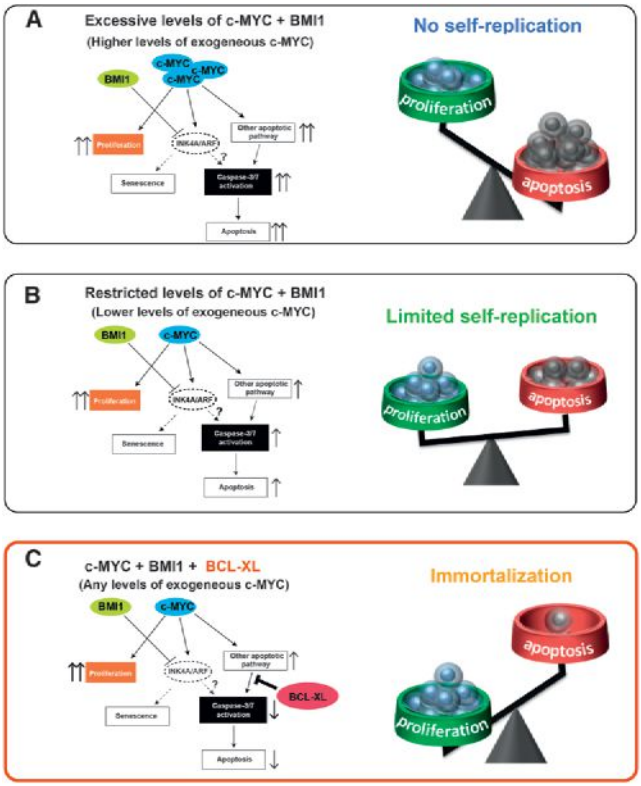

Figure 7. Models of MKCL Self-Replication Systems

(A) Excessive c-MYC induces strong activation of caspase 3 and 7 and apoptotic pathways, despite the suppression of INK4A/ARF by ectopic BMI1, leading to no self-replication.

(B) Appropriate activation of c-MYC induces a relatively low level of caspase 3 and 7 activation, leading to limited self-replication.

(C) Added BCL-XL acts in concert with BMI1 to suppress c-MYC-related apoptotic pathways, leading to MKCL immortalization.

(Eto et al., 2007; Takayama et al., 2010). We amplified the DD-encoding sequence from pPTunerC vector and Shield1 (Clontech and Takara Biotechnology) to generate the *cMYC-DD* construct. Shield1 was used to block DD-domain-mediated protein degradation. The use of viral vectors was approved by committees at the University of Tokyo or Kyoto University.

Cell Culture

On day 14 of culture, during hematopoietic differentiation from hESCs and hiPSCs (Takayama et al., 2008), HPCs were collected and transferred onto irradiated C3H10T1/2 cells in the presence of 50 ng/ml human SCF (R&D Systems) and 50 ng/ml human TPO (R&D) (Takayama et al., 2010). Gene expression was controlled by the presence or absence of 2 μM β-estradiol or 1 μg/ml doxycycline (Clontech) for modified pMXs inducible vector or the presence of 1 μg/ml doxycycline for Ai-LV, respectively. MK differentiation from CB $CD34^+$ cell was accomplished as described previously (Proulx et al., 2004).

In Vitro Analysis of imMKCLs, imMKCL Platelets, and Human Platelets

qRT-PCR, cell-surface markers of imMKCLs and platelets, electron microscopy, and PAC-1 binding were examined as described previously (Takayama et al., 2010). Flow-cytometry-based platelet aggregation assays were performed as described previously (De Cuyper et al., 2013). Clot retraction assays were carried out as described previously (Takizawa et al., 2010). An ex vivo flow chamber precoated with human vWF (10 μg/ml, provided by K. Soejima, Kaketsuken) was utilized to observe shear (1,600 s^{-1})-dependent thrombus formation under an inverted microscope equipped with fluorescence (Nikon A1R) and microfluid systems (Ibidi Products). Platelets were stained with CFSE dye (5 μM, Invitrogen) and used in the presence of CD42b (HIP1; Abcam; 10 μg/ml) or isotype-matched antibodies (BioLegend). Human pooled platelets were prepared by 5-day culture at 37°C under serum-free conditions.

In Vivo Analysis in Mice

Nine days later, irradiation in NOG mice, fresh or pooled human platelets from a donor, or imMKCL-derived platelets were intravenously administered (100 μl). Then, blood samples (50–100 μl) were collected from the retro-orbital plexus in the mice 30 min, 2 hr, and 24 hr after transfusion. The samples were labeled with human CD41a-APC and mouse CD41-PE antibodies (EMFRET Analytics), after which chimerism was analyzed. Similar NOG mice with thrombocytopenia were also used for in vivo imaging studies. To visually analyze thrombus formation in the microcirculation of the mesentery in living animals, we used in vivo laser- and reactive-oxygen-species-induced injury with a visualization technique developed through modification of conventional methods (Nishimura et al., 2012; Takizawa et al., 2010). Some experiments were performed with AK4 (human P-selectin antibody; Abcam; 20 μg/ml). Additional details of the methods and other information for imaging are presented in the Supplemental Information.

Statistical Analysis

All data are presented as means ± SEM. The statistical significance of the observed differences was determined with one-way ANOVA followed by Tukey's multiple comparison test and two-tailed Student's t tests for pairwise comparisons. Values of $p < 0.05$ were considered significant.

ACCESSION NUMBERS

Raw and normalized microarray data have been deposited in the NCBI Gene Expression Omnibus database under accession number GSE54168.

SUPPLEMENTAL INFORMATION

Supplemental Information contains Supplemental Experimental Procedures, seven figures, and three movies and can be found with this article online at http://dx.doi.org/10.1016/j.stem.2014.01.011.

(C) Time-lapse confocal microscopy showing potential in vivo platelet function. Mice were transfused with 1×10^8 platelets derived from different groups. Top: representative sequential images showing initial adhesion by imMKCL-derived platelets onto injured vessel walls. CSFE-labeled imMKCL platelets (Cl-2 and Cl-7; green) along with dextran (Texas Red) are shown. Bottom: the number of initially attached platelets per 100 μm vessel length were counted. Actual results are shown in Movie S2. The results are averaged data from 40 vessels from three to five animals in each group. N.S., not significant; ***$p < 0.001$, ****$p < 0.0001$. AK4; human P-selectin antibody. The scale bar represents 10 μm.

(D) Representative sequential images showing thrombus formation by imMKCL-derived platelets within a small capillary and artery. CSFE-labeled imMKCL platelets (green) along with dextran (Texas Red) are shown. Hematoporphyrin was administrated in order to induce thrombus formation prior to laser-induced injury. Platelets adhered to the site of laser injury, finally contributing to the complete occlusion of vessels. Original videos are available as Movie S3. The scale bars represent 10 μm.

(E) Fresh donor platelets, pooled donor platelets, and imMKCL-derived platelets incorporated into thrombi were quantified. Pooled platelets were stored for 5 days at 37°C. Platelets from imMKCL Cl-1, Cl-2, Cl-3, and Cl-7 were used. The results summarize four independent experiments (n = 40 vessels from three to five animals for each group). N.S., not significant; ***$p < 0.001$, ****$p < 0.0001$.

ACKNOWLEDGMENTS

The authors thank H. Suemori, T. Kitamura, M. Onodera, H. Mano, M. Nakanishi, R. Mulligan, H. Kashiwagi, K. Soejima, and Y. Kurose. Electron microscopy was supported by Integrated Imaging Research Support (nonprofit organization). This work was supported by grants-in-aid from MEXT (K.E.) and the Project of Realization of Regenerative Medicine and Highway Program from MEXT/JST (K.E.), A-STEP, and CREST from JST (K.E.) and a Health Labor Sciences Research Grant from the Ministry of Health Labor and Welfare (K.E.). This research was also supported in part by the first Program from JSPS (S.Y.). Visiting fellows S.H. (Kaken Pharmaceutical), T.K. (Nissan Chemical), and K.H. (Toray Industries) were supported by each company. S.Y. is a member without salary of scientific advisory board (SAB) of iPierian, iPS Academia Japan, Megakaryon, and HEALIOS K. K. Japan. H.N. and K.E. are members without salary of SAB of Megakaryon. H.N. is an outside board member of ReproCELL. S.N., N.T., H.N., and K.E. submitted the patent related with this manuscript.

Received: January 31, 2013
Revised: October 2, 2013
Accepted: January 12, 2014
Published: February 13, 2014

REFERENCES

Banaszynski, L.A., Chen, L.C., Maynard-Smith, L.A., Ooi, A.G., and Wandless, T.J. (2006). A rapid, reversible, and tunable method to regulate protein function in living cells using synthetic small molecules. Cell *126*, 995–1004.

Bergmeier, W., Burger, P.C., Piffath, C.L., Hoffmeister, K.M., Hartwig, J.H., Nieswandt, B., and Wagner, D.D. (2003). Metalloproteinase inhibitors improve the recovery and hemostatic function of in vitro-aged or -injured mouse platelets. Blood *102*, 4229–4235.

Chen, C., Fuhrken, P.G., Huang, L.T., Apostolidis, P., Wang, M., Paredes, C.J., Miller, W.M., and Papoutsakis, E.T. (2007). A systems-biology analysis of isogenic megakaryocytic and granulocytic cultures identifies new molecular components of megakaryocytic apoptosis. BMC Genomics *8*, 384.

De Cuyper, I.M., Meinders, M., van de Vijver, E., de Korte, D., Porcelijn, L., de Haas, M., Eble, J.A., Seeger, K., Rutella, S., Pagliara, D., et al. (2013). A novel flow cytometry-based platelet aggregation assay. Blood *121*, e70–e80.

Eto, K., Nishikii, H., Ogaeri, T., Suetsugu, S., Kamiya, A., Kobayashi, T., Yamazaki, D., Oda, A., Takenawa, T., and Nakauchi, H. (2007). The WAVE2/Abi1 complex differentially regulates megakaryocyte development and spreading: implications for platelet biogenesis and spreading machinery. Blood *110*, 3637–3647.

Fuentes, R., Wang, Y., Hirsch, J., Wang, C., Rauova, L., Worthen, G.S., Kowalska, M.A., and Poncz, M. (2010). Infusion of mature megakaryocytes into mice yields functional platelets. J. Clin. Invest. *120*, 3917–3922.

Gardiner, E.E., Al-Tamimi, M., Andrews, R.K., and Berndt, M.C. (2012). Platelet receptor shedding. Methods Mol. Biol. *788*, 321–339.

Hirata, S., Takayama, N., Jono-Ohnishi, R., Endo, H., Nakamura, S., Dohda, T., Nishi, M., Hamazaki, Y., Ishii, E.I., Kaneko, S., et al. (2013). Congenital amegakaryocytic thrombocytopenia iPS cells exhibit defective MPL-mediated signaling. J. Clin. Invest. *123*, 3802–3814.

Hirose, S., Takayama, N., Nakamura, S., Nagasawa, K., Ochi, K., Hirata, S., Yamazaki, S., Yamaguchi, T., Otsu, M., Sano, S., et al. (2013). Immortalization of erythroblasts by c-MYC and BCL-XL enables large-scale erythrocyte production from human pluripotent stem cells. Stem Cell Reports *1*, 499–508.

Hotti, A., Järvinen, K., Siivola, P., and Hölttä, E. (2000). Caspases and mitochondria in c-Myc-induced apoptosis: identification of ATM as a new target of caspases. Oncogene *19*, 2354–2362.

Isakari, Y., Sogo, S., Ishida, T., Kawakami, T., Ono, T., Taki, T., and Kiwada, H. (2009). Gene expression analysis during platelet-like particle production in phorbol myristate acetate-treated MEG-01 cells. Biol. Pharm. Bull. *32*, 354–358.

Josefsson, E.C., James, C., Henley, K.J., Debrincat, M.A., Rogers, K.L., Dowling, M.R., White, M.J., Kruse, E.A., Lane, R.M., Ellis, S., et al. (2011). Megakaryocytes possess a functional intrinsic apoptosis pathway that must be restrained to survive and produce platelets. J. Exp. Med. *208*, 2017–2031.

Juin, P., Hunt, A., Littlewood, T., Griffiths, B., Swigart, L.B., Korsmeyer, S., and Evan, G. (2002). c-Myc functionally cooperates with Bax to induce apoptosis. Mol. Cell. Biol. *22*, 6158–6169.

Junt, T., Schulze, H., Chen, Z., Massberg, S., Goerge, T., Krueger, A., Wagner, D.D., Graf, T., Italiano, J.E., Jr., Shivdasani, R.A., and von Andrian, U.H. (2007). Dynamic visualization of thrombopoiesis within bone marrow. Science *317*, 1767–1770.

Kaluzhny, Y., Yu, G., Sun, S., Toselli, P.A., Nieswandt, B., Jackson, C.W., and Ravid, K. (2002). BclxL overexpression in megakaryocytes leads to impaired platelet fragmentation. Blood *100*, 1670–1678.

Kumar, S., and Cakouros, D. (2004). Transcriptional control of the core cell-death machinery. Trends Biochem. Sci. *29*, 193–199.

Lambert, M.P., Sullivan, S.K., Fuentes, R., French, D.L., and Poncz, M. (2013). Challenges and promises for the development of donor-independent platelet transfusions. Blood *121*, 3319–3324.

Leytin, V., Allen, D.J., Gwozdz, A., Garvey, B., and Freedman, J. (2004). Role of platelet surface glycoprotein Ibalpha and P-selectin in the clearance of transfused platelet concentrates. Transfusion *44*, 1487–1495.

Lu, S.J., Li, F., Yin, H., Feng, Q., Kimbrel, E.A., Hahm, E., Thon, J.N., Wang, W., Italiano, J.E., Cho, J., and Lanza, R. (2011). Platelets generated from human embryonic stem cells are functional in vitro and in the microcirculation of living mice. Cell Res. *21*, 530–545.

Nakagawa, Y., Nakamura, S., Nakajima, M., Endo, H., Dohda, T., Takayama, N., Nakauchi, H., Arai, F., Fukuda, T., and Eto, K. (2013). Two differential flows in a bioreactor promoted platelet generation from human pluripotent stem cell-derived megakaryocytes. Exp. Hematol. *41*, 742–748.

Nishikii, H., Eto, K., Tamura, N., Hattori, K., Heissig, B., Kanaji, T., Sawaguchi, A., Goto, S., Ware, J., and Nakauchi, H. (2008). Metalloproteinase regulation improves in vitro generation of efficacious platelets from mouse embryonic stem cells. J. Exp. Med. *205*, 1917–1927.

Nishimura, S., Manabe, I., Nagasaki, M., Kakuta, S., Iwakura, Y., Takayama, N., Ooehara, J., Otsu, M., Kamiya, A., Petrich, B.G., et al. (2012). In vivo imaging visualizes discoid platelet aggregations without endothelium disruption and implicates contribution of inflammatory cytokine and integrin signaling. Blood *119*, e45–e56.

Oguro, H., Iwama, A., Morita, Y., Kamijo, T., van Lohuizen, M., and Nakauchi, H. (2006). Differential impact of Ink4a and Arf on hematopoietic stem cells and their bone marrow microenvironment in Bmi1-deficient mice. J. Exp. Med. *203*, 2247–2253.

Ohmine, K., Ota, J., Ueda, M., Ueno, S., Yoshida, K., Yamashita, Y., Kirito, K., Imagawa, S., Nakamura, Y., Saito, K., et al. (2001). Characterization of stage progression in chronic myeloid leukemia by DNA microarray with purified hematopoietic stem cells. Oncogene *20*, 8249–8257.

Okita, K., Yamakawa, T., Matsumura, Y., Sato, Y., Amano, N., Watanabe, A., Goshima, N., and Yamanaka, S. (2013). An efficient nonviral method to generate integration-free human-induced pluripotent stem cells from cord blood and peripheral blood cells. Stem Cells *31*, 458–466.

Ono, Y., Wang, Y., Suzuki, H., Okamoto, S., Ikeda, Y., Murata, M., Poncz, M., and Matsubara, Y. (2012). Induction of functional platelets from mouse and human fibroblasts by p45NF-E2/Maf. Blood *120*, 3812–3821.

Patel, S.R., Hartwig, J.H., and Italiano, J.E., Jr. (2005). The biogenesis of platelets from megakaryocyte proplatelets. J. Clin. Invest. *115*, 3348–3354.

Proulx, C., Dupuis, N., St-Amour, I., Boyer, L., and Lemieux, R. (2004). Increased megakaryopoiesis in cultures of CD34-enriched cord blood cells maintained at 39 degrees C. Biotechnol. Bioeng. *88*, 675–680.

Sato, T., Fuse, A., Eguchi, M., Hayashi, Y., Ryo, R., Adachi, M., Kishimoto, Y., Teramura, M., Mizoguchi, H., Shima, Y., et al. (1989). Establishment of a human leukaemic cell line (CMK) with megakaryocytic characteristics from a Down's syndrome patient with acute megakaryoblastic leukaemia. Br. J. Haematol. *72*, 184–190.

Schiffer, C.A. (2001). Diagnosis and management of refractoriness to platelet transfusion. Blood Rev. *15*, 175–180.

Suemori, H., Yasuchika, K., Hasegawa, K., Fujioka, T., Tsuneyoshi, N., and Nakatsuji, N. (2006). Efficient establishment of human embryonic stem cell lines and long-term maintenance with stable karyotype by enzymatic bulk passage. Biochem. Biophys. Res. Commun. *345*, 926–932.

Takahashi, K., Tanabe, K., Ohnuki, M., Narita, M., Ichisaka, T., Tomoda, K., and Yamanaka, S. (2007). Induction of pluripotent stem cells from adult human fibroblasts by defined factors. Cell *131*, 861–872.

Takayama, N., Nishikii, H., Usui, J., Tsukui, H., Sawaguchi, A., Hiroyama, T., Eto, K., and Nakauchi, H. (2008). Generation of functional platelets from human embryonic stem cells in vitro via ES-sacs, VEGF-promoted structures that concentrate hematopoietic progenitors. Blood *111*, 5298–5306.

Takayama, N., Nishimura, S., Nakamura, S., Shimizu, T., Ohnishi, R., Endo, H., Yamaguchi, T., Otsu, M., Nishimura, K., Nakanishi, M., et al. (2010). Transient activation of c-MYC expression is critical for efficient platelet generation from human induced pluripotent stem cells. J. Exp. Med. *207*, 2817–2830.

Takizawa, H., Nishimura, S., Takayama, N., Oda, A., Nishikii, H., Morita, Y., Kakinuma, S., Yamazaki, S., Okamura, S., Tamura, N., et al. (2010). Lnk regulates integrin alphaIIbbeta3 outside-in signaling in mouse platelets, leading to stabilization of thrombus development in vivo. J. Clin. Invest. *120*, 179–190.

Terui, Y., Furukawa, Y., Kikuchi, J., Iwase, S., Hatake, K., and Miura, Y. (1998). Bcl-x is a regulatory factor of apoptosis and differentiation in megakaryocytic lineage cells. Exp. Hematol. *26*, 236–244.

Ware, J., Russell, S., and Ruggeri, Z.M. (2000). Generation and rescue of a murine model of platelet dysfunction: the Bernard-Soulier syndrome. Proc. Natl. Acad. Sci. USA *97*, 2803–2808.

Wong, C.H., Jenne, C.N., Petri, B., Chrobok, N.L., and Kubes, P. (2013). Nucleation of platelets with blood-borne pathogens on Kupffer cells precedes other innate immunity and contributes to bacterial clearance. Nat. Immunol. *14*, 785–792.

Yamamoto, R., Morita, Y., Ooehara, J., Hamanaka, S., Onodera, M., Rudolph, K.L., Ema, H., and Nakauchi, H. (2013). Clonal analysis unveils self-renewing lineage-restricted progenitors generated directly from hematopoietic stem cells. Cell *154*, 1112–1126.

Yu, M., Mazor, T., Huang, H., Huang, H.T., Kathrein, K.L., Woo, A.J., Chouinard, C.R., Labadorf, A., Akie, T.E., Moran, T.B., et al. (2012). Direct recruitment of polycomb repressive complex 1 to chromatin by core binding transcription factors. Mol. Cell *45*, 330–343.

Cell Stem Cell
Clinical Progress

Spermatogonial Stem Cell Transplantation into Rhesus Testes Regenerates Spermatogenesis Producing Functional Sperm

Brian P. Hermann,[1,4,7,15] Meena Sukhwani,[7] Felicity Winkler,[7] Julia N. Pascarella,[7] Karen A. Peters,[7] Yi Sheng,[1,7] Hanna Valli,[6,7] Mario Rodriguez,[7] Mohamed Ezzelarab,[5] Gina Dargo,[13] Kim Peterson,[13] Keith Masterson,[8] Cathy Ramsey,[8] Thea Ward,[12] Maura Lienesch,[14] Angie Volk,[14] David K. Cooper,[5] Angus W. Thomson,[5] Joseph E. Kiss,[3,13] Maria Cecilia T. Penedo,[12] Gerald P. Schatten,[1,7] Shoukhrat Mitalipov,[8,9,10,11] and Kyle E. Orwig[1,2,4,7,*]
[1]Department of Obstetrics, Gynecology, and Reproductive Sciences
[2]Department of Developmental Biology
[3]Department of Medicine
[4]Center for Research in Reproductive Physiology
[5]Thomas E. Starzl Transplantation Institute
[6]Molecular Genetics and Developmental Biology Graduate Program
[7]Magee-Womens Research Institute
University of Pittsburgh School of Medicine, Pittsburgh, PA 15260
[8]Oregon National Primate Research Center
[9]Oregon Stem Cell Center
[10]Department of Obstetrics and Gynecology
[11]Department of Molecular and Medical Genetics
Oregon Health and Science University, Beaverton, OR 97006, USA
[12]Veterinary Genetics Laboratory, University of California, Davis, Davis, CA 95616, USA
[13]Hemapheresis Department, ITxM Diagnostics Pittsburgh, PA 15213, USA
[14]CaridianBCT, Incorporated, Lakewood, CO 80401, USA
[15]Present address: Department of Biology, The University of Texas at San Antonio, One UTSA Circle, San Antonio, TX 78249, USA
*Correspondence: orwigke@upmc.edu
http://dx.doi.org/10.1016/j.stem.2012.07.017

SUMMARY

Spermatogonial stem cells (SSCs) maintain spermatogenesis throughout a man's life and may have application for treating some cases of male infertility, including those caused by chemotherapy before puberty. We performed autologous and allogeneic SSC transplantations into the testes of 18 adult and 5 prepubertal recipient macaques that were rendered infertile with alkylating chemotherapy. After autologous transplant, the donor genotype from lentivirus-marked SSCs was evident in the ejaculated sperm of 9/12 adult and 3/5 prepubertal recipients after they reached maturity. Allogeneic transplant led to donor-recipient chimerism in sperm from 2/6 adult recipients. Ejaculated sperm from one recipient transplanted with allogeneic donor SSCs were injected into 85 rhesus oocytes via intracytoplasmic sperm injection. Eighty-one oocytes were fertilized, producing embryos ranging from four-cell to blastocyst with donor paternal origin confirmed in 7/81 embryos. This demonstration of functional donor spermatogenesis following SSC transplantation in primates is an important milestone for informed clinical translation.

INTRODUCTION

In 1994, Ralph Brinster and colleagues transplanted mouse spermatogonial stem cells (SSCs) into the seminiferous tubules of infertile recipient mice and observed donor-derived spermatogenesis that was competent to produce viable progeny (Brinster and Avarbock, 1994; Brinster and Zimmermann, 1994). SSC transplantation has since become the gold standard bioassay for experimental assessment of SSC activity (Phillips et al., 2010) and may also have application in the human fertility clinic. One potential clinical application of SSC transplantation is to preserve and restore the fertility of male cancer patients (Kubota and Brinster, 2006; Geens et al., 2008; Schlatt et al., 2009; Wyns et al., 2010; Hermann and Orwig, 2011).

Chemotherapy and radiation treatments for cancer or other conditions can permanently damage fertility (Mitchell et al., 2009). Adult male patients have the option to preserve their future fertility by cryopreserving sperm. Unfortunately, there are no standard-of-care options to preserve the fertility of prepubertal boys who are not yet producing mature sperm. For these patients, it may be possible to isolate and freeze SSCs obtained via testicular biopsy prior to gonadotoxic therapy and have these cells reintroduced into their testes after cure (Brinster, 2007; Clark et al., 2011). If results in animal models translate to the clinic, this autologous transplantation paradigm may permanently restore natural fertility. The feasibility of this approach is supported by observations in lower animal models that SSCs from donors of all ages, newborn to adult, can regenerate

spermatogenesis (Shinohara et al., 2001; Ryu et al., 2003) and that SSCs can be cryopreserved and retain spermatogenic function upon thawing and transplantation (Dobrinski et al., 1999, 2000; Brinster, 2002).

Large animal models are critical for examining the safety and feasibility of experimental therapies before they are translated to the clinic. SSC transplantation has been reported in seven previous large animal studies (Table S1 available online). All of those studies, except for one in the boar (Mikkola et al., 2006), employed irradiation to destroy spermatogenesis and cause infertility. There is a dearth of information on the efficacy of SSC transplantation in chemotherapy-treated large animals, probably due to the significant challenges associated with clinical management of animals treated systemically with high-dose chemotherapies that cause severe hematopoietic deficits (Hermann et al., 2007). However, the importance of this experimental paradigm should not be overlooked because high-dose alkylating chemotherapies are used routinely for conditioning prior to hematopoietic stem cell (HSC) transplantation and are associated with high risk of infertility (Wallace et al., 2005; Lee et al., 2006; Mitchell et al., 2009; Green et al., 2010).

The first large animal SSC transplants were performed in monkeys by Schlatt and colleagues (see Table S1), who described autologous transplants into irradiated monkey recipients in 2002 and again in 2011 (Schlatt et al., 2002; Jahnukainen et al., 2011). Each study reported that the transplanted right testis was larger than the untransplanted left testis in one animal, but presence or function of donor sperm was not evaluated. Thus, the question of whether SSC transplant can be translated to the primate system and produce functional sperm still remains. The translational significance of this question is high because clinics around the world (Keros et al., 2007; Wyns et al., 2008; Ginsberg et al., 2010; Sadri-Ardekani et al., 2011; Oktay, 2011; Orwig et al., 2011; Schlatt and Kliesch, 2012) are already cryopreserving testicular tissue for boys in anticipation that SSCs in that tissue can be used to restore fertility via autologous SSC transplantation, autologous tissue grafting, xenografting, or in vitro germ cell differentiation (Brinster, 2007; Rodriguez-Sosa and Dobrinski, 2009; Sato et al., 2011; Clark et al., 2011). Establishing the feasibility of SSC transplantation in the primate model will have important implications for how testicular tissue should be processed and for educating patients and physicians about the potential downstream applications.

We previously described a nonhuman primate model of cancer survivorship in rhesus macaques where infertility was caused by alkylating chemotherapy (busulfan) (Hermann et al., 2007). We employed that model in the current study to examine the feasibility of SSC transplantation in prepubertal and adult rhesus macaques, which have testis biology, endocrine regulation, and immune function that is similar to that of humans (Plant and Marshall, 2001; Hermann et al., 2010; Messaoudi et al., 2011). Prophylactic autologous peripheral blood stem cell (PBSC) transplant (Donahue et al., 2005; Kang et al., 2006) was used to counteract the hematopoietic deficits in all animals. This complex experimental design involving HSC and SSC transplantation models the clinical scenario of HSC (bone marrow or PBSC) transplant patients who are at high risk for infertility (Wyns et al., 2010). Our results indicate that transplanted SSCs can regenerate spermatogenesis in busulfan-treated primates and produce functional sperm capable of fertilizing oocytes and leading to preimplantation embryo development.

RESULTS

SSC Transplantation by Ultrasound-Guided Rete Testis Injection in Monkeys

Schlatt and coworkers pioneered ultrasound-guided rete testis injection into monkey testes in 1999 (Schlatt et al., 1999) and this technique has now been applied to introduce testis cell suspensions into the seminiferous tubules of several large animal species (Schlatt et al., 1999, 2002; Honaramooz et al., 2003; Izadyar et al., 2003; Mikkola et al., 2006; Kim et al., 2008; Herrid et al., 2009). In contrast to a typical rodent SSC transplant where the testis efferent ducts and/or rete testes are accessed surgically through an abdominal incision (Ogawa, 2001), ultrasound-guided rete testis injection does not require surgery. Briefly, ultrasound is used to visualize the rete testis and guide the injection needle through the scrotal skin and into the rete testis space, which is contiguous with all seminiferous tubules (Figure 1 and Movie S1). With this approach, we introduced an average of 1,041 ± 82 μl of cell suspension into the rete testis and seminiferous tubules of adult recipients and 222 ± 26 μl into juvenile recipients. Cell concentrations ranged from 58 to 232 × 10^6 viable cells/ml; an average of 88 × 10^6 viable cells were injected per adult testis and 45.8 × 10^6 viable cells were injected per juvenile testis (Table S2).

Transplanted Autologous SSCs Produce Spermatogenesis in Busulfan-Treated Macaques

To assess the regenerative capacity of primate SSCs, we performed a series of autologous transplant experiments in busulfan-treated macaques (Hermann et al., 2007). Because the doses of busulfan required to deplete endogenous spermatogenesis are also myelosuppressive, all animals received autologous PBSC transplants to support rapid hematopoietic recovery (Figure 2). Testis cells were obtained via hemicastration or biopsy of one testis and were cryopreserved prior to busulfan chemotherapy.

In order to distinguish transplanted SSCs and their progeny from endogenous cells, we treated donor cells with lentiviral vectors containing Ubiquitin-C (UBC)-eGFP, elongation factor 1α (EF1α)-GFP, or EF1α-mCherry transgene inserts (Table S2) prior to transplant. This approach permanently marks donor cells and allows detection of the labeled donor cells in tissue or ejaculated sperm by their genotype (e.g., a specific lentiviral DNA sequence).

Approximately 10–12 weeks after busulfan treatment (corresponding to the time when sperm counts reach 0 in adults), cells were thawed, treated with lentivirus, and transplanted back into the other testis of the same animal (Figure 2). Lentivirus-treated autologous SSCs were transplanted into the seminiferous tubules of 12 adult and 5 prepubertal recipient macaques by ultrasound-guided rete testis injection. Polymerase chain reaction (PCR) was used to detect sperm produced from lentivirus-marked SSCs in the ejaculates of recipient animals. Overall, spermatogenesis was evident in 11/12 adult and 5/5 prepubertal (after puberty) recipients after transplant (Figure 3A and Tables S2, S3, and S4).

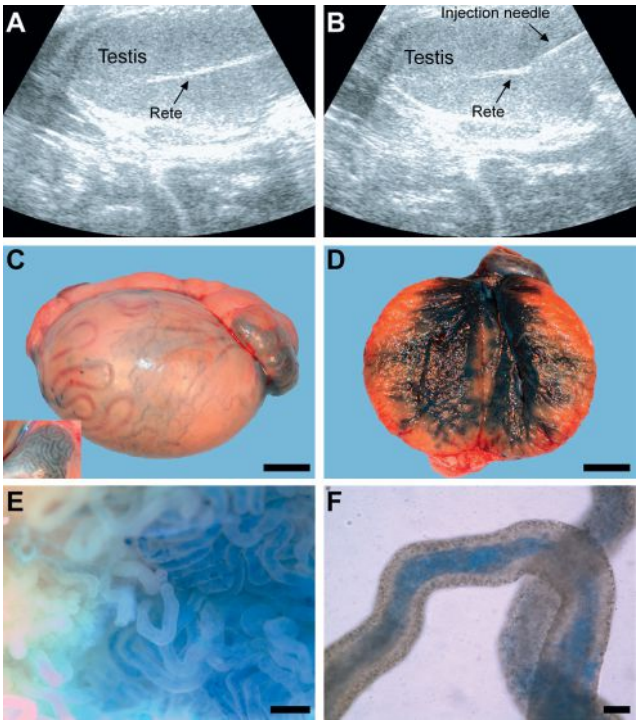

Figure 1. Rhesus SSC Transplantation by Ultrasound-Guided Rete Testis Injection

Donor testis cells (including SSCs) are introduced into recipient seminiferous tubules via injection into the rete testis space. (A) The rete testis in rhesus can be visualized by ultrasound as a linear echo-dense structure and (B) ultrasound is used to guide an echo-dense injection needle into the rete testis space, allowing cells to be injected by slow, positive pressure. (C) After this injection, presence of dye in the ductules of the caput epididymis (inset), which is contiguous via the efferent ducts with the rete testis, confirmed successful injection. (D) Bisection of the transplanted testis revealed that blue dye radiated from the rete testis into approximately 60%–80% of seminiferous tubules. (E and F) Subsequent evaluation of intact seminiferous tubules confirmed the presence of blue dye in the lumen of seminiferous tubules. Scale bar = 1 cm (C and D), 500 μm (E), and 100 μm (F). See also Movie S1.

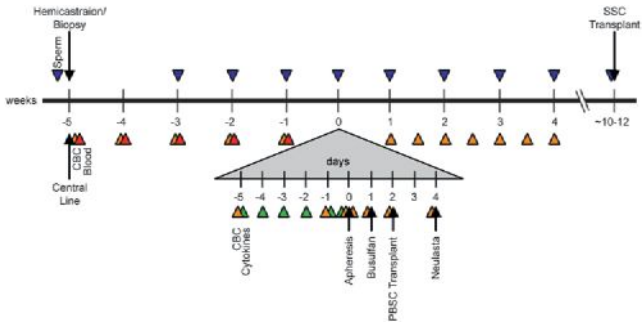

Figure 2. Experimental Timeline for Recipient Preparation and SSC Transplantations

This cartoon shows relative timing of experimental procedures for recipient animals, including autologous transplants of peripheral blood stem cells (PBSCs) used to restore the hematopoietic system after busulfan chemotherapy. Indwelling central venous catheters were placed in the right internal jugular vein at the time of testicular tissue harvesting or approximately 5 weeks before PBSC harvest via apheresis. Autologous blood was collected for 5 weeks (red triangles) and pooled to prime the apheresis tubing set. Animals received daily subcutaneous injections with the cytokine G-CSF (and in some cases, SCF) (green triangles) for 6 days to mobilize hematopoietic stem cells from the bone marrow into the general circulation. PBSCs were collected on day 0 by apheresis using the indwelling central line for venous access. Twenty-four hours after completing apheresis, animals were treated with busulfan (labeled arrow). Approximately 42 hours after completing apheresis (~18 hr after busulfan treatment), animals were transfused with autologous PBSCs collected by apheresis. Two days later, animals received one subcutaneous injection of neulasta (long-acting G-CSF) to stimulate rapid expansion of engrafted stem cells and hematopoietic recovery. Animals were monitored closely for hematopoietic deficits with weekly (or more frequent) complete blood count (CBC, orange triangles). Approximately 10–12 weeks after busulfan treatment, animals received SSC transplants (when sperm counts were 0 for 2 consecutive weeks). Weekly ejaculated sperm counts (blue triangles) measured the effect of busulfan on spermatogenesis and the progression of spermatogenic recovery after transplant. See also Figure S1 and Table S2.

The duration of spermatogenesis, from SSC to sperm, is roughly 42–44 days, followed by 10.5 days of epididymal transport time (Amann et al., 1976; Clermont and Antar, 1973; Hermann et al., 2010). Recovery of spermatogenesis to normal levels ($\geq 15 \times 10^6$) was observed in adult autologous recipients an average of 40.1 ± 4.9 weeks after busulfan treatment (11 of 12 adults; ranged from 15 to 63 weeks; Table S3). In our previous study, recovery of spermatogenesis from endogenous SSCs occurred by 24 weeks after a low dose of busulfan (4 mg/kg) that did not eliminate endogenous SSCs; spermatogenic recovery was not observed in animals treated with the higher busulfan doses (8 and 12 mg/kg) employed in this study (Hermann et al., 2007). The time to spermatogenic recovery in this study can likely be attributed to the substantial depletion of the endogenous SSC pool, which is not completely replenished by transplanted SSCs. Thus, spermatogenesis originates from sporadic foci of individual endogenous and/or transplanted SSCs that must expand laterally to repopulate the seminiferous tubules as well as differentiate to produce sperm. These factors apparently prolong the time required to reach a steady state threshold sufficient to produce normal sperm counts in the ejaculate.

PCR genotyping for the lentiviral backbone indicated stable donor signal in the ejaculates of 9/12 adult and 3/5 prepubertal autologous recipients (Figure 3B and Tables S2, S3, and S4). Donor signal was considered stable when lentiviral genotype was observed in at least four separate semen samples collected over the course of at least three months. Results from autologous recipient M037 are shown in Figure 3 where sperm reappeared in the ejaculate between 20 and 30 weeks after transplant (Figure 3A). Donor lentiviral sequence was detected by PCR coincident with the appearance of sperm (Figure 3B). Overall, PCR signal from lentivirus marked SSCs decayed over time (see Tables S3 and S4), suggesting a low efficiency of virus-marked SSC engraftment. Histological comparison of the testis and cauda epididymis from M037 (Figure 3C) clearly demonstrates more spermatogenic recovery (60% of seminiferous tubule cross-sections contained spermatogenesis) compared with a transplant recipient that failed to exhibit sperm in the ejaculates after transplant (M214; Figure 3D) and had spermatogenesis in only 24% of tubule cross-sections. For reference, all seminiferous tubules were devoid of germ cells

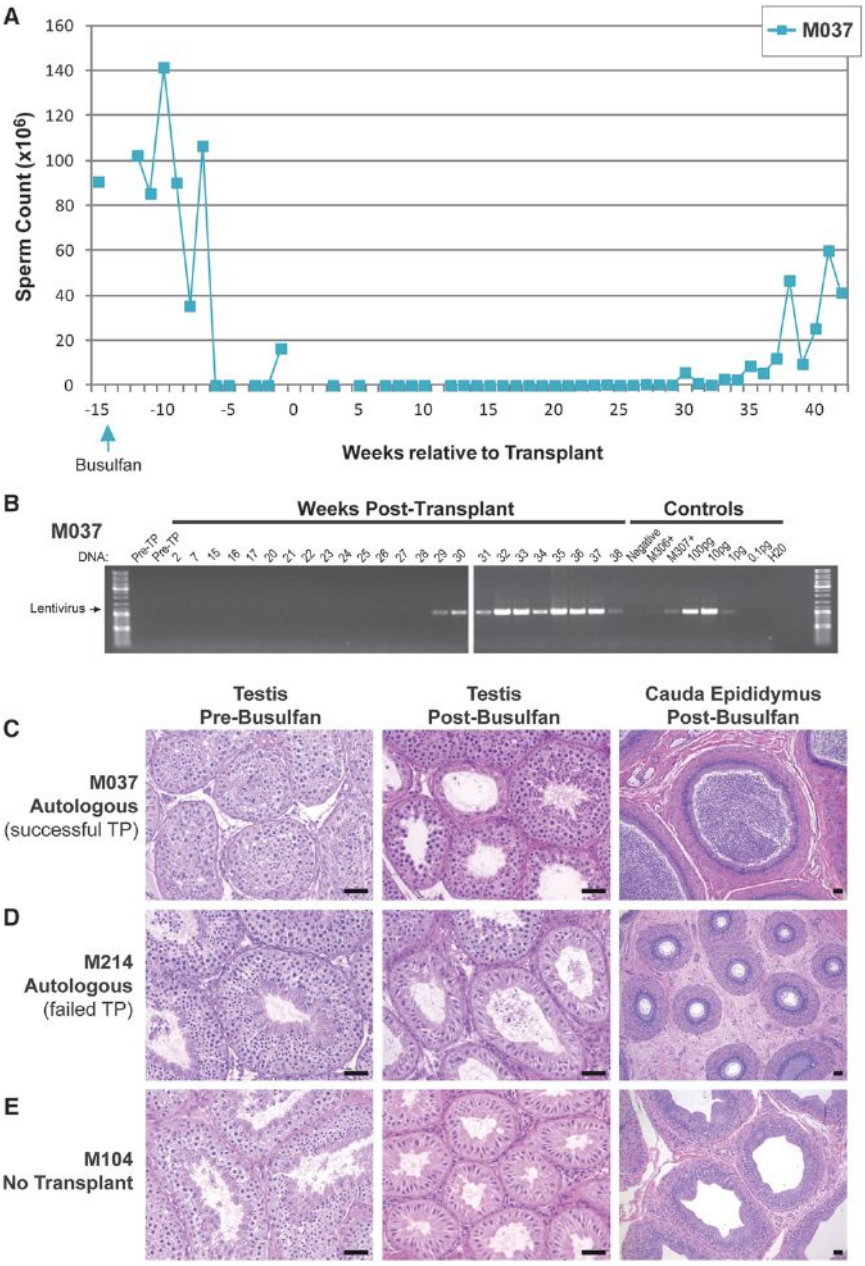

Figure 3. Spermatogenic Recovery following Autologous SSC Transplantation

(A) Weekly sperm counts (total sperm per ejaculate) are shown for one autologous recipient (M037 treated with 10 mg/kg busulfan). In this animal, busulfan was administered at week −14 (noted by blue arrow) relative to SSC transplant at week 0. (B) DNA from each ejaculate containing sperm was genotyped by PCR for a 1.1 kb segment of the lentiviral backbone. Negative controls included prebusulfan/pretransplant (pre-TP) ejaculates, ejaculates from untransplanted controls (negative), and H_2O. Positive controls included cultured testis cells treated with lentivirus (M306+ and M307+) and dilutions of lentiviral plasmid DNA (100 pg, 10 pg, 1 pg, and 0.1 pg). Histological (hematoxylin and eosin staining) comparison of testicular parenchyma before and after busulfan treatment (at necropsy) as well as the cauda epididymis after busulfan treatment reveals the degree of spermatogenesis in (C) M037, which exhibited successful transplant engraftment based on presence of sperm in the ejaculate (60% of tubule cross-sections contained spermatogenesis; necropsied 80 weeks after busulfan), and (D) transplant recipient M214, which never exhibited sperm in the ejaculate after transplant (24% of tubule cross-sections contained spermatogenesis; necropsied 67 weeks after busulfan). (E) Histology from the testis and epididymis of an untransplanted animal, M104 (no spermatogenesis evident; necropsied 26 weeks after busulfan), illustrates the appearance of an azoospermic (empty) testis after busulfan treatment. Scale bars = 50 μm. See also Tables S2, S3, and S4.

in a busulfan-treated animal that received no transplant 26 weeks after busulfan treatment (M104; Figure 3E). We were unable to observe fluorescent segments of seminiferous tubules (i.e., those marked by the lentivirus and those that regenerated spermatogenesis) after systematic evaluation of each autologous recipient testis at necropsy by epifluorescence microscopy. The failure to observe lentiviral reporter expression may result from epigenetic silencing of the transgene, insufficient expression for this detection mode, or both.

The best way to demonstrate that transplanted SSCs produce functional sperm is to demonstrate their ability to fertilize oocytes. Unfortunately, our autologous transplant approach was not amenable to fertilization studies because the efficiency of marking SSCs was very low (data not shown). In addition, we were not able to distinguish fluorescence from lentivirus-marked sperm from autofluorescence that was observed in most ejaculates (data not shown). Fertilizing oocytes from a random population of sperm of which only a very small percentage were genetically marked was not practical. Therefore, we performed additional experiments using an allogeneic recipient approach in which all donor sperm had unique DNA microsatellite allele profiles that could be distinguished from those of endogenous recipient sperm.

Transplanted Allogeneic SSCs Regenerate Spermatogenesis and Produce Functional Sperm

We utilized an allogeneic transplant paradigm where donor testis cells from unrelated individual animals were transplanted into recipient testes. While some previous reports demonstrated that transplanted allogeneic testis cells were tolerated in large animal models allowing engraftment of unrelated donor SSCs (Honaramooz et al., 2002, 2003; Kim et al., 2008), SSCs from unrelated donors failed to regenerate spermatogenesis in bull testes (Izadyar et al., 2003) (Table S1). Thus, the potential for immune effects on SSC engraftment is unclear. Therefore, donor

and recipient pairs were matched based on low recipient T cell reactivity to donor antigens using multiple lymphocyte reaction (MLR; data not shown) analysis (Ezzelarab et al., 2008). In addition, five of six allogeneic recipients were treated with an immune suppression regimen (anti-CD154; Table S2) (Kirk et al., 1999). We discriminated sperm originating from donor and recipient SSCs using microsatellite fingerprinting, as described previously, to detect donor sperm production in SSC-transplanted dogs (Kim et al., 2008).

All six allogeneic recipients exhibited low levels of spermatogenic recovery in the posttransplant period of evaluation (Figure 4A and Tables S2 and S3). Microsatellite DNA fingerprinting revealed donor/recipient chimerism in sperm from two of the six allogeneic recipients (M212 and M027, Tables S2 and S3). Sperm retrieved from the left cauda epididymis at necropsy from animal M212 exhibited a minor peak of donor signal (donor M214; 236 bp and 244 bp alleles at locus DS11S2002; 194 bp and 244 bp alleles at locus D12S67) amidst a background of recovering endogenous spermatogenesis (Figures 4B–4D). Donor signal was not detectable in ejaculated sperm from M212 likely due to inflammation in the left epididymis evident in the posttransplant period and confirmed at necropsy, preventing donor sperm transit to the ejaculate (data not shown). A second allogeneic recipient, M027, produced ejaculated sperm exhibiting donor signal (donor M092; 187 bp allele at locus D3S1768; 263 bp allele at locus D17S1300) for more than 17 months (50 total samples) (Figure 4E–4G). Thus, these data show that transplanted allogeneic SSCs produce sperm in recipient testes. To quantify the degree of donor sperm production as a function of time, we identified single nucleotide polymorphisms (SNPs) that distinguish donor sperm from recipient sperm essentially as described previously (Alizadeh et al., 2002; Kim et al., 2008). We screened 23 SNPs reported in the Monkey SNP database at Oregon National Primate Research Center (Khouangsathiene et al., 2008), but none distinguished donor and recipient and/or were suitable for qPCR. However, while screening one reported SNP (rs4543622) within the *class II major histocompatibility complex transactivator* (*CIITA*) locus, we identified a previously unreported SNP for which the recipient (M027) was homozygous for one allele (G) and the donor (M092) heterozygous both alleles (A/G). Standard curves for the relative abundance of each allele as previously described were used to determine the percent of donor chimerism in DNA isolated from recipient M027 following monthly semen samples collected between 3 and 17 months after transplant (Figure 4H). We observed a consistent level of donor (M092) chimerism (ranging from 1.7 to 17.2%) in M027 sperm samples for the duration of the 14 months analyzed (Figure 4H).

To assess function of donor (M092) sperm, ejaculated sperm from recipient M027 (collected 30 weeks after transplant) were used to fertilize rhesus oocytes by intracytoplasmic sperm injection (ICSI) (Hewitson et al., 1999; Mitalipov et al., 2006). Of 85 oocytes injected, 81 (95%) were fertilized (formed male and female pronuclei) and subsequently cleaved (Figure 5 and Table S5). Upon in vitro culture, 23% of embryos reached the blastocyst stage with normal morphology (Table S5). To determine sire by microsatellite DNA fingerprinting, all blastocysts and arrested embryos were individually harvested and used for whole-genome DNA amplification. Genotyping was done for the gender marker AME to determine sex of embryo and for eight microsatellite loci, two of which (DXS2506 and D15S823) definitively discriminate the genotype of the SSC donor (M092) from the transplant recipient (M027) and oocyte donors (Figure 5 and Table S6). In this genotyping paradigm, the 286 bp allele at the X-linked locus DXS2506 and the 337 bp allele at locus D15S823 were both unique to M092 and their presence in an embryo could only arise from M092 paternal contribution (Figure 5 and Table S6). Of the 81 embryos genotyped, 7 exhibited definitive donor (M092) sire, 3 of which advanced to the morula stage of preimplantation development (Figure 5 and Table S6). Since DXS2506 is an X-linked marker, male (XY) embryos, including three XY M092-sired embryos (embryos 1, 8 and 63; Figures 5L and 5O and Table S6), displayed only the maternal allele at this locus. M092 donor paternal contribution in these embryos was confirmed by the presence of the 337 bp allele at locus D15S823. These results indicate that sperm generated from transplanted primate SSCs are competent for fertilization and preimplantation embryo development.

DISCUSSION

Adult stem cell transplantation for homologous tissue regeneration was first described for primates in the 1950s when bone marrow stem cells were used to reconstitute the hematopoietic systems of monkeys and humans treated with chemotherapy or radiation (Crouch and Overman, 1957; Thomas et al., 1957). Large animals, primarily the dog and monkey, were instrumental for establishing the safety, feasibility, and range of applications for bone marrow transplantation. Today, approximately 50,000 bone marrow or HSC transplant procedures are performed worldwide each year for diseases ranging from cancer to thalassemia, sickle cell anemia, and autoimmune and immune-deficiency disorders (Appelbaum, 2007; Powell et al., 2009).

Like hematopoiesis, spermatogenesis is a highly productive stem-cell-based system that produces millions of sperm per gram of tissue each day (Sharpe, 1994). This productivity is possible because a relatively small stem cell pool generates progeny that undergo several rounds of transit-amplifying divisions before producing the terminally differentiated sperm (Potten, 1992). Two sequelae of highly productive stem-cell-based systems are (1) that they can become targets of chemotherapy or radiation treatments that damage rapidly dividing cells (Potten, 1995; Meistrich, 1993; Mauch et al., 1995) and (2) that transplantation of a small number of stem cells is adequate to functionally reconstitute the dependent systems (e.g., hematopoiesis and spermatogenesis) (Potten et al., 1979; Potten, 1992; Osawa et al., 1996; Ogawa et al., 2000; Shinohara et al., 2001; Copelan, 2006). Here we demonstrate the feasibility of SSC transplantation in a nonhuman primate model that is infertile due to alkylating chemotherapy (busulfan) and suggest that this technique has application for restoring the fertility of cancer survivors or bone marrow transplant recipients.

SSC transplantation has now been reported in mice, rats, monkeys, goats, bulls, pigs, sheep, and dogs (Brinster and Avarbock, 1994; Brinster and Zimmermann, 1994; Ogawa et al., 1999; Schlatt et al., 2002; Honaramooz et al., 2003; Izadyar

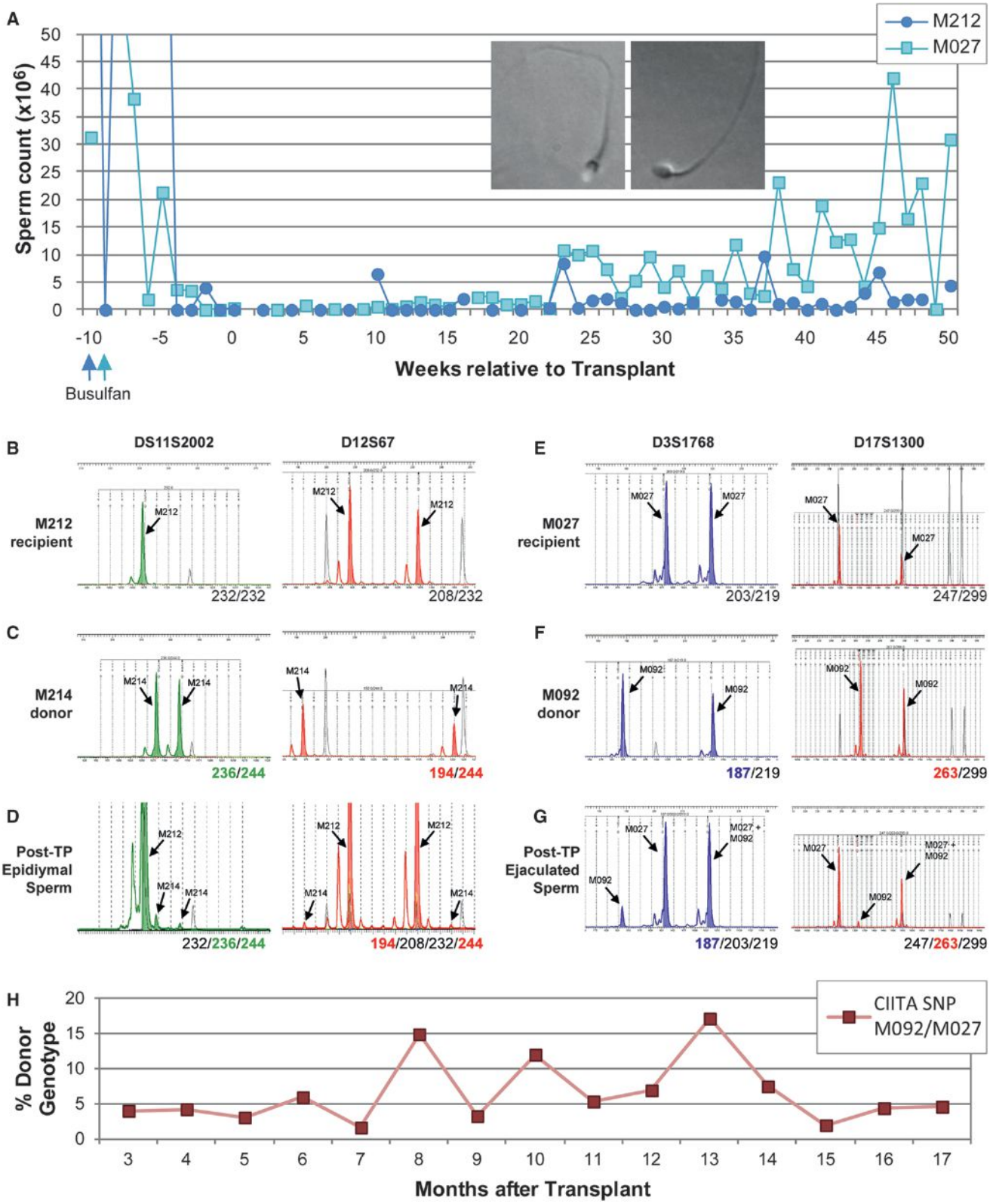

Figure 4. Donor Spermatogenesis in Two Allogeneic Transplant Recipients Determined by Microsatellite DNA Fingerprinting of Recipient Sperm

(A) Weekly sperm counts (total sperm per ejaculate) from two allogeneic recipients treated with 8 mg/kg busulfan (M212; treated with busulfan on week −11, dark blue arrow) or 11 mg/kg busulfan (M027; treated with busulfan on week −9, light blue arrow); sperm from M027 (inset) are shown as examples. DNA from each

et al., 2003; Mikkola et al., 2006; Kim et al., 2008; Herrid et al., 2009). Among the seven other large animal SSC transplant studies reviewed in Table S1, four reported evidence of donor sperm in the ejaculate (goat, boar, dog, and sheep) and two reported functional sperm (goat and sheep) that produced donor-derived progeny. Although the first large animal SSC transplants were performed in monkeys in 2002 (Schlatt et al., 2002), evidence of donor sperm from transplanted SSCs was lacking until the present study. It is important to demonstrate that transplanted SSCs can produce sperm in higher primate models that have the greatest relevance to human testis anatomy and physiology. It is equally important to demonstrate in primates that the testicular environment is competent to support spermatogenesis from transplanted SSCs following chemotherapy or radiation. Schlatt and colleagues previously reported SSC transplant in nonhuman primates that were rendered infertile by testicular irradiation (Schlatt et al., 2002; Jahnukainen et al., 2011). To date, SSC transplantation into a chemotherapy-treated large animal recipient has been reported only in the pig (Mikkola et al., 2006). Our results indicated that SSCs from prepubertal or adult rhesus macaques could engraft chemotherapy-treated recipient testes and generate spermatogenesis, including the production of donor sperm that were competent to fertilize rhesus oocytes resulting in preimplantation embryo development.

We found evidence of donor spermatogenesis from both autologous and allogeneic transplant recipients and donor sperm function was evaluated in one allogeneic recipient (M027, the recipient of transplanted SSCs from M092). Donor spermatogenesis in autologous recipients was generally transient in recipient semen samples, appearing several times during posttransplant follow-up and sometimes in a cyclic manner. This result could be linked to a low efficiency of engraftment from virus-marked donor SSCs. Allogeneic recipient M027, on the other hand, demonstrated steady donor spermatogenesis that did not decline over time. The function of donor (M092) sperm in the ejaculates of recipient M027 (which contained a mixture of M092 and M027 sperm) was assessed by ICSI of rhesus oocytes and was conducted in the Assisted Reproductive Technology/Embryonic Stem Cell Support Core of the Oregon National Primate Research Center (by K.M, C.R., and S.M). In vitro fertilization (IVF) is an alternative approach to test sperm function that would also assess the ability of donor sperm to penetrate the zona pellucida. The efficiency of IVF is similar to ICSI when using sperm from proven male donors. However, since the males used in this study were not proven breeders, ICSI was selected as the approach most likely to produce a definitive outcome with donor-derived embryos. The ICSI approach also eliminated the potential for contamination of genotyping results with a mixture of donor and endogenous recipient sperm. The ability of M092 SSC-derived donor sperm to fertilize rhesus oocytes by ICSI and stimulate early embryo development suggests that they were functionally normal.

In future studies it will be important to demonstrate that donor-derived embryos can be transferred to surrogate females for the production of viable donor-derived offspring. This was considered premature in the current study because only 7/81 embryos (8.6%, Tables S5 and S6) had the donor genotype. Embryo biopsy to select only donor type embryos for transfer was not considered feasible and pregnancy rates after transfer are about 25% (Bavister et al., 1984; Wolf et al., 1989, 2004; Chan et al., 2001). Therefore, the chances of achieving donor type progeny would be about 2.15% (8.6% donor embryos × 25% pregnancy rate). Besides the prohibitive cost, there were an insufficient number of recipient females available to reasonably expect donor offspring in this study. These challenges were less onerous in herd animal species where a single SSC transplant recipient could be used to fertilize a herd of females by natural breeding (Honaramooz et al., 2003) or artificial insemination (Herrid et al., 2009). Improvements in recipient preparation to more completely eliminate endogenous spermatogenesis, combined with development of donor SSC enrichment strategies (Hermann et al., 2009, 2011), should substantially increase the proportion of donor sperm and enhance the opportunity to produce donor offspring in future nonhuman primate studies.

Due to concerns about immune rejection of cells from unrelated animals, five out of six allogeneic transplant recipients in this study were treated with antibodies against CD154 (Kirk et al., 1999), which blocks the T cell costimulatory pathway. Donor spermatogenesis was observed in 2/5 immune-suppressed recipients, but not in the one nonsuppressed recipient (Table S2). Beginning in meiosis, spermatocytes and their progeny express novel autoantigens that are tolerated by the immune system, allowing production of genetically divergent gametes. Multiple mechanisms regulate immune privilege in the testis including the blood-testis barrier that limits access of immune components to the differentiated germ cells via Sertoli cell tight junctions, and somatic cell production of soluble factors (e.g., FAS ligand) that suppress the rejection of immunologically disparate cells (Fijak and Meinhardt, 2006). Testicular immune privilege has been used to explain the success of allogeneic SSC transplants between unrelated, immune-competent individuals that were previously reported in several large-animal species (Honaramooz et al., 2002, 2003; Mikkola et al., 2006;

ejaculate containing sperm was genotyped by microsatellite DNA fingerprinting to determine the presence of donor genotype. Both of these allogeneic recipients showed evidence of donor spermatogenesis.

(B–D) Epididymal sperm obtained at necropsy from recipient M212 contained a mixture of M212 recipient and M214 donor signal at the two microsatellite loci examined.

(E–G) Ejaculated sperm from M027 (collected 14 weeks after transplant) also demonstrated a mixture of M027 recipient and M092 donor signal at the two microsatellite loci examined. This result persisted for at least 17 months after transplant with analysis ongoing. Microsatellite loci are noted above each column of electropherograms and alleles for each animal or sample are indicated at the bottom right of each electropherogram panel. Discriminating alleles for donor are noted by bold/colored text.

(H) Allelic discrimination qPCR (TaqMan probes) was used for SNP genotyping to determine the degree of M092 donor spermatogenesis in M027 sperm samples between 3 and 17 months after transplant. Shown is the degree of M092 genotype (%) in each sperm DNA sample based on presence of SNPs in the rhesus *CIITA* locus. Percent donor genotype was determined by standard curve with known amounts of donor and recipient gDNA.

Additional information about the specific samples used for SNP analysis is indicated in Table S3. See also Table S2.

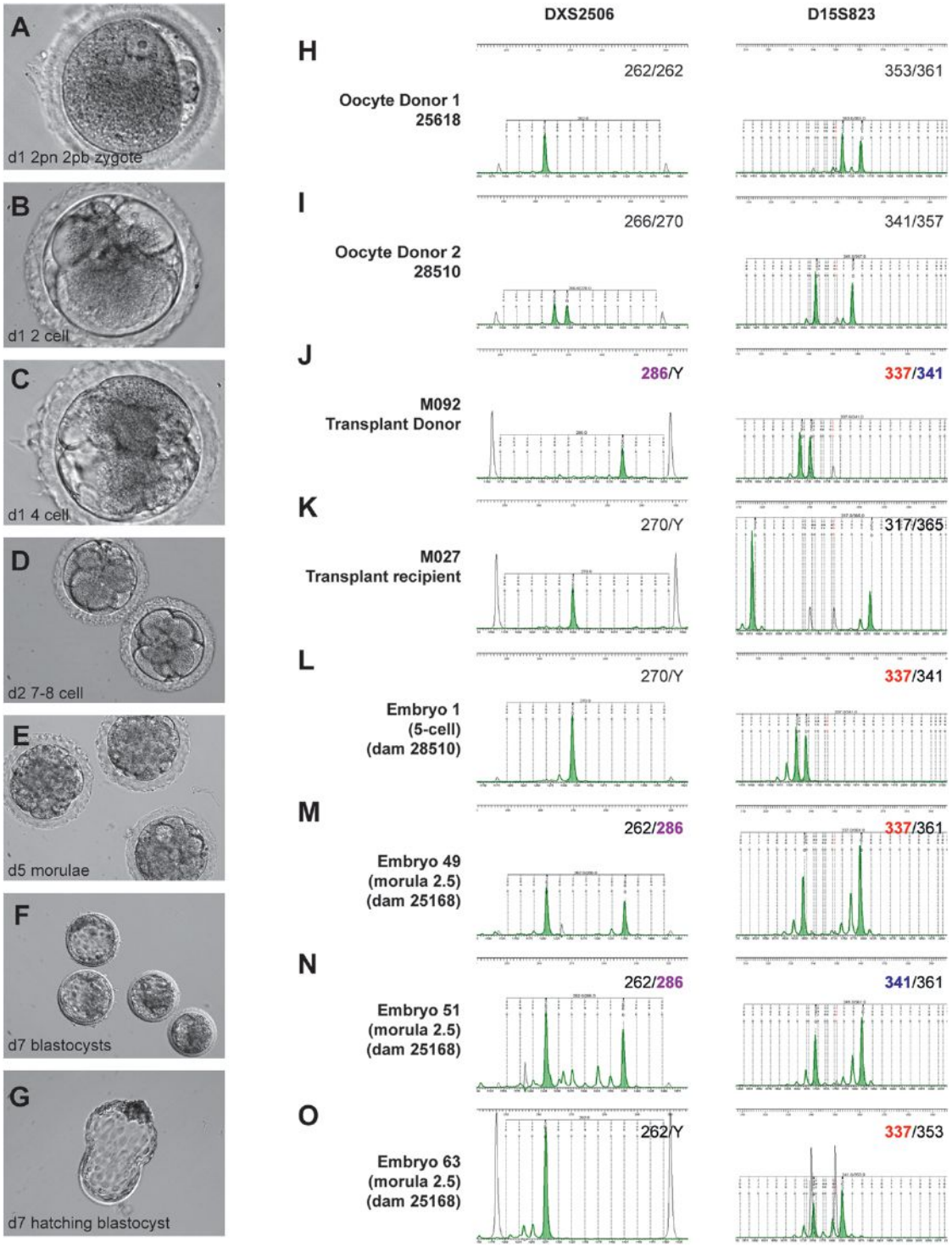

Figure 5. Donor-Derived Sperm in Allogeneic Recipient Rhesus Macaques Are Functional

Ejaculated sperm from allogeneic recipient M027 (collected 30 weeks after transplant) were used to fertilize rhesus oocytes by intracytoplasmic sperm injection (ICSI).

(A) Pronuclear stage zygote produced using sperm from M027 (see Figure 4).

(B–G) Subsequent in vitro culture resulted in embryos ranging from two-cell to blastocysts.

(H–O) Following whole-genome amplification, microsatellite DNA fingerprinting at two tetranucleotide repeat loci (DXS2506 and D15S823) confirmed SSC transplant donor (M092) paternity in 7 of 81 embryos generated from M027 sperm. Microsatellite profiles of four M092 donor-derived embryos are shown in panels (L)–(O). Embryo 1 (L) was from dam 28510 and embryos 49, 51, and 63 (M–O) were from dam 25168. Microsatellite loci are noted above each column of

Kim et al., 2008). Although animal numbers in this study were not sufficient to demonstrate that immune suppression was required, our data clearly indicated that cells from unrelated donor animals were tolerated in immune-suppressed nonhuman primates.

Several promising techniques are in the research pipeline (i.e., SSC transplantation, testicular tissue grafting or xenografting, and in vitro development of gametes) that may allow patients receiving gonadotoxic therapies to preserve their future fertility (Brinster, 2007; Rodriguez-Sosa and Dobrinski, 2009; Sato et al., 2011). SSC transplantation has the unique potential to regenerate spermatogenesis in the autologous environment of the seminiferous tubules, enabling the recipient male to father his own genetic children, possibly through normal coitus. As with hematopoiesis, large animal models that are relevant to human anatomy and physiology will be important for translating the SSC transplantation technique to the human fertility clinic. Considering the successful regeneration of spermatogenesis in the nonhuman primate model reported here and the fact that patients are already preserving testicular tissue and/or cells, clinical translation of the SSC transplantation technique appears imminent. Responsible development of the technology in a clinically relevant nonhuman primate system will help to address issues of safety and feasibility. As with hematopoiesis, the clinical significance and breadth of applications for SSC transplantation will ultimately be established in human patients.

EXPERIMENTAL PROCEDURES

Animals

All experiments utilizing animals were approved by the responsible Institutional Animal Care and Use Committees of Magee-Womens Research Institute and the University of Pittsburgh (Assurance #A3654-01) and the Oregon National Primate Research Center, Oregon Health and Sciences University (Assurance #A3304-01) and were performed in accordance with the National Institutes of Health Guide for the Care and Use of Laboratory Animals.

Preparation of Donor Rhesus Macaque Testis Cell Suspensions

Testis tissue was collected from rhesus macaques by hemicastration or subcapsular biopsy. For biopsies, less than 30% of the testicular parenchyma was removed (3.8g–8.7g) through a transverse incision in the tunica albuginea on the lateral side of the right testis. In one case (M036), the biopsied testis was later removed by hemicastration due to formation of an abscess. Cells were recovered from testicular parenchyma using a two-step enzymatic digestion procedure, cryopreserved, and stored in liquid nitrogen, as described (Hermann et al., 2007, 2009).

Busulfan Treatment

Recipient animals were treated with the alkylating chemotherapeutic agent busulfan (Busulfex IV; PDL BioPharma, Fremont, CA), at doses of 8, 10, 11, or 12 mg/kg (Table S2). Busulfex was diluted in physiological saline and administered intravenously at 0.6 mg/ml over 10–20 min.

PBSC Transplants

Autologous transplants of PBSCs were employed to restore the hematopoietic system after busulfan treatment. Briefly, PBSCs were mobilized with six, daily subcutaneous injections with the cytokines G-CSF (10 μg/kg/day, Neupogen; Amgen; Thousand Oaks, CA) and SCF (200 μg/kg/day; Amgen) or G-CSF alone (20 μg/kg/day), essentially as described (Figure 2) (Donahue et al., 2005). PBSC collections were performed by apheresis using either a Spectra or Spectra Optia apheresis device (Caridian BCT; Lakewood, CO). Twenty-four hours after apheresis, animals were treated with busulfan, and 18 hr later animals received autologous PBSC transfusions (Figure 2). Two days later, animals received one subcutaneous injection of long-acting G-CSF (300 μg/kg; Neulasta, Amgen). Additional details are available in the Supplemental Experimental Procedures.

Histology

Portions of testicular parenchyma and epididymis collected above and at necropsy were fixed with Bouin's solution (Accustain; Sigma-Aldrich, St. Louis, MO), paraffin embedded, sectioned (5 μm), and stained with hematoxylin and eosin.

SSC Transplant

Spermatogonial stem cell transplants were performed 9–15 weeks after busulfan treatment (autologous: unilateral; allogeneic: bilateral). In biopsied animals, autologous transplants were performed into the contralateral testis. Cryopreserved donor cells were recovered for transplant from storage in liquid nitrogen, as described (Hermann et al., 2007, 2009). In some cases, donor cells were enriched for spermatogonia, including SSCs, on a 24% Percoll cushion (GE Healthcare Life Sciences, Piscataway, NJ) prior to transplant (see Figure S1 and Table S2). Cells were then suspended at approximately 100 × 10^6 cells/ml in MEMalpha medium (Invitrogen) containing 10% FBS, 20% trypan blue, 20% Optison (ultrasound contrast agent; GE Healthcare, Waukesha, WI) and 0.7 mg/ml DNase I in a total volume of $\leq$1ml, depending on recipient testis size and available cells. SSC transplants were performed using ultrasound-guided rete testis injections (Figure 1 and Movie S1). For this purpose, a 13 MHz linear superficial probe was used to visualize the rete testis space on a MicroMaxx ultrasound machine (Sonosite, Bothell, WA) and guide a 25G 2" spinal needle into the rete testis. Cells were injected under slow constant pressure and chased with saline.

Lentiviral Treatment of Donor Testis Cells

For autologous transplants, donor cells were treated with lentiviral vectors modified from the FUGW construct originally described by Lois and coworkers (Lois et al., 2002). Details of virus constructs and viral treatments are available in the Supplemental Experimental Procedures.

Immune Suppression

Five of six allogeneic transplant recipients were treated with human/mouse chimeric anti-CD154 IgG 5C8 (NIH Nonhuman Primate Reagent Resource, Beth Israel Deaconess Medical Center, Boston, MA) at 20 mg/kg on d−1, d0, d3, d10, d18, d28, and monthly thereafter to block the T cell costimulatory pathway and prevent T cell-mediated rejection of the grafted cells (Kirk et al., 1999).

Semen Collection and Analysis

Semen samples were collected from experimental animals at weekly intervals before and after busulfan treatment, as described (Gould and Mann, 1988). Total sperm count per ejaculate was determined by hemocytometer. Genomic DNA was extracted from sperm samples and assessed for donor genotype by PCR for lentivirus sequence or by microsatellite DNA fingerprinting (see Supplemental Experimental Procedures).

Microsatellite DNA Fingerprinting

Genomic DNA isolated from sperm of allogeneic transplants or amplified from embryos was used for microsatellite repeat fingerprinting (details in the Supplemental Experimental Procedures). Primer sequences and primer concentrations in multiplexed PCR are described elsewhere (Larsen et al., 2010).

electropherograms and alleles for each animal or sample are indicated in the upper right of each electropherogram panel. Discriminating alleles for donor are noted by bold/colored text. In cases where embryos were male (i.e., XY; panels L and O), paternal contribution at the X-linked DXS2506 locus was nil, and thus, simply noted by Y. In both cases M092 paternal origin could be confirmed by the D15S823 locus.
See also Tables S5 and S6.

Quantitative SNP Genotyping

TaqMan probe-based allelic discrimination qPCR was used essentially as described (Alizadeh et al., 2002; Kim et al., 2008) to detect an SNP in the rhesus *CIITA* locus that distinguishes genomic DNA from the donor (M092) and recipient (M027) of an allogeneic SSC transplant. See the Supplemental Experimental Procedures for additional details.

ICSI, Embryo Culture, and Whole-Genome Amplification

Controlled ovarian stimulation was performed on two female rhesus macaques as previously described (Byrne et al., 2007). Oocytes were collected and fertilized with M027 sperm by ICSI, and resulting embryos were cultured as described (Hewitson et al., 1999; Mitalipov et al., 2006). Following ICSI and in vitro development, individual embryos were placed into 8 μl nuclease-free water. Genomic DNA from each embryo was amplified using the WGA4 GenomePlex Single Cell Whole Genome Amplification kit according to manufacturer recommendations (Sigma-Aldrich) and was used for microsatellite DNA fingerprinting. Additional detail is available in the Supplemental Experimental Procedures.

SUPPLEMENTAL INFORMATION

Supplemental Information for this article includes one figure, five tables, Supplemental Experimental Procedures, and one movie and can be found with this article online at http://dx.doi.org/10.1016/j.stem.2012.07.017.

ACKNOWLEDGMENTS

We would like to acknowledge the outstanding work of Tony Battelli, Pam Wintruba, and Joe Hrach, the lab animal staff at Magee-Womens Research institute, who were critical to the conduct of these experiments. Artwork for the graphical abstract was produced by Dr. Bart Phillips. We are grateful to Drs. Robert Donahue and Cynthia Dunbar of the National Heart, Lung and Blood Institute, NIH, who provided critical advice for PBSC transplantation in nonhuman primates. Drs. Tony Plant and Judy Cameron provided advice about central line catheter placement in nonhuman primates. We also thank Drs. Regina Norris, Danielle Sweeney, David Rodeberg, and Francis Schneck from the Departments of Urology and General Surgery at the Children's Hospital of Pittsburgh of UPMC for their assistance with subcapsular testis biopsies. The FUGW lentiviral backbone was provided by Dr. Carlos Lois, University of Massachusetts. The anti-CD154 reagent used in these studies was provided by the NIH Nonhuman Primate Reagent Resource (R24 RR016001, N01 AI040101). The work was supported by Magee-Womens Research Institute and Foundation, The Richard King Mellon Foundation, NIH grants R01 HD055475 and R21 HD061289 to K.E.O., U54 HD008610 to Tony M. Plant and K.E.O., P01 HD047675 to G.P.S., and K99/R00 HD062687 to B.P.H.

Received: January 26, 2012
Revised: June 16, 2012
Accepted: July 12, 2012
Published: November 1, 2012

REFERENCES

Alizadeh, M., Bernard, M., Danic, B., Dauriac, C., Birebent, B., Lapart, C., Lamy, T., Le Prisé, P.Y., Beauplet, A., Bories, D., et al. (2002). Quantitative assessment of hematopoietic chimerism after bone marrow transplantation by real-time quantitative polymerase chain reaction. Blood *99*, 4618–4625.

Amann, R.P., Johnson, L., Thompson, D.L., Jr., and Pickett, B.W. (1976). Daily spermatozoal production, epididymal spermatozoal reserves and transit time of spermatozoa through the epididymis of the rhesus monkey. Biol. Reprod. *15*, 586–592.

Appelbaum, F.R. (2007). Hematopoietic-cell transplantation at 50. N. Engl. J. Med. *357*, 1472–1475.

Bavister, B.D., Boatman, D.E., Collins, K., Dierschke, D.J., and Eisele, S.G. (1984). Birth of rhesus monkey infant after in vitro fertilization and nonsurgical embryo transfer. Proc. Natl. Acad. Sci. USA *81*, 2218–2222.

Brinster, R.L. (2002). Germline stem cell transplantation and transgenesis. Science *296*, 2174–2176.

Brinster, R.L. (2007). Male germline stem cells: from mice to men. Science *316*, 404–405.

Brinster, R.L., and Avarbock, M.R. (1994). Germline transmission of donor haplotype following spermatogonial transplantation. Proc. Natl. Acad. Sci. USA *91*, 11303–11307.

Brinster, R.L., and Zimmermann, J.W. (1994). Spermatogenesis following male germ-cell transplantation. Proc. Natl. Acad. Sci. USA *91*, 11298–11302.

Byrne, J.A., Pedersen, D.A., Clepper, L.L., Nelson, M., Sanger, W.G., Gokhale, S., Wolf, D.P., and Mitalipov, S.M. (2007). Producing primate embryonic stem cells by somatic cell nuclear transfer. Nature *450*, 497–502.

Chan, A.W., Chong, K.Y., Martinovich, C., Simerly, C., and Schatten, G. (2001). Transgenic monkeys produced by retroviral gene transfer into mature oocytes. Science *291*, 309–312.

Clark, A.T., Phillips, B.T., and Orwig, K.E. (2011). Fruitful progress to fertility: male fertility in the test tube. Nat. Med. *17*, 1564–1565.

Clermont, Y., and Antar, M. (1973). Duration of the cycle of the seminiferous epithelium and the spermatogonial renewal in the monkey Macaca arctoides. Am. J. Anat. *136*, 153–165.

Copelan, E.A. (2006). Hematopoietic stem-cell transplantation. N. Engl. J. Med. *354*, 1813–1826.

Crouch, B.G., and Overman, R.R. (1957). Chemical protection against x-radiation death in primates: a preliminary report. Science *125*, 1092.

Dobrinski, I., Avarbock, M.R., and Brinster, R.L. (1999). Transplantation of germ cells from rabbits and dogs into mouse testes. Biol. Reprod. *61*, 1331–1339.

Dobrinski, I., Avarbock, M.R., and Brinster, R.L. (2000). Germ cell transplantation from large domestic animals into mouse testes. Mol. Reprod. Dev. *57*, 270–279.

Donahue, R.E., Kuramoto, K., and Dunbar, C.E. (2005). Sources and Methods to obtain Stem and Progenitor Cells. In Current Protocols in Immunology (Hoboken, NJ: John Wiley & Sons, Inc.), 22A.1.1–22A.1.29.

Ezzelarab, M., Welchons, D., Torres, C., Hara, H., Long, C., Yeh, P., Ayares, D., and Cooper, D.K. (2008). Atorvastatin down-regulates the primate cellular response to porcine aortic endothelial cells in vitro. Transplantation *86*, 733–737.

Fijak, M., and Meinhardt, A. (2006). The testis in immune privilege. Immunol. Rev. *213*, 66–81.

Geens, M., Goossens, E., De Block, G., Ning, L., Van Saen, D., and Tournaye, H. (2008). Autologous spermatogonial stem cell transplantation in man: current obstacles for a future clinical application. Hum. Reprod. Update *14*, 121–130.

Ginsberg, J.P., Carlson, C.A., Lin, K., Hobbie, W.L., Wigo, E., Wu, X., Brinster, R.L., and Kolon, T.F. (2010). An experimental protocol for fertility preservation in prepubertal boys recently diagnosed with cancer: a report of acceptability and safety. Hum. Reprod. *25*, 37–41.

Gould, K.G., and Mann, D.R. (1988). Comparison of electrostimulation methods for semen recovery in the rhesus monkey (Macaca mulatta). J. Med. Primatol. *17*, 95–103.

Green, D.M., Kawashima, T., Stovall, M., Leisenring, W., Sklar, C.A., Mertens, A.C., Donaldson, S.S., Byrne, J., and Robison, L.L. (2010). Fertility of male survivors of childhood cancer: a report from the Childhood Cancer Survivor Study. J. Clin. Oncol. *28*, 332–339.

Hermann, B.P., and Orwig, K.E. (2011). Translating spermatogonial stem cell transplantation to the clinic. In Male Germline Stem Cells: Developmental and Regenerative Potential, K.E. Orwig and B.P. Hermann, eds. (New York, NY: Humana Press).

Hermann, B.P., Sukhwani, M., Lin, C.C., Sheng, Y., Tomko, J., Rodriguez, M., Shuttleworth, J.J., McFarland, D., Hobbs, R.M., Pandolfi, P.P., et al. (2007). Characterization, cryopreservation, and ablation of spermatogonial stem cells in adult rhesus macaques. Stem Cells *25*, 2330–2338.

Hermann, B.P., Sukhwani, M., Simorangkir, D.R., Chu, T., Plant, T.M., and Orwig, K.E. (2009). Molecular dissection of the male germ cell lineage identifies

putative spermatogonial stem cells in rhesus macaques. Hum. Reprod. *24*, 1704–1716.

Hermann, B.P., Sukhwani, M., Hansel, M.C., and Orwig, K.E. (2010). Spermatogonial stem cells in higher primates: are there differences from those in rodents? Reproduction *139*, 479–493.

Hermann, B.P., Sukhwani, M., Salati, J., Sheng, Y., Chu, T., and Orwig, K.E. (2011). Separating spermatogonia from cancer cells in contaminated prepubertal primate testis cell suspensions. Hum. Reprod. *26*, 3222–3231.

Herrid, M., Olejnik, J., Jackson, M., Suchowerska, N., Stockwell, S., Davey, R., Hutton, K., Hope, S., and Hill, J.R. (2009). Irradiation enhances the efficiency of testicular germ cell transplantation in sheep. Biol. Reprod. *81*, 898–905.

Hewitson, L., Dominko, T., Takahashi, D., Martinovich, C., Ramalho-Santos, J., Sutovsky, P., Fanton, J., Jacob, D., Monteith, D., Neuringer, M., et al. (1999). Unique checkpoints during the first cell cycle of fertilization after intracytoplasmic sperm injection in rhesus monkeys. Nat. Med. *5*, 431–433.

Honaramooz, A., Megee, S.O., and Dobrinski, I. (2002). Germ cell transplantation in pigs. Biol. Reprod. *66*, 21–28.

Honaramooz, A., Behboodi, E., Megee, S.O., Overton, S.A., Galantino-Homer, H., Echelard, Y., and Dobrinski, I. (2003). Fertility and germline transmission of donor haplotype following germ cell transplantation in immunocompetent goats. Biol. Reprod. *69*, 1260–1264.

Izadyar, F., Den Ouden, K., Stout, T.A., Stout, J., Coret, J., Lankveld, D.P., Spoormakers, T.J., Colenbrander, B., Oldenbroek, J.K., Van der Ploeg, K.D., et al. (2003). Autologous and homologous transplantation of bovine spermatogonial stem cells. Reproduction *126*, 765–774.

Jahnukainen, K., Ehmcke, J., Quader, M.A., Saiful Huq, M., Epperly, M.W., Hergenrother, S., Nurmio, M., and Schlatt, S. (2011). Testicular recovery after irradiation differs in prepubertal and pubertal non-human primates, and can be enhanced by autologous germ cell transplantation. Hum. Reprod. *26*, 1945–1954.

Kang, E.M., Hsieh, M.M., Metzger, M., Krouse, A., Donahue, R.E., Sadelain, M., and Tisdale, J.F. (2006). Busulfan pharmacokinetics, toxicity, and low-dose conditioning for autologous transplantation of genetically modified hematopoietic stem cells in the rhesus macaque model. Exp. Hematol. *34*, 132–139.

Keros, V., Hultenby, K., Borgström, B., Fridström, M., Jahnukainen, K., and Hovatta, O. (2007). Methods of cryopreservation of testicular tissue with viable spermatogonia in pre-pubertal boys undergoing gonadotoxic cancer treatment. Hum. Reprod. *22*, 1384–1395.

Khouangsathiene, S., Pearson, C., Street, S., Ferguson, B., and Dubay, C. (2008). MonkeySNP: a web portal for non-human primate single nucleotide polymorphisms. Bioinformatics *24*, 2645–2646.

Kim, Y., Turner, D., Nelson, J., Dobrinski, I., McEntee, M., and Travis, A.J. (2008). Production of donor-derived sperm after spermatogonial stem cell transplantation in the dog. Reproduction *136*, 823–831.

Kirk, A.D., Burkly, L.C., Batty, D.S., Baumgartner, R.E., Berning, J.D., Buchanan, K., Fechner, J.H., Jr., Germond, R.L., Kampen, R.L., Patterson, N.B., et al. (1999). Treatment with humanized monoclonal antibody against CD154 prevents acute renal allograft rejection in nonhuman primates. Nat. Med. *5*, 686–693.

Kubota, H., and Brinster, R.L. (2006). Technology insight: In vitro culture of spermatogonial stem cells and their potential therapeutic uses. Nat. Clin. Pract. Endocrinol. Metab. *2*, 99–108.

Larsen, C.P., Page, A., Linzie, K.H., Russell, M., Deane, T., Stempora, L., Strobert, E., Penedo, M.C., Ward, T., Wiseman, R., et al. (2010). An MHC-defined primate model reveals significant rejection of bone marrow after mixed chimerism induction despite full MHC matching. Am. J. Transplant. *10*, 2396–2409.

Lee, S.J., Schover, L.R., Partridge, A.H., Patrizio, P., Wallace, W.H., Hagerty, K., Beck, L.N., Brennan, L.V., and Oktay, K.; American Society of Clinical Oncology. (2006). American Society of Clinical Oncology recommendations on fertility preservation in cancer patients. J. Clin. Oncol. *24*, 2917–2931.

Lois, C., Hong, E.J., Pease, S., Brown, E.J., and Baltimore, D. (2002). Germline transmission and tissue-specific expression of transgenes delivered by lentiviral vectors. Science *295*, 868–872.

Mauch, P., Constine, L., Greenberger, J., Knospe, W., Sullivan, J., Liesveld, J.L., and Deeg, H.J. (1995). Hematopoietic stem cell compartment: acute and late effects of radiation therapy and chemotherapy. Int. J. Radiat. Oncol. Biol. Phys. *31*, 1319–1339.

Meistrich, M.L. (1993). Effects of chemotherapy and radiotherapy on spermatogenesis. Eur. Urol. *23*, 136–141, discussion 142.

Messaoudi, I., Estep, R., Robinson, B., and Wong, S.W. (2011). Nonhuman primate models of human immunology. Antioxid. Redox Signal. *14*, 261–273.

Mikkola, M., Sironen, A., Kopp, C., Taponen, J., Sukura, A., Vilkki, J., Katila, T., and Andersson, M. (2006). Transplantation of normal boar testicular cells resulted in complete focal spermatogenesis in a boar affected by the immotile short-tail sperm defect. Reprod. Domest. Anim. *41*, 124–128.

Mitalipov, S., Kuo, H.C., Byrne, J., Clepper, L., Meisner, L., Johnson, J., Zeier, R., and Wolf, D. (2006). Isolation and characterization of novel rhesus monkey embryonic stem cell lines. Stem Cells *24*, 2177–2186.

Mitchell, R.T., Saunders, P.T., Sharpe, R.M., Kelnar, C.J., and Wallace, W.H. (2009). Male fertility and strategies for fertility preservation following childhood cancer treatment. Endocr. Dev. *15*, 101–134.

Ogawa, T. (2001). Spermatogonial transplantation: the principle and possible applications. J. Mol. Med. *79*, 368–374.

Ogawa, T., Dobrinski, I., and Brinster, R.L. (1999). Recipient preparation is critical for spermatogonial transplantation in the rat. Tissue Cell *31*, 461–472.

Ogawa, T., Dobrinski, I., Avarbock, M.R., and Brinster, R.L. (2000). Transplantation of male germ line stem cells restores fertility in infertile mice. Nat. Med. *6*, 29–34.

Oktay, K. (2011). Institute for Fertility Preservation at the Center for Human Reproduction, Center for Reproductive Medicine, New York Medical College. http://www.fertilitypreservation.org.

Orwig, K.E., Sanfilippo, J.S., Shaw, P.H., Cannon, G.M., and Dovey, S.L. (2011). Fertility Preservation Program in Pittsburgh, Magee-Womens Research Institute, University of Pittsburgh Medical Center. http://www.mwrif.org/220.

Osawa, M., Hanada, K., Hamada, H., and Nakauchi, H. (1996). Long-term lymphohematopoietic reconstitution by a single CD34-low/negative hematopoietic stem cell. Science *273*, 242–245.

Phillips, B.T., Gassei, K., and Orwig, K.E. (2010). Spermatogonial stem cell regulation and spermatogenesis. Philos. Trans. R. Soc. Lond. B Biol. Sci. *365*, 1663–1678.

Plant, T.M., and Marshall, G.R. (2001). The functional significance of FSH in spermatogenesis and the control of its secretion in male primates. Endocr. Rev. *22*, 764–786.

Potten, C.S. (1992). Cell lineages. In Oxford Textbook of Pathology, J.O. McGee, P.G. Isaacson, and N.A. Wright, eds. (Oxford: Oxford University Press), pp. 43–52.

Potten, C.S. (1995). Interleukin-11 protects the clonogenic stem cells in murine small-intestinal crypts from impairment of their reproductive capacity by radiation. Int. J. Cancer *62*, 356–361.

Potten, C.S., Schofield, R., and Lajtha, L.G. (1979). A comparison of cell replacement in bone marrow, testis and three regions of surface epithelium. Biochim. Biophys. Acta *560*, 281–299.

Powell, J.L., Hingorani, P., and Kolb, E.A. (2009). Pediatric Hematopoietic Stem Cell Transplantation. Medscape Reference *WebMD LLC, 09/11/2009*. http://emedicine.medscape.com/article/991032-overview.

Rodriguez-Sosa, J.R., and Dobrinski, I. (2009). Recent developments in testis tissue xenografting. Reproduction *138*, 187–194.

Ryu, B.Y., Orwig, K.E., Avarbock, M.R., and Brinster, R.L. (2003). Stem cell and niche development in the postnatal rat testis. Dev. Biol. *263*, 253–263.

Sadri-Ardekani, H., Akhondi, M.A., van der Veen, F., Repping, S., and van Pelt, A.M. (2011). In vitro propagation of human prepubertal spermatogonial stem cells. JAMA *305*, 2416–2418.

Sato, T., Katagiri, K., Gohbara, A., Inoue, K., Ogonuki, N., Ogura, A., Kubota, Y., and Ogawa, T. (2011). In vitro production of functional sperm in cultured neonatal mouse testes. Nature *471*, 504–507.

Schlatt, S., and Kliesch, S. (2012). Center for Reproductive Medicine and Andrology, University of Münster. http://repro.klinikum.uni-muenster.de/html/quadega.html.

Schlatt, S., Rosiepen, G., Weinbauer, G.F., Rolf, C., Brook, P.F., and Nieschlag, E. (1999). Germ cell transfer into rat, bovine, monkey and human testes. Hum. Reprod. *14*, 144–150.

Schlatt, S., Foppiani, L., Rolf, C., Weinbauer, G.F., and Nieschlag, E. (2002). Germ cell transplantation into X-irradiated monkey testes. Hum. Reprod. *17*, 55–62.

Schlatt, S., Ehmcke, J., and Jahnukainen, K. (2009). Testicular stem cells for fertility preservation: preclinical studies on male germ cell transplantation and testicular grafting. Pediatr. Blood Cancer *53*, 274–280.

Sharpe, R.M. (1994). Regulation of Spermatogenesis. In The Physiology of Reproduction, E. Knobil and J.D. Neill, eds. (New York: Raven Press, Ltd.), pp. 1363–1434.

Shinohara, T., Orwig, K.E., Avarbock, M.R., and Brinster, R.L. (2001). Remodeling of the postnatal mouse testis is accompanied by dramatic changes in stem cell number and niche accessibility. Proc. Natl. Acad. Sci. USA *98*, 6186–6191.

Thomas, E.D., Lochte, H.L., Jr., Lu, W.C., and Ferrebee, J.W. (1957). Intravenous infusion of bone marrow in patients receiving radiation and chemotherapy. N. Engl. J. Med. *257*, 491–496.

Wallace, W.H., Anderson, R.A., and Irvine, D.S. (2005). Fertility preservation for young patients with cancer: who is at risk and what can be offered? Lancet Oncol. *6*, 209–218.

Wolf, D.P., Vandevoort, C.A., Meyer-Haas, G.R., Zelinski-Wooten, M.B., Hess, D.L., Baughman, W.L., and Stouffer, R.L. (1989). In vitro fertilization and embryo transfer in the rhesus monkey. Biol. Reprod. *41*, 335–346.

Wolf, D.P., Thormahlen, S., Ramsey, C., Yeoman, R.R., Fanton, J., and Mitalipov, S. (2004). Use of assisted reproductive technologies in the propagation of rhesus macaque offspring. Biol. Reprod. *71*, 486–493.

Wyns, C., Van Langendonckt, A., Wese, F.X., Donnez, J., and Curaba, M. (2008). Long-term spermatogonial survival in cryopreserved and xenografted immature human testicular tissue. Hum. Reprod. *23*, 2402–2414.

Wyns, C., Curaba, M., Vanabelle, B., Van Langendonckt, A., and Donnez, J. (2010). Options for fertility preservation in prepubertal boys. Hum. Reprod. Update *16*, 312–328.

Cell Stem Cell
Clinical Progress

Prostaglandin E2 Enhances Human Cord Blood Stem Cell Xenotransplants and Shows Long-Term Safety in Preclinical Nonhuman Primate Transplant Models

Wolfram Goessling,[1,2] Robyn S. Allen,[3] Xiao Guan,[4] Ping Jin,[5] Naoya Uchida,[6] Michael Dovey,[7] James M. Harris,[7] Mark E. Metzger,[3] Aylin C. Bonifacino,[3] David Stroncek,[5] Joseph Stegner,[8] Myriam Armant,[8] Thorsten Schlaeger,[4] John F. Tisdale,[6] Leonard I. Zon,[2,4,9] Robert E. Donahue,[3] and Trista E. North[2,7,*]

[1]Genetics and Gastroenterology Divisions, Brigham and Women's Hospital, Gastrointestinal Cancer Center, Dana-Farber Cancer Institute, Boston, MA 02115, USA
[2]Harvard Stem Cell Institute and Harvard Medical School, Boston, MA 02115, USA
[3]Hematology Branch, National Heart, Lung, and Blood Institute (NHLBI), NIH, Rockville, MD 20850, USA
[4]Stem Cell Program, Children's Hospital, Boston, MA 02115, USA
[5]Department of Transfusion Medicine, Clinical Center, NIH, Bethesda, MD 20892, USA
[6]Molecular and Clinical Hematology Branch, National Heart, Lung, and Blood Institute (NHLBI)/National Institute of Diabetes and Digestive and Kidney Diseases (NIDDK), NIH, Bethesda, MD 20892, USA
[7]Department of Pathology, Beth Israel Deaconess Medical Center, Boston, MA 02115, USA
[8]Center for Human Cell Therapy, Immune Disease Institute, Boston, MA 02115, USA
[9]Howard Hughes Medical Institute, Boston, MA 02115, USA
*Correspondence: tnorth@bidmc.harvard.edu
DOI 10.1016/j.stem.2011.02.003

SUMMARY

Hematopoietic stem cells (HSCs) are used in transplantation therapy to reconstitute the hematopoietic system. Human cord blood (hCB) transplantation has emerged as an attractive alternative treatment option when traditional HSC sources are unavailable; however, the absolute number of hCB HSCs transplanted is significantly lower than bone marrow or mobilized peripheral blood stem cells (MPBSCs). We previously demonstrated that dimethyl-prostaglandin E2 (dmPGE2) increased HSCs in vertebrate models. Here, we describe preclinical analyses of the therapeutic potential of dmPGE2 treatment by using human and nonhuman primate HSCs. dmPGE2 significantly increased total human hematopoietic colony formation in vitro and enhanced engraftment of unfractionated and $CD34^+$ hCB after xenotransplantation. In nonhuman primate autologous transplantation, dmPGE2-treated $CD34^+$ MPBSCs showed stable multilineage engraftment over 1 year postinfusion. Together, our analyses indicated that dmPGE2 mediates conserved responses in HSCs from human and nonhuman primates and provided sufficient preclinical information to support proceeding to an FDA-approved phase 1 clinical trial.

INTRODUCTION

HSCs alone possess the ability to both self-renew and differentiate into all mature blood lineages, thereby maintaining immune function, tissue perfusion, and hematopoietic homeostasis throughout the lifetime of the organism. HSCs are therapeutically valuable for transplantation in the treatment of hematologic malignances. They are a rare population in the bone marrow (BM), and methods for direct isolation and expansion of a pure population of functional human HSCs remain elusive. The development of therapeutic options to manipulate and maintain human HSCs is of major clinical interest; however, to date, no such therapy has proven effective in large-scale clinical trials.

HSC transplantation is the only curative option for many patients with leukemia, lymphoma, or BM failure. Stem cells obtained from the BM or peripheral blood (PB) must be human leukocyte antigen (HLA) matched to the patient in order to avoid rejection. Only 25%–30% of patients can utilize BM from a related sibling donor, and matched unrelated donors cannot be found in BM registries for all patients, particularly for those from ethnic minorities (Laver et al., 2001). In the past two decades, human cord blood (hCB) stem cells have emerged as an option for unmatched patients, because they are readily obtained in registries and have less stringent requirements for HLA matching (Broxmeyer et al., 1989). The use of hCB transplantation has steadily grown since the first transplant occurred in 1988 to more than 20,000 recipients worldwide (Rocha and Broxmeyer, 2010). In the United States, hCB transplants account for almost 20% of all HSC transplants annually (Broxmeyer et al., 2009); among minority populations, the number of hCB transplants reaches 40% (Ballen et al., 2002). Because of limited volume, the absolute number of HSCs available in hCB specimens is only ~10% of that utilized in traditional BM transplants, leading to delayed engraftment and increased peritransplant complications (Rocha and Broxmeyer, 2010). One approach to alleviate this problem is to transplant two unrelated hCB specimens (Ballen et al., 2007b). Although this change correlated with improved adult engraftment rates, the time to engraftment was not shortened; engraftment after a hCB transplant can take >50% longer than traditional HSC transplants (Broxmeyer

et al., 2009). The identification of agents to increase hCB HSC homing, engraftment, or total stem cell number is of significant therapeutic value.

Given this important clinical challenge, many investigators have sought to accelerate hCB HSC engraftment and blood count recovery after transplantation. The most clinically advanced approach thus far appears to be short-term culture with the notch ligand Delta (Delaney et al., 2010). This in vitro expansion procedure has been evaluated with significant evidence of success in an ongoing clinical trial; however, Delta treatment may lead to the depletion of long-term engrafting HSCs in the hCB unit, indicating that even this promising approach could need modifications before it can be broadly employed. In vitro expansion potential has also been described for insulin-like growth factor binding protein 2 in xenotransplantation studies (Zhang et al., 2008) and more recently for inhibition of the aryl hydrocarbon receptor (Boitano et al., 2010). Short ex vivo treatment of hCB with a chemical inhibitor of dipeptidyl-peptidase IV (CD26) boosts homing to the hematopoietic niche to enhance engraftment in xenotransplantation models (Campbell et al., 2007). Rather than targeting HSCs, parathyroid hormone (PTH) has been used in vivo to enhance engraftment by modifying the murine osteoblastic HSC niche (Adams et al., 2007); PTH has also been used to safely facilitate stem cell mobilization in a clinical trial (Ballen et al., 2007a).

Murine hematopoietic transplantation assays are limited by the relatively short life span of mice compared to humans, enabling the detailed study of HSC function only over a limited time window. This often requires secondary transplant experiments to assess long-term HSC function, including self-renewal. Nonhuman primates have emerged as a valuable vertebrate model to perform longitudinal HSC transplantation studies. Engraftment and expansion can be examined after autologous transplantation of mobilized peripheral blood stem cells (MPBSCs). Further, efficient viral transduction techniques, utilizing fluorescent markers, allow the direct comparison of differently treated, uniquely labeled cell populations in an in vivo competitive transplantation assay (Donahue et al., 2005; Uchida et al., 2009). Significantly, the life span of nonhuman primates approaches that of humans, making it possible to study the long-term effects of different treatment modalities on the graft and host under conditions that approximate the demands on the human hematopoietic system (Trobridge and Kiem, 2010).

We previously demonstrated that dmPGE2 increased HSC number in vitro and in vivo (North et al., 2007). Murine limiting dilution competitive transplantation analysis demonstrated a 2- to 4-fold increase in HSC number after short ex vivo dmPGE2 exposure, without impacting multilineage hematopoietic differentiation or decreasing serial transplantation and self-renewal potential (Hoggatt et al., 2009; North et al., 2007). dmPGE2 functions through cAMP-mediated regulation of the Wnt signaling pathway to control cell proliferation and apoptosis of HSCs in vivo (Goessling et al., 2009). Recent work has expanded these findings (Frisch et al., 2009; Hoggatt et al., 2009) to demonstrate the ability of dmPGE2 to modulate the BM niche and enhance homing.

Here, we present preclinical investigations of the safety and therapeutic potential of ex vivo dmPGE2 treatment to enhance human hematopoietic transplantation protocols. We found that hCB HSCs differentially express PGE2 receptors, and dmPGE2 treatment elevates cAMP activity in human cells. In vitro, dmPGE2 treatment of $CD34^+$ hCB decreased apoptosis, while significantly increasing HSC proliferation and hematopoietic colony formation. Further, dmPGE2 treatment enhanced the rates of human $CD45^+$ chimerism in NOD/SCID mice xenotransplanted with whole or $CD34^+$ hCB cells. By using $CD34^+$ MPBSCs in a nonhuman primate (rhesus macaque) competitive autologous transplantation scheme, we showed that dmPGE2 treatment has no negative impact on HSC function, including multilineage repopulation, compared to matched controls at >1 year postinfusion. Human and rhesus MPBSCs had reduced expression of EP2 and EP4 compared to hCB HSCs; however, each exhibited dose-responsive increases in cAMP activity after PGE2 treatment. Microarray gene expression analysis of human and rhesus $CD34^+$ MPBSCs revealed conserved regulation of cell cycle, PGE2 pathway, and HSC-related genes, representing a potential mechanism of action for dmPGE2; qPCR analysis of hCB samples after dmPGE2 stimulation confirmed similar gene regulation. These results predict that dmPGE2 will be safe for use in clinical HSC transplantation protocols.

RESULTS

hCB HSCs Express PGE2 Receptors and Respond to Exogenous PGE2 Stimulation

We, and others, have shown PGE2 enhances HSC engraftment in isogenic murine transplantation models (Hoggatt et al., 2009; North et al., 2007). To examine the therapeutic potential of dmPGE2 for human HSC transplantation, we investigated the safety and efficacy of ex vivo exposure of hCB HSCs. To assess whether hCB was capable of responding to exogenous PGE2 stimulation, subfractionated samples were examined for the presence of each of the four PGE2 receptors. Quantitative PCR (qPCR) was performed with purified cell fractions contained within the umbilical cord, i.e., $CD34^+$, $CD133^+$, or mononuclear cells (MNC); human umbilical vein endothelial cells (HUVEC) were used as a nonhemogenic control population. The $CD34^+$ population predominantly expressed *EP2* and *EP4* (Figure 1A); the level of *EP4* expression is highly correlated with $CD34^+$ status. *EP2* and *EP4* are similarly expressed in $CD133^+$ hCB HSCs. Analysis of the total hCB MNC population showed maintenance of *EP2* expression, while *EP4* was significantly downregulated. In contrast, *EP1* and *EP3* are not significantly expressed in any hCB populations. *SCL* and *RUNX1* were utilized to confirm that the $CD34^+$ and $CD133^+$ hCB cell fractions contained HSCs (Figure 1B).

Having established the distribution of PGE2 receptors in hCB, the intracellular response to dmPGE2 stimulation was examined. Upon ligand binding, EP2 and EP4, $G\alpha_s$-coupled protein receptors, enhance intracellular cAMP levels (Regan et al., 1994) to initiate signaling cascades. We have recently shown that PGE2-mediated cAMP elevation regulates HSC number by modification of Wnt activity in vitro and in vivo (Goessling et al., 2009). To determine whether cAMP elevation would occur in response to dmPGE2, whole hCB cells were exposed to increasing doses of dmPGE2 for 5, 15, and 30 min. dmPGE2 caused a dose-dependent increase in cAMP in hCB cells (Figure 1C), which is similar to the cAMP activator forskolin. Given

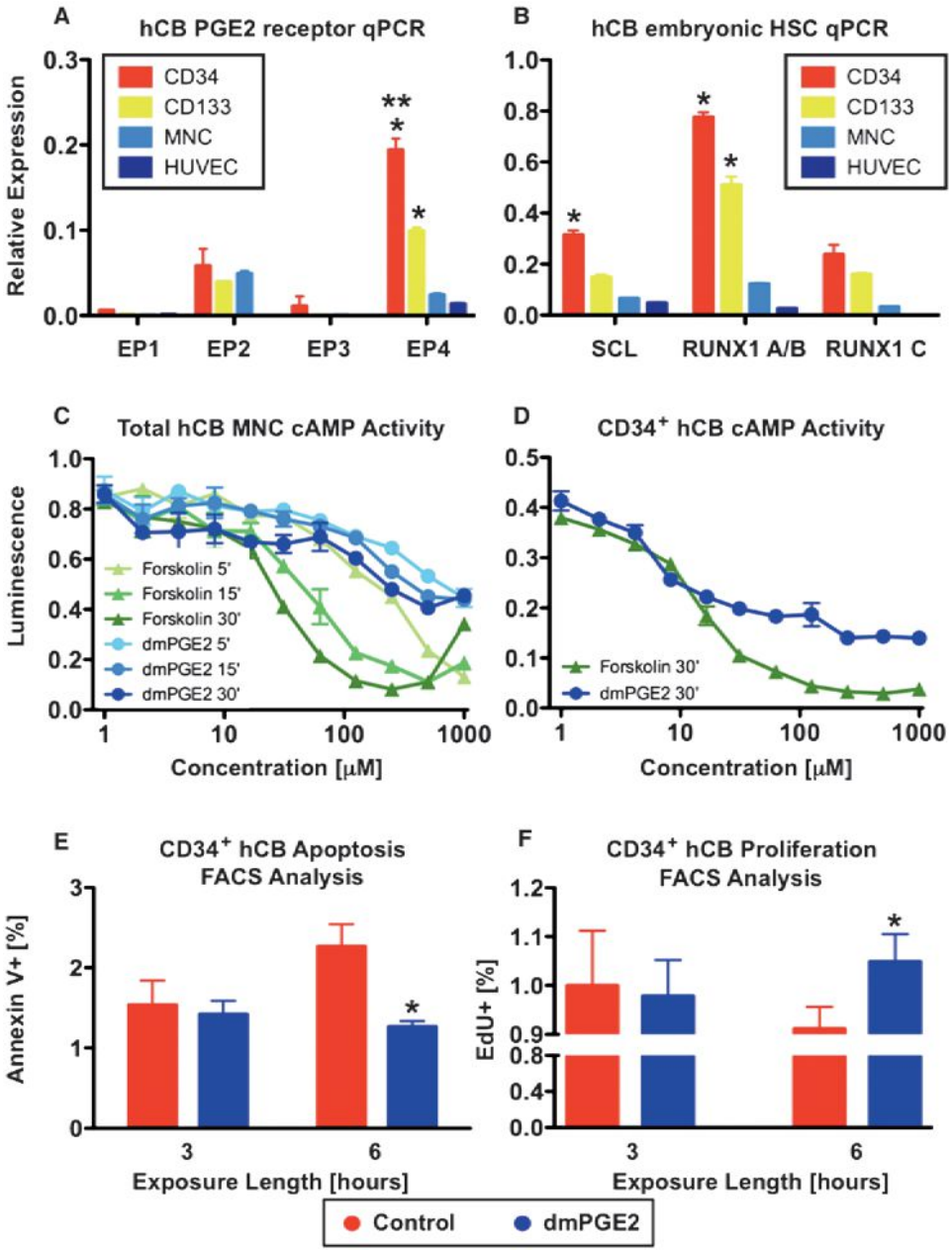

Figure 1. hCB Expresses Prostaglandin Receptors and Responds to PGE2 Signaling

(A) CD34$^+$ cells have the highest expression of PGE receptors, particularly *EP4*. n = 3; ANOVA, *p < 0.001, compared to other EPs, **p < 0.001, compared to other hCB cells.

(B) CD34$^+$ cells express the immature HSC markers *SCL* and *RUNX1*. n = 3; ANOVA, *p < 0.001, compared to other hCB cells.

(C and D) Total hCB (C) and CD34$^+$ hCB (D) cells were incubated with increasing concentrations of dmPGE2 or forskolin and subjected to a luminescence-based cAMP assay. cAMP levels increased in response to treatment (mean ± SD of 3–5 samples).

(E) Annexin V FACS analysis revealed that dmPGE2 exposure significantly decreased apoptotic CD34$^+$ cells at 6 hr posttreatment compared to controls. n = 8, t test; *p = 0.024.

(F) EdU incorporation measured by FACS was significantly enhanced in CD34$^+$ cells in response to dmPGE2 exposure. n = 8; t test, *p = 0.006.

See also Figure S1.

the enrichment of EP2 and EP4 receptors in the CD34$^+$ population, we directly examined cAMP responsiveness in this cell fraction; interestingly, the effective dose response occurred at a lower concentration in the CD34$^+$ population (Figure 1D), possibly reflecting the high level of expression of EP4 on purified hCB HSCs. Importantly, both unfractionated and CD34$^+$ hCB cells elicited rapid responses to dmPGE2 stimulation over the dose range tested.

PGE2 treatment was previously reported to have an antiapoptotic effect on murine HSCs (Goessling et al., 2009; Hoggatt et al., 2009); to further analyze the conserved impact of dmPGE2 exposure, apoptosis and cell proliferation studies were conducted. Pooled $CD34^+$ hCB samples were thawed, split for parallel processing, and treated with 1 μM dmPGE2 or DMSO vehicle control. At 3 and 6 hr after exposure, apoptosis was measured by AnnexinV FACS analysis. Both treatment cohorts demonstrated similar levels of apoptotic cell death at 3 hr; however, by 6 hr, cells treated with dmPGE2 showed a significant reduction in apoptosis compared to controls (Figure 1E; Figure S1A available online). Complementary results were observed for cellular proliferation, where PGE2 caused significant changes in EdU incorporation at 6 hr after dmPGE2 treatment (Figure 1F; Figure S1B).

dmPGE2 Enhances hCB HSC Function In Vitro and In Vivo

dmPGE2 was previously found to increase hematopoietic colony formation of murine embryonic stem cells (ESCs) (Goessling et al., 2009; North et al., 2007). To determine whether dmPGE2 exposure impacted the functional potential of hCB samples, pooled $CD34^+$ hCB cells were exposed to DMSO or dmPGE2 (1 μM) for fixed incubation periods (15, 30, 60, 180, 360 min), then plated in triplicate on H4434 methylcellulose at limiting dilution (2000, 800, 320) (Figure 2A; Table S1). The majority of hematopoietic colony types increased in response to dmPGE2; in particular, the GEMM population was significantly elevated after only 1 hr of dmPGE2 treatment. When colony numbers were combined and normalized for initial plating density, differences in total colonies across all replicates of the limiting dilution and dose-response assay demonstrated a 1.4-fold enhancement after dmPGE2 stimulation (Figure 2B). Together, the in vitro CFU-C data strongly suggest that dmPGE2 enhances colony-forming potential of $CD34^+$ cells.

In limiting dilution competitive transplantation assays, dmPGE2 significantly increased the multilineage serial transplantable long-term repopulating ability of murine HSCs (Hoggatt et al., 2009; North et al., 2007). We examined the ability of dmPGE2 to enhance hematopoietic engraftment of hCB stem cells in vivo by using a xenotransplantation model. To mimic clinical transplantation protocols, which primarily utilize unmanipulated (non-lineage-depleted, non-NK/T cell-depleted, non-CD34-enriched) samples, and to assess the potential impact on all cell populations contained within a hCB unit, whole hCB samples were initially employed for xenotransplantation. Individual hCB units were split to account for cord-to-cord alterations in HSC content and viability, then treated in parallel ex vivo with dmPGE2 (10 μM) or DMSO for 1 hr in dextran/albumin suspension media; alterations in incubation time and media from our original studies (North et al., 2007) did not impact the effect of dmPGE2 stimulation in murine short-term CFU-S_{12} evaluations (Figures S2A and S2B). To best mimic clinical conditions, recipient NOD/SCID mice were not conditioned to enhance engraftment beyond a standard regimen to clear the hematopoietic niche. After sublethal irradiation (6.5 Gy), NOD/SCID mice were transplanted with either 20 million matched dmPGE2-treated or control-treated whole hCB cells; this dose was chosen to detect positive effects of dmPGE2 on human chimerism in xenotransplant recipients based on prior whole hCB studies (Trowbridge et al., 2006). Human PB chimerism was evaluated by FACS analysis for hCD45; antibody reactivity >1% was used to identify positively engrafted recipients (Figure S3A). At 1 and 3 months posttransplant, more recipients of hCB cells treated ex vivo with dmPGE2 exhibited human $CD45^+$ hematopoietic repopulation than recipients of matched controls, with overall higher average levels of PB chimerism (Figures 2C and 2D). $hCD45^+$ BM engraftment >0.2% at 3 months posttransplantation was also higher in recipients of dmPGE2-treated hCB (Figures 2C and 2D; Figure S3B). Multilineage analysis of mice with hCB BM engraftment values >1% revealed contribution to each of the major blood lineages and the absence of lineage skewing in recipients of dmPGE2-treated cells; significant increases in the overall percentage of hCB-derived phenotypic stem/progenitor cells, myeloid, and T cell lineages were observed compared to matched controls (Figures S4A–S4C). Importantly, we were unable to detect any toxicity related to ex vivo dmPGE2 treatment over the duration of analyses: secondary transplants showed PB repopulation by PGE2-treated hCB cells; no excessive cell death, leukemic transformation, or disproportional loss of murine hosts were observed between recipients of dmPGE2-treated hCB and matched controls; and histological analysis of tissue (skin, liver, spleen, intestine, and bone) taken at the time of sacrifice showed no differences in cellular morphology, architecture, or vascularity from controls (data not shown).

To confirm whether the enhanced hCB engraftment was due to direct effects on $CD34^+$ HSCs and progenitors, fresh hCB units were enriched by MACS for hCD34 and split for parallel treatment with either dmPGE2 or DMSO control as indicated above. 2500 $CD34^+$ cells were transplanted per recipient; this dose can provide repopulation without cytokine supplementation or the injection of "helper" cells, while testing the lower end of engraftment efficiency. As seen with whole hCB, dmPGE2 treatment led to a higher percentage of mice exhibiting $hCD45^+$ PB and BM chimerism (Figures S5A and S5B). Our results suggest that ex vivo treatment of whole hCB units with dmPGE2 will be safe and effective in achieving expansion of HSCs for transplantation in the clinical setting because of preferential targeting of the $CD34^+$ population.

Human and Nonhuman Primate Mobilized Peripheral Blood Stem Cells Can Functionally Respond to dmPGE2 Treatment

To further assess the long-term safety of ex vivo dmPGE2 exposure for clinical transplantation protocols, a nonhuman primate model was employed. Because CB samples are not routinely harvested from primates, safety evaluations were conducted with $CD34^+$ MPBSCs isolated after a G-CSF/SCF conditioning protocol optimized for rhesus macaques (Donahue et al., 2005). To assess the inherent ability of rhesus MPBSCs (rhMPBSC) to respond to PGE2 stimulation, subfractionated $CD34^+$ samples were examined for the presence of each of the four PGE2 receptors by qPCR; results were compared to that observed on similarly mobilized human MPBSC (hMPBSC) samples. $CD34^+$ hMPBSCs predominantly expressed *EP2* and *EP4* (Figure 3A); however, expression of *EP4* in hMPBSC was relatively equal to that of *EP2*, and unlike hCB HSCs

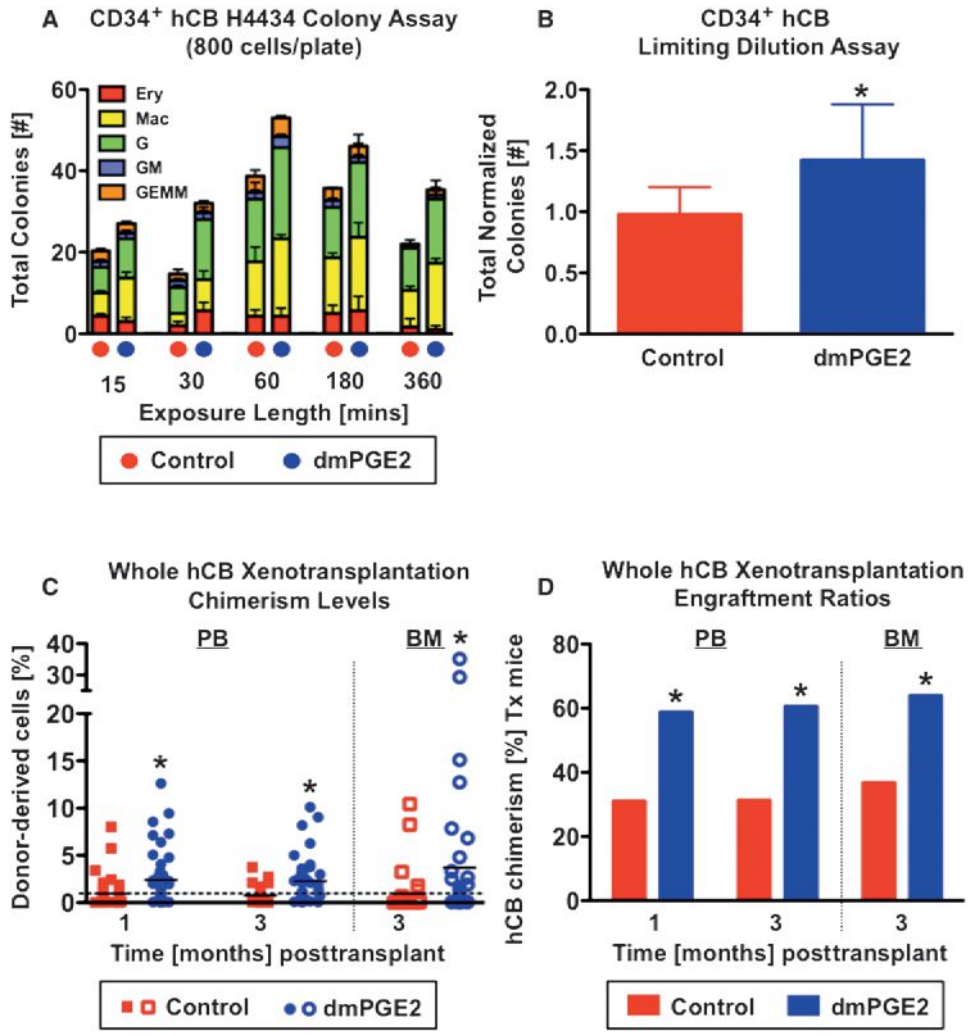

Figure 2. dmPGE2 Enhances hCB Proliferation In Vitro and Engraftment In Vivo

(A and B) CD34$^+$ hCB cells were exposed to 1 μM dmPGE2 over a matrix of cell densities and exposure times.

(A) Colony formation at day 13 was enhanced after dmPGE2 exposure for 15 min to 6 hr; shown are the results of 800 cells/plate (n = 3).

(B) Normalization and combination of cell counts over all exposure times and cell densities revealed a significant increase in total colony number after dmPGE2 exposure (n = 45; t test, *p = 0.018).

(C and D) Whole hCB was transplanted into sublethally irradiated NOD/SCID mice. PB was analyzed at 1 and 3 months and recipient BM at ≥3 months posttransplantation. Asterisk indicates results were statistically different from control.

(C) Individual hCD45$^+$ chimerism values for mice receiving control (red squares) or dmPGE2-treated hCB (blue circles). The mean is indicated by a solid horizontal line; a dashed line shows the 1% cut-off for positive engraftment. PB: 1 month, control 0.94 ± 0.2414, dmPGE2 2.41 ± 0.4118; t test, p = 0.0017; 3 months, control 0.76 ± 0.1418, dmPGE2 2.27 ± 0.3778; t test, p = 0.0004. BM: control 0.95 ± 0.4373, dmPGE2 3.70 ± 1.310; t test, p = 0.0348.

(D) Cumulative summary of the percent of NOC/SCID recipients engrafted with hCB. PB: 1 month, control 13/42, dmPGE2 27/46; Fisher's exact, p = 0.011; 3 months, control 10/32, dmPGE2 23/28; Fisher's exact, p = 0.018; BM: control 11/30, dmPGE2 23/36; Fisher's exact, p = 0.047.

See also Figures S2–S5 and Table S1.

(see Figure 1), *EP1* also was prominently expressed (Figure 3A). qPCR analysis of rhMPBSCs revealed 5-fold lower EP receptor expression in nonhuman primate HSCs than hMPBSCs, with *EP2* particularly underrepresented (Figure 3B). However, by using the luminescent assay described above, dose-dependent responses to dmPGE2 were observed for both MPBSCs populations; hMPBSC showed a comparable response to CD34$^+$ hCB, while rhMPBSC required a slightly higher dose for cAMP activation (Figures 3C and 3D). These data indicate that human and rhesus CD34$^+$ HSCs can react to dmPGE2.

dmPGE2-Treated rhMPBSCs Show Stable Long-Term Multilineage Engraftment in Nonhuman Primate Competitive Transplantation Study

Receptor distribution and response assays suggested that the nonhuman primate model would be relevant to assess the potential long-term safety of the therapeutic use of dmPGE2. To examine the functional impact of dmPGE2 exposure on rhMBPSCs, a competitive autologous transplant study was performed. A two-pronged design scheme was developed to internally control for compound treatment and vector transduction

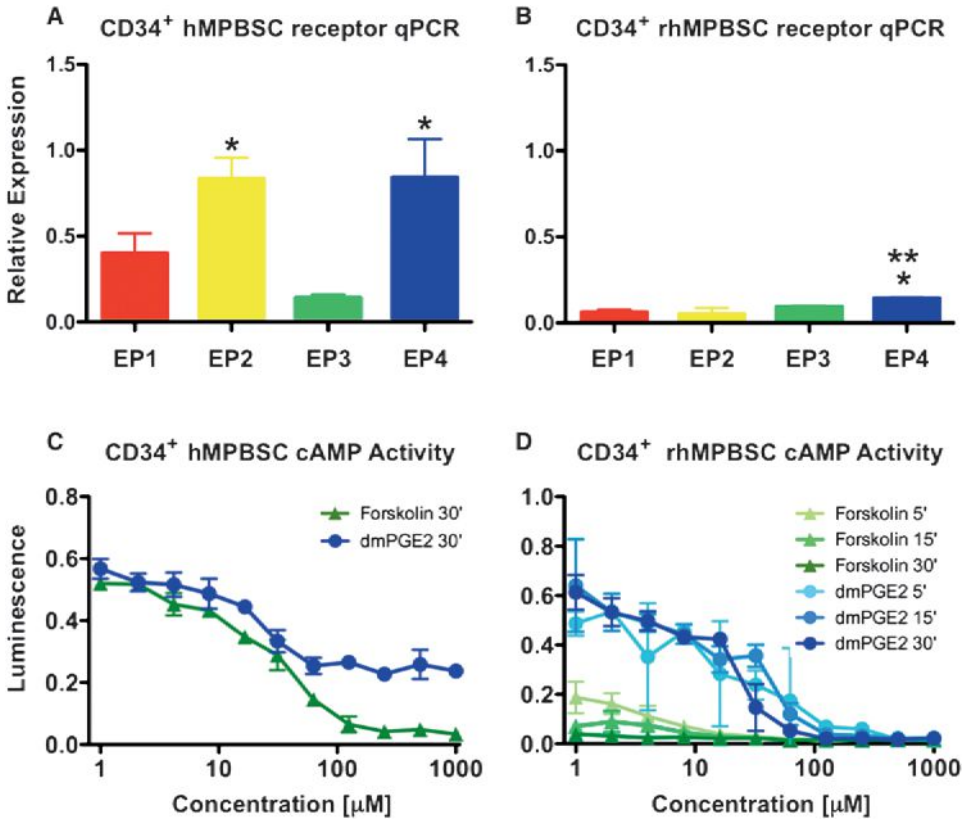

Figure 3. PGE2 Receptors and cAMP Response Are Preserved between Human and Nonhuman Primate Peripheral Blood Stem Cells

PB stem cells were mobilized from humans and nonhuman primates.

(A) qPCR analysis showed that *EP2* and *EP4* are equally and predominantly expressed in hMPBSC. n = 3; ANOVA, *p < 0.001 EP2 or EP4 versus EP1 and EP3.

(B) qPCR revealed low EP receptor expression on rhesus MPBSC, with *EP4* predominant. n = 3–6; ANOVA, *p < 0.001 versus EP1, 2; **p = 0.01 versus EP3.

(C and D) The cAMP response to dmPGE2 is preserved in human and rhesus MPBSC.

parameters; reporter vectors utilized and transduction protocols were previously described in rhesus macaques (Uchida et al., 2009). $CD34^+$ rhMPBSCs were split for parallel processing and treated ex vivo with 10 μM dmPGE2 or X-Vivo10 for 1 hr either prior to or after transduction; dmPGE2 dose was selected based on prior murine (North et al., 2007) and xenotransplant data. Retroviral vectors expressing either EGFP or EYFP were transduced in order to differentiate the treatment groups in vivo; treatment/vector pairings were alternated between individuals to control for potential protocol-related bias. Transduction efficiencies varied between primates but were similar for EGFP and EYFP in each experiment (Table S2). Treated, differentially labeled cells were combined and reinfused into each donor for competitive repopulation analysis; PB samples were taken at fixed intervals beginning at >2 weeks posttransplantation, and the contribution of each labeled population followed via multilineage FACS analysis. Neither pre- nor posttransduction treatment with dmPGE2 negatively affected the engraftment potential of rhMPBSCs; both the percentage of total PB contribution of dmPGE2-treated cells, and that of each lineage remained present, stable, and comparable to controls at all time points examined up to 1 year postreinfusion (Figures 4A and 4B; Figure S6). In all transplant recipients, reconstitution was uneventful and no toxicity was observed; cells transduced with EGFP showed greater PB engraftment than cells expressing EYFP, regardless of treatment. dmPGE2 was demonstrated to be safe to the long-term functional potential of rhMPBSCs.

Comparative Genomic Analysis of Human and Nonhuman Primate $CD34^+$ MPBSCs Exposed to Increasing Doses of dmPGE2 Shows High Conservation of Gene Expression

In order to identify the potential mechanism of action of dmPGE2 on gene expression and HSC function, and to possibly explain the muted response of rhesus $CD34^+$ MPBSCs to dmPGE2 exposure, microarray gene expression analysis was conducted. Human and rhesus $CD34^+$ MPBSCs were exposed to DMSO or dmPGE2 (10 and 50 μM dose) and processed for microarray analysis at 2, 6, and 12 hr posttreatment (Figure S7). 10 μM dmPGE2 had minimal impact on gene expression in rhMPBSCs compared to treatment at 50 μM, while significant changes were observed at each dose with hMPBSCs (Figures 5A–5C). The greatest relative alterations in gene expression were observed for all treatments at 6 hr postexposure, so that time point was utilized for further comparative analysis. 110 genes were commonly regulated between human and rhesus MPBSCs, indicating an evolutionarily conserved response to PGE2 stimulation (Figure 5D; Table S3A); among this set were genes

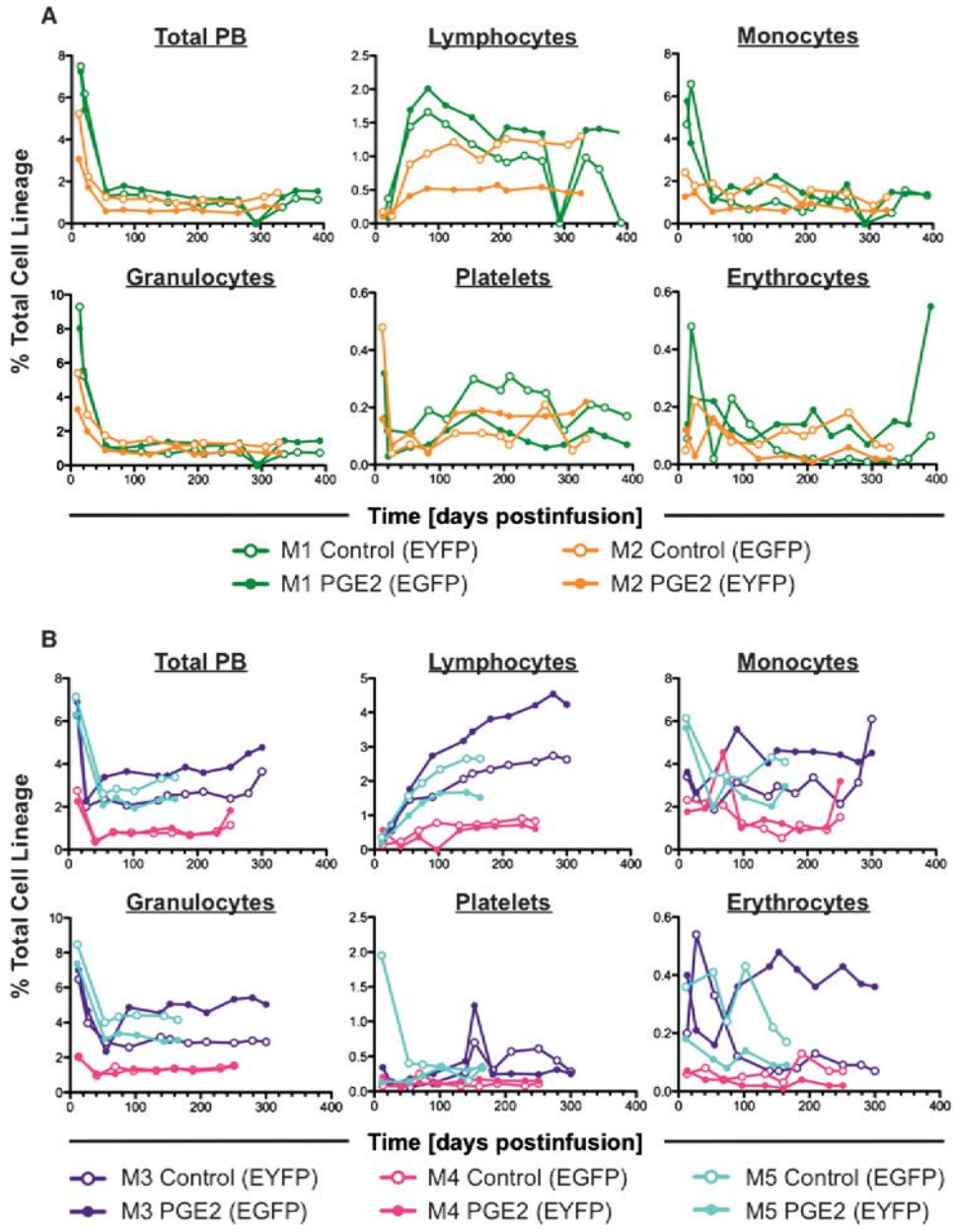

Figure 4. dmPGE2 Exposure of Nonhuman Primate MPBSC Shows Long-Term Safety

(A) Whole PB and multilineage longitudinal FACS analysis of primates treated with dmPGE2 prior to transduction (n = 2). Equivalent long-term function of fluorescently marked control (open circles) and dmPGE2-treated MPBSCs (solid circles) was shown.

(B) Whole PB and multilineage longitudinal FACS analysis of primates treated with dmPGE2 posttransduction (n = 3). Long-term survival and differentiation capacity is maintained irrespective of compound exposure (as indicated above).

See also Figure S6 and Table S2.

representative of PGE2/cAMP signaling including *CREM, CREB, PDE4B,* and *PTGER2*; several chemokines and cytokines including *CXCL1, CXCL3, CXCL10, IL1R1, IL18R1, IL23A*, and *ANG*; and many genes known to be specific to cell cycle regulation or hematopoietic cell differentiation. 262 genes were similarly regulated in human cells at both dmPGE2 doses (Figure 5D; Table S3B) but not significantly altered in rhesus samples; among these were many major regulators of HSC development and maturation such as *CXCR4, HHEX, HOXA9, JUNB, LCK, LMO2, LY6A, RUNX1*, and *TF*. Considerable and exclusive overlap was also found between each of the PGE2 doses in human cells and that of the high dose in rhesus macaques (Figure 5D; Tables S3C and S3D); in particular, 10 μM hMPBSC/50 μM rhMPBSC show coordinated upregulation of genes like *FLT3, JAK1, CCR1*, and *CD8a*, perhaps indicative of enhanced proliferative and differentiation potential in the transplantation assays, while 50 μM hMPBSC/50 μM rhMPBSC displayed common regulation among genes influencing hematopoietic quiescence

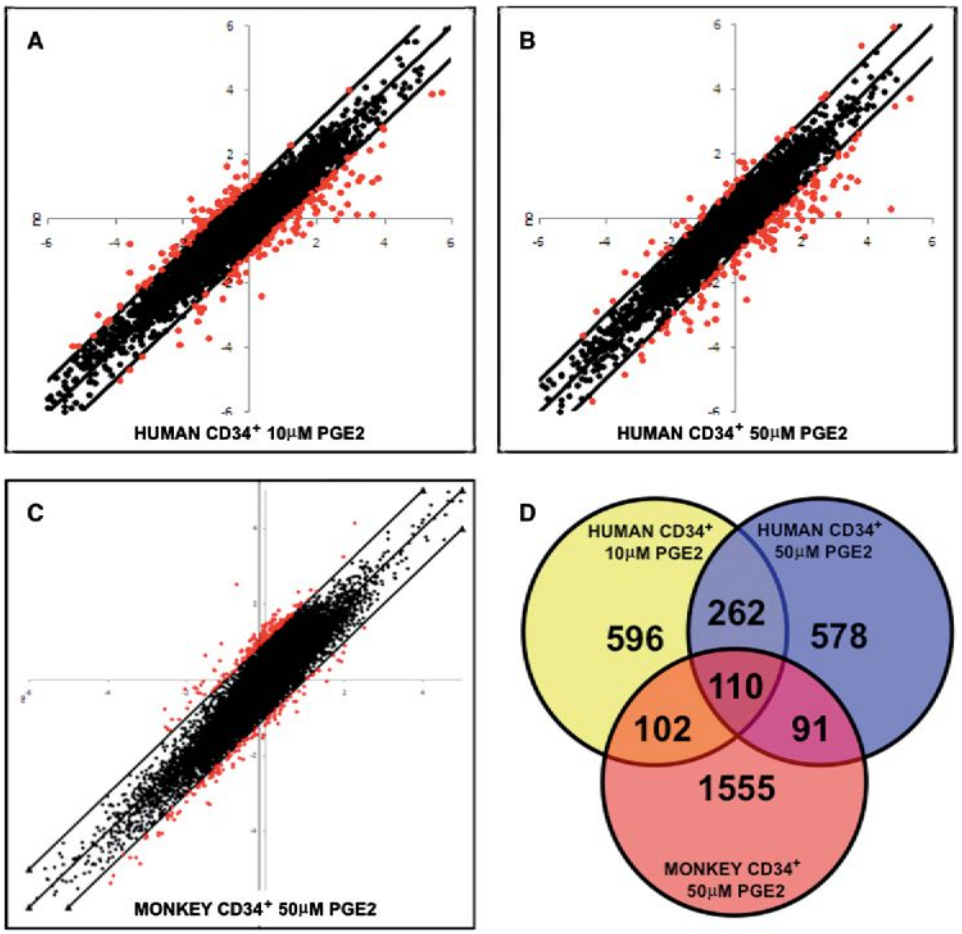

Figure 5. Genome-wide Expression Analysis Reveals Commonly Regulated Genes in Human and Rhesus MPBSCs

(A–C) Scatter plots show genes significantly up- and downregulated in response to dmPGE2 (*x* axis) compared to controls (*y* axis). Genes with >2-fold changes are highlighted in red.

(D) Schematic display of genes regulated in response to dmPGE2 treatment, showing overlap between treatment groups of MPBSCs.

See also Figure S7 and Table S3.

such as *ANGPT1, ATXN1, FOXO1, HIF1A, STAT3*, and *VAV1*. Together these data suggest that rhMPBSC may require a higher level of PGE2 stimulation for optimal HSC-related gene regulation than hMPBSCs, correlating with receptor distribution and transplant results.

PGE2 Regulates Common Signaling Pathways in Human and Rhesus CD34$^+$ MPBSC

To futher delineate the cellular signals mediated by dmPGE2, the microarray data were subjected to ingenuity pathway analysis, which revealed a number of commonly upregulated (24) and downregulated (12) pathways across all treatment groups and in pairwise comparisons (Figures 6A and 6B; Tables S4A and S4B). Strikingly, among the upregulated gene sets, three of the top five are directly influenced by cAMP-mediated signaling cascades (Figure 6C), suggesting high conservation of immediate early responses to PGE2 stimulation across vertebrate species (Goessling et al., 2009); chemokine/cytokine-related pathways were likewise represented by multiple gene families. The significance of the downregulated pathways is less clear, although several gene sets appear to be related to alternative differentiation potential, including that of endothelial cells (Figure 6D). A roughly equal number of pathways were commonly upregulated (17) and downregulated (18) in hMPBSCs treated at varying dmPGE2 concentrations (Tables S5A and S5B). Through ingenuity analysis, we again find that while many pathways are coordinately regulated between the 50 μM human MPBSC and rhesus treatment groups (33 up, 7 down), a number of pathways were conversely common only to the 10 μM PGE2 dose of hMPBSC and 50 μM PGE2 in rhesus macaques (11 up, 8 down) (Tables S6A, S6B, S7A, and S7B), indicating that PGE2-stimulation potential of rhesus CD34$^+$ MPBSCs may be several fold lower than that of human CD34$^+$ cells.

hCB Exposed to dmPGE2 Shows Gene Expression Alterations in Cell Cycle, PGE2 Signaling, and Stem Cell Behavior which Correlate to the MPBSC Microarray Analysis

To validate the gene expression signatures observed in the MPBSC analysis and to show conservation of the potential

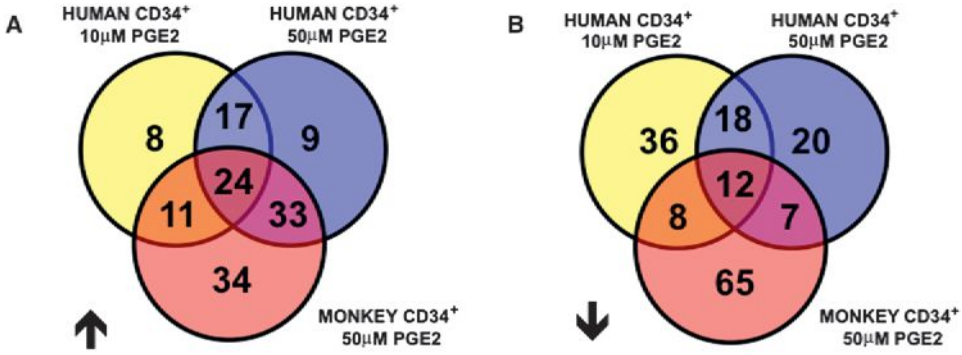

C

Common UPREGULATED	Human 10 μM		Human 50 μM		Monkey 50 μM	
Ingenuity Canonical Pathways	p value	Ratio	p value	Ratio	p value	Ratio
ERK/MAPK Signaling	1.32E-03	0.067	5.13E-05	0.083	8.51E-05	0.109
Protein Kinase A Signaling	1.95E-03	0.056	1.78E-04	0.066	3.72E-05	0.097
Molecular Mechanisms of Cancer	6.03E-03	0.048	2.95E-04	0.059	4.79E-07	0.102
PI3K/AKT Signaling	6.17E-03	0.065	6.76E-04	0.079	4.47E-05	0.122
T Helper Cell Differentiation	1.26E-02	0.083	8.32E-04	0.111	4.47E-02	0.097
Axonal Guidance Signaling	2.82E-02	0.042	1.02E-03	0.054	4.17E-02	0.062
Oncostatin M Signaling	3.24E-04	0.171	2.82E-03	0.143	2.09E-02	0.143
IL-6 Signaling	1.10E-02	0.075	3.72E-03	0.086	2.19E-02	0.097
IGF-1 Signaling	1.45E-02	0.070	5.25E-03	0.080	3.02E-02	0.090
IL-10 Signaling	6.46E-03	0.086	7.76E-03	0.086	1.95E-03	0.129
B Cell Receptor Signaling	1.86E-02	0.058	8.51E-03	0.065	1.15E-03	0.104
p70S6K Signaling	2.14E-03	0.076	8.71E-03	0.069	1.91E-04	0.122
Thrombin Signaling	3.89E-02	0.049	8.91E-03	0.059	2.34E-04	0.103
Acute Phase Response Signaling	2.00E-02	0.056	1.00E-02	0.062	2.88E-02	0.079
Thrombopoietin Signaling	2.88E-03	0.102	1.58E-02	0.085	2.57E-03	0.136
Aryl Hydrocarbon Receptor Signaling	1.32E-02	0.058	1.62E-02	0.058	2.57E-02	0.078
Breast Cancer Regulation by Stathmin1	3.31E-02	0.050	1.78E-02	0.055	1.62E-04	0.106
Gα 12/13 Signaling	4.47E-02	0.056	1.95E-02	0.064	8.91E-03	0.096
PPARα/RXRα Activation	6.17E-03	0.061	2.04E-02	0.056	1.91E-03	0.094
Acute Myeloid Leukemia Signaling	1.38E-03	0.098	2.40E-02	0.073	9.77E-04	0.134
VDR/RXR Activation	2.09E-02	0.075	2.40E-02	0.075	9.77E-04	0.138
Relaxin Signaling	2.40E-02	0.054	2.88E-02	0.054	2.75E-04	0.107
CXCR4 Signaling	2.63E-02	0.054	3.24E-02	0.054	2.19E-03	0.096
Role of NFAT in Cardiac Hypertrophy	3.02E-02	0.048	3.72E-02	0.048	9.12E-04	0.092

D

Common DOWNREGULATED	Human 10 μM		Human 50 μM		Monkey 50 μM	
Ingenuity Canonical Pathways	p value	Ratio	p value	Ratio	p value	Ratio
Colorectal Cancer Metastasis Signaling	4.47E-03	0.05	2.00E-04	0.06	4.68E-03	0.07
Endothelin-1 Signaling	7.08E-03	0.05	7.41E-03	0.05	1.70E-02	0.06
Role of NFAT in Cardiac Hypertrophy	1.35E-03	0.06	1.23E-02	0.05	1.26E-02	0.06
Renin-Angiotensin Signaling	8.13E-04	0.08	1.26E-02	0.06	3.72E-03	0.08
RAR Activation	4.57E-02	0.04	1.91E-02	0.05	3.47E-02	0.06
Glucocorticoid Receptor Signaling	7.76E-03	0.05	1.95E-02	0.04	3.63E-02	0.05
Axonal Guidance Signaling	1.51E-02	0.04	3.24E-02	0.04	1.48E-03	0.06
Reelin Signaling in Neurons	2.09E-03	0.09	3.47E-02	0.06	1.74E-02	0.09
IL-2 Signaling	3.80E-02	0.07	3.89E-02	0.07	3.98E-02	0.09
Dendritic Cell Maturation	5.01E-03	0.05	3.98E-02	0.04	2.75E-02	0.06
Complement System	4.79E-02	0.08	4.79E-02	0.08	3.24E-02	0.11
CREB Signaling in Neurons	1.86E-02	0.05	4.90E-02	0.04	1.62E-02	0.06

Figure 6. Ingenuity Pathway Analysis Reveals Conserved Response Patterns between Human and Rhesus MPBSCs

Microarray data were subjected to ingenuity pathway analysis.

(A and B) Venn diagram illustrations of the overlap of significantly up- and downregulated signaling pathways between human and rhesus macaque MPBSCs.

(C and D) List of significantly up- and downregulated pathways common between human and rhesus dmPGE2-treated MPBSCs; the ratio indicates the fraction of affected genes of the number of total genes included in each pathway.

See also Tables S4–S7.

mechanism of action of dmPGE2 in hCB samples, we examined relative changes in gene expression after 10 μM dmPGE2 treatment at fixed intervals after exposure (1, 3, 6, and 9 hr) by qPCR. To confirm that dmPGE2 was mediating effects on hCB cell proliferation and apoptosis, we examined a panel of 10 cell cycle-related genes (Figure 7A). As previously shown for murine HSCs, expression of the classical WNT-pathway target and proproliferative cell cycle regulator, *CYCLIN D1*, increased after PGE2 treatment; *CYCLIN E1* showed a similar response. Expression of the antiapoptotic genes *BCLXL* and *BCL2* were enhanced by PGE2, while that of the proapoptotic gene *BAX* decreased at 3 and 6 hr. These data suggest that one

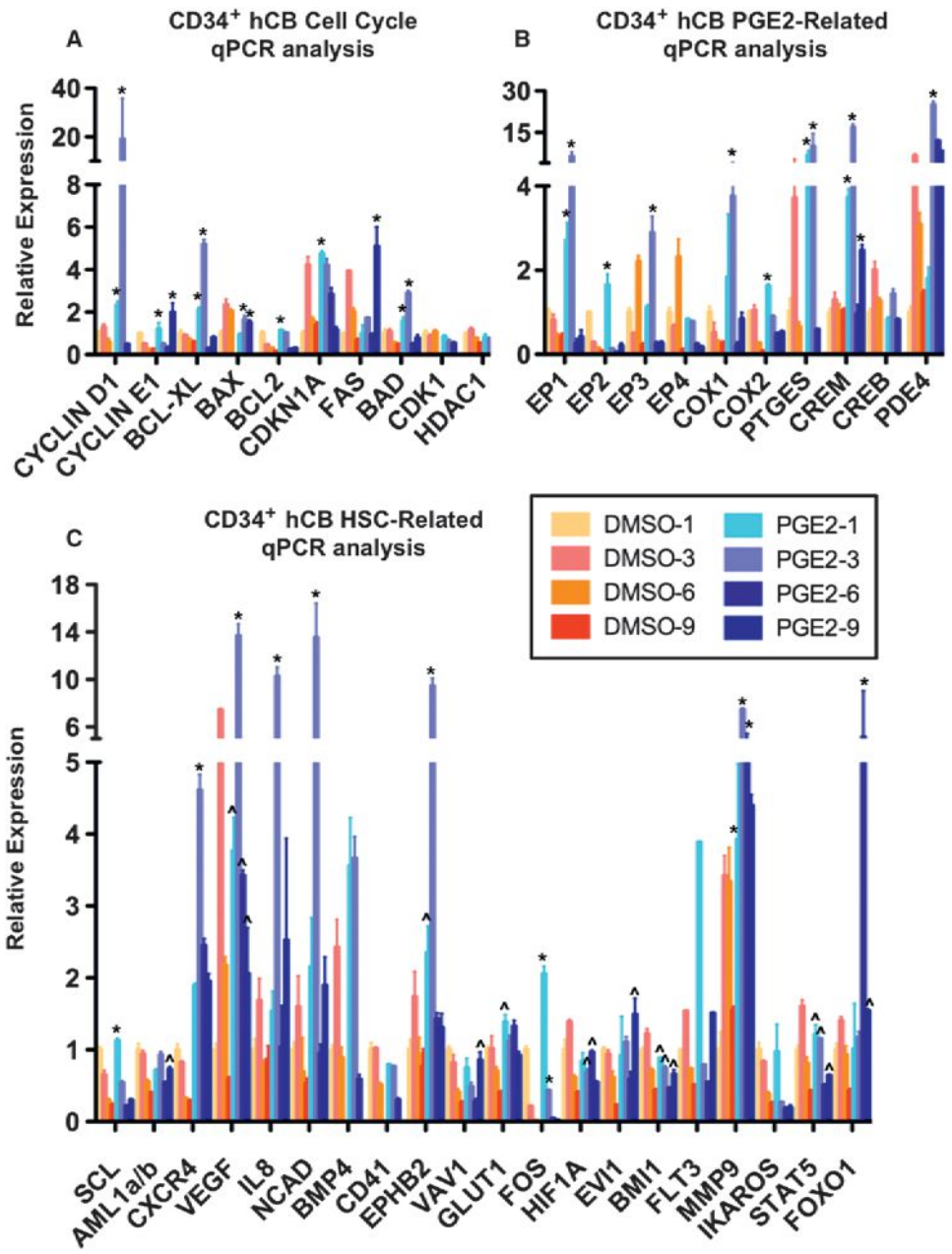

Figure 7. dmPGE2 Affects Expression of Cell Cycle, PGE2-Related, and HSC Genes

CD34+ hCB was incubated with 10 μM dmPGE2 over a range of 1–9 hr; results of qPCR analysis are shown. n = 3–5; ANOVA, *p < 0.001 versus all untreated controls. *p < 0.001 versus control at corresponding time point.

(A) dmPGE2 exposure altered expression of genes related to cell cycle and apoptosis.

(B) dmPGE2 induced expression of PGE2 pathway-related genes.

(C) dmPGE2 affected genes associated with hematopoietic stem cell function.

consequence of dmPGE2 treatment may be to preserve hCB cells in a viable state, capable of homing, engrafting, and proliferating to repopulate the BM niche and reconstitute PB lineages.

We have previously shown that PGE2 not only enhances HSC formation and function but also is required for the normal kinetics of hematopoietic recovery (North et al., 2007). Clinical and murine studies have demonstrated elevated levels of PGE2 after hematopoietic transplantation (Ballinger et al., 2006; Cayeux et al., 1993). Additionally, PGE2 is a well-characterized mediator of inflammatory responses to injury, where we have recently shown it can stimulate wnt activity and regeneration (Goessling et al., 2009). While PGE2 is capable of binding its four cognate receptors with high affinity, to rapidly elicit changes in cAMP-mediated signaling, it has an extremely short serum half-life. Here, after stimulation of CD34+ hCB cells with dmPGE2, we find that several components related to PGE2 production and

signaling are specifically regulated (Figure 7B): dmPGE2 treatment induces expression of prostaglandin synthesis enzymes *COX1* and *2*, as well as the PGE-specific endoperoxidase *PTGES*, which could thereby enable a perpetuation of PGE2-mediated signaling. Conversely, the PGE2 receptors *EP1* and *EP3*, generally considered to be negative response elements, were also upregulated in response to dmPGE2. These seemingly opposing responses could serve as a means to "fine tune" the extent and targets of PGE2-mediated signaling; similar counter-regulatory responses have been observed for pathways that partner with PGE2, such as WNT (Dichtel-Danjoy et al., 2009). In support of this concept, correlative responses were also observed for pathway components downstream of ligand binding: the *cAMP response element* (*CREM*), as well as *phosphodiesterase 4D* (*PDE4D*), which regulates the breakdown of cAMP, were 13- and 3.8-fold upregulated, respectively.

To assess which factors critical to HSC formation and function in a vascular niche, such as the umbilical cord, may be influenced by dmPGE2 to positively impact $CD34^+$ hCB cells, we conducted qPCR expression analysis of matched samples after 10 μM dmPGE2 treatment for a panel of 20 HSC-related genes identified in the literature and/or in the microarray analysis. *CXCR4* expression was highly responsive to dmPGE2 exposure (Figure 7C), consistent with previous reports (Hoggatt et al., 2009). Vascular endothelial growth factor (VEGF) is a potent stimulator of endothelial and HSC proliferation, which regulates the maturation of the vascular endothelial niche, thereby enabling HSC induction from hemogenic endothelium (Gerber et al., 2002); *VEGF* expression was robustly increased, 3.7-fold, by dmPGE2. IL8 (CXCL8) is one of the inflammatory cytokines involved in proliferation and migration of endothelial progenitors and HSCs (Laterveer et al., 1995); *IL8* expression increased up to 6-fold in response to dmPGE2. N-cadherin, which has a controversial role in adult HSC function (Li and Zon, 2010) but is expressed in the arterial HSC niche, was elevated up to 8.5-fold after dmPGE2 treatment. Expression of *Bone-Morphogenic Protein-4* (*BMP4*), required to demarcate and specify the hemogenic endothelial population in the arterial niche (Durand et al., 2007), and that of *Ephrin B2* (*EPHB2*), required for arterial niche identify (Lawson et al., 2001), were 3.5-fold and >9-fold upregulated, respectively. Expression of traditional markers of immature HSCs such as *RUNX1 (AML1)* and *SCL* decreased over time in untreated cells, consistent with the observation that HSCs progressively dedifferentiate in culture; dmPGE2 limited the loss of *RUNX1* expression and increased the expression of regulators of quiescence such as *FOXO1* (Tothova et al., 2007), suggesting that it may enable the hCB HSCs to maintain their identity or bias HSCs toward self-renewal.

DISCUSSION

The data presented here suggest that ex vivo stimulation of human HSCs with dmPGE2 prior to transplantation may positively impact gene expression, engraftment capacity, and HSC function in the clinical setting. While advantageous in both its availability and immunologic flexibility, hCB contains significantly fewer HSCs than BM or mobilized PB. The development of a rapid and safe means to enhance hCB HSC number and/or function has been an area of significant research. The data presented here and previously (Goessling et al., 2009; Hoggatt et al., 2009; North et al., 2007) suggest that short ex vivo dmPGE2 treatment can enhance several factors that should improve human HSC function and multilineage hematopoietic recovery including homing, apoptosis, and proliferation. Interestingly, gene programs indicative of HSC production from a vascular niche (*VEGF, BMP4*) are also significantly upregulated or maintained (*RUNX1*) in response to dmPGE2 stimulation of hCB. As the CD34 antigen is expressed on both HSCs and hemogenic endothelium, these data could imply that a portion of the effect of PGE2 in hCB is mediated by endothelial cells, which have recently been shown to provide signals that retain HSCs in an undifferentiated state (Butler et al., 2010); dmPGE2 exposure could alternatively promote the "budding" or transition of immature HSCs from hemogenic endothelial precursors, similar to the original HSC screen in zebrafish (North et al., 2007). More work is needed to examine these intriguing alternatives; however, the maintenance of a significant number of PGE2-regulated gene programs across species suggests that dmPGE2 may elicit beneficial regulatory responses over multiple hematopoietic contexts.

As recently discussed (McDermott et al., 2010), despite years of intensive investigation, the xenotransplantation model remains an approximation of human engraftment potential. As part of the preclinical evaluation of the safety of dmPGE2 for ex vivo treatment of hCB, we made several selective choices in the treatment scheme to optimize the potential to elucidate any effects—positive or negative—of dmPGE2 on the hCB sample. In particular, we chose to treat and transplant whole cord blood samples, in addition to purified $CD34^+$ cells; this was done to mimic current clinical protocols, which use whole hCB units, and to elucidate any unanticipated or unwanted effects on non-HSC cell types contained in the cord. We observed no significant differences in negative outcomes between recipients of dmPGE2-treated versus control-treated cords, with or without CD34 enrichment. Despite the positive effect of dmPGE2 on both in vitro and in vivo models of hCB HSC function, these assays still cannot directly account for the variety of factors that influence the ultimate ability of a given hCB sample to engraft. The immunological consequences of HSC transplantation alone, notwithstanding the complexities added by the use of two independent immune systems in the setting of double cord transplantation, are still difficult to model; the standard isogenic murine competitive transplantation schemes do not account for immunological reactions, while cross-species transplantation introduces rejection and engraftment scenarios that do not exist in the clinical setting. Meaningful xenotransplantation of two unmatched hCB units to fully illustrate advantageous treatment protocols is not possible at this time because no specific criteria exist to reliably predict engraftment success of each individual cord unit prior to use in transplant assays.

The competitive autologous transplantation protocol in the nonhuman primate model enables the comparison of dual-treated, retrovirally marked HSC populations in vivo without the confounding influences of immunorejection. Although these experiments are resource intensive, prohibiting in vivo dose-finding studies to demonstrate a statistically significant benefit for dmPGE2, they allow for longitudinal evaluation of individual primates to assess durability, functionality, and overall safety

of the treated HSC samples. Here, we show that cells treated with dmPGE2 prior to reinfusion are capable of contributing to stable multilineage repopulation at time points more than 1 year postinjection, with an absence of any lineage skewing or compromise of HSC self-renewal potential. Long-term nonhuman primate transplantation experiments were initiated with 10 μM dmPGE2 based on available safety and engraftment data from murine (North et al., 2007) and xenotransplantation models. While this treatment was not able to elicit a significant enhancement in repopulation potential compared to matched controls in the majority of rhesus macaques subjected to the protocol utilized, the result most probably reflects suboptimal compound dosing rather than the inability of dmPGE2 to elicit functional responses in HSCs. Receptor distribution analysis obtained while the primate studies were ongoing revealed a significant difference in EP receptor expression between human and nonhuman primate $CD34^+$ HSCs. Further, while 10 μM dmPGE2 could elicit changes in cAMP activity, higher doses caused more dramatic effects, and statistically meaningful differences in gene expression were observed only at 50 μM dmPGE2. We anticipate that use of 50 μM dmPGE2 in the transplant protocol may cause a more discernable difference in repopulation potential in the autologous transplantation assay, but strong conservation of genetic regulation across species and clear evidence of safety and efficacious results in alternate vertebrate models preclude the justification of repeating these studies in the nonhuman primate model to confirm these expectations.

Through our investigations, we identified EP4 as marker highly enriched in the hCB $CD34^+$ and $CD133^+$ population. Additional studies are needed to define whether EP4 could be used alone or in combination to further refine the isolation of cells with in vivo hCB HSC function. In the setting of clinical hematopoietic transplantation, the entire hCB sample will be treated with dmPGE2 ex vivo prior to transplant; the selective distribution of EP4 indicates that despite the presence of multiple cell types in the whole hCB sample, the main effect of treatment is probably focused on the stem and progenitor cell populations. The fact that similar results were obtained for whole hCB and $CD34^+$ cell xenotransplantation into NOD/SCID mice further supports a targeted effect on nonlineage-specified cell types. The selective distribution of the EP4 receptor to the $CD34^+$ population in hCB samples will hopefully serve to minimize any potential negative side effects while mediating the full benefits of dmPGE2 stimulation on hematopoietic recovery in the clinical setting.

Many signaling pathways have been identified that regulate aspects of both HSC production and adult homeostasis, but it is unclear whether HSCs from a developmental vascular niche, such as $CD34^+$ hCB, will respond predictably to stimulation from BM-derived factors in the clinic. No prospective study to date has examined whether the simple process of stem cell isolation prior to in vitro culture and transplantation may deprive HSCs of factors normally produced by supporting cell types that influence their long-term function and maintenance in the patient. Similarly, a theoretical risk of any in vivo treatment approach is that it may affect not only the transplanted cells but also cells of the host, particularly surviving cancer cells, which could be more receptive to stimulation. One advantage of the brief ex vivo whole hCB unit incubation method is that no long-term manipulation or cell isolation is required, and there is limited potential of in vivo stimulation of persisting cancer cells in the transplant recipient. Based on the data presented herein, the FDA approved an investigational new drug (IND) application for dmPGE2 in April 2009; this represents the first compound discovered in zebrafish to be used in patients. An independently conducted phase 1 clinical trial evaluating dmPGE2 in hCB transplantation is in progress (http://clinicaltrials.gov/ct2/show/NCT00890500). Further investigation will be needed to refine the ex vivo treatment approach for optimal clinical use in multicenter trials; furthermore, combinatorial strategies with other bourgeoning therapies may prove to elicit the largest benefit for the transplant patient while minimizing complications.

EXPERIMENTAL PROCEDURES

16,16-Dimethyl Prostaglandin E2

dmPGE2, purchased from Cayman Chemicals, was resuspended in DMSO and diluted to working concentrations of 1 μM to 1 mM as indicated; ex vivo dmPGE2 exposure duration was as indicated, followed by substrate removal and washing prior to analysis or use.

hCB Samples

Xenotransplant studies utilized fresh whole hCB samples discarded from clinical use (due to low cell number), obtained through the Center for Human Cell Therapy (Dana-Farber Cancer Institute, Boston, MA) and the Carolinas Cord Blood Bank (Duke University Medical Center, Durham, NC). After red cell depletion (50%–60%) and FACS-based viability assessment, samples were divided for parallel treatment. In vitro viability, proliferation, cell culture, and gene expression analyses utilized frozen purified ($CD34^+$, $CD133^+$, MNC, or HUVEC) deidentified hCB samples from pooled donors (Stem Cell Technologies). Cells were prepared to manufacturer's directions, assessed for viability, and split for use.

Apoptosis and Proliferation Analysis

5 million frozen $CD34^+$ hCB cells were thawed, split, and treated with 1 μM dmPGE2 or DMSO in 2% FCS in IMDM for 3, 6, or 9 hr at 37°C. Apoptosis was assessed by Annexin V-FITC (R&D Systems) and 7-AAD (BD PharMingen) FACS. Proliferating cells were identified with the Click-iT EdU Flow Cytometry Assay Kit (Invitrogen).

Colony Forming Units Culture

$CD34^+$ CB cells were treated with DMSO or 1 μM dmPGE2 for 15 min, 30 min, 1 hr, 3 hr, or 6 hr in 2% FCS-supplemented IMDM at 37°C. Cell suspensions were mixed with MethoCult H4434 (Stem Cell Technologies), plated in triplicate at limiting dilutions (2000, 800, or 320 cells per 33 mm plate/1.5 ml H4434), and counted on day 13.

NOD/SCID Xenotransplantation

Individual whole or CD34-enriched hCB samples were split and exposed to dmPGE2 (10 μM) or DMSO vehicle control ex vivo for 1 hr in dextran/albumin. After sublethal irradiation (6.5Gy), 20 million whole or 2500 $CD34^+$ hCB cells were introduced by retroorbital injection into NOD/SCID (Charles River) recipients, maintained and utilized according to approved IACUC protocols at Children's Hospital. PB was obtained at 1 and 3 months, and BM was isolated at >3 months posttransplant. After red cell lysis, hCD45 (Becton-Dickenson) expression was examined by FACS; 1% PB and 0.2% BM hCB chimerism were utilized to indentify positively engrafted recipients.

Quantitative PCR

$CD34^+$ CB cells treated with DMSO or 1 μM dmPGE2 for 1 hr in IMDM with 2% FCS at 37°C were washed and incubated for a fixed time (+2, 5, or 8 hr) prior to RNA extraction (Trizol, Invitrogen). cDNA was synthesized with the SuperScript III first-strand synthesis kit (Invitrogen). Quantitative RT-PCR (58°C annealing) was performed in triplicate with SybrGreen (Invitrogen) on the iQ5 Multicolor RTPCR Detection System (BioRad); primer sequences are listed

in Supplemental Experimental Procedures. Data were normalized to β-actin and shown relative to DMSO at 1 hr postexposure.

Statistical Analysis

SigmaStat software was used for statistical analysis. Differences between treatments for all in vitro and qPCR analyses were calculated by t test and one-way ANOVA. hCB engraftment in NOD/SCID mice was analyzed by Fisher's exact test (one-tailed).

Nonhuman Primate Cell Collection

Rhesus macaques (*Macaca mulata*) were housed and handled in accordance with the guidelines set by the Committee on Care and Use of Laboratory Animals of the Institute of Laboratory Animal Resources, National Research Council (DHHS publication No. NIH 85-23). PB HSCs were mobilized with granulocyte colony-stimulating factor (G-CSF) and stem cell factor (gift of Amgen), harvested by leukapheresis, and enriched for $CD34^+$ cells as previously described (Donahue et al., 2005).

Human $CD34^+$ Cell Collection

hMPBSCs were collected after G-CSF mobilization and enriched by $CD34^+$ immunoselection according to IRB-approved protocols (02-H-0160, 96-H-0049).

Microarray Analysis

Human and nonhuman primate MPBSCS were incubated with either 10 or 50 μM dmPGE2 in X-Vivo media (Lonza) for 1 hr. Cells were collected at 6, 12, and 24 hr postincubation, and total RNA (Trizol extraction) was cohybridized to custom-made 17.5K cDNA (UniGene cluster) microarrays. Hierarchical cluster analysis and TreeView software were used for visualization. Gene clustering analysis was performed with Ingenuity Pathway Analysis software.

Autologous Competitive Transplant Study

Rhesus macaques (n = 5) were mobilized daily with 10 μg/kg G-CSF and 200 μg/kg stem cell factor (SCF) for 5 days. On day 5, $CD34^+$ enriched MPBSC were isolated from leukapheresed blood as described (Donahue et al., 2005). $CD34^+$ cells from each donor were split and transduced with a chimeric HIV vector to express EGFP or EYFP (Uchida et al., 2009). Rhesus $CD34^+$ cells were treated with 10 μM dmPGE2 for 1 hr at 37°C either prior to or after viral transduction (Supplemental Experimental Procedures). Cells were reinfused on day 3 after leukapheresis, after 2 consecutive days of 500 Gy total body irradiation.

ACCESSION NUMBERS

The complete list of genes in the Hs-CCDTV-17.5k-1px printing are available in the GEO database (http://nciarray.nci.nih.gov/galfiles) under the accession number GSE27126.

SUPPLEMENTAL INFORMATION

Supplemental Information includes Supplemental Experimental Procedures, seven figures, and seven tables and can be found with this article online at doi:10.1016/j.stem.2011.02.003.

ACKNOWLEDGMENTS

The HMS researchers thank J. Trowbridge, C. Walkley, G.Q. Daley J. Ritz, L. Silberstein, G. Kao, J. Antin, R. Soiffer, K. Ballen, C. Cutler, and the members of the Center for Human Cell Therapy at Harvard Medical School, Dana-Farber Cancer Institute for helpful discussions and guidance on the clinical application of dmPGE2 and the FDA application process. We are grateful to the Carolinas Cord Blood Bank for providing us with discarded cord blood units. The NIH researchers thank K. Keyvanfar for cell-sorting assistance, Y. Tian for assisting with the processing of the microarray data, and the veterinary and animal care staff at 5 Research Court and Poolesville for maintaining the nonhuman primates used in this study. This research was supported by the Harvard Stem Cell Institute (W.G., L.I.Z., T.E.N.), NIH NIDDK (W.G., L.I.Z., T.E.N.), Howard Hughes Medical Institute (L.I.Z.), the Intramural Research Program of the National Institutes of Health, NHLBI, and/or NIDDK (R.S.A., N.U., M.E.M., A.C.B., J.F.T., R.E.D.), and the Department of Transfusion Medicine at the NIH Clinical Center (P.J., D.S.). T.E.N. and W.G. receive patent royalties and consulting fees from FATE Therapeutics; L.I.Z. is a scientific founder and stockholder of and receives patent royalties from FATE Therapeutics, which is currently testing the use of prostaglandin E2 to enhance the efficacy of hCB transplants in an independently conducted phase I clinical trial.

Received: June 8, 2010
Revised: November 18, 2010
Accepted: January 28, 2011
Published: April 7, 2011

REFERENCES

Adams, G.B., Martin, R.P., Alley, I.R., Chabner, K.T., Cohen, K.S., Calvi, L.M., Kronenberg, H.M., and Scadden, D.T. (2007). Therapeutic targeting of a stem cell niche. Nat. Biotechnol. *25*, 238–243.

Ballen, K.K., Hicks, J., Dharan, B., Ambruso, D., Anderson, K., Bianco, C., Bemiller, L., Dickey, W., Lottenberg, R., O'Neill, M., et al. (2002). Racial and ethnic composition of volunteer cord blood donors: comparison with volunteer unrelated marrow donors. Transfusion *42*, 1279–1284.

Ballen, K.K., Shpall, E.J., Avigan, D., Yeap, B.Y., Fisher, D.C., McDermott, K., Dey, B.R., Attar, E., McAfee, S., Konopleva, M., et al. (2007a). Phase I trial of parathyroid hormone to facilitate stem cell mobilization. Biol. Blood Marrow Transplant. *13*, 838–843.

Ballen, K.K., Spitzer, T.R., Yeap, B.Y., McAfee, S., Dey, B.R., Attar, E., Haspel, R., Kao, G., Liney, D., Alyea, E., et al. (2007b). Double unrelated reduced-intensity umbilical cord blood transplantation in adults. Biol. Blood Marrow Transplant. *13*, 82–89.

Ballinger, M.N., Aronoff, D.M., McMillan, T.R., Cooke, K.R., Olkiewicz, K., Toews, G.B., Peters-Golden, M., and Moore, B.B. (2006). Critical role of prostaglandin E2 overproduction in impaired pulmonary host response following bone marrow transplantation. J. Immunol. *177*, 5499–5508.

Boitano, A.E., Wang, J., Romeo, R., Bouchez, L.C., Parker, A.E., Sutton, S.E., Walker, J.R., Flaveny, C.A., Perdew, G.H., Denison, M.S., et al. (2010). Aryl hydrocarbon receptor antagonists promote the expansion of human hematopoietic stem cells. Science *329*, 1345–1348.

Broxmeyer, H.E., Douglas, G.W., Hangoc, G., Cooper, S., Bard, J., English, D., Arny, M., Thomas, L., and Boyse, E.A. (1989). Human umbilical cord blood as a potential source of transplantable hematopoietic stem/progenitor cells. Proc. Natl. Acad. Sci. USA *86*, 3828–3832.

Broxmeyer, H.E., Cooper, S., Hass, D.M., Hathaway, J.K., Stehman, F.B., and Hangoc, G. (2009). Experimental basis of cord blood transplantation. Bone Marrow Transplant. *44*, 627–633.

Butler, J.M., Nolan, D.J., Vertes, E.L., Varnum-Finney, B., Kobayashi, H., Hooper, A.T., Seandel, M., Shido, K., White, I.A., Kobayashi, M., et al. (2010). Endothelial cells are essential for the self-renewal and repopulation of Notch-dependent hematopoietic stem cells. Cell Stem Cell *6*, 251–264.

Campbell, T.B., Hangoc, G., Liu, Y., Pollok, K., and Broxmeyer, H.E. (2007). Inhibition of CD26 in human cord blood CD34+ cells enhances their engraftment of nonobese diabetic/severe combined immunodeficiency mice. Stem Cells Dev. *16*, 347–354.

Cayeux, S.J., Beverley, P.C., Schulz, R., and Dörken, B. (1993). Elevated plasma prostaglandin E2 levels found in 14 patients undergoing autologous bone marrow or stem cell transplantation. Bone Marrow Transplant. *12*, 603–608.

Delaney, C., Heimfeld, S., Brashem-Stein, C., Voorhies, H., Manger, R.L., and Bernstein, I.D. (2010). Notch-mediated expansion of human cord blood progenitor cells capable of rapid myeloid reconstitution. Nat. Med. *16*, 232–236.

Dichtel-Danjoy, M.L., Caldeira, J., and Casares, F. (2009). SoxF is part of a novel negative-feedback loop in the wingless pathway that controls proliferation in the *Drosophila* wing disc. Development *136*, 761–769.

Donahue, R.E., Kuramoto, K., and Dunbar, C.E. (2005). Large animal models for stem and progenitor cell analysis. Curr. Protoc. Immunol., Chapter 22, Unit 22A.1.

Durand, C., Robin, C., Bollerot, K., Baron, M.H., Ottersbach, K., and Dzierzak, E. (2007). Embryonic stromal clones reveal developmental regulators of definitive hematopoietic stem cells. Proc. Natl. Acad. Sci. USA *104*, 20838–20843.

Frisch, B.J., Porter, R.L., Gigliotti, B.J., Olm-Shipman, A.J., Weber, J.M., O'Keefe, R.J., Jordan, C.T., and Calvi, L.M. (2009). In vivo prostaglandin E2 treatment alters the bone marrow microenvironment and preferentially expands short-term hematopoietic stem cells. Blood *114*, 4054–4063.

Gerber, H.P., Malik, A.K., Solar, G.P., Sherman, D., Liang, X.H., Meng, G., Hong, K., Marsters, J.C., and Ferrara, N. (2002). VEGF regulates haematopoietic stem cell survival by an internal autocrine loop mechanism. Nature *417*, 954–958.

Goessling, W., North, T.E., Loewer, S., Lord, A.M., Lee, S., Stoick-Cooper, C.L., Weidinger, G., Puder, M., Daley, G.Q., Moon, R.T., and Zon, L.I. (2009). Genetic interaction of PGE2 and Wnt signaling regulates developmental specification of stem cells and regeneration. Cell *136*, 1136–1147.

Hoggatt, J., Singh, P., Sampath, J., and Pelus, L.M. (2009). Prostaglandin E2 enhances hematopoietic stem cell homing, survival, and proliferation. Blood *113*, 5444–5455.

Laterveer, L., Lindley, I.J., Hamilton, M.S., Willemze, R., and Fibbe, W.E. (1995). Interleukin-8 induces rapid mobilization of hematopoietic stem cells with radioprotective capacity and long-term myelolymphoid repopulating ability. Blood *85*, 2269–2275.

Laver, J.H., Hulsey, T.C., Jones, J.P., Gautreaux, M., Barredo, J.C., and Abboud, M.R. (2001). Assessment of barriers to bone marrow donation by unrelated African-American potential donors. Biol. Blood Marrow Transplant. *7*, 45–48.

Lawson, N.D., Scheer, N., Pham, V.N., Kim, C.H., Chitnis, A.B., Campos-Ortega, J.A., and Weinstein, B.M. (2001). Notch signaling is required for arterial-venous differentiation during embryonic vascular development. Development *128*, 3675–3683.

Li, P., and Zon, L.I. (2010). Resolving the controversy about N-cadherin and hematopoietic stem cells. Cell Stem Cell *6*, 199–202.

McDermott, S.P., Eppert, K., Lechman, E.R., Doedens, M., and Dick, J.E. (2010). Comparison of human cord blood engraftment between immunocompromised mouse strains. Blood *116*, 193–200.

North, T.E., Goessling, W., Walkley, C.R., Lengerke, C., Kopani, K.R., Lord, A.M., Weber, G.J., Bowman, T.V., Jang, I.H., Grosser, T., et al. (2007). Prostaglandin E2 regulates vertebrate haematopoietic stem cell homeostasis. Nature *447*, 1007–1011.

Regan, J.W., Bailey, T.J., Pepperl, D.J., Pierce, K.L., Bogardus, A.M., Donello, J.E., Fairbairn, C.E., Kedzie, K.M., Woodward, D.F., and Gil, D.W. (1994). Cloning of a novel human prostaglandin receptor with characteristics of the pharmacologically defined EP2 subtype. Mol. Pharmacol. *46*, 213–220.

Rocha, V., and Broxmeyer, H.E. (2010). New approaches for improving engraftment after cord blood transplantation. Biol. Blood Marrow Transplant. *16* (1, Suppl), S126–S132.

Tothova, Z., Kollipara, R., Huntly, B.J., Lee, B.H., Castrillon, D.H., Cullen, D.E., McDowell, E.P., Lazo-Kallanian, S., Williams, I.R., Sears, C., et al. (2007). FoxOs are critical mediators of hematopoietic stem cell resistance to physiologic oxidative stress. Cell *128*, 325–339.

Trobridge, G.D., and Kiem, H.P. (2010). Large animal models of hematopoietic stem cell gene therapy. Gene Ther. *17*, 939–948.

Trowbridge, J.J., Xenocostas, A., Moon, R.T., and Bhatia, M. (2006). Glycogen synthase kinase-3 is an in vivo regulator of hematopoietic stem cell repopulation. Nat. Med. *12*, 89–98.

Uchida, N., Washington, K.N., Hayakawa, J., Hsieh, M.M., Bonifacino, A.C., Krouse, A.E., Metzger, M.E., Donahue, R.E., and Tisdale, J.F. (2009). Development of a human immunodeficiency virus type 1-based lentiviral vector that allows efficient transduction of both human and rhesus blood cells. J. Virol. *83*, 9854–9862.

Zhang, C.C., Kaba, M., Iizuka, S., Huynh, H., and Lodish, H.F. (2008). Angiopoietin-like 5 and IGFBP2 stimulate ex vivo expansion of human cord blood hematopoietic stem cells as assayed by NOD/SCID transplantation. Blood *111*, 3415–3423.

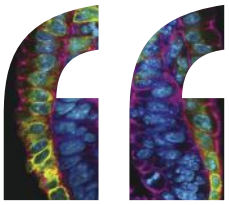

We are tough but fair.

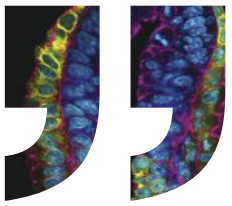

Whether your paper is accepted or rejected, we'll make sure that the feedback you get is appropriate, balanced and respectful.

When you choose Cell Press you get the attention you deserve.

For more information visit: www.cell.com/values

Your **work** is our **life**

Cell PRESS

Cell Stem Cell
Clinical Progress

Rapid Expansion of Human Hematopoietic Stem Cells by Automated Control of Inhibitory Feedback Signaling

Elizabeth Csaszar,[1,2] Daniel C. Kirouac,[1,7] Mei Yu,[1] WeiJia Wang,[1] Wenlian Qiao,[1] Michael P. Cooke,[4] Anthony E. Boitano,[4] Caryn Ito,[1,8] and Peter W. Zandstra[1,2,3,5,6,*]
[1]Institute for Biomaterials and Biomedical Engineering
[2]Department of Chemical Engineering and Applied Chemistry
[3]Terrence Donnelly Centre for Cellular and Biomolecular Research
University of Toronto, Toronto, ON M5S 3E1, Canada
[4]Genomics Institute of the Novartis Research Foundation, 10675 John J. Hopkins Drive, San Diego, CA 92121, USA
[5]Heart and Stroke/Richard Lewar Centre of Excellence, University of Toronto, Toronto, ON M5G 1L7, Canada
[6]McEwen Centre for Regenerative Medicine, University Health Network, Toronto Medical Discovery Tower, Toronto, ON M5G 1L7, Canada
[7]Present address: Merrimack Pharmaceuticals, Cambridge, MA 02139, USA
[8]Present address: Ottawa Hospital Research Institute, Ottawa, ON K1Y 4E9, Canada
*Correspondence: peter.zandstra@utoronto.ca
DOI 10.1016/j.stem.2012.01.003

SUMMARY

Clinical hematopoietic transplantation outcomes are strongly correlated with the numbers of cells infused. Anticipated novel therapeutic implementations of hematopoietic stem cells (HSCs) and their derivatives further increase interest in strategies to expand HSCs ex vivo. A fundamental limitation in all HSC-driven culture systems is the rapid generation of differentiating cells and their secreted inhibitory feedback signals. Herein we describe an integrated computational and experimental strategy that enables a tunable reduction in the global levels and impact of paracrine signaling factors in an automated closed-system process by employing a controlled fed-batch media dilution approach. Application of this system to human cord blood cells yielded a rapid (12-day) 11-fold increase of HSCs with self-renewing, multilineage repopulating ability. These results highlight the marked improvements that control of feedback signaling can offer primary stem cell culture and demonstrate a clinically relevant rapid and relatively low culture volume strategy for ex vivo HSC expansion.

INTRODUCTION

Emerging data suggest that robustness and responsiveness in hematopoiesis is a property of the system, not an individual cell. The hematopoietic system is able to dynamically maintain appropriate proportions of cells of all hematopoietic lineages throughout the lifetime of the individual, both during homeostasis and in response to regenerative demand. This regulation depends on intercellular (between cell) communication networks, resulting from both local and systemic factor secretion (Kirouac et al., 2010). Hematopoietic stem cells (HSCs) must respond to and integrate cues from the microenvironment to ensure sustained production of all hematopoietic lineages (Rizo et al., 2006). As such, self-renewal versus differentiation decisions of HSCs critically depend on feedback-mediated paracrine factors and the associated signaling networks, both in vivo and in vitro.

Several decades of successful bone marrow transplantations have demonstrated the therapeutic importance of HSCs. The use of noninvasively accessible umbilical cord blood (UCB)-derived HSCs provides many advantages over bone marrow, including enhanced long-term immune recovery and decreased graft versus host disease (Gluckman, 2009; Wagner and Gluckman, 2010). However, because clinical studies have indicated that the most important factor for patient survival after UCB transplantation is infusing a cell dose above a minimum threshold of 3×10^7 cells/kg (Gluckman, 2009), low cell numbers in single UCB units have limited the suitability of UCB transplantation for adult patients. Methods to robustly increase the number of cells that give a rapid and sustained blood count recovery would enable the use of UCB in all patients (Hofmeister et al., 2007).

Strategies to expand HSC numbers in vitro have focused on identifying molecules that specifically target the stem cell population. Recent data demonstrating that there are multiple subpopulations of HSCs and that these cells are molecularly closely related (Benveniste et al., 2010; Dykstra et al., 2007) suggest that the opportunity of finding molecules that uniquely expand the long-term HSC pool (Antonchuk et al., 2002; Boitano et al., 2010; Delaney et al., 2010; Durand and Zon, 2010; Zhang et al., 2008) without impacting the distribution and growth of their more restricted progeny is challenging, especially after extended periods of time in culture. Herein we propose a fundamentally different and complementary approach, examining the impact of feedback signaling control on HSC output.

Feedback control is complicated by the fact that the hematopoietic system is regulated by a complex hierarchy of cellular and molecular networks. We have previously performed cell-cell

signaling network analysis to identify and experimentally validate the mode of action of endogenously produced HSC-inhibitory factors generated during in vitro UCB culture (Kirouac et al., 2010). Recognition that large numbers of these factors are produced in a time-dependent manner makes the addition of binding and signaling inhibitors challenging. We sought to identify a strategy to globally control feedback regulation. We performed computational simulations of in vitro hematopoiesis and iteratively predicted and evaluated candidate strategies for the reduction of endogenously produced negative regulators. In silico optimization resulted in the identification and development of a ''fed-batch'' culture strategy for HSC growth enhancement. By linking dynamic cell growth and endogenous factor secretion to a tunable media dilution algorithm, we experimentally confirmed predictions of significant enhancements in stem and progenitor growth, including an 80-fold increase in $CD34^+$ cells and an 11-fold increase in NOD.Cg-*Prkdc*^{scid} *Il2rg*^{tm1Wjl}/SzJ (NSG) repopulating cells (detected at limiting dilution after 16 weeks) within a 12-day culture period. Furthermore, this platform complements known HSC-enhancing factors and has provided insight into their mode of action. The integration of our strategy into an automated and closed-system bioreactor has produced a clinically relevant system for HSC expansion.

RESULTS

In Silico Design of a "Fed-Batch" Media Dilution Strategy

Hematopoietic culture systems generate a large number of endogenously produced soluble factors as a result of the rapid production of mature blood cells (Kirouac et al., 2010; Majka et al., 2001; Sautois et al., 1997). In order to investigate the impact of these secreted ligands, we first measured a sampling of the secreted factor profile under our previously optimized in vitro expansion conditions (Madlambayan et al., 2005) and found the rapid accumulation of many physiologically relevant ligands and large fluctuations resulting from periodic media exchanges (Figure 1A). Many of these factors have been reported to have inhibitory effects on human hematopoietic stem and progenitor cell expansion (Bonnet et al., 1995; Broxmeyer et al., 1995; Broxmeyer and Kim, 1999; Cashman et al., 1998; Fortunel et al., 2000; Zhang et al., 1995), and our previous studies have validated that several factors which are present at high levels in the culture system have a significant inhibitory effect on hematopoietic progenitor expansion, including TGF-β, MCP-1 (CCL2), MIP-1α (CCL3), MIP-1β (CCL4), and IP-10 (CXCL10) (Kirouac et al., 2010).

The large number and nonlinear nature of the secreted factor profiles limit the likely success of using molecularly targeted approaches to reduce the inhibitory impact of these factors and, instead, necessitates a global and unbiased strategy for feedback regulation. In order to identify and optimize an appropriate strategy, we performed computational simulations of cell population dynamics to investigate and predict the effect of candidate culture manipulations. Our computational approach (Kirouac et al., 2009) incorporated the effect of feedback signaling from differentiated cells on stem and progenitor cell expansion. This feedback is coded through different classes of paracrine signaling loops, as depicted in Figure 1B.

As a first step, we explored in silico strategies of regulating the effective concentration of the different classes (SF1–SF4) of secreted ligands. Under baseline conditions, with a full media exchange every 4 days, simulations depict a predominant accumulation of inhibitory factors (SF1 and SF2) (Figure 1C). As such, a net increase in stem and progenitor proliferation was predicted to result from minimizing the entire set of endogenously produced ligands. Rationalizing that the frequency of conditioned media removal would be an important parameter (Madlambayan et al., 2005), we first compared the effects of frequent full or partial media exchanges with our control culture process. The model predicted that a full media exchange every day (Figure 1D) or a half media exchange every 12 hr (Figure 1E) would outperform less frequent exchanges, emphasizing the importance of strong and frequent secreted factor regulation.

To limit periodic fluctuations and intermittent exposure to high concentrations of secreted ligands and to attain a continuous and tunable mode of media regulation, we simulated the effects of perfusion and fed-batch culture systems. A perfusion system (Figure 1F) is characterized by a continuous input of fresh media and output of spent media, while maintaining a constant volume, whereas a fed-batch system (Figure 1G) contains an input stream only, resulting in a continuous increase in culture volume. These cell culture systems are commonly used as feeding strategies for biopharmaceutical production (Farid, 2006), and previous studies have explored the use of perfusion systems for HSC culture (Koller et al., 1998). Simulations predicted that a fed-batch media dilution approach would achieve the most effective enhancement in stem and progenitor expansion and was predicted to outperform perfusion cultures and frequent media exchange strategies (Figures 1C–1G). Although all strategies act by reducing the concentration of accumulating secreted factors, the increasing culture volume of the fed-batch strategy additionally maintains lower cell densities, thereby slowing the rate and impact of endogenous factor accumulation.

The dilution rate (D) of a fed-batch culture system is defined as the input flow rate divided by the culture volume. This rate can be constant throughout the reaction period, proportional to the current volume of the culture or tuned based on predicted or measured parameters. As shown in Figure 1H, the volume of a culture initially containing 1 ml, will increase continuously with time depending on the defined dilution rate. Simulations predicted that the dilution rate would regulate the concentration of all secreted factors (Figure 1I), which in turn would regulate expansions of total nucleated cells (TNCs), colony-forming cells (CFCs), long-term culture-initiating cells (LTC-ICs), and SCID repopulating cells (SRCs) (Figure 1J). The slopes of the predicted increases in expansions are greatest from D = 0 to D = 1, suggesting that a significant impact on HSC expansion should be achievable at moderate dilution rates, while maintaining moderate media and cytokine needs.

Automated Closed System Fed-Batch Culture Enhances Progenitor Cell Expansion

We next undertook experiments to test the predicted superiority of the in silico optimized fed-batch strategy. These studies were

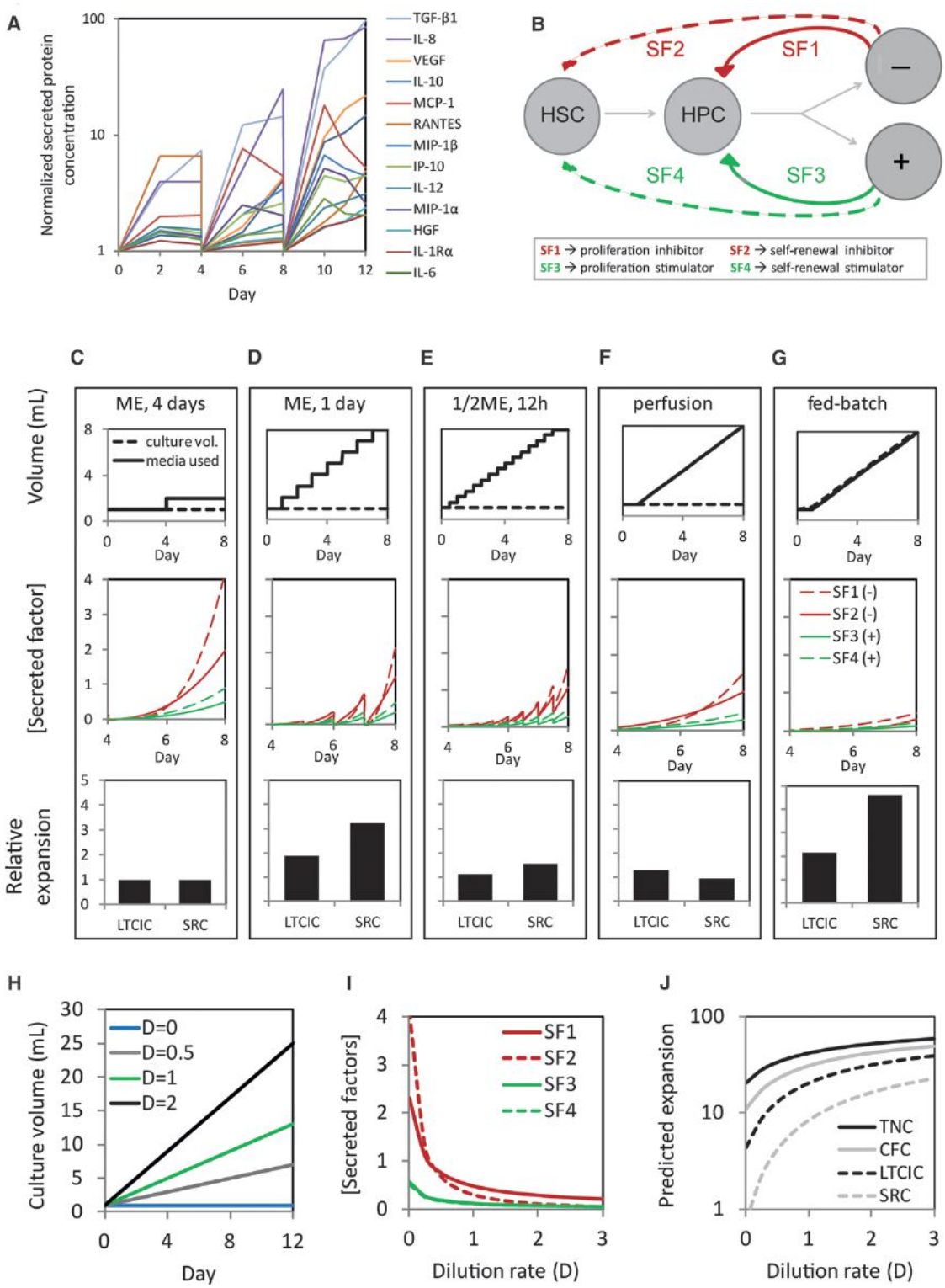

Figure 1. Computational Simulations Predict a Fed-Batch Strategy, at Moderate Dilution Rates, to Greatly Reduce Secreted Factor Concentrations and Give a Significant Enhancement of Expansion

(A) Time course of experimentally measured secreted factor concentrations from UCB culture, with complete media exchange every 4 days.

(B) Schematic of mathematical model, indicating the presence of paracrine feedback signaling. Groups of secreted factors are categorized depending on whether they act in a stimulatory or inhibitory manner and whether they impact stem cell self-renewal or proliferation.

(C–G) Simulated volume, secreted factor concentrations, and relative expansions under different media manipulation strategies: (C) "control" culture with complete media exchange (ME) every 4 days; (D) culture with complete media exchange every 24 hr; (E) culture with 50% media exchange every 12 hr; (F) perfusion

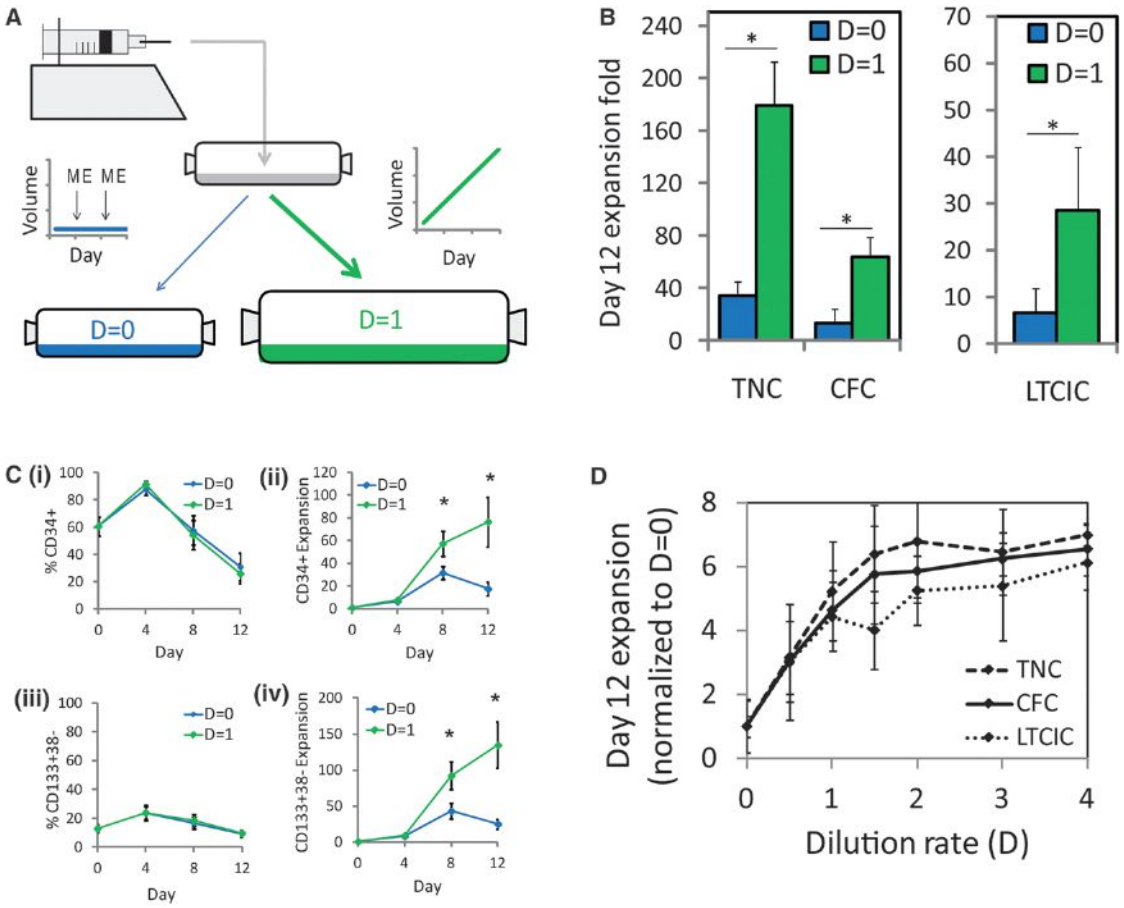

Figure 2. The Fed-Batch Strategy Is Experimentally Validated In Vitro to Give Significantly Improved Expansion of Progenitor Cells

(A) Schematic of experimental set-up comparing control (D = 0) strategy with 100% media exchange (ME) every 4 days to fed-batch (D = 1) strategy.

(B) Expansions of TNC, CFC, and LTC-IC, after 12 days of culture. n > 5.

(C) (i, iii) Surface marker analysis of $CD34^+$ and $CD133^+CD38^-$ frequencies throughout in vitro culture. (ii, iv) Expansion of $CD34^+$ cells and $CD133^+CD38^-$ cells, accounting for total cell expansion. n > 5.

(D) Normalized expansion of TNC, CFC, and LTC-IC after 12 days of culture, dependent on dilution rate. n = 3.

Data are expressed as mean ± SD. See also Figures S1 and S2.

facilitated with the use of an automated media delivery system (Csaszar et al., 2009). This system allows the user to control media input flow rates and enables the entire culture process to be performed in a closed system with minimal manual intervention. A constant flow rate, corresponding to a dilution rate of D = 1, was compared to our previously described optimal culture strategy (Madlambayan et al., 2005) (referred to here as D = 0) (Figure 2A).

We first confirmed that the D = 1 fed-batch strategy significantly outperformed the D = 0 control at our previously optimal day 8 endpoint (Figure S1). We next computationally predicted that the D = 1 strategy would achieve maximum expansions after 12 days of in vitro culture, because the regulation strategy inherent in the fed-batch system would allow for a positive rate of expansion to be maintained for a greater length of time (Figure S1). As shown in Figure 2B, the D = 1 strategy reached 12-day expansions of 179-fold (range 105- to 344-fold) of TNCs, 64-fold (22- to 166-fold) of CFCs, and 29-fold (14- to 53-fold) of LTC-ICs. Phenotypic analysis by flow cytometry (Figure 2C) indicated that the percentage of progenitor cells as measured by $CD34^+$ and $CD133^+CD38^-$ remained unchanged between the D = 0 and D = 1 cultures. However, the increased total cell expansion with the D = 1 strategy led to a significant increase in the absolute numbers of $CD34^+$ cells (80-fold) and $CD133^+CD38^-$ cells (135-fold). Similar results were found with $CD34^+CD90^+$ and $CD34^+CD49f^{hi}$ cells (Figure S1).

culture with one unit of media perfused every 24 hr; (G) fed-batch culture with one unit of media added every 24 hr. Conditions (D–G) are normalized to same media and cytokine requirements (one additional unit of media every 24 hr).

(H) Media volume requirements for a fed-batch culture at different constant dilution rates, assuming a 1 ml initial volume.

(I) Predicted effect of increasing constant dilution rate of fed-batch strategy on secreted factor concentrations.

(J) Predicted effect of increasing constant dilution rate of fed-batch strategy on population expansions.

To further validate our modeling predictions, we compared the fed-batch strategy to alternative strategies for the reduction of endogenously produced factors by investigating frequent media exchange approaches (Figure S2). Although small apparent improvements over the D = 0 cultures were achieved with frequent feeding strategies, these strategies produced significantly lower expansions than the D = 1 strategy, despite having the same overall media usage. We also assessed the effect of varying the dilution rate of the fed-batch culture. As predicted, the rate of increased expansion began to slow at dilution rates greater than D = 1, leading to diminishing returns of cell expansion at the expense of rapidly increasing media needs (Figure 2D). Taken together, these findings confirm our computational predictions of enhanced progenitor expansion achieved with a robust media dilution approach.

Global Maintenance of Subthreshold Levels of Inhibitory Factors Enables Fed-Batch-Mediated Expansion of Primitive UCB Cells

The observed enhancement in progenitor expansion was predicted to result from a global reduction in inhibitory paracrine factor levels in the culture media. To test this hypothesis, we investigated the effect of the fed-batch strategy on the output of specific mature blood cell types. Analysis of hematopoietic cell lineage markers did not reveal any change in the relative frequency of any of the differentiated cell types assessed ($CD14^+$, $CD7^+$, $CD41^+$, GyA^+, $CD33^+$, $CD19^+$, $CD56^+$, $CD8^+$, $CD4^+$) with the D = 1 strategy, as compared to the D = 0 control. Although the absolute number of cells in each of these populations was greater with the D = 1 strategy, resulting from the enhanced TNC expansion, the lower cell densities achieved with the D = 1 strategy resulted in lower concentrations (cells/ml) of each mature cell population (Figure S3).

We next asked how the reduction in mature cell concentrations would impact soluble factor concentrations. Figure 3A depicts the degree by which the concentration of each measured soluble factor was changed with the D = 1 strategy, as compared to D = 0. The nonlinear nature of factor accumulation means that the dynamics of individual factors and the degree by which the fed-batch strategy affects the concentration of specific factors varies; however, the net global reduction in factor concentrations provides an overall minimization of feedback inhibition in the culture system. Figure 3B highlights the concentration dynamics for several factors known to impact stem and progenitor growth, demonstrating the reduction of ligand concentrations achieved with the fed-batch strategy.

The functional effect of secreted ligand reduction on cell growth was further tested by culturing cells in media that had been previously conditioned for 8 days in a culture maintained with either the D = 0 or the D = 1 strategy. Exogenous cytokines (SCF, FL, TPO) were added to the conditioned media to ensure that the difference between the fresh and conditioned media was the presence of endogenously produced soluble factors. Both conditioned media led to a significant reduction in TNC expansions as compared to cultures utilizing fresh media, as expected. However, the expansion achieved with the D = 1 conditioned media were significantly greater than with the D = 0 conditioned media (Figure 3C). This shows the ability of reduced endogenous factor concentrations to better sustain primitive UCB cells in culture.

It remained unclear whether the fed-batch strategy was acting by simply regulating one or a few key inhibitory ligands or whether a more comprehensive (global) manipulation of the culture environment was important. To test this directly, we compared the D = 1 strategy to the targeted inhibition of TGF-β1, a known endogenous inhibitor of HSC growth (Fortunel et al., 2000). Targeted inhibition of TGF-β1 was achieved by adding the small molecule SB431542 to the culture every 4 days, a manipulation that yielded increases in progenitor cell expansions that approached those achieved by the fed-batch strategy on day 8. However, after 12 days of culture, TGF-β1 inhibition no longer had a significant effect on progenitor expansion (Figure 3D). This demonstrated that although some degree of culture regulation could be initially provided through the inhibition of one key endogenously produced factor, the impact of this approach is limited, particularly at the later time points of culture when the accumulation of many inhibitory factors is high, and targeting one factor alone is no longer effective.

In previous studies (Kirouac et al., 2010), we used expression analysis to identify 74 factors whose genes were upregulated during UCB culture. Many of these factors were hypothesized to be inhibitory to HSC growth and seven of these (TGF-β, TNFSF9, MIP-1α, MIP-1β, IP-10, NAP-2, SPARC) were experimentally validated to have an inhibitory effect on LTC-IC expansion. To investigate whether these factors contribute to HSC inhibition in an additive manner, we performed a combinatorial analysis of inhibitory soluble factors on $Lin^-Rho^{lo}CD34^+CD38^-CD45RA^-CD49f^+$ cells, which have been reported to be highly enriched for HSCs (Notta et al., 2011). The addition of TGF-β1 (10 ng/ml), MIP-1α (100 ng/ml), MIP-1β (100 ng/ml), and IP-10 (100 ng/ml) individually each caused a reduced expansion of this population after 7 days of culture, and the simultaneous addition of these four inhibitors produced a significant reduction of expansion, demonstrating that multiple inhibitory factors present in the culture system act in an additive manner (Figure 3E). Importantly, when lower concentrations (10 ng/ml each) of MIP-1α, MIP-1β, and IP-10 were used, the effect of the individual factors was negligible; however, the combination of the three led to reduced cell expansions (Figure 3F). This study illustrates how subthreshold levels of factors that individually do not provide significant inhibition can produce an inhibitory effect when acting in combination, highlighting the global nature of feedback inhibition.

In order to rule out the possibility that the fed-batch strategy was primarily acting by preventing critical metabolites from becoming limiting and inhibiting cell growth (Collins et al., 1997; Patel et al., 2000), we monitored the glucose and lactate concentrations of the media. Glucose levels did not become limiting under any of the culture conditions tested, including the D = 0 control, as shown by the fact that glucose concentrations below 7 mM were never observed (Figure S4). Furthermore, when glucose was added to the D = 0 culture in order to normalize the glucose levels to the corresponding D = 1 culture, no effect on expansion levels was observed (Figure S4). Lactate levels reached a maximum of 15 mM in the D = 0 cultures and the pH did not drop below 7.0, both of which were well within the range that support normal hematopoietic cell proliferation

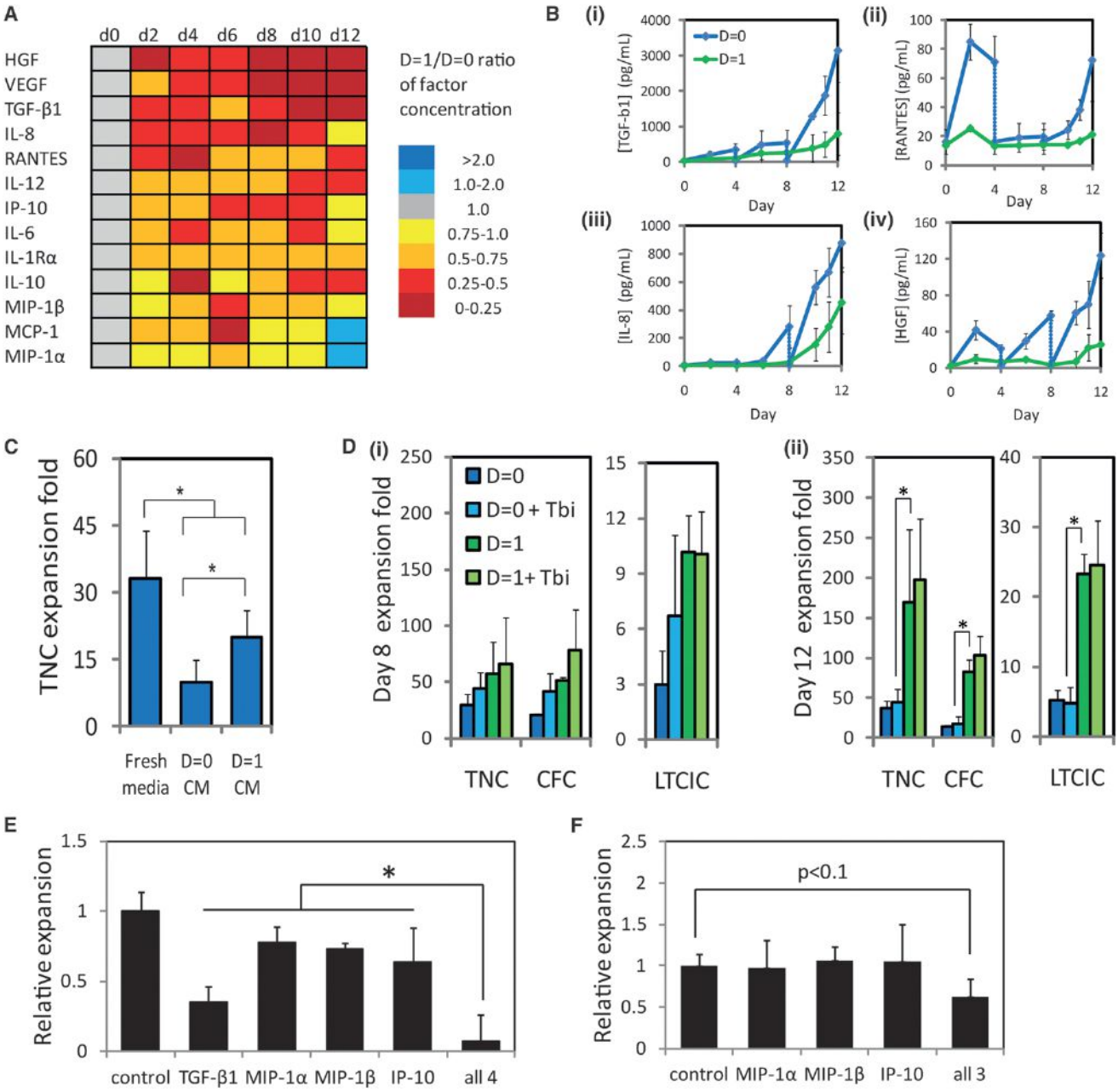

Figure 3. The Fed-Batch Strategy Enhances Expansion through the Global Reduction of Endogenously Produced Inhibitory Secreted Factors

(A) Heat map of secreted factor concentration ratios (D = 1/D = 0) showing the effect of the D = 1 strategy on secreted factor profiles as compared to the D = 0 strategy.

(B) Representative samples of reduction in secreted factor concentrations for: (i) TGF-β1; (ii) RANTES; (iii) IL-8; (iv) HGF with the D = 1 strategy as compared to the D = 0 strategy. n = 5.

(C) TNC expansion after 8 days of D = 0 culture with either fresh media or conditioned media (CM) from day 8 of previous D = 0 or D = 1 cultures. n = 3.

(D) Comparison of the fed-batch D = 1 strategy to the addition of a TGF-β1 small molecule inhibitor, SB431542, based on expansions of TNC, CFC, and LTC-IC at (i) day 8 and (ii) day 12. n = 3.

(E) Inhibitory factors, TGF-β1 (10 ng/ml), MIP-1α (100 ng/ml), MIP-1β (100 ng/ml), and IP-10 (100 ng/ml) were added to a sorted HSC population ($Lin^-Rho^{lo}CD34^+CD38^-CD45RA^-CD49f^+$), and total cell expansion was assessed after 7 days of culture. n = 3.

(F) Low concentrations of inhibitory factors, MIP-1α (10 ng/ml), MIP-1β (10 ng/ml), and IP-10 (10 ng/ml) were added to a sorted HSC population ($Lin^-Rho^{lo}CD34^+CD38^-CD45RA^-CD49f^+$), and total cell expansion was assessed after 7 days of culture. n = 3.

Data are expressed as mean ± SD. See also Figures S3 and S4.

(Figure S4; Patel et al., 2000). Collectively, these studies support the interpretation that the global reduction of inhibitory ligands was providing the supportive conditions for improved progenitor growth.

Transplantation Studies Show an 11-fold SRC Expansion under Fed-Batch Conditions

To determine whether the enhanced expansions observed with the progenitor populations would also apply to long-term repopulating HSCs (LTR-HSCs), we performed transplantation studies with the NSG mouse model (McDermott et al., 2010). Repopulation was quantified by bone marrow analysis for human hematopoietic cell contribution 16 weeks after transplantation, and freshly isolated (day 0) Lin^- UCB cells were compared to cells cultured for 8 or 12 days. Figure 4A shows representative flow cytometry plots of repopulated and nonrepopulated mice. For each condition tested, a dose response of average human contribution was seen, as determined by the quantification of human CD45 and HLA-ABC double-positive populations (Table S1).

All positively repopulated mice were found to have multilineage repopulation, as indicated by human cells that were positive for a myeloid lineage marker (CD33), a B cell lymphoid lineage marker (CD19), a T cell lineage marker (CD3), and an erythroid lineage marker (GyA). Representative plots are shown in Figures 4B and 4C and full details are presented in Table S2. Human progenitor cells were detected from 16-week transplanted mice by both surface marker analysis ($CD34^+$ and $CD133^+$) and CFC assays (Figures 4D and 4E). Cells from 8 mice repopulated for 16 weeks with day 12 D = 1 cells (19%–62% human cells in the marrow of primary recipients) were retransplanted into secondary mice to determine whether the culture-expanded cells had retained LTR-HSC activity. Five out of eight secondary mice were positive for human cells (human contribution ranging from 0.5% to 2.1%), all of which showed multilineage repopulation (Table S3), indicating that the expanded cells are able to maintain their long-term repopulation potential in vivo.

In order to quantify LTR-HSC expansion, limiting dilution analyses were performed (Figure 4F). The frequency of LTR-HSCs in the fresh Lin^- cells was 1 in 14,700 (95% CI: 1/8,659 to 1/24,979, n = 26). After 8 days of culture, the D = 1 culture produced a corrected LTR-HSC frequency of 1 in 1,940 (1 in 110,000 corrected for the concomitant 57-fold expansion of TNCs, 95% CI: 1/1,195 to 1/3,149, n = 33), giving a 7.6-fold LTR-HSC expansion, relative to the fresh cells. The D = 0 strategy gave a 3.6-fold LTR-HSC expansion, as reported previously (Ito et al., 2010; Madlambayan et al., 2005) (1 in 121,000 corrected for a 28-fold TNC expansion to give a 1 in 4,330 corrected frequency, 95% CI: 1/2,223 to 1/8,428, n = 17). We predicted that the 12 day culture would give the greatest LTR-HSC expansion, based on both computational simulations and progenitor assays. Indeed, the corrected LTR-HSC frequency after 12 days of culture was 1 in 1,334 (after a 1 in 233,000 frequency was corrected for 178× total cell expansion, 95% CI: 1/759 to 1/2,345, n = 24), producing an 11-fold LTR-HSC expansion. LTR-HSC frequencies were used to determine SRC numbers per 10^6 cells (Figure 4G).

Collectively, these results demonstrate that the fed-batch D = 1 culture strategy is effective at expanding clinically relevant numbers of mature cells, progenitor cells, and LTR-HSCs in a short (12 day) culture time with an automated closed system bioprocess.

The Fed-Batch Strategy Complements the Effects of Other of HSC-Enhancing Factors and Provides Insight into Their Modes of Action

The fed-batch strategy provides a means to assess the effect of feedback signaling under different conditions and thus serves as a platform to interrogate the mode of action of factors known to enhance blood stem and progenitor cell growth (Figure 5A). We hypothesized that HSC culture additives could be classified into two major categories depending on whether they act directly on HSC self-renewal or act indirectly on a mature cell population, which feeds back positively on HSCs. If the mode of action is HSC self-renewal specific, the fed-batch strategy should minimize inhibitory feedback signals, providing an enhancing environment for HSCs growth. Alternatively, if the mode of action is non-stem cell autonomous, the fed-batch strategy should dilute the mature cell population and dilute the soluble signaling molecules that have been produced. In this case, the fed-batch strategy should reduce the impact of the factor added.

To test this hypothesis, we investigated the interaction between the fed-batch culture and two known HSC growth-supportive factors, the aryl hydrocarbon receptor antagonist (SR1), and the transcription factor HOXB4. SR1 has been shown to enhance $CD34^+$ and HSC outputs by inhibiting HSC differentiation (Boitano et al., 2010). We thus predicted that the fed-batch strategy would complement the effect of SR1 by reducing the impact of endogenous inhibitory feedback signaling. Figure 5B demonstrates that under our culture conditions, SR1 produced an increase in LTC-IC expansion with both the D = 0 and D = 1 strategy, and the absolute levels of LTC-IC expansion were significantly enhanced with the D = 1 strategy. Primitive cell phenotypes were also enhanced with the addition of SR1 (Figure S5). To validate that this factor was acting directly on a population with a very primitive phenotype and not through a feedback-mediated response, we added the molecule to the $Lin^-Rho^{lo}CD34^+CD38^-CD45RA^-CD49f^+$ population. Figure 5C shows that treatment with SR1 leads to a significant increase in primitive ($CD34^+CD133^+CD90^+$) cells in this assay, illustrating that it is directly targeting a population that is highly enriched in HSCs. Given the apparent additive impact of SR1 and the fed-batch strategy on the output of primitive cell phenotypes, it is possible that combining these technologies under the conditions described herein will enhance the number of LTR-HSCs above that which has been obtained with the D = 1 strategy alone (Figure S5). However, because the $CD34^+CD133^+CD90^+$ phenotype has not been validated under these culture conditions, limiting dilution long-term transplantation studies are required to confirm the potential additive effects between these two technologies.

We next investigated the transcription factor HOXB4, which has been shown to increase stem and progenitor expansion by either viral overexpression or delivered as a TAT-HOXB4 soluble protein (Antonchuk et al., 2002; Csaszar et al., 2009; Krosl et al., 2003). HOXB4 has been shown to cause increases in the production of $CD41^+$ megakaryocytes (Zhong et al., 2010), a finding that we reproduced in our culture system with the TAT-HOXB4 protein (Figure S5). Notably, we have previously reported that $CD41^+$ cells have a stimulatory feedback effect on LTC-IC

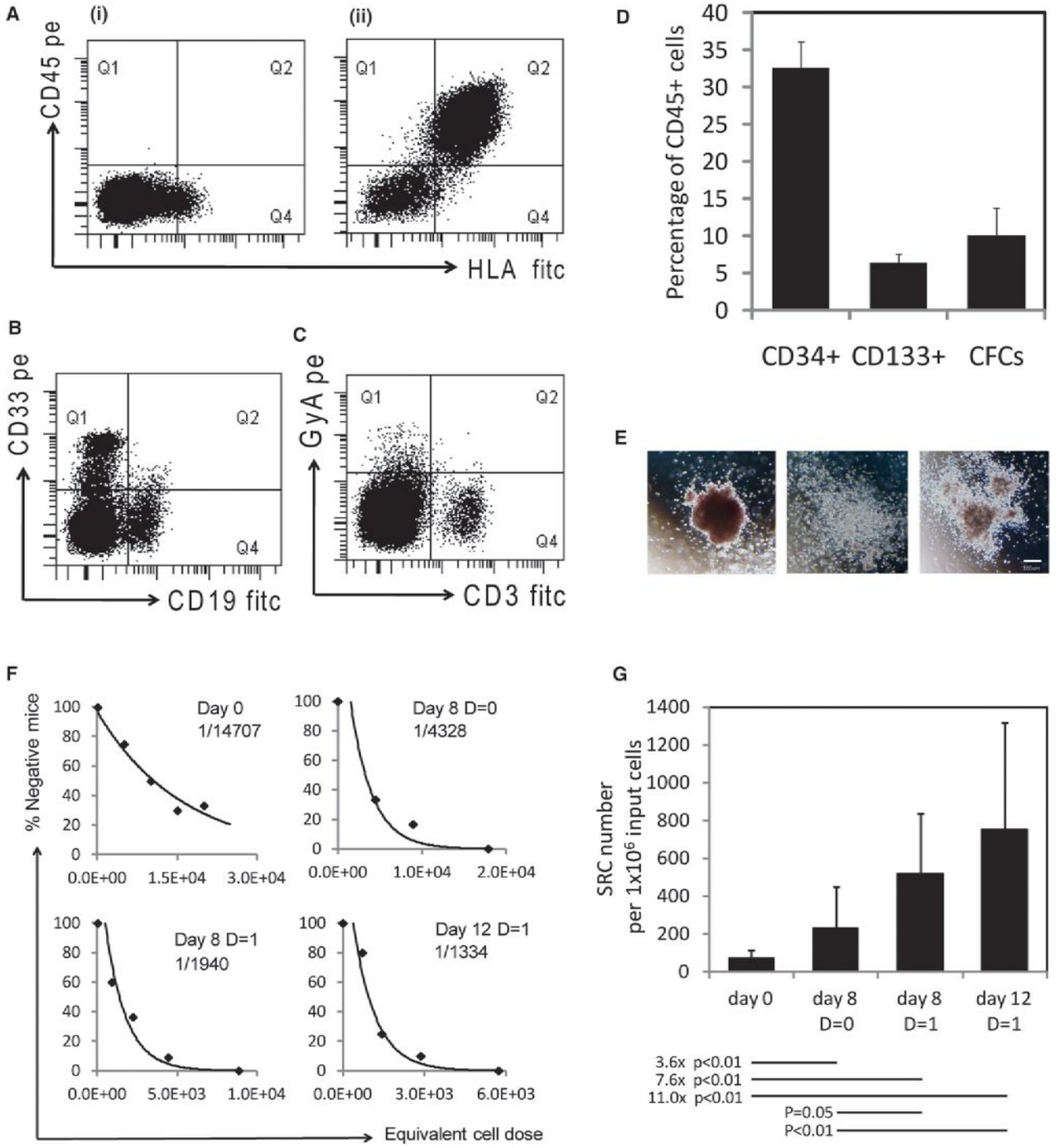

Figure 4. In Vivo SRC Assay with D = 1 Fed-Batch Strategy Shows an 11-fold Multilineage Expansion of LTR-HSCs

(A) Representative flow cytometry images of bone marrow analysis of (i) nonrepopulated and (ii) repopulated recipient mice. The quantification of the double-positive quadrant was used to determine the percentage donor contribution for each recipient.

(B and C) Representative images showing multilineage repopulation of recipients, as measured by $CD33^+$, $CD19^+$, GyA^+, and $CD3^+$.

(D) Quantification of progenitor cells in repopulated recipient mice.

(E) Representative images of CFCs formed with human cells from repopulated mice.

(F) Limiting dilution curves quantifying LTR-HSC contribution of uncultured (day 0) Lin^- cells; day 8 cells cultured with the D = 0 strategy; day 8 cells cultured with the D = 1 strategy; and day 12 cells cultured with the D = 1 strategy. LTR-HSC frequencies corrected to day 0 equivalent cell numbers are indicated for each. Data are fit with exponential curves.

(G) LTR-HSC expansions were used to calculate SRC numbers, based on 1×10^6 Lin^- cell input.

Results show the pooled data from two independent experiments. Data are expressed as mean ± 95% CI. See also Tables S1, S2, and S3.

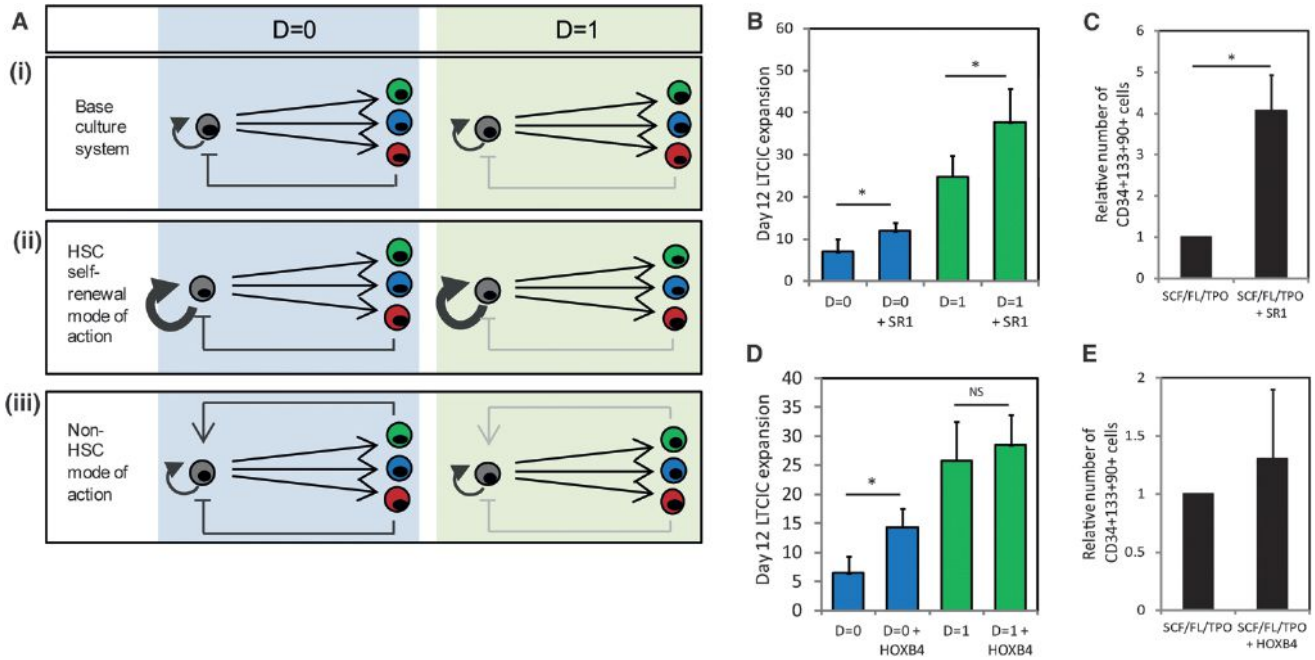

Figure 5. Fed-Batch System Complements the Effects HSC-Enhancing Molecules and Provides Insight into Their Mode of Action

(A) Schematic of in vitro expansion mode of action. (i) Under base conditions, static (D = 0) culture systems balance HSC self-renewal and feedback inhibition. The fed-batch (D = 1) strategy minimizes feedback, while allowing for self-renewal. (ii) The addition of a factor that targets HSC self-renewal gives increased self-renewal under both D = 0 and D = 1 conditions but the impact will be in enhanced with D = 1 conditions resulting from the reduced feedback. (iii) The addition of a factor with a positively acting indirect mode of action will increase stimulatory feedback signaling while maintaining self-renewal. Under D = 1 conditions, this stimulatory feedback will be reduced that will reduce the impact of the added factor.

(B) The addition of the aryl hydrocarbon receptor antagonist (SR1) gives a significant increase in LTC-IC expansion under both D = 0 and D = 1 conditions. n = 5.

(C) When added to a sorted HSC population ($Lin^-Rho^{lo}CD34^+CD38^-CD45RA^-CD49f^+$), SR1 shows an increase in $CD34^+CD133^+CD90^+$ numbers. n = 3.

(D) The addition of TAT-HOXB4 yields a significant increase in LTC-IC expansion under D = 0 conditions but not D = 1 conditions, suggesting a non-HSC mode of action. n = 5.

(E) TAT-HOXB4 shows minimal effect when added to the sorted $Lin^-Rho^{lo}CD34^+CD38^-CD45RA^-CD49f^+$ population. n = 3.

Data are expressed as mean ± SD. See also Figure S5.

expansion (Kirouac et al., 2010). Thus, we hypothesized that the mode of action of HOXB4 on UCB HSCs was, at least in part, resulting from an indirect feedback-mediated effect, as has also been suggested in ESC-derived hematopoiesis (Jackson et al., 2011). As Figure 5D shows, TAT-HOXB4 produced a significant increase in LTC-ICs when added to D = 0 conditions but the impact of the molecule was reduced with D = 1 conditions. Furthermore, TAT-HOXB4 did not produce a significant increase in expansion when added to $Lin^-Rho^{lo}CD34^+CD38^-CD45RA^-CD49f^+$ cells (Figure 5E). Collectively, these data provide further insight into the feedback signaling control mechanism that underpins the HSC-supportive effects of the fed-batch system.

DISCUSSION

A robust strategy to generate ex-vivo-expanded HSCs will enable the use of UCB for transplantation in patients for whom a single cord blood unit would not contain the desired progenitor content and ensure that a much greater proportion of current and future banked UCB units are applicable for use by any patient meeting the HLA matching criteria. In this study, we have computationally interrogated and experimentally validated a highly tunable hematopoietic progenitor cell expansion strategy that can produce 11 times more blood stem cells than originally present over a 12 day culture period. The short culture time and continuous tight regulation of cell densities also allows this system to have reduced media volume needs as compared to other expansion strategies, which is an important feature for cost-effective clinical implementation. This system has been designed to be adaptable for direct scale-up to accommodate cell numbers needed for human transplantations and we are planning to integrate this technology into clinical trials in the near future.

The fed-batch strategy relies on simplifying the complexity of dynamic and heterogeneous hematopoietic culture systems. In doing so, the need for targeted inhibition of individual endogenously produced factors is eliminated. We have previously shown evidence that mature hematopoietic cells and their associated secreted factors have a net inhibitory effect on stem cell self-renewal during in vitro culture (Madlambayan et al., 2005). Strategies to overcome this typically involve a significant amount of undesired manipulation and handling and provide only a temporary solution, because undesired factors will quickly reaccumulate after each manipulation. Perfusion cultures have been shown to enhance UCB progenitor cell expansion (Koller et al., 1998), but these cultures are subject to the challenge of high

cell densities and rapid factor reaccumulation. This challenge can be overcome with the use of higher perfusion flow rates, but this then fails to maintain desired usage limits of media and cytokines. The fed-batch strategy has the benefit of slowing the rate of factor accumulation through the continuous dilution of both endogenous factors and the cells that secrete these factors.

All current expansion strategies that rely on the direct regulation of the hematopoietic stem and progenitor cell populations are subject to the unregulated accumulation of inhibitory endogenous factors which, if unaccounted for, limit achievable expansion levels. Recent reports of human HSC expansion with apparently stem-cell-autonomous factors include SR1, producing a 17-fold LTR-HSC expansion (analyzed 16 weeks posttransplantation) after 21 days of in vitro culture, the immobilized Notch Delta-1 ligand described by Delaney et al. (2010) producing a 15.6-fold and 6.2-fold in vivo repopulation cell expansion (analyzed at 3 and 9 weeks posttransplantation, respectively) after 17–21 days of culture, and the growth factors Angiopoietin-like 5 and IGFBP2 (Zhang et al., 2008), producing a 14-fold repopulating cell expansion (analyzed at 8 weeks posttransplantation in NOD/SCID recipients) after 10 days of culture. The fed-batch strategy reported here gives a LTR-HSC expansion of comparable magnitude with a 12 day culture time and a conservative 16 week posttransplantation analysis. Because this strategy affects nonautonomous feedback regulation and acts on the microenvironment of the culture system, it suggests strong potential to synergize with primarily autonomously acting expansion strategies, the combinations predicted to lead to greater and more sustained cell expansions.

It is clear that in vitro (and in vivo) hematopoiesis is dynamic and regulated, at least in part, through nonlinear feedback control. The trajectories of factor secretion vary widely among individual factors and do not always correlate with the exponential trajectory of total cell expansion. Factor concentration dynamics may follow the dynamics of specific lineage subpopulations or may result from multiple interacting feedback networks. Moving to nonlinear media dilution strategies is one example of how more sophisticated dilution dynamics can be predicted to further tune regulatory interaction and HSC growth in the system. In order to maximize this control, a feedback-regulated system in which a set of critical factors is measured, either ''offline'' by ELISA assay or ''online'' with the adaption of current technologies to quantify multiple soluble factors in real-time (Klostranec et al., 2007), could be linked to a threshold level process control mechanism. This should allow for the dilution strategy to be tuned in real-time and would provide a means to account for sample-to-sample biological variability, ensuring that optimal expansion can be achieved for each specific cord blood unit.

The fed-batch strategy is a globally acting expansion strategy amenable for clinical use, alone or in combination with other expansion protocols. It also provides a platform with which to more closely study the dynamic nature of the in vitro hematopoietic cell culture system. We have illustrated how the fed-batch strategy has different effects when acting in combination with factors that directly or indirectly enhance HSC growth. These studies provide insight into the mode of action of the aryl hydrocarbon receptor antagonist SR1 and the TAT-HOXB4 protein, through the differing effect that the D = 1 strategy has on their efficacy. More broadly, they demonstrate that regulating feedback signaling can act to reduce inhibitory feedback, thereby allowing factors that target HSC self-renewal to act with maximal impact.

The ability to modulate secreted factor concentrations and measure corresponding functional outputs of cell expansions will allow for a more precise study of links between specific endogenous protein secretion and lineage subpopulations and their associated cell-cell interactions. This strategy serves as a robust clinically relevant system for rapid and automated in vitro cell expansion as well as a platform for further study of the regulation of cell-cell interactions in vitro and in vivo.

EXPERIMENTAL PROCEDURES

Mathematical Simulations

The model that we previously developed and described (Kirouac et al., 2009) was used to run all culture simulations with MATLAB 2009 software (Mathworks, Natick, MA). The model simulates in vitro hematopoietic culture by incorporating self-renewal and differentiation of cell populations and soluble factors secreted by mature cells. For this study, the model was adapted to simulate fed-batch and perfusion strategies by adjusting the rate of change of secreted factor concentrations. The fed-batch strategy incorporated a continuous input stream, which resulted in an increase in culture volume and a dilution of all cells and all endogenously produced secreted factors. The perfusion strategy included a continuous input and output stream, resulting in a constant cell culture volume and a continuous reduction of endogenously produced soluble factors. See Supplemental Experimental Procedures for details.

Umbilical Cord Blood Cell Collection and Processing

UCB samples were collected from consenting donors according to ethically approved procedures at Mt. Sinai Hospital (Toronto, ON, Canada). Mononuclear cells were obtained as previously described (Kirouac et al., 2009). Lineage-negative (Lin^-) progenitor cells were isolated from the mononuclear cell fraction with the StemSep system or EasySep system with the human progenitor cell enrichment kit (StemCell Technologies, Inc., Vancouver, BC, Canada), according to the manufacturer's protocol.

Cell Seeding and In Vitro Culture

Freshly isolated Lin^- cells were seeded at an initial density of 1×10^5 cells/ml in serum-free IMDM media (GIBCO, Rockville, MD) with 20% BIT serum substitute (StemCell Technologies) and 1% Glutamax (GIBCO). The media was supplemented with 100 ng/ml Stem Cell Factor (SCF, R&D Systems, Minneapolis, MN), 100 ng/ml FMS-like Trysine Kinase 3 Ligand (FL, R&D Systems), 50 ng/ml Thrombopoietin (TPO, R&D Systems), and 1 μg/ml low-density lipoproteins (LDL, Calbiochem, La Jolla, CA). The syringe loaded pumping system was assembled and connected to the cell culture bag, as previously described (Csaszar et al., 2009). The initial cell suspension was injected into a 2-port 12 ml culture bag (VueLife, American Fluoroseal Corporation, Gaithersburg, MD) and maintained on an orbital shaker at 37°C and 5% CO_2. The pump was set to deliver the desired volume of media (based on the user-defined dilution rate) to the cell culture. Media delivery was automated to occur at 0.5 hr intervals at a flow rate of 30 μl/min, for a semicontinuous delivery. For SR1 studies, SR1 was added to fresh media at 0.75 μM as previously described (Boitano et al., 2010). For TAT-HOXB4 studies, TAT-HOXB4 was produced and delivered semicontinuously as previously described (Csaszar et al., 2009; Krosl et al., 2003).

Cell Assays

Colony-forming cell (CFC) assays and long-term culture-initiating cell (LTC-IC) assays were performed as previously described (Kirouac et al., 2009). Surface marker staining was performed with conjugated human antibodies: CD4, CD7, CD8, CD14, CD19, CD33, CD34, CD38, CD41, CD49f, CD56, CD90, CD133, and GyA (BD Biosciences, San Jose, CA).

7-AAD dye was added to assess cell viability and isolate live cells for quantification. All samples were analyzed on a FACSCanto flow cytometer (BD Biosciences).

Sorted Cell Assay

Freshly isolated Lin^- cells were sorted for $Rho^{lo}CD34^+CD38^-CD45RA^-CD49f^+$ with a FACSAria flow cytometer (BD Biosciences), according to the gating strategy previously described (Notta et al., 2011). 40 sorted cells were dispensed per well in a 96-well plate in the above-described media and cultured for 7 days. After culture, cells were assessed for total cell number and number of $CD34^+CD133^+CD90^+$ cells by flow cytometry.

Limiting Dilution Transplantation Studies

All animal studies were performed according to procedures approved by appropriate animal ethics boards. Female NSG mice were sublethally irradiated (250 rad) <24 hr before transplantation. Uncultured Lin^- cells (n = 26) or cells cultured for 8 days (n = 50) or 12 days (n = 25) were transplanted at limiting dilution via tail vein injection. Mice were sacrificed 16 weeks after transplantation and bone marrow was collected from femurs and tibias. Cells were assessed by flow cytometry. Mice were scored positive for human repopulation if at least 0.5% of bone marrow cells were positive for both human CD45 and human HLA-ABC. For secondary transplantations, 33% of the harvested bone marrow cells of positively engrafted mice were transplanted into secondary NSG recipients. Bone marrow harvest and analysis was performed after 16 weeks. All limiting dilution analysis was performed with the L-calc software (StemCell Technologies, Inc.). Limiting dilution analysis was based on the combined data of two independent transplantation studies.

Secreted Factor Analysis

Secreted factor concentrations were sampled in duplicate from conditioned media samples using the Human Cytokine 30-Plex panel (Invitrogen, Burlington, ON, Canada), designed for the Luminex microsphere detection platform (Luminex Co. Austin, TX), to screen for EGF, Eotaxin, FGF-β, G-CSF, GM-CSF, HGF, IFN-α, IFN-γ, IL-1β, IL-IRA, IL-2, IL-2R, IL-4, IL-5, IL-6, IL-7, IL-8, IL-10, IL-12, IL-13, IL-15, IL-17, IP-10 (CXCL10), MCP-1 (CCL2), MIG (CLCL9), MIP-1α (CCL3), MIP-1β (CCL4), RANTES (CCL5), TNF-α, and VEGF. Samples were prepared and assessed with a BD FACSCanto flow cytometer, as previously described (Kirouac et al., 2009). TGF-β1 was analyzed separately in parallel, with a TGF-β1 Quantikine ELISA Kit (R&D Systems, Minneapolis, MN), according to the manufacturer's directions.

Glucose and Lactate Assay

Conditioned media samples were analyzed for glucose levels, with the Amplex Red Glucose/Glucose Oxidase Assay kit (Invitrogen), according to the manufacturer's protocol. In the subsequent glucose normalization study, D-glucose was added to the D = 0 cell culture media every 2 days. Lactate concentrations were analyzed with a L-lactate assay kit (Eton Bioscience, San Diego, CA), according to the manufacturer's protocol.

Statistical Analysis

Statistical significance was computed via a Student's t test. All error bars represent the standard deviation of three or more biological replicates. Asterisks indicate statistical significance between conditions of $p < 0.05$.

SUPPLEMENTAL INFORMATION

Supplemental Information includes Supplemental Experimental Procedures, five figures, and three tables and can be found with this article online at doi:10.1016/j.stem.2012.01.003.

ACKNOWLEDGMENTS

The authors thank the donors and the Research Centre for Women's and Infants' Health BioBank of Mount Sinai Hospital for the human specimens used in this study. The authors thank Dr. Connie Eaves and members of the P.W.Z. laboratory for their helpful discussion. This work was funded by the Leukemia and Lymphoma Society of Canada, the Canadian Stem Cell Network, the Canadian Institutes for Health Research (MOP-57885), and the Ontario Ministry of Research and Innovation. E.C. and D.C.K. were supported by NSERC Graduate Scholarships. P.W.Z. is the Canada Research Chair in Stem Cell Bioengineering.

Received: September 15, 2011
Revised: December 15, 2011
Accepted: January 6, 2012
Published: February 2, 2012

REFERENCES

Antonchuk, J., Sauvageau, G., and Humphries, R.K. (2002). HOXB4-induced expansion of adult hematopoietic stem cells ex vivo. Cell *109*, 39–45.

Benveniste, P., Frelin, C., Janmohamed, S., Barbara, M., Herrington, R., Hyam, D., and Iscove, N.N. (2010). Intermediate-term hematopoietic stem cells with extended but time-limited reconstitution potential. Cell Stem Cell *6*, 48–58.

Boitano, A.E., Wang, J., Romeo, R., Bouchez, L.C., Parker, A.E., Sutton, S.E., Walker, J.R., Flaveny, C.A., Perdew, G.H., Denison, M.S., et al. (2010). Aryl hydrocarbon receptor antagonists promote the expansion of human hematopoietic stem cells. Science *329*, 1345–1348.

Bonnet, D., Lemoine, F.M., Najman, A., and Guigon, M. (1995). Comparison of the inhibitory effect of AcSDKP, TNF-alpha, TGF-beta, and MIP-1 alpha on marrow-purified CD34+ progenitors. Exp. Hematol. *23*, 551–556.

Broxmeyer, H.E., and Kim, C.H. (1999). Regulation of hematopoiesis in a sea of chemokine family members with a plethora of redundant activities. Exp. Hematol. *27*, 1113–1123.

Broxmeyer, H.E., Cooper, S., Hague, N., Benninger, L., Sarris, A., Cornetta, K., Vadhan-Raj, S., Hendrie, P., and Mantel, C. (1995). Human chemokines: enhancement of specific activity and effects in vitro on normal and leukemic progenitors and a factor-dependent cell line and in vivo in mice. Ann. Hematol. *71*, 235–246.

Cashman, J.D., Eaves, C.J., Sarris, A.H., and Eaves, A.C. (1998). MCP-1, not MIP-1alpha, is the endogenous chemokine that cooperates with TGF-beta to inhibit the cycling of primitive normal but not leukemic (CML) progenitors in long-term human marrow cultures. Blood *92*, 2338–2344.

Collins, P.C., Nielsen, L.K., Wong, C.K., Papoutsakis, E.T., and Miller, W.M. (1997). Real-time method for determining the colony-forming cell content of human hematopoietic cell cultures. Biotechnol. Bioeng. *55*, 693–700.

Csaszar, E., Gavigan, G., Ungrin, M., Thérien, C., Dubé, P., Féthière, J., Sauvageau, G., Roy, D.C., and Zandstra, P.W. (2009). An automated system for delivery of an unstable transcription factor to hematopoietic stem cell cultures. Biotechnol. Bioeng. *103*, 402–412.

Delaney, C., Heimfeld, S., Brashem-Stein, C., Voorhies, H., Manger, R.L., and Bernstein, I.D. (2010). Notch-mediated expansion of human cord blood progenitor cells capable of rapid myeloid reconstitution. Nat. Med. *16*, 232–236.

Durand, E.M., and Zon, L.I. (2010). Newly emerging roles for prostaglandin E2 regulation of hematopoiesis and hematopoietic stem cell engraftment. Curr. Opin. Hematol. *17*, 308–312.

Dykstra, B., Kent, D., Bowie, M., McCaffrey, L., Hamilton, M., Lyons, K., Lee, S.J., Brinkman, R., and Eaves, C. (2007). Long-term propagation of distinct hematopoietic differentiation programs in vivo. Cell Stem Cell *1*, 218–229.

Farid, S.S. (2006). Established bioprocesses for producing antibodies as a basis for future planning. Adv. Biochem. Eng. Biotechnol. *101*, 1–42.

Fortunel, N.O., Hatzfeld, A., and Hatzfeld, J.A. (2000). Transforming growth factor-beta: pleiotropic role in the regulation of hematopoiesis. Blood *96*, 2022–2036.

Gluckman, E. (2009). History of cord blood transplantation. Bone Marrow Transplant. *44*, 621–626.

Hofmeister, C.C., Zhang, J., Knight, K.L., Le, P., and Stiff, P.J. (2007). Ex vivo expansion of umbilical cord blood stem cells for transplantation: growing knowledge from the hematopoietic niche. Bone Marrow Transplant. *39*, 11–23.

Ito, C.Y., Kirouac, D.C., Madlambayan, G.J., Yu, M., Rogers, I., and Zandstra, P.W. (2010). The AC133+CD38-, but not the rhodamine-low, phenotype tracks LTC-IC and SRC function in human cord blood ex vivo expansion cultures. Blood *115*, 257–260.

Jackson, M., Axton, R.A., Taylor, A.H., Wilson, J.A., Gordon-Keylock, S.A., Kokkaliaris, K., Brickman, J.M., Schulz, H., Hummel, O., Hubner, N., and Forrester, L.M. (2011). HOXB4 can enhance the differentiation of embryonic stem cells by modulating the haematopoietic niche. Stem Cells, in press. Published online November 14, 2011.

Kirouac, D.C., Madlambayan, G.J., Yu, M., Sykes, E.A., Ito, C., and Zandstra, P.W. (2009). Cell-cell interaction networks regulate blood stem and progenitor cell fate. Mol. Syst. Biol. *5*, 293.

Kirouac, D.C., Ito, C., Csaszar, E., Roch, A., Yu, M., Sykes, E.A., Bader, G.D., and Zandstra, P.W. (2010). Dynamic interaction networks in a hierarchically organized tissue. Mol. Syst. Biol. *6*, 417.

Klostranec, J.M., Xiang, Q., Farcas, G.A., Lee, J.A., Rhee, A., Lafferty, E.I., Perrault, S.D., Kain, K.C., and Chan, W.C. (2007). Convergence of quantum dot barcodes with microfluidics and signal processing for multiplexed high-throughput infectious disease diagnostics. Nano Lett. *7*, 2812–2818.

Koller, M.R., Manchel, I., Maher, R.J., Goltry, K.L., Armstrong, R.D., and Smith, A.K. (1998). Clinical-scale human umbilical cord blood cell expansion in a novel automated perfusion culture system. Bone Marrow Transplant. *21*, 653–663.

Krosl, J., Austin, P., Beslu, N., Kroon, E., Humphries, R.K., and Sauvageau, G. (2003). In vitro expansion of hematopoietic stem cells by recombinant TAT-HOXB4 protein. Nat. Med. *9*, 1428–1432.

Madlambayan, G.J., Rogers, I., Kirouac, D.C., Yamanaka, N., Mazurier, F., Doedens, M., Casper, R.F., Dick, J.E., and Zandstra, P.W. (2005). Dynamic changes in cellular and microenvironmental composition can be controlled to elicit in vitro human hematopoietic stem cell expansion. Exp. Hematol. *33*, 1229–1239.

Majka, M., Janowska-Wieczorek, A., Ratajczak, J., Ehrenman, K., Pietrzkowski, Z., Kowalska, M.A., Gewirtz, A.M., Emerson, S.G., and Ratajczak, M.Z. (2001). Numerous growth factors, cytokines, and chemokines are secreted by human CD34(+) cells, myeloblasts, erythroblasts, and megakaryoblasts and regulate normal hematopoiesis in an autocrine/paracrine manner. Blood *97*, 3075–3085.

McDermott, S.P., Eppert, K., Lechman, E.R., Doedens, M., and Dick, J.E. (2010). Comparison of human cord blood engraftment between immunocompromised mouse strains. Blood *116*, 193–200.

Notta, F., Doulatov, S., Laurenti, E., Poeppl, A., Jurisica, I., and Dick, J.E. (2011). Isolation of single human hematopoietic stem cells capable of long-term multilineage engraftment. Science *333*, 218–221.

Patel, S.D., Papoutsakis, E.T., Winter, J.N., and Miller, W.M. (2000). The lactate issue revisited: novel feeding protocols to examine inhibition of cell proliferation and glucose metabolism in hematopoietic cell cultures. Biotechnol. Prog. *16*, 885–892.

Rizo, A., Vellenga, E., de Haan, G., and Schuringa, J.J. (2006). Signaling pathways in self-renewing hematopoietic and leukemic stem cells: do all stem cells need a niche? Hum. Mol. Genet. *15* (Spec No 2), R210–R219.

Sautois, B., Fillet, G., and Beguin, Y. (1997). Comparative cytokine production by in vitro stimulated mononucleated cells from cord blood and adult blood. Exp. Hematol. *25*, 103–108.

Wagner, J.E., and Gluckman, E. (2010). Umbilical cord blood transplantation: the first 20 years. Semin. Hematol. *47*, 3–12.

Zhang, Y., Harada, A., Bluethmann, H., Wang, J.B., Nakao, S., Mukaida, N., and Matsushima, K. (1995). Tumor necrosis factor (TNF) is a physiologic regulator of hematopoietic progenitor cells: increase of early hematopoietic progenitor cells in TNF receptor p55-deficient mice in vivo and potent inhibition of progenitor cell proliferation by TNF alpha in vitro. Blood *86*, 2930–2937.

Zhang, C.C., Kaba, M., Iizuka, S., Huynh, H., and Lodish, H.F. (2008). Angiopoietin-like 5 and IGFBP2 stimulate ex vivo expansion of human cord blood hematopoietic stem cells as assayed by NOD/SCID transplantation. Blood *111*, 3415–3423.

Zhong, Y., Sullenbarger, B., and Lasky, L.C. (2010). Effect of increased HoxB4 on human megakaryocytic development. Biochem. Biophys. Res. Commun. *398*, 377–382.